Semi-classical Theories of Quantum Magnets

A Dissertation Presented for the

Doctor of Philosophy

Degree

The University of Tennessee, Knoxville

Hao Zhang

August 2022

© by Hao Zhang, 2022
All Rights Reserved.

世之奇伟、瑰怪，非常之观，常在于险远，而人之所罕至焉，故非有志者不能至也

Acknowledgments

I want to express my deep gratitude to my advisor, Prof. Cristian Batista, for teaching me from the ABCs of condensed matter physics to several original research ideas that led to this dissertation. Furthermore, I have been greatly influenced and benefited by his novel and critical way of thinking about physics problems through numerous enlighting discussions during my Ph.D. Cristian is also a constant source of inspiration beyond physics. He offered me considerable guidance to improve my communication skills, which I will benefit from for the rest of my career. Foremost, Cristian always treats me with care, patience, and respect, for which I will be forever grateful. ¡Gracias, profesor!

The atmosphere of Cristian's research group at the University of Tennessee, Knoxville (UTK) is visibly supportive and encouraging. Therefore, I want to thank all the past and current members of the group, including Dr. Shangshun Zhang, Dr. Zhentao Wang, Prof. Hidemaro Suwa, (soon to be) Dr. Vikram Sharma, Dr. Esteban ("Colo") Ghioldi, and Dr. David Dahlbom. Specifically, I want to thank Shangshun for teaching me various analytical many-body techniques and Zhentao for helping me set up numerical methods for simulating skyrmions. Both of them are always patient with my naive and stupid questions. In addition, I want to thank Maro for the exciting discussions about machine learning applications in physics and for playing soccer with me. I want to thank Vikram for many interesting talks throughout the years and for sharing the happiness and sorrow of being a young researcher with me. I want to thank Colo for many illuminating discussions on the Schwinger boson approximation. Special thanks to Colo for introducing me to the spirit drink of South America—Yerba Mate. The "mateine" has helped with the writing of this dissertation. Finally, I want to thank David for bringing new perspectives to me on physics problems and for reading this dissertation and correcting grammatical mistakes.

The work discussed in this dissertation could not have been finished without incredible collaborations with brilliant experimentalists. So, first of all, I want to thank Dr. Andrew Christianson for letting me get involved in his experimental group at the Oak Ridge National Laboratory (ORNL). I had many valuable discussions directly with him and with his postdocs/students, which helped me understand better the reality of my calculation. I want to specifically thank Andy and his postdoc Dr. Seunghwan Do, for providing fantastic neutron scattering data on $Ba_2FeSi_2O_7$ to test our theories. Moreover, I appreciate Hwan's patience in making nice figures after several rounds of corrections in my calculation. The collaboration with Prof. Martin Mourigal's group at Georgia Tech on the compound FeI_2 produced another series of excellent results. Martin and (back then, his student, now soon to be) Prof. Xiaojian Bai always came to us with high quality data and interesting ideas. I think their high standards of scientific conduct are one of the most important secrets leading to the success of our collaborations. Special thanks to Xiaojian for inviting Shangshun and me to join the on-the-beamline analysis for FeI_2. That was an unforgettable and unusual experience for me as a theorist.

Nothing could be more exciting than having a group of people work relentlessly to improve some of our ideas and transform them into an advanced open-source code package. Therefore, I want to thank all people in the `Sunny.jl` group led by Dr. Kipton Barros and Dr. Ying-Wai Li at Los Alamos National Laboratory (LANL), including Xiaojian, Cole Miles, Cristian, David Brooks, David D., Leandro Chinellato, Martin, Dr. Matthew Wilson, and Dr. Sakib Matin. The weekly "Sunny" meeting is always fruitful and stimulating. I also want to thank Kipton and Ying-Wai for inviting me to join these discussions and teaching me the parallel tempering method.

I want to thank all the members of my Ph.D. committee for their service and for providing valuable critiques during my Ph.D., including Prof. Steven Johnston, Prof. Haidong Zhou, Prof. David Mandrus, and Dr. Shizeng Lin (LANL).

I also want to thank all my friends in Knoxville for their help, for organizing exciting parties, and for some unforgettable conversations. Specifically, I want to thank my roommates and best friends in Knoxville, Dr. Zichao Yang and (soon to be) Dr. Xin Wen, for their help when I am in trouble and their cheers for my success. Special thanks to the

staff member of the physics department of UTK Ms. Chrisanne Romeo for her countless help in solving my problems as an international student.

I am deeply indebted to my family. I want to thank my father, Shaohai Zhang, and my mother, Kunrong Deng, for their unconditional love and support. They are the first teachers of my life and will forever be my role models. Words are simply not enough to express my gratitude. Upon writing this acknowledgment, I understand this ancient Chinese quote more deeply "谁言寸草心，报得三春晖" . Lastly, I want to thank my cat "Mi" for his company and for sleeping on my keyboard and typing words into this dissertation "n b jmujhfgvhgbnhhbfvg" (the only remaining sentence after endless deletions). I wish him a healthy and happy cat life.

This dissertation was partially supported by the U.S. Department of Energy, Office of Science, Basic Energy Sciences, Materials Sciences and Engineering Division. The author also acknowledges the additional support from the Shull Wollan Center Graduate Research Fellowship and the Graduate Advancement, Training, and Education (GATE) fellowship.

Abstract

Recent progress in magnetism has been driven by embracing the complexity associated with entangled spin, orbital, and lattice degrees of freedom, and by understanding the emergent quantum behaviors of magnetic systems. Over the past decades, intense efforts have been devoted to "extreme quantum materials," comprising low-dimensional lattices of spin $S = 1/2$ degrees of freedom, that are candidates to host quantum spin liquid phases with no classical counterpart. Finite-spin ($S \geq 1$) systems that exhibit ground states with short-ranged entanglement have not been the center of much attention because they are expected to behave semi-classically. However, as we will demonstrate in this dissertation, the traditional classical limit ($1/S$ expansion) does not work for large classes of finite-spin systems, which still admit an accurate classical or semi-classical treatment. To address this important problem, we will exploit the fact that N-level systems admit more than one classical limit. As we will demonstrate in this dissertation, different classical limits lead to different generalizations of the so-called Landau-Lifshitz dynamics. In particular, we will introduce a generalized classical spin dynamics based on coherent states of SU(N), where N is the dimension of the local Hilbert space. This new approach also allows the generalization of the semi-classical spin dynamics ($1/S$-expansion) from SU(2) to SU(N), providing a better approximation that incorporates quantum effects in the spin dynamics of large classes of realistic spin Hamiltonians, including $S \geq 1$ systems with large single-ion anisotropy and weakly coupled multi-spin units, such as dimers, trimers or tetramers. Besides developing the mathematical formalism, we illustrate these ideas by comparing our theoretical predictions against inelastic neutron scattering data of two realistic effective $S = 1$ iron-based compounds. In the last part of this dissertation, we generalize the concepts of the magnetic skyrmions by taking alternative classical limits of quantum spin systems. In

particular, we report the emergence of magnetic CP^2 skyrmions in realistic spin-1 models based on SU(3) coherent states.

Table of Contents

1 Introduction **1**

2 The classical limit of a spin system **12**

2.1 Lie groups, Lie algebras, representation theory, and coherent states 13

2.1.1 Properties of a group 13

2.1.2 Lie group, Lie algebra, and representations 14

2.1.3 Coherent states of a Lie group 19

2.2 Coherent states and classical limits 23

2.3 Classical spin dynamics 29

2.3.1 Classical equations of motion for spins 30

2.3.2 Single-ion model 35

2.3.3 Single-dimer problem 42

2.4 Numerical methods 49

2.4.1 Monte Carlo sampling on CP^{N-1} 50

2.4.2 Dynamical spin structure factor (classical) 51

3 Applications of the classical spin dynamics **53**

3.1 Motivation 53

3.2 The $Ba_2FeSi_2O_7$ compound 53

3.3 Inelastic neutron scattering data 55

3.4 Simulation details 57

3.5 Comparison with experiments 57

3.6 Conclusions 61

4 Generalized spin wave theory **62**

4.1 Introduction . . . 62

4.2 SU(2) spin wave theory . . . 63

4.3 SU(N) spin wave theory . . . 64

4.3.1 SU(N) Schwinger boson representation . . . 64

4.3.2 Choice of N . . . 66

4.3.3 $1/M$-expansion . . . 66

4.3.4 Dynamical spin structure factor (quantum) . . . 74

5 Applications of the generalized spin wave theory **80**

5.1 Decay and renormalization of a longitudinal mode in $Ba_2FeSi_2O_7$ . . . 81

5.1.1 Introduction: longitudinal mode in spin-1 magnets . . . 81

5.1.2 Inelastic neutron scattering data . . . 83

5.1.3 Generalized spin wave theory calculations . . . 85

5.1.4 Comparison with INS experiments . . . 91

5.1.5 Conclusions . . . 96

5.2 Many-body effects observed in FeI_2 . . . 97

5.2.1 Introduction: two magnon bound state in spin-1 magnets . . . 97

5.2.2 The FeI_2 compound . . . 99

5.2.3 Non-interacting theory: The hybridization mechanism . . . 100

5.2.4 Perturbative approach: The field-induced decay of quasi-particles . . . 104

5.2.5 Non-perturbative approach: The effects of 4-magnon bound states . . . 109

5.2.6 Conclusions . . . 110

6 CP^2 Skyrmions and Skyrmion crystals **111**

6.1 Introduction: magnetic skyrmions and their generalization . . . 111

6.2 Spin-1 model . . . 113

6.3 Methods and simulation details . . . 115

6.4 Phase diagram . . . 117

6.4.1 SkX phases . . . 117

6.4.2 Single-**Q** orderings . . . 117

6.4.3 Modulated double-**Q** orderings . . . 119
6.4.4 3**Q** spiral orderings . . . 119
6.5 Large-D limit . . . 121
6.6 Discussion . . . 124

7 Conclusions and outlooks **127**

Bibliography **131**

Appendices **149**
A Representation of SU(3) . . . 150
A.1 Fundamental representation . . . 150
A.2 Adjoint representation . . . 151
B Symplectic structure on the manifold of coherent states . . . 153
B.1 Some concepts from differential geometry . . . 153
B.2 Classical phase space . . . 160
C Classical to quantum correspondence . . . 165
D Miscellaneous calculations for the SU(N) spin wave theory . . . 171
D.1 Bogoliubov transformation for boson operators . . . 171
D.2 Single-particle Green's function G . . . 172
D.3 Matsubara sum in the continuum channel . . . 172
E Supplemental Info for Sec. 5.1 . . . 174
E.1 Expressions for the generalized linear spin-wave calculation . . . 174
E.2 Cubic vertex functions . . . 174
E.3 Quartic vertex . . . 176
E.4 One-loop diagrams in the long-wavelength limit . . . 177
E.5 Estimation of the quantum critical point (QCP) . . . 178
F Berry phase and solid angle in CP^2 . . . 182
F.1 Continuum limit . . . 182
F.2 On the lattice . . . 185
G Mapping between color field and SU(3) coherent states . . . 188

Vita **189**

List of Tables

5.1 The parameters of the effective $S = 1$ model extracted by fitting the Gaussian-peak centers of the experimental dispersion with the GLSWT and GLSWT + one loop calculated energies at the zone center $\boldsymbol{Q}_m = (1, 0, 0.5)$. In both cases, we assume $\tilde{J}' = 0.1\tilde{J}$, and $\tilde{\Delta} = \tilde{\Delta}' = 1/3$, i.e. $\Delta = \Delta' = 1$ for the $S = 2$ model (Heisenberg model without exchange anisotropy). The parameter set is referred to by its label ($\mathcal{A}$ or $\mathcal{B}$) in the text. 92

5.2 The best GLSWT fitting parameters in units of **Kelvin** (K) of inelastic neutron-scattering data for FeI_2. 105

List of Figures

1.1 Frustration leads to degeneracy. The triangular lattice in the Ising limit (left). The Kagome lattice AFM (right). 7

2.1 Comparisons of the transverse dynamical spin structure factor between the quantum (red triangle) and the SU(2) classical results (black line) for three different spin values: (a) $S = 1$, (b) $S = 10$, and (c) $S = 1000$. In all three panels, the inverse temperature $\beta DS^2 = 10^{-5}$, and the values of the dynamical structure factor are normalized to the maximum intensity of the exact result. 37

2.2 Comparison of the transverse dynamical spin structure factor for the $S = 1$ single-ion model as a function of the energy transfer at the inverse temperature $\beta DS^2 = 0.1$: quantum (red star), SU(3) classical (blue cross), and SU(2) classical (black line). 40

2.3 Comparisons of $\mathcal{S}^{\alpha\alpha}(\pi, \omega)$ for the single dimer as a function of the energy transfer at the inverse temperature $\beta J = 0.1$: quantum (red star), SU(4) classical (blue cross), and SU(2) classical (black line). 44

2.4 The spin ladder problem. **a.** The original problem: J denotes the exchange interactions between the dimers (rungs of the ladder) and J' labels the inter-dimer exchange interactions (along the legs of the ladder); $m = d, u$ is the label of the two chains. **b.** The SU(4) representation: The anisotropic "exchange" model with an exchange tensor $\mathcal{J}^{\mu\nu}(J')$ in a "magnetic field" $\boldsymbol{\mathcal{B}}(J)$. 48

3.1 (a) Crystal structure of $Ba_2FeSi_2O_7$. Ba atoms separate layers (with exchange interaction J') composed of $FeSi_2O_7$, resulting in a quasi-two-dimensional structure. (b) In-plane magnetic unit cell formed by Fe^{2+} with exchange interaction J. (c) The Brillouin zone. The coordinates (H K L) of the reciprocal lattice of the origin lattice are related to (k_x k_y k_z) of the magnetic lattice formed by the Fe^{2+} atoms through $k_x = 2\pi(H-K)$, $k_y = 2\pi(H+K)$, and $k_z = 2\pi L$. (d) Illustration of the spin fluctuation modes. T_1 and T_2 indicate transverse fluctuation in the ab-plane and out-of the plane, respectively. L indicates longitudinal fluctuation of spin. 54

3.2 (a) Orbital energy states of Fe^{2+} with a tetrahedral crystal field (Δ_{Td}), tetragonal distortion (δ_{Tetra}), and spin orbit coupling (λ). (b) The left panel shows inelastic neutron scattering data measured at T=90 K, symmetrized over negative and positive H and integrated over L=[0.9, 2.1] and K=[-0.1,0.1]. The integrated scattering intensity over H=[-2, 2] is shown in the right panel. The two peaks were fitted with Gaussian functions (solid blue line). Arrows indicate the peak centers at 1.32 meV and 3.2 meV. 54

3.3 (a) Contour maps of the INS data as a function of energy and momentum transfer along the $[H, 0, 1.5]$ direction measured at T = 1.6 K, 6 K, 10 K, and 40 K. The T_1, T_1, and L indicate the acoustic and optical transverse modes, and the longitudinal mode in the spectra. (b) Resolution convoluted INS intensities calculated by the LLD method at the temperatures indicated in each subpanel. (c) Polarized neutron scattering at $\boldsymbol{Q} = (1, 0, 0)$ measured at 10 K ($T > T_N$). The Non-spin-flip (spin-flip) channel for the z-polarization response correspond to the transverse (longitudinal) component of $I(\boldsymbol{Q}, E)$. The green-shaded region indicates the magnetic INS response extracted by fitting a DLDHO function to data. (d) Green (red) shaded region indicates the transverse (longitudinal) component of $I(\boldsymbol{Q}, E)$ calculated by LLD. . . . 56

3.4 (a) Measured constant momentum scans at the ZC with temperatures below $T_{\rm N}$ and (b) corresponding calculated spectra from LLD. The transverse and longitudinal modes are indicated with labels 'T_1', 'T_2', and 'L'. (c) Comparison of the measured and calculated momentum scans above $T_{\rm N}$. The spectral weight for the resonant excitation (longitudinal mode) arising above $T_{\rm N}$ (below $T_{\rm N}$) was fitted with DLDHO function, and the fitting results are indicated by the shaded regions. The extracted spectral shapes of the resonant modes are compared with the LLD calculations shown by the blue solid line in (c). (d)(e) Comparison of contour plots of the constant momentum scans between data and LLD calculation across $T_{\rm N}$. 60

3.5 (a) Comparison of the measured energy scans at the ZC above $T_{\rm N}$ and $I(\boldsymbol{Q}, E)$ (b) At T=10 K and (c) at T=40 K, with the results obtained from LLD simulations with renormalized SU(3) spins ($n^{\eta}_{\boldsymbol{r}} \to \kappa n^{\eta}_{\boldsymbol{r}}$). 60

4.1 In terms of the SU(2) Schwinger bosons (SBs), we have $\hat{S}^z = (b_1^\dagger b_1 - b_2^\dagger b_2)/2$. Left panel: the total number of SBs is $M = 1$ in the fundamental representation of SU(2). Right panel: $M = 2$ for the $S = 1$ representation of SU(2). 65

4.2 (a) The interaction vertex $V_i^{(n)}$. (b) An example diagram that contributes to the self-energy Σ with $L = 2$ loops, $I = 5$ internal lines, and $n = 4$ cubic vertices $V^{(3)}$. (c) Diagrammatic representation of the Dyson equation $\mathcal{G} = \mathcal{G}_0 + \mathcal{G}_0\Sigma\mathcal{G}$ [equivalent to (4.16)]: the blue bold line denotes the dressed (interacting) quasi-particle propagator $\mathcal{G}$ and the thin line denotes the bare (non-interacting) propagator $\mathcal{G}_0$. 72

5.1 Schematic phase diagram illustrating the O(2) quantum critical point (QCP) between the antiferromagnetic (AFM) state and the quantum paramagnet (QPM) as a function of J/D (J is a Heisenberg exchange and D is a easy-plane single-ion anisotropy). The low-energy excitations of the QPM are two degenerate $S^z=\pm 1$ modes (black line) with a gap, Δ, which closes at the QCP. The spontaneous U(1) symmetry breaking leads to a gapless magnon or transverse mode ($T-$mode), indicated with a blue line, which is accompanied by a gapped longitudinal mode ($L-$mode) indicated with the orange line. Near the QCP, the energy and the lifetime of the $L-$mode are strongly renormalized (dashed orange line) due to the decay into the continuum of two transverse modes (shaded orange region). 82

5.2 (a) Contour map of the inelastic neutron scattering (INS) data as a function of energy and momentum transfer along the [H,0,0.5] direction measured at T=1.6 K ($< T_{\rm N}$) using the HYSPEC time-of-flight spectrometer at SNS. (d) Contour map of the INS data as a function of energy and momentum transfer along [H,H,0.5] direction measured at T=1.4 K ($< T_{\rm N}$) using the cold Neutron Triple-Axis spectrometer (CTAX) at HFIR. The instrumental resolutions at dE=2.5 meV for each instrument are indicated with blue bars along the y-axis in (a) and (d). The two transverse modes and the longitudinal mode are labeled with T_1, T_2, and L, respectively. (b),(c),(e), and (f) INS intensities calculated by the generalized linear spin wave theory (GLSWT) and GLSWT plus one-loop corrections (GLSWT+one-loop) with the parameter sets $\mathcal{A}$ and $\mathcal{B}$ given in Table 5.1, respectively. The instrumental resolution of HYSPEC and CTAX was modeled in the calculated spectra using a Lorentzian function. 84

5.3 Basic ingredients of the perturbative field theory in $1/M$ for $Ba_2FeSi_2O_7$. Solid (dash) lines represent the bare propagator of the transverse (longitudinal) boson. The symmetry-allowed cubic vertices are shown on the second and third lines. The red (blue) dot represents a decay (sink) vertex. The cubic-linear vertices are listed on the fourth line. The last line represents the normal vertex $V_{\alpha\alpha}^{(4,N)}$ from $\mathcal{H}^{(4)}$. 89

5.4 Diagrammatic representation of the Dyson equation for $Ba_2FeSi_2O_7$. (a) One-loop diagrams that contribute up to the order M^0 for the transverse boson. (b) One-loop diagrams that contribute up to the order M^0 for the longitudinal boson. The dressed propagator is denoted by a thick line, whereas the bare propagator is denoted by a thin line. 89

5.5 Comparison of the measured and calculated dispersion along the $[H, 0, 0.5]$ (a, b) and $[H, H, 0.5]$ (c, d) directions. In all panels of this figure, the theoretical results are obtained for the parameter set $\mathcal{B}$ in Table 5.1. a–d Blue and orange filled circles indicate the measured transverse and longitudinal modes. Dots and error bars indicate peak centers and full width at half maxima (FWHM) of the observed modes, respectively. Lines indicate the calculated dispersions obtained from the GLSWT and GLSWT+one-loop corrections. The red-shaded region in b and d depict the decay (line broadening) of the longitudinal mode given by the one-loop corrections. e–g Comparison between the measured (blue dots) and calculated (orange and black lines) INS intensities at three high-symmetric $\boldsymbol{Q}$-points at (1, 0, 0.5), (0, 0, 0.5), and (0.5, 0.5, 0.5). For GLSWT, two transverse and longitudinal modes are denoted with T_1, T_2, and L. 92

5.6 Kinematic constraints for the decay of the longitudinal mode. The blue (orange) curve shows the calculated transverse (longitudinal) band dispersions along $[H, 0, 0.5]$ with the GLSWT (using parameters set $\mathcal{B}$ in Table 5.1). The light blue-shaded areas indicate the two-transverse mode continuum, whose lower edge is indicated with a black solid line ($E_2^{\mathbf{min}}$). **a** Results of the effective $S = 1$ model. **b** Same as **a** but for a gapped branch of transverse modes (an ad hoc gap has been added to Eq. (5.5)). 94

5.7 Single-ion states of Fe^{2+} ions accessible at low energy correspond to $S = 1$ magnetic moments with uniaxial anisotropy. The sketches represent a plane of spins in the **a** ground state configuration, and examples of **b** a one-magnon elementary excitation, **c** a two-magnon bound-state (TMBS), **d** a 4-magnon bound-state, **e** a 4-magnon anti-bound-state, and **f** a 6-magnon bound-state. The grey shadows represent the particular spins that are deviated as compared to the ground state. Reprinted from Fig. 1 of Ref. [91]. 98

5.8 **a.** Local coordination environment of Fe^{2+} ions and hierarchy of single-ion energy-scales. **b.** Trigonal crystal structure of FeI_2, showing triangular layers of Fe^{2+} ions and resulting symmetry-inequivalent magnetic exchange pathways, mediated by I^- ligands, up to third nearest neighbors in-plane (J_1, J_2, J_3) and fourth nearest neighbors out-of-plane $(J_0', J_1', J_{2a}', J_{2b}')$. **c.** Magnetic structure of FeI_2, showing ferromagnetic planes (gray) arranged in a up-up-down-down (blue-blue-green-green) sequence. 101

5.9 **a.** Energy-resolved neutron-scattering intensity collected at $T = 1.8$ K. White boxes indicate symmetry-equivalent positions in reciprocal space with large intensity disparities that are predicted by a Heisenberg model with the usual Fe^{2+} form factor. **b.** Generalized spin-wave theory fit to the data using the anisotropic model. **c.** Hybridization effect from anisotropic exchange interaction $J^{z\pm}$ represented through the relative weight of $b^\dagger_{i,-1}$ (TMBS, red) and b_{i0} (one-magnon, blue) in a given excitation eigenvector. 101

5.10 (Left). All symmetry-allowed cubic interaction vertices between initial single-quasiparticle and final two-quasiparticle states for a $S = 1$ system. The green and red lines represent propagators for the SM and TMBS quasiparticles, respectively. The processes highlighted in gray are the relevant magnon decay channels in FeI_2. (Right). Effect of a magnetic field on the kinematic condition underlying decay processes. The Zeeman shift of a given (initial or final) state α depends on the total spin quantum number $[\Delta S^z]_\alpha$ as $E_\alpha(H) = -g\mu_B\mu_0 H[\Delta S^z]_\alpha$ where $g = 3.8$. Decays are kinematically allowed if $E_{\text{final}}(H) - E_{\text{inital}}(H) \leq 0$. 105

5.11 **Magnetic field dependence of neutron scattering spectra of FeI_2 and comparison with SU(3)-generalized linear spin-wave (GLSW) calculations.** **a**, Momentum- and energy-dependence of the neutron-scattering intensity at $T = 1.8$ K and $\mu_0 H = 0$, 1 and 2 T (AF phase). Momenta perpendicular to the $(h, -0.5h, 0)$ cut direction are integrated over $|\Delta k| \leq 0.05$ and $|\Delta l| \leq 0.05$. The arrows mark and track the dominant character of the corresponding bands: solid green for single-magnon (SM) and dashed red for single-ion two-magnon bound-states (TMBS). **b**, Same cuts at $\mu_0 H = 3$ and 4 T revealing departures from GLSW calculations. The black arrows mark the energy of a 4-magnon excitation, originating from the binding of two single-ion bound-states by exchange interactions, and effect not accounted for by GLSW calculations as highlighted by the white double-sided arrow. The yellow dashed box indicates regions of momentum-energy where excitations lineshape are dramatically broadened, indicating strong magnon decay. **c-d**, Constant-**Q** cuts through the data (open symbols) and GLSW predictions (lines) for various magnetic fields highlighting: **c**, the 4-magnon bound-state as an extra peak shoulders around $E \approx 2.5$ meV for $h = -0.8$ and $\mu_0 H = 3$ and 4 T (dashed arrows), and **d**, magnon decay around $E \approx 3.5$-4.5 meV for $h = -0.5$ and $\mu_0 H = 3$ T (dashed box). 106

5.12 SU(3)-generalized non-linear spin-wave (GNLSW) calculations at the one-loop order for in the $(h, -0.5h, 0)$ cut direction showing in turn: the renormalized spectra + kinematic conditions for decay, decay rate, and realistic neutron scattering intensity. **A** 3 T. **B** 4 T. In the left-most panels for both **A** and **B**, The eight hybridized bands are numbered and color-coded to reflect the value of ΔS^z they carry as a function of momentum-transfer. Shaded regions indicate two-particle continua. 108

6.1 $T = 0$ phase diagram of the classical Hamiltonian $\mathcal{H}$ as a function of the single-ion anisotropy D and the external field h, for $J_2/|J_1| = 2/(1+\sqrt{5})$ and $\Delta = 2.6$. The two insets show the phases for small-D and large-D, respectively. The solid (dashed) lines indicate 1st- (2nd-) order phase transitions. 116

6.2 **a**, **b** Real space distribution of the dipolar sector of the CP^2 skyrmion crystals SkX-I and SkX-II. The length of the arrow represents the magnitude of the dipole moment of the color field $|\langle \hat{\boldsymbol{S}}_j \rangle| = \sqrt{(n_j^7)^2 + (n_j^5)^2 + (n_j^2)^2}$. The color scale of the arrows indicates $\langle \hat{S}_j^z \rangle = -n_j^2$. The insets display the static spin structure factors $\mathcal{S}^{\perp}(\boldsymbol{q}) = n_{\boldsymbol{q}}^7 n_{\bar{\boldsymbol{q}}}^7 + n_{\boldsymbol{q}}^5 n_{\bar{\boldsymbol{q}}}^5$ and $\mathcal{S}^{zz}(\boldsymbol{q}) = n_{\boldsymbol{q}}^2 n_{\bar{\boldsymbol{q}}}^2$, with $\boldsymbol{n}_{\boldsymbol{q}} = \sum_j e^{i\boldsymbol{q}\cdot\boldsymbol{r}_j} \boldsymbol{n}_j / L$. The CP^2 skyrmion density distribution ρ_{jkl} [see Eq. (6.8)] is indicated by the color of the triangular plaquettes 118

6.3 Real space distribution of the dipolar sector of the color fields for the three single-$\boldsymbol{Q}$ orderings. **a** MVS-I. **b** MVS-II. **c** CS. The length of the arrow represents the magnitude of the dipole moment of the color field $|\langle \hat{\boldsymbol{S}}_j \rangle| = \sqrt{(n_j^7)^2 + (n_j^5)^2 + (n_j^2)^2}$. The color scale of the arrows indicates $\langle \hat{S}_j^z \rangle = -n_j^2$. The insets display the static spin structure factors $\mathcal{S}^{\perp}(\boldsymbol{q}) = \langle n_{\boldsymbol{q}}^7 n_{\bar{\boldsymbol{q}}}^7 + n_{\boldsymbol{q}}^5 n_{\bar{\boldsymbol{q}}}^5 \rangle$ and $\mathcal{S}^{zz}(\boldsymbol{q}) = \langle n_{\boldsymbol{q}}^2 n_{\bar{\boldsymbol{q}}}^2 \rangle$, with $\boldsymbol{n}_{\boldsymbol{q}} = \sum_j e^{i\boldsymbol{q}\cdot\boldsymbol{r}_j} \boldsymbol{n}_j / \sqrt{N}$. 120

6.4 Real space distribution of the dipolar sector of the color fields for the three modulated double-$\boldsymbol{Q}$ orderings: **a** MDQ-I, **b** MDQ-II, and **c** MDQ-III. The length of the arrow represents the magnitude of the dipole moment of the color field $|\langle \hat{\boldsymbol{S}}_j \rangle| = \sqrt{(n_j^7)^2 + (n_j^5)^2 + (n_j^2)^2}$. The color scale of the arrows indicates $\langle \hat{S}_j^z \rangle = -n_j^2$. The insets display the static spin structure factors $\mathcal{S}^{\perp}(\boldsymbol{q}) = \langle n_{\boldsymbol{q}}^7 n_{\bar{\boldsymbol{q}}}^7 + n_{\boldsymbol{q}}^5 n_{\bar{\boldsymbol{q}}}^5 \rangle$ and $\mathcal{S}^{zz}(\boldsymbol{q}) = \langle n_{\boldsymbol{q}}^2 n_{\bar{\boldsymbol{q}}}^2 \rangle$, with $\boldsymbol{n}_{\boldsymbol{q}} = \sum_j e^{i\boldsymbol{q}\cdot\boldsymbol{r}_j} \boldsymbol{n}_j / \sqrt{N}$. The CP^2 skyrmion density distribution ρ_{jkl} [see Eq. (16) of the main text] is indicated by the color of the triangular plaquettes in all three panels. 120

6.5 Real space distribution of the dipolar sector of the color fields for the three $3\boldsymbol{Q}$ spiral orderings: **a** $3\boldsymbol{Q}$S-I, **b** $3\boldsymbol{Q}$S-II, and **c** $3\boldsymbol{Q}$S-III. The length of the arrow represents the magnitude of the dipole moment of the color field $|\langle\hat{\boldsymbol{S}}_j\rangle| = \sqrt{(n_j^7)^2 + (n_j^5)^2 + (n_j^2)^2}$. The color scale of the arrows indicates $\langle\hat{S}_j^z\rangle = -n_j^2$. The insets display the static spin structure factors $\mathcal{S}^{\perp}(\boldsymbol{q}) = \langle n_{\boldsymbol{q}}^7 n_{\bar{\boldsymbol{q}}}^7 + n_{\boldsymbol{q}}^5 n_{\bar{\boldsymbol{q}}}^5\rangle$ and $\mathcal{S}^{zz}(\boldsymbol{q}) = \langle n_{\boldsymbol{q}}^2 n_{\bar{\boldsymbol{q}}}^2\rangle$, with $\boldsymbol{n}_{\boldsymbol{q}} = \sum_j e^{i\boldsymbol{q}\cdot\boldsymbol{r}_j}\boldsymbol{n}_j/\sqrt{N}$. The CP^2 skyrmion density distribution ρ_{jkl} [see Eq. (16) of the main text] is indicated by the color of the triangular plaquettes in all three panels. 122

6.6 Spectrum of the single-ion model $\hat{\mathcal{H}}_{\mathrm{SI}} = D(\hat{S}^z)^2 - h\hat{S}^z$. The shaded region denotes the effective regime with a quasi-degenerate doublet: $\{|0\rangle, |1\rangle\}$. . . . 122

6.7 Dipolar sector of CP^2 skyrmions. The color scale indicates the value of n_j^2 ($\langle\hat{S}_j^z\rangle$). **a**, **b** Skyrmion excitation on top of a QPM background. **c**, **d** Skyrmion excitation on top of a fully polarized background. $J_2/|J_1| = 2/(1+\sqrt{5})$ and $\Delta = 2.6$ in (a), (c), and (d). $J_2/|J_1| = 2/(3+\sqrt{5})$ and $\Delta = 2.2$ in **b**. In these panels, **a**. $D = 17.1|J_1|$, $H = 13|J_1|$. **b**. $D = 18.3|J_1|$, $H = 14|J_1|$. **c**. $D = 7|J_1|$, $H = 5|J_1|$. **d**. $D = 4|J_1|$, $H = 2|J_1|$. 125

1 The AFM order on a square lattice at $T = 0$ 166

2 Dispersion relations for the longitudinal mode L obtained from the SU(3) generalized linear spin wave theory (GLSWT) calculation (black line), GLSWT+one-loop correction calculation (red stars), and the non-perturbative calculation (blue triangles) described in this section. The orange vertical line denotes the position corresponding to the AFM ordering wave vector $\boldsymbol{q} = (\pi, \pi, \pi)$ in the magnetic lattice or $(1, 0, 0.5)$ in the chemical lattice. All results in this figure are obtained by using parameter set $\mathcal{B}$ listed in Table 5.1. 181

Chapter 1

Introduction

Magnetism was discovered in the ancient world. The first well-known application was the magnetic compass, the earliest examples of which are from the 11th century. People in Europe and China started using the so-called *lodestone*, which would align itself from north to south (pole of the Earth) if allowed to move freely. This property turned out to be crucial for navigation. A lodestone is actually a piece of naturally magnetic iron or magnetite Fe_3O_4, which is the etymology of the word *ferromagnetism*. In a more modern formulation, ferromagnetic materials are those which undergo a phase transition into a state that spontaneously breaks time reversal symmetry below the so-called Curie temperature. The characteristic of this state is that the electronic magnetic moments become spontaneously aligned along a given direction. The origin of ferromagnetism must be attributed to intrinsic magnetic interactions between electrons. Without these interactions, and in absence of an external magnetic field, the magnetic moments would be thermally disordered, i.e., pointing randomly in different directions. Dipole-dipole interactions can be ruled out as the possible origin of ferromagnetism in most materials because this interaction is of the order of 10^{-5} eV$\simeq$ 0.1 K for two electrons that are separated by distance of a few angstroms [15], whereas the observed magnetic Curie temperatures are of the order 10^2–10^3 K (10^{-3}–10^{-2} eV). It was not until the early days of quantum mechanics that scientists understood the microscopic origin of ferromagnetism. This state of matter derives from four fundamental properties of electrons [16]: 1. The electron's spin; 2. The electron's kinetic energy; 3. The Pauli exclusion principle; 4. Coulomb repulsion between electrons.

As a first approach, we can try to understand the microscopic origin of the magnetic coupling by considering two electrons that are spatially localized by an external potential and repel each other through the Coulomb interaction (Here we follow Auerbach [16]). We will find out that the nature of non-interacting states determines the sign of interaction: ferromagnetic vs. antiferromagnetic. First, we consider two electrons in two nearly degenerate but *orthogonal* single-particle states: two electrons can occupy either or both of the two states. Recall that due to the Fermi statistics (Pauli exclusion principle), the full state (orbital times spin) of the two-electron system must be antisymmetric: if the orbital state is symmetric the spin state must be antisymmetric and vice versa. To reduce the effect of the Coulomb repulsion, two electrons may align with each other to form a symmetric spin state, forcing an antisymmetric orbital state with zero probability of finding both electrons at the same point (when the Coulomb interaction is largest). This quantum mechanical property leads to an effective *ferromagnetic* (FM) interaction between the spins of both electrons that explains the first Hund's rule (the effective ferromagnetic interaction is of the order one eV for valence electrons that occupy different orbitals of the same atom).

Let us consider now the simplest model for a Mott insulator, that is a two-site Hubbard model with two electrons (one electron per orbital on average):

$$\mathcal{H} = -t \sum_{\sigma} (c_{1\sigma}^{\dagger} c_{2\sigma} + h.c.) + U \sum_{i=1,2} n_{i\uparrow} n_{i\downarrow}. \tag{1.1}$$

The hopping amplitude t accounts for the finite electronic tunneling between the two orbitals[1] and U is the on-site Coulomb repulsion. The off-site Coulomb interaction is ignored here because we are assuming that the screening length is very short. The Hilbert space of this half-filled two-site fermonic system has dimension six because the Pauli exclusion principle rules out the possibility of two parallel spins on the same site. This means that we can exactly diagonalize the two-site Hamiltonian.[2] The first step is to choose a basis. We note that the total spin is a good quantum number because the Hamiltonian is invariant under

[1] The first term is sometimes referred as the "kinetic" energy (hopping integral of the tight-binding model), which has an overall minus sign because the hopping term includes the combined effect of the actual kinetic energy of electrons and their attractive interactions with the lattice to be bounded in a solid.

[2] This is not possible for large (more than a few tens of sites) system size due to the exponential growth of Hilbert space dimension.

global spin rotations:

$$[\boldsymbol{S}_{\rm tot}, \mathcal{H}] = 0, \tag{1.2}$$

where

$$S^z_{\rm tot} = \frac{1}{2}(n_{1\uparrow} - n_{1\downarrow}) + \frac{1}{2}(n_{2\uparrow} - n_{2\downarrow}),\ S^+_{\rm tot} = c^\dagger_{1\uparrow}c_{1\downarrow} + c^\dagger_{2\uparrow}c_{2\downarrow},\ S^-_{\rm tot} = (S^+_{\rm tot})^\dagger. \tag{1.3}$$

As a result, we can categorize the six basis states according to the eigenvalues of $\boldsymbol{S}^2_{\rm tot}$ and $S^z_{\rm tot}$. The $S_{\rm tot} = 1$ subspace is generated by the triplet

$$|S_{\rm tot} = 1\rangle_1 = |\uparrow,\uparrow\rangle, \quad |S_{\rm tot} = 1\rangle_2 = |\downarrow,\downarrow\rangle, \quad |S_{\rm tot} = 1\rangle_3 = \frac{1}{\sqrt{2}}(|\uparrow,\downarrow\rangle + |\downarrow,\uparrow\rangle), \tag{1.4}$$

while the $S_{\rm tot} = 0$ subspace has also dimension three

$$\begin{aligned}
|S_{\rm tot} = 0\rangle_1 &= \frac{1}{\sqrt{2}}(|\uparrow\downarrow, 0\rangle + |0, \downarrow\uparrow\rangle), \\
|S_{\rm tot} = 0\rangle_2 &= \frac{(|\uparrow,\downarrow\rangle - |\downarrow,\uparrow\rangle) + (|\uparrow\downarrow, 0\rangle - |0,\uparrow\downarrow\rangle)}{2}, \\
|S_{\rm tot} = 0\rangle_3 &= \frac{(|\uparrow,\downarrow\rangle - |\downarrow,\uparrow\rangle) - (|\uparrow\downarrow, 0\rangle - |0,\uparrow\downarrow\rangle)}{2}.
\end{aligned} \tag{1.5}$$

Due to the Pauli exclusion principle, we conclude that $|S_{\rm tot} = 1\rangle$ is an eigenstate of $\mathcal{H}$ (a given electron cannot hop to the other orbital). Consequently, the diagonalization of $\mathcal{H}$ can be restricted to the orthogonal 3-dimensional $S_{\rm tot} = 0$ subspace. The resulting eigenstates include $|S_{\rm tot} = 0\rangle_1$ with eigenvalue U, the $S_{\rm tot} = 1$ triplet with degenerate eigenvalue 0, and the remaining two eigenstates are linear combinations of $|S_{\rm tot} = 0\rangle_2$ and $|S_{\rm tot} = 0\rangle_3$ with eigenvalues $U(1 \pm \sqrt{1 + 16t^2/U^2})/2$. In the limit $U/t \gg 1$ [3], the two eigenstates can be approximated as

$$|\psi_{\rm gs}\rangle \simeq \frac{1}{\sqrt{2}}(|\uparrow,\downarrow\rangle - |\downarrow,\uparrow\rangle), \quad \text{with eigenvalue} \simeq -\frac{4t^2}{U}, \tag{1.6}$$

and

$$|\psi_{\rm hes}\rangle \simeq \frac{1}{\sqrt{2}}(|\uparrow\downarrow, 0\rangle - |0,\uparrow\downarrow\rangle), \quad \text{with eigenvalue} \simeq U + \frac{4t^2}{U}. \tag{1.7}$$

[3] Hubbard provided an estimation [74] for $3d$-transition metals: $t \sim$1 eV and $U \sim$10 eV.

The spectrum of Eq. (1.1) in the large-U/t limit then consists of a low-energy sector including an antisymmetric singlet ground state $|\psi_{\rm gs}\rangle$ and an excited $S_{\rm tot}=1$ triplet state separated by the small energy gap $4t^2/U$, and a high-energy sector spanned by the states $\{|S_{\rm tot}=0\rangle_1, |\psi_{\rm hes}\rangle\}$ that accounts for "charge fluctuations" above the so-called Mott-Hubbard gap of order U. Since $U/|t|\gg 1$, the low-energy physics of Eq. (1.1) is well described by an effective spin Hamiltonian:

$$\tilde{\mathcal{H}} = J\left(\boldsymbol{S}_1\cdot\boldsymbol{S}_2-\frac{1}{4}\right), \quad J=4t^2/U, \tag{1.8}$$

known as the isotropic *antiferromagnetic* (AFM) Heisenberg model, whose spectrum includes the singlet ground state $|\psi_{\rm gs}\rangle$ with energy $\epsilon_s=-J$ and the excited $S_{\rm tot}=1$ triplet state with energy $\epsilon_t=0$, which leads to a spin gap $\Delta_s=J=4t^2/U$. This simple exercise illustrates the microscopic origin of the antiferromagnetism: the singlet configuration takes advantage of the finite tunneling (hopping) into another site to *reduce the "kinetic" energy* while the other electron is there. A similar virtual process is forbidden for the triplet state because of the Pauli exclusion principle from this *virtual* process, implying that $\epsilon_t>\epsilon_s$. In his seminal paper [74], Hubbard pointed out that the Hamiltonian Eq. (1.1) (on the lattice) provides a good approximation in modeling the correlation effects in the d-bands of transition metals. For this reason, antiferromagnetism is more common than ferromagnetism in nature. In realistic systems, electrons (spins) cannot directly tunnel into another site, because the d- or f-orbitals of magnetic ions are usually separated by a non-magnetic "bridge" ion such as O^{2-}. Nevertheless, as proposed by Kramer [82] and further developed by Anderson [9], electrons (spins) of the magnetic ions can still interact with each other by hopping into the p-orbital of the non-magnetic ion through a fourth-order process known as *superexchange* [9]. Depending on the bond angles and filling of the atomic orbitals, the superexchange interaction can either be ferromagnetic or antiferromagnetic, which is summarized by a set of semi-empirical Goodenough-Kanamori rules (see Refs. [64, 78]). Other exchange mechanisms such as the *double exchange* [166]—where the effective hopping of an electron is strongly affected by its ferromagnetic Hund's interaction with localized spins (first Hund's rule)—are not analyzed in this dissertation.

We have seen that the the large-U/t limit of the half-filled Hubbard model is well approximated by the isotropic AFM Heisenberg model (see Auerbach [16] for a more mathematically rigorous derivation). In realistic materials, different types of magnetic anisotropy can also emerge from various microscopic mechanisms. For example, the combination of the (relativistic) spin-orbit interaction and crystal field splitting of a given magnetic ion may lead to more general bilinear interactions in spin operators (*anisotropic exchange interactions*) [49, 105]. In other words, besides the isotropic (scalar product) Heisenberg interaction of Eq. (1.8), the exchange tensor can include a symmetric traceless component (symmetric exchange anisotropies), and an antisymmetric component (the Dzyaloshinskii–Moriya interaction). The allowed exchange anisotropies are obtained by analyzing the space group symmetry of the material (two open-source codes provide such symmetry analysis [147, 22]). In addition, the combination of the spin-orbit interaction and crystal field splitting also leads to *single-ion anisotropy* terms for magnetic ions with spin higher than one. These (exchange + single-ion) anisotropies in spin space turn out play a rather important role in the low-energy physics for a large class of d- (transition-metal) and f- (rare-earth) systems. In particular, we will consider two iron-based magnetic systems in this dissertation, where the magnetic anisotropies are essential to explain some of the observed experimental phenomena.

After examining the microscopic origin of the spin models, we proceed to study these models themselves. The first challenge is that spins are intrinsic quantum mechanical objects with no well-defined classical counterparts. Nevertheless, as a first approach, we can still adopt the naive (and widely accepted) classical limit for a spin, i.e. a classical dipole field. The ground state of the classical spin model is obtained by minimizing the classical energy [4]. At low enough temperatures, excitations of the classical spin model correspond to small oscillations around the ground state configuration, known as *spin waves*, which are described by the Landau-Lifshitz dynamics (LLD) — a classical spin (dipole field) precessing around the molecular field, or by the *semiclassical* spin wave theory (SWT) that is obtained by quantizing the harmonic oscillator Hamiltonian of each normal mode.

[4] By treating the spin as a rigid classical vector of length S, the minimization is done with respect to $2N_s$ real parameters, where N_s is the number of spins.

The procedure described above turns out to be successful for bipartite lattices with only nearest-neighbor AFM exchange interactions, such as the square and the honeycomb lattices [5]. However, this approach becomes problematic for non-bipartite lattices. For example, let us consider the triangular lattice antiferromagnet in the Ising limit: $\mathcal{H} = J\sum_{\langle i,j\rangle} S_i^z S_j^z$. As shown in Fig. 1.1, after anti-aligning two spins, the third spin can only be kept anti-parallel to one of the previous two spins. This property is known as *geometric frustration* and it typically leads to ground state degeneracy: there are six degenerate ground state configurations for an Ising model on a single triangle (the number of ground states grows exponentially with the triangular lattice size [154]). The AFM Heisenberg model $\mathcal{H} = J\sum_{\langle i,j\rangle} \boldsymbol{S}_i \cdot \boldsymbol{S}_j$ on a Kagome lattice provides another example of geometric frustration. The total energy of the Kagome lattice system is minimal for spin configurations that minimize the energy on each triangle [see Fig. 1.1]: $\mathcal{H} = J\left[(\boldsymbol{S}_1 + \boldsymbol{S}_2 + \boldsymbol{S}_3)^2 - (\boldsymbol{S}_1^2 + \boldsymbol{S}_2^2 + \boldsymbol{S}_3^2)\right]/2$ [34]. The second parentheses gives a constant contribution, whereas the first parentheses is non-negative, i.e. the minimal energy of each triangle is given by any configuration that satisfies $\boldsymbol{S}_1 + \boldsymbol{S}_2 + \boldsymbol{S}_3 = 0$. This very loose constraint leads to an infinite number of degenerate ground states [34]!

The lattice geometry is not the only source of frustration: competing further neighbor exchange interactions can also lead to frustration. For instance, the bipartite honeycomb lattice becomes frustrated after introducing a second neighbor AFM interaction. The large ground state degeneracy (originated from frustration) typically leads to stronger quantum or/and thermal fluctuations that can preclude long-range magnetic ordering. Even in the classical limit, thermal fluctuations can suppress long-range magnetic ordering leading to the so-called classical spin liquid phase, which is believed to be a good starting point to look for more exotic *quantum spin liquid* phases [114]. Since Anderson's proposal of the resonating-valence bond (RVB) theory for the triangular lattice in 1973 [11], tremendous theoretical/numerical and experimental efforts [6] have been devoted to searching and understanding the physics of quantum spin liquids. The main motivations are: a) it is

[5] This procedure works for a ferromagnet regardless of the lattice geometry, because the classical FM ground state is an exact eigenstate of the Hamiltonian.

[6] At the time of writing, 30,952 articles related to the topic of quantum spin liquids have been appeared since the publication of Anderson's paper, according to the Web of Science database.

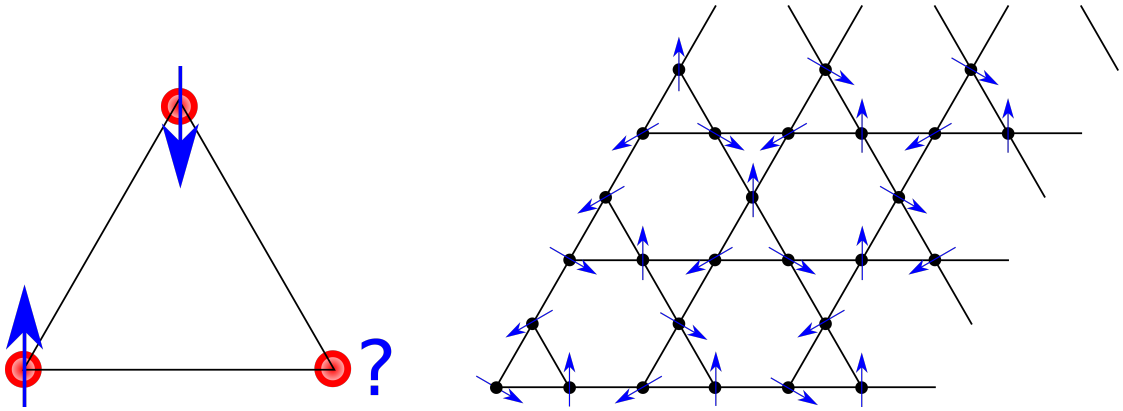


Figure 1.1: Frustration leads to degeneracy. The triangular lattice in the Ising limit (left). The Kagome lattice AFM (right).

theoretically challenging for existing analytical and numerical approaches, b) the combination of quantum phenomena and many-body effects leads to novel emergent behaviors, such as fractional excitations, topological order, and long-range quantum entanglement [133].

Long-range magnetically ordered (spontaneous symmetry broken) materials appear to be much more common. (To date there is no conclusive evidence of a quantum spin liquid state in a real material). For instance, a series of numerical studies [25, 33, 156] suggest that Anderson's initial proposal of the RVB quantum spin liquid phase for the triangular lattice is incorrect: the system develops the 3-sublattice long-range magnetic order in spite of strong quantum fluctuations [38]. We also note that the extensive classical ground state degeneracy does not always guarantee a disordered quantum ground state, because such degeneracy is accidental, i.e., it is not a consequence of any (local) symmetry of the model and it is typically lifted by the addition of other terms to the Hamiltonian. Zero-point/thermal fluctuations of each competing ordering can lift the degeneracy and select a long-range ordered ground state. This mechanism is known as "order by disorder" [151, 137, 87].

A widely advocated guiding principle to look for quantum spin liquids is to search for low-spin frustrated systems [133] because the $1/S$-expansion [10, 83, 97, 39, 101, 16] (conventional spin wave theory) suggests that spin-S systems behave classically in the large-S limit. For this reason, many efforts have been dedicated to the smallest spin $S = 1/2$ systems. However, in this dissertation, we want to point out that the applicability of the traditional classical (LLD) dynamics and semiclassical (SWT) dynamics to realistic spin systems (with a finite value of S) is not just limited by the presence of large quantum fluctuations. As we will show in this dissertation, there are large classes of realistic spin models whose spin dynamics is not well described by the traditional SWT or LLD, but still admit an accurate semiclassical or classical treatment. This apparent paradox disappears when we recognize that there is more than one way of taking the classical limit of a spin system [62].

The necessity of introducing other classical limits for spins (or the failure of viewing spins as classical dipole moments) can be understood by considering a very simple spin one model, such as the single-ion Hamiltonian $\hat{\mathcal{H}} = D(\hat{S}^z)^2$ with $D > 0$ (easy-plane). The excited eigenstates are the $|S^z = \pm 1\rangle$ doublet, while the ground state is the non-magnetic state $|S^z = 0\rangle$, which has vanishing expectation values for all three dipole operators $\langle S^z =$

$0|\hat{S}^{\mu}|S^z = 0\rangle = 0,\ \mu = x, y, z$. As a result, there are only two characteristic frequencies: $\omega = 0$ corresponding to transitions between states with the same energy and $\omega = D$ that connects the ground state with the excited doublet. However, as we will see in Ch. 2, the traditional classical limit, where spin states are represented with a classical dipolar field, leads to a continuum of frequencies (the precession frequency depends on the initial value of the z-component of the dipole moment). Consequently, instead of the two frequencies associated with two discrete energy levels, the traditional classical approach produces a continuum of excitations centered around $\omega = 0$, which reflects the continuous Boltzmann distribution of S^z for the dipole moment at a given temperature. As another example, we will revisit the two-site isotropic AFM Heisenberg model Eq. (1.8) (hereafter we refer the system as a single dimer) in Ch. 2 to illustrate the limitations of the conventional approach. Instead of two frequencies associated discrete levels at $\omega = 0$ and $\omega = J$, the traditional Landau-Lifshitz dynamics also predicts a continuum of excitation frequencies, as in the above-mentioned example of the single-ion problem.

Although the two examples correspond to the extreme quantum limit, they reflect a peculiarity of spins systems that arises from their intrinsic quantum mechanical origin. Moreover, the two Hamiltonians correspond to the models of realistic materials in certain limits. As we already mentioned, the combined effects of spin-orbit interaction and crystal field splitting may lead to the easy-plane single-ion anisotropy in real d- (f-) electron materials. When zJ (z is the coordination number and J is the characteristic energy scale for exchange interactions) is smaller or comparable to D, the conventional classical approach would definitely lead to a qualitatively incorrect description. In addition, there are multiple examples of magnetic materials comprising weakly coupled dimers, which can be treated with the generalized classical limit that is discussed in Ch. 2. Except for very particular cases, it is impossible to solve the exact quantum dynamics of spin lattice systems because the numerical cost grows exponentially in the number of spins N_s. Nevertheless, we can still try to take an alternative classical limit of the spin system to vastly reduce the numerical cost to *linear in* N_s.

Coherent states [121, 80], which have their origin in an early paper of Schrödinger [134], were always considered as providing a possible link between quantum and classical mechanics.

Since the local Hilbert space of a quantum spin-S system has dimension $N = 2S + 1$, the coherent states of the special unitary group SU(N) provide a natural platform to take the classical limit of a quantum spin-S system. We note that the traditional approach of viewing spins as classical dipole moments corresponds to taking classical limit based on SU(2) coherent states. As we will demonstrate in Ch. 2, by taking the classical limit based on SU(3) coherent states for the single-ion problem, or SU(4) for the dimer problem, we can capture the correct discrete nature of the transition frequencies. The SU(N) representation of spins should not be confused with the symmetry of the spin Hamiltonian, i.e. the model Hamiltonian need *not* be SU(N) invariant [7].

In summary, the classical limit for a spin system is associated with the coherent states of a given group. The "optimal" choice of this group depends on the spin Hamiltonian under consideration. In this dissertation, we will exploit this observation to generalize several concepts and unify different approaches in the field of quantum magnetism. First, we will consider the generalization for the classical dynamics, also known as LLD, which is only known for traditional classical limit based on SU(2) coherent states. The generalization is based on SU(N) coherent states that span the space of quantum mechanical states of an N-dimensional Hilbert space. The original Landau-Lifshitz equation, that was first introduced by Landau and Lifshitz [88] to describe the precession of the magnetization under the influence of a (dipolar) molecular field in a solid, is generalized to describe the precession of a classical SU(N) "color field" under the influence of an SU(N) molecular field. This generalization enables us to describe the coherent multipolar excitations in an $S \geq 1$ system at any finite temperature. The next step corresponds to a generalization of the semiclassical spin dynamics, i.e., the traditional SWT, from SU(2) to SU(N). The well-known $1/S$-expansion is generalized to an $1/M$-expansion, where M is an integer number that parametrizes different degenerate irreducible representations of SU(N). In particular, we demonstrate that the $1/M$-expansion is simply a loop-expansion [138]. The generalized SWT provides a systematic scheme for including quantum many-body effects in magnets with $N - 1$ "flavors" of low-energy excitations. Finally, we generalize the concept of magnetic

[7] Recall that this is already true for the traditional SWT and LLD: the SU(2) description of spins does not require an SU(2) invariant spin Hamiltonian.

skyrmions—one type of topological soliton that emerges in magnetic systems. The traditional CP^1 magnetic skyrmions are topological spin textures observed in quantum magnets. The magnetic dipole moment rotates continuously from one direction to the opposite as we move away from the origin in a radial direction. The skyrmion number represents the number of times that the target manifold $\mathrm{CP}^1 \cong S^2$ wraps around the base manifold S^2. As we will show in this dissertation, different classical limits lead to a different target manifolds. In particular, the classical limit of a spin system based on the fundamental representation of $\mathrm{SU}(N)$ leads to the target manifold CP^{N-1}. This generalization opens up a new way of thinking and searching for different types of emergent topological solitons in quantum magnets.

The outline of the dissertation is then organized as follows. In Ch. 2, we present the rigorous formalism for taking the classical limit of a quantum spin system based on $\mathrm{SU}(N)$ coherent states to generalize the well-known Landau-Lifshitz dynamics from SU(2) to $\mathrm{SU}(N)$. In Ch. 3, we apply the generalized SU(3) Landau-Lifshitz dynamics to study the finite-temperature dynamics of the effective $S = 1$ compound $Ba_2FeSi_2O_7$. In Ch. 4, we discuss the generalization of the conventional spin wave theory from SU(2) to $\mathrm{SU}(N)$ to incorporate quantum effects semi-classically. Subsequently, in Ch. 5, we apply the SU(3) spin wave theory to two effective $S = 1$ compounds $Ba_2FeSi_2O_7$ and FeI_2 to explain quantum many-body phenomena revealed by inelastic neutron scattering data. In Ch. 6 we return to the classical limit and explore the topological properties of a spin-1 model. In particular, we report the emergence of CP^2 magnetic skyrmions and skyrmion crystals in a realistic spin-1 model, which generalizes the concept of the CP^1 magnetic skyrmions resulting from the usual classical limit of spins based on SU(2) coherent states. The final conclusions and outlook are given in Ch. 7.

Chapter 2

The classical limit of a spin system

The classical mechanics of a point particle can be recovered by taking the $\hbar \to 0$ limit of the quantum theory. However, this classical limit is not well defined for spins, which are intrinsically quantum mechanical objects. In this chapter, we introduce a classical limit of the dynamics of quantum spin systems based on coherent states of the special unitary group SU(N), where N is the dimension of the local Hilbert space. This approach, which generalizes the well-known Landau-Lifshitz dynamics from SU(2) to SU(N), provides a better approximation to the exact quantum dynamics for a large class of realistic spin Hamiltonians, including $S \geq 1$ systems with large single-ion anisotropy and weakly coupled multi-spin units, such as dimers or trimers. In Sec. 2.1, we review some basic concepts of group theory and coherent states along with the mathematical background that is required to understand the rest of the chapter. Sec. 2.2–2.3 includes the formalism of the generalized SU(N) Landau-Lifshitz dynamics. In Sec. 2.3, we illustrate the necessity of the generalized dynamics by computing the spin structure factors of I) a single-ion $S = 1$ model and II) a single dimer with two $S = 1/2$ using different approaches and comparing the results against the exact solution. In Sec. 2.4, we introduce numerical methods for solving the equations of motion of the generalized dynamics.

2.1 Lie groups, Lie algebras, representation theory, and coherent states

The aim of this section is to review some basic notions of Lie groups/algebras and their coherent states. It is an *over-simplified* summary of relevant material that has been extracted from standard textbooks [80, 44, 120, 65], review articles [121, 172, 58], and lecture notes of D. Arovas [13].

2.1.1 Properties of a group

A group G is a set of elements with a group operation $*$ (usually called multiplication) [denoted as $(G, *)$], satisfying the following conditions:

- **Closure**: $\forall\ g_1, g_2 \in G,\ \ g_3 = g_1 * g_2 \in G$.
- **Associativity**: $g_1 * (g_2 * g_3) = (g_1 * g_2) * g_3,\ \forall\ g_{1,2,3} \in G$.
- **Identity**: $\exists\ e \in G, e * g = g * e = g,\ \forall\ g \in G$.
- **Inverse**: $\exists\ g \in G, \exists\ g^{-1} \in G,\ \ g * g^{-1} = g^{-1} * g = e$.

The following concepts are useful to understand the structure of a group.

- **Group homomorphism**: Given two groups $(G, *)$ and $(H, \cdot)$, a group homomorphism is a map ϕ: $G \to H$ such that $\phi(g_1) \cdot \phi(g_2) = \phi(g_1 * g_2)$, where $g_{1,2} \in G$ and $\phi(g_{1,2}) \in H$. If ϕ is *bijective* (one-to-one and onto), it is an *isomorphism* (denoted as $G \cong H$). *Example*: consider the group of positive real numbers $(\mathbb{R}^+, \cdot)$ and the group of complex numbers $(\mathbb{C}, \cdot)$, where $\cdot$ is the normal multiplication operator, the function $f_u : \mathbb{R}^+ \to \mathbb{C}$ defined by $f_u(a) = a^u$ is a group homomorphism for $u \in \mathbb{R}^+$ and $a \in \mathbb{C}$.
- **Subgroups**: A subgroup H of G is a set of elements that forms a group itself under the same group operation. An *invariant (normal)* subgroup $H \subset G$ such that $g^{-1} H g = H,\ \forall\ g \in G$. *Example*: the group of real numbers under addition $(\mathbb{R}, +)$ is an invariant subgroup of the complex number $(\mathbb{C}, +)$.

- **Direct product group**: Given two groups $(G, *)$ and $(H, \cdot)$, one can prove that (see [65, 44]) the algebraic structure of the direct product $G \times H$ satisfies the group axioms, whose elements are ordered pairs (g, h), where $g \in G$ and $h \in H$, and the group operation $\triangle$ is defined as $(g_1, h_1) \triangle (g_2, h_2) = (g_1 * g_2, h_1 \cdot h_2)$. Note that for $F = G \times H$, both G and H are the invariant subgroups of F.

- **Left coset and Quotient (factor) group**: Let H be a subgroup of G. The left coset gH is defined as multiplying each element of H by an element $g \in G$. The set of all left cosets is denoted as $G/H = \{gH, g \in G\}$. If H is an invariant subgroup of G, then G/H also forms a group [65, 44], known as the quotient (factor) group. Here we focus on the proof of closure: $(g_a h_a)(g_b h_b) = g_a g_b g_b^{-1} h_a g_b h_b = g_a g_b h_c h_b$, where $h_c = g_b^{-1} h_a g_b \in H$ because H is an invariant subgroup of G. The usefulness of left coset is that it provides a natural "regrouping" of the group structure. *Example*: consider the group of integers $(\mathbb{Z}, +)$, which possesses an invariant subgroup formed by even integers $(2\mathbb{Z}, +)$. The left cosets of even integers consists of the set of odd integers and the set of even integers. As a result, the quotient group $\mathbb{Z}/2\mathbb{Z}$ has only two elements, which is isomorphic to the cyclic group $\{0, 1\}$ with addition modulo 2.

2.1.2 Lie group, Lie algebra, and representations

The motivation for introducing Lie groups in physics is to describe continuous symmetries, which are ubiquitous in nature. In particular, most discussions of this dissertation are based on the seminal example of the Lie group $\mathrm{SU}(N)$, which arises naturally in the description of an N-level quantum-mechanical system. $\mathrm{SU}(N)$ is the set of all (continuous) unitary transformations with determinant equal to one. The formal definition of a *Lie group* is a smooth manifold endowed with a group structure, such that the group operation $G \times G \to G : (g, g') \to gg'$ and the inverse $G \to G : g \to g^{-1}$ are smooth [65]. Loosely speaking, we can think of a Lie group as an n-dimensional space $\mathcal{M}_n$ [a manifold is everywhere locally equivalent (so-called homeomorphic) to $\mathbb{R}^n$, see Appendix B], so an element of G is written as $g = g(\boldsymbol{x})$ and $g(\boldsymbol{x}_3) = g(\boldsymbol{x}_1) g(\boldsymbol{x}_2)$, where $\boldsymbol{x}_{1,2,3}$ are points on $\mathcal{M}_n$. Here $\boldsymbol{x}_3(\boldsymbol{x}_1, \boldsymbol{x}_2)$ is a continuous and differentiable function. In addition, the inverse function $[g(\boldsymbol{x})]^{-1} = \psi(\boldsymbol{x})$ is

also continuous and differentiable. *Example*: the SU(2) group element is parameterized as

$$g = \begin{pmatrix} a+bi & c+di \\ -c+di & a-bi \end{pmatrix}, \tag{2.1}$$

under the constraint $a^2+b^2+c^2+d^2=1$, where these numbers are all real. As a result, the group multiplication and the inverse of SU(2) can be written as continuous and differentiable functions of the real numbers. Note that a Lie group is not necessarily a matrix group (see an example given in page 25-26 of [65]), but all Lie groups discussed in this dissertation are matrix Lie groups.

In physics, a lot of information can be deduced by considering the infinitesimal form of a continuous symmetry. For example, the Noether theorem, which relates a conserved current with a continuous symmetry, was derived by considering the infinitesimal symmetry transformation. This leads to the definition of a Lie algebra. The *Lie algebra* $\mathfrak{g}$ of a matrix Lie group G is the set of all matrices X such that $\exp(tX) \in G$ for all $t \in \mathbb{R}$. In physics texts, the exponential map is usually written as $\exp(-itT)$ because the symmetry operation of some Lie groups is usually unitary. Therefore, an extra i is added in the exponent to guarantee that T is Hermitian, corresponding to some physical observables. We will follow the physics convention in this dissertation. Equivalently, from the above definition, $\mathfrak{g}$ is the tangent space of G at the identity element because

$$-iT = \left.\frac{d\exp(-itT)}{dt}\right|_{t=0}. \tag{2.2}$$

We note that the matrix of the Lie algebra can be obtained from the linearization of the exponential map—which is valid when $t \ll 1$—this is the reason that a Lie algebra is related to the infinitesimal form of the Lie group. A Lie algebra has the following three important properties:

- **Vector space over a field** $\mathbb{F}$: $\forall\ T_{1,2} \in \mathfrak{g}$, $\alpha_1 T_1 + \alpha_2 T_2 \in \mathfrak{g}$, where $\alpha_{1,2}$ are some scalars of some field $\mathbb{F}$.

- **Closed under a Lie bracket**: $\forall\ T_{1,2} \in \mathfrak{g}$, $[T_1, T_2] \equiv T_1T_2 - T_2T_1 \in \mathfrak{g}$.

- **The Jacobi identity**: $\forall\ T_{1,2,3} \in \mathfrak{g}$, $[T_1,[T_2,T_3]]+[T_2,[T_3,T_1]]+[T_3,[T_1,T_2]]=0$.

The basis vectors of a Lie algebra are called *generators*. In particular, the action of the Lie bracket between generators tells us about the structure of the Lie algebra: $[T_a,T_b]=if_{abc}T_c$ (summation over repeated indices is assumed), where the so-called *structure constants* f_{abc} are antisymmetric under exchange of any pair of indices.

The above discussions treat elements of Lie groups/algebras as abstract entities. Here we will consider the representation of a Lie group/algebra: a finite-dimensional representation of a Lie group is a homomorphism Π: $G \to \mathrm{GL}(\mathcal{V}_n)$, where $\mathcal{V}_n$ is an n-dimensional vector space and $\mathrm{GL}(\mathcal{V}_n)$ is the set of all $n \times n$ invertible matrices with matrix multiplication as the group operation. Similarly, a finite-dimensional representation of a Lie algebra is also an homomorphism π: $\mathfrak{g} \to \mathrm{gl}(\mathcal{V})$ with the matrix commutator as the Lie bracket. The dimension of the representation is the dimension of the vector space $n = \dim \mathcal{V}_n$. Note that one should not confuse the dimension of the group with the dimension of the representation. We will illustrate this idea below with example for $\mathrm{SU}(N)$. If the homomorphism Π or π is one-to-one, the representation is said to be *faithful*. A proper subspace $\mathcal{W}_w$ of $\mathcal{V}_n$ with $w<n$ is said to be invariant if $\Pi(g)\omega \in \mathcal{W}_w,\ \forall\ g \in G, \forall\ \omega \in \mathcal{W}_w$. A similar definition holds for the Lie algebra. If there is no proper invariant subspace, a representation is said to be *irreducible* (irrep).

Let us conclude this subsection with two concrete examples of Lie groups.

- *The Heisenberg-Weyl group*: The Heisenberg-Weyl group H_3 consists of translation operators of a quantum mechanical particle in phase space (coordinates+momentum). The corresponding Lie algebra h_3 has three generators: the identity $\hat{1}$, the position operator $\hat{x}$, and the momentum operator $\hat{p}$. The structure of h is determined by the canonical commutation relations $[\hat{x},\hat{p}]=i\hbar$, $[\hat{x},\hat{1}]=[\hat{p},\hat{1}]=0$. Any finite translation in phase space can be written as an exponential map of the generators $\exp\left(i\left(x\hat{x}+p\hat{p}+c\hat{1}\right)\right) \in H_3$, where $x,p,c \in \mathbb{R}$.

- *The SU(N) group*: The Lie algebra $\mathfrak{su}(N)$, that is defined as the tangent space at the identity element of $\mathrm{SU}(N)$, is a vector space over $\mathbb{C}^N$ of dimension N^2-1. In the fundamental representation, the following matrices provide a basis for the generators

of $\mathfrak{su}(N)$

$$\hat{g}_{ij}\ (i \neq j),\ \hat{H}_1 = \frac{1}{2}(\hat{g}_{11} - \hat{g}_{22}), \dots\ \hat{H}_{N-1} = \frac{1}{2}(\hat{g}_{N-1N-1} - \hat{g}_{NN}), \tag{2.3}$$

where

$$\hat{g}_{ij} \equiv |i\rangle\langle j|,\ i,j = 1,2,\dots N \tag{2.4}$$

and

$$|i\rangle = (0,\ \dots,\ \overset{i\text{th}}{1}, \dots, 0)^T \tag{2.5}$$

represents the standard basis of $\mathbb{C}^N$. The matrices satisfy the following commutation relations

$$\left[\hat{g}_{ij}, \hat{g}_{kl}\right] = \delta_{kj}\hat{g}_{il} - \delta_{il}\hat{g}_{kj}, \tag{2.6}$$

and

$$\left[\hat{H}_k, \hat{H}_l\right] = 0,\ k,l = 1, \dots, N-1, \tag{2.7}$$

where the set of $N-1$ generators $\{\hat{H}_k\}$ with $k = 1, \dots, N-1$ spans the *Cartan subalgebra* (maximal commutative subalgebra [65]) of $\mathfrak{su}(N)$, and the remaining $N(N-1)$ generators $\hat{g}_{ij}$ are the so-called raising (lowering) operators if $i < j$ ($i > j$). It is important to keep in mind that the commutation relations given in Eqs. (2.6) and (2.7) remain invariant under unitary changes of basis: $\hat{g}_{ij} \to U^{-1}\hat{g}_{ij}U$, $\hat{H}_k \to U^{-1}\hat{H}_k U$.

Consider now an irreducible representation (irrep) of $\mathfrak{su}(N)$ on the vector space V, where $\dim(V)$ is equal to N. This is the so-called fundamental representation. The *highest-weight state* $|\mu\rangle \in V$ is defined by the condition

$$\hat{g}_{ij}|\mu\rangle \equiv 0\ \ \forall\ i < j, \tag{2.8}$$

i.e. the highest weight state vanishes under the operation of any raising operator. Note that $|\mu\rangle$ is also a common eigenvector of the Cartan subalgebra generators

$$\hat{H}_1|\mu\rangle = \frac{1}{2}\lambda_1|\mu\rangle, \dots, \hat{H}_{N-1}|\mu\rangle = \frac{1}{2}\lambda_{N-1}|\mu\rangle. \tag{2.9}$$

The $N-1$ eigenvalues $[\lambda_1,\ldots,\lambda_{N-1}]$ are used to label the irreps of $\mathfrak{su}(N)$ and the dimension of the representation is given by Weyl's dimension formula [44]. It is obvious that the dimension of the representation is different from the dimension of $\mathfrak{su}(N)$, N^2-1.

As an example, let us consider the particular cases of the $\mathfrak{su}(2)$ and $\mathfrak{su}(3)$ algebras. The Cartan subalgebra of $\mathfrak{su}(2)$ is one-dimensional, i.e., it is generated by a single element $\{\hat{H}_1 = 2S^z\}$ (hereafter we will use $\hbar$ as the unit of angular momentum). Consequently, the irreducible representations of $\mathfrak{su}(2)$ are labeled by a single number λ_1 and their dimension is $\lambda_1+1 = 2S+1$. For $\mathfrak{su}(3)$, the Cartan subalgebra is bi-dimensional, implying that the irreducible representations are labeled by λ_1 and λ_2 and their dimension is

$$\dim[\lambda_1,\lambda_2] = \frac{1}{2}(\lambda_1+1)(\lambda_2+1)(\lambda_1+\lambda_2+2). \tag{2.10}$$

It is interesting to note that a given vector space $\mathcal{V}$ can host irreducible representations of two different algebras: π_1: $\mathfrak{g}_1 \to \mathrm{gl}_1(\mathcal{V})$ and π_1: $\mathfrak{g}_2 \to \mathrm{gl}_2(\mathcal{V})$. As an example, let us consider the Hilbert space of a spin one system (three-level system) with a basis of states $\{|S^z=1\rangle, |S^z=-1\rangle, |S^z=0\rangle\}$. By definition, this is the linear space associated with the irreducible representation $S=1$ of the $\mathfrak{su}(2)$ algebra. The same linear space can be used to introduce the fundamental representation of the $\mathfrak{su}(3)$ algebra. In this representation, the generators of the Cartan subalgebra of $\mathfrak{su}(3)$ are $\hat{H}_1 = \hat{S}^z/2$ and $\hat{H}_2 = 3(\hat{S}^z)^2/4 - \hat{S}^z/4 - 1/2$ and the highest-weight state is $|1\rangle$ ($\hat{S}^z|1\rangle = |1\rangle$) with $\lambda_1 = 1$ and $\lambda_2 = 0$. As expected, Eq. (2.10) confirms that the fundamental representation of $\mathfrak{su}(3)$ has dimension $\dim[1,0] = 3$. As we will see later, this freedom can be exploited to express a given physical Hamiltonian in more than one way. For instance, a spin-one Hamiltonian can be expressed in terms of generators of $\mathfrak{su}(2)$ or in terms of generators of $\mathfrak{su}(3)$. These different "languages" lead to different approximations. Depending on the Hamiltonian under consideration, one of these approximations will be better than the rest.

2.1.3 Coherent states of a Lie group

The concept of "coherent states" was first proposed by Schrödinger in 1926 [134]. He derived them as the most classical states (i.e., minimum uncertainty $\Delta x \Delta p = \hbar/2$) of a quantum harmonic oscillator. The first practical application of this concept was introduced by Glauber and Sudarshan in 1963 [60, 61, 59, 142] to describe the maximally coherent light state in quantum optics, hence the name *coherent state*. Coherent states were originally constructed as eigenstates of the annihilation operator of the Heisenberg-Weyl group:

$$\hat{a} = \sqrt{\frac{1}{\hbar}}(\hat{x} + i\hat{p}) \tag{2.11}$$

The *base state* $|0\rangle$ for coherent states is defined by the condition

$$\hat{a}|0\rangle = 0. \tag{2.12}$$

A coherent state is obtained by applying an element of the Heisenberg-Weyl group to the base state [59]

$$|\alpha\rangle = e^{\alpha\hat{a}^\dagger - \bar{\alpha}\hat{a}}|0\rangle, \tag{2.13}$$

where $e^{\alpha\hat{a}^\dagger - \bar{\alpha}\hat{a}} \in H$ is the so-called displacement operator [172] and $\alpha, \bar{\alpha} \in \mathbb{C}$. By convention, one can use two real numbers p and q with $\alpha = q + ip$ to label a coherent state. The wave function of the coherent state $|\alpha\rangle = |p, q\rangle$ corresponds to the ground state of a simple harmonic oscillator centered around the equilibrium position q and with average momentum p (we can think of the description of a harmonic oscillator from a reference frame that moves at a finite and constant speed). The square of the absolute value of this wave function is

$$|\langle x|p, q\rangle|^2 = (\pi\hbar)^{-1/2} \exp\left\{(1/\hbar)\left[-(x-q)^2\right]\right\}. \tag{2.14}$$

The manifold of coherent states forms an over-complete basis of the Hilbert space of a point particle in one-dimension [80]. The non-orthogonality of the coherent states leads to the

finite overlap:

$$|\langle p,q|p',q'\rangle|^2 = \exp\left\{-(1/2\hbar)\left[(p-p')^2+(q-q')^2\right]\right\}$$
$$= \exp\left\{-(1/2\hbar)(\alpha-\alpha')(\bar{\alpha}-\bar{\alpha}')\right\}. \tag{2.15}$$

In his third seminal paper in 1963 [59], Glauber pointed out that there are three equivalent definitions of coherent states: (i) the eigenstate of the annihilation operator, (ii) the state obtained by applying a displacement operator of the Heisenberg-Weyl group on the vacuum state of the harmonic oscillator, as given in Eq. (2.13), and (iii) the state with minimum Heisenberg uncertainty. Ten years later, Perelomov [121] and Gilmore [57] observed that the second definition of Glauber can be extended to an arbitrary Lie group by following the same recipe as in Eq. (2.13). Below we focus our discussion on the SU(N) group.

We start by considering the simplest non-trivial case corresponding to coherent states of SU(2). The three operators

$$\hat{S}^+ = \hat{g}_{12},\ \hat{S}^- = \hat{g}_{21},\ \hat{S}^z = \hat{H}_1, \tag{2.16}$$

form a basis of $\mathfrak{su}(2)$ generators. The corresponding highest-weight state $|\mu\rangle = |S^z = S\rangle$, which satisfies $\hat{S}^+|S^z = S\rangle = 0$, is chosen as the reference state. Like any other state, $|\mu\rangle$ is defined up to an arbitrary multiplicative phase. To remove this redundancy in the definition of coherent states, it is necessary to identify the *isotropic subgroup* I, that leaves the reference state invariant up to a multiplicative phase [172]. Since $I = \mathrm{U}(1)$ for the particular case of SU(2), the manifold of coherent states is isomorphic to the coset space $\hat{\Omega} \in \mathrm{SU}(2)/\mathrm{U}(1)$:

$$|\Omega(\theta,\phi)\rangle \equiv \hat{\Omega}(\theta,\phi)|S^z = S\rangle = e^{-i\hat{S}^z\phi}e^{-i\hat{S}^y\theta}|S^z = S\rangle, \tag{2.17}$$

where $\hat{S}^y = (\hat{S}^+ - \hat{S}^-)/2i$ and θ, ϕ are two real parameters that parameterize the two-sphere $S^2 \simeq \mathrm{CP}^1$. In general, the manifold of the coherent states is isomorphic to G/I [172, 62], and it is known as the *quotient orbit*. In the fundamental ($S = 1/2$) representation of SU(2),

an arbitrary SU(2) coherent state can be expressed as

$$|\Omega(\theta,\phi)\rangle = \cos\frac{\theta}{2}e^{-i\phi/2}|1\rangle + \sin\frac{\theta}{2}e^{i\phi/2}|2\rangle. \tag{2.18}$$

Let us consider now the case of SU(3) coherent states. Unlike the SU(2) case, the manifold of SU(3) coherent states depends on the irreducible representation under consideration. This is so because the base (highest-weight) state for SU(3) coherent states is labelled by the two integer numbers λ_1 and λ_2. The isotropic group becomes bigger when one of the two numbers is zero, which corresponds to the so-called *degenerate representations*. Without loss of generality, we consider the highest-weight state $|1\rangle = (1,\ 0,\ 0)^T$ in the fundamental $[1,0]$-representation of $\mathfrak{su}(3)$ in order to identify the isotropic subgroup for degenerate representations. This state is invariant under the SU(2) group of transformations restricted to the orthogonal subspace. In addition, the global multiplication by a phase [U(1) subgroup] also leaves the reference state invariant in the quantum mechanical sense, implying that $I = \mathrm{SU}(2)\times\mathrm{U}(1) \simeq \mathrm{U}(2)$. The resulting manifold of SU(3) coherent states in the degenerate representation is then isomorphic to the coset space $\mathrm{SU}(3)/\mathrm{U}(2) \simeq S^5/S^1 \simeq \mathrm{CP}^2$. Note that the dimension of this manifold is $8-4=4$ (recall that $\mathfrak{su}(3)$ is eight-dimensional and $\mathfrak{u}(2)$ is four-dimensional). In the fundamental representation, a generic SU(3) coherent state can be expressed as

$$\begin{aligned}|\Omega(\theta,\phi,\alpha_1,\alpha_2)\rangle &= R(\theta,\phi,\alpha_1,\alpha_2)|1\rangle \\ &= e^{i\alpha_1}\sin\theta\cos\phi|1\rangle + e^{i\alpha_2}\sin\theta\sin\phi|2\rangle + \cos\theta|3\rangle,\end{aligned} \tag{2.19}$$

where $R(\theta,\phi,\alpha_1,\alpha_2) \in \mathrm{SU}(3)/\mathrm{U}(2)$, that takes the form [99]

$$\begin{pmatrix} \sin\theta\cos\phi e^{i\alpha_1} & \cos\theta\cos\phi e^{i\alpha_1} & -\sin\phi e^{-i\alpha_2} \\ \sin\theta\sin\phi e^{i\alpha_2} & \cos\theta\sin\phi e^{i\alpha_2} & \cos\phi e^{-i\alpha_1} \\ \cos\theta & -\sin\theta & 0 \end{pmatrix}. \tag{2.20}$$

Now we consider the simplest case when neither λ_1 nor λ_2 is zero (so-called *non-degenerate representation*): the $[1,1]$-representation. According to Eq. (2.10), the dimension of the $[1,1]$-representation is eight, which is the same as the *adjoint representation* [see Appendix A for details]. Note that the underlying vector space of the adjoint representation is the Lie algebra itself. As a result, the highest-weight state is now a linear combination of the eight generators of $\mathfrak{su}(3)$. At the same time, the highest-weight state is the common eigenstate of the two Cartan subalgebra generators. Consequently, the highest-weight state is invariant under an arbitrary U(1) transformation generated by H_1 or H_2. Therefore, the resulting manifold of coherent states is isomorphic to $\mathrm{SU}(3)/[\mathrm{U}(1)\times\mathrm{U}(1)]$ [62], whose dimension is $8-2=6$.

In general, the manifold of coherent states of SU(N) with $N>3$ depends on the representations. Here we focus on degenerate representations with only one non-zero eigenvalue for the $N-1$ elements of the Cartan subalgebra. In this scenario, a general SU(N) coherent state with $N>3$ can be constructed by a straightforward generalization of the procedure that we applied to the SU(2) and SU(3) cases:

$$|\Omega(\{p_i\})\rangle \equiv \hat{\Omega}(\{p_i\})|\mu\rangle, \tag{2.21}$$

where $\hat{\Omega}(\{p_i\}) \in \mathrm{SU}(N)/I$ with $I \simeq \mathrm{SU}(N-1)\times\mathrm{U}(1) \simeq \mathrm{U}(N-1)$. The SU($N$) coherent state, which is topologically equivalent to the complex projective space CP^{N-1}, is then parameterized by $N^2-1-(N-1)^2 = 2(N-1)$ real parameters $\{p_i\}$. The explicit forms of the SU(N) coherent states can be found in Ref. [113] [in the spherical coordinates with $2(N-1)$ real parameters] and in Ref. [58] (in terms of $N-1$ complex parameters). Similarly to the H_3 coherent states [see Eq. (2.15)], the SU(N) coherent states form an over-complete basis of the Hilbert space of an N-level system. The overlap between two SU(N) coherent states and the corresponding integration measure over the parameters $\{p_i\}$ can be found in Ref. [113].

2.2 Coherent states and classical limits

In this section, we will see that the coherent states of a general Lie group can be used to define the classical limit of a quantum mechanical system. The manifold of coherent states possesses a natural symplectic structure, which allows us to introduce a Poisson bracket. We refer the interested readers to Appendix. B and Refs. [159, 58, 62] for detailed discussions on the symplectic structure of the manifold of coherent states. Moreover, one can extend and prove Dirac's conjecture — the commutator between two quantum operators reduces to the Poisson bracket in the classical limit — based on the coherent states for general Lie groups.

To begin with, we include the demonstration of Dirac's conjecture for point particles that was sketched by Yaffe in Ref. [159]. The expectation value of a quantum operator for a coherent state of the Heisenberg-Weyl group [see Eq. (2.13)] is denoted as:

$$A(p,q) \equiv \langle p,q|\hat{A}|p,q\rangle. \tag{2.22}$$

Similarly, the expectation value of the product of two operators $\langle p,q|\hat{A}\hat{B}|p,q\rangle$ is given by

$$\begin{aligned}(AB)(p,q) = &\int \frac{dp'dq'}{2\pi\hbar}|\langle p,q|p',q'\rangle|^2 \\ &\times \frac{\langle p,q|\hat{A}|p',q'\rangle}{\langle p,q|p',q'\rangle}\frac{\langle p',q'|\hat{B}|p,q\rangle}{\langle p',q'|p,q\rangle},\end{aligned} \tag{2.23}$$

where we inserted the resolution of identity

$$\hat{I} = \int \frac{dpdq}{2\pi\hbar}|p,q\rangle\langle p,q|. \tag{2.24}$$

Dirac's conjecture can be proved by taking the $\hbar \to 0$ limit of Eq. (2.23) [159]. According to Eq. (2.15), the first factor of the integrand of Eq. (2.23) is a Gaussian that has a sharp peak at $p' = p$ and $q' = q$ as $\hbar \to 0$. Note that the second factor is an analytical function of $\alpha' = (q' + ip')$ for fixed p and q, while the third factor is an analytical function of $\bar{\alpha}' = (q' - ip')$. Therefore, we can expand the second and the third factors up to quadratic order in $(\alpha' - \alpha)$

and $(\bar{\alpha}' - \bar{\alpha})$, respectively,

$$\frac{\langle p, q|\hat{A}|p', q'\rangle}{\langle p, q|p', q'\rangle} = A(\alpha) + \frac{dA}{d\alpha'}\bigg|_{\alpha'=\alpha}(\alpha' - \alpha) + \frac{1}{2}\frac{d^2A}{d\alpha'^2}\bigg|_{\alpha'=\alpha}(\alpha' - \alpha)^2 + \mathcal{O}\big[(\alpha' - \alpha)^3\big], \quad (2.25)$$

$$\frac{\langle p', q'|\hat{B}|p, q\rangle}{\langle p', q'|p, q\rangle} = B(\alpha) + \frac{dB}{d\bar{\alpha}'}\bigg|_{\bar{\alpha}'=\bar{\alpha}}(\bar{\alpha}' - \bar{\alpha}) + \frac{1}{2}\frac{d^2B}{d\bar{\alpha}'^2}\bigg|_{\bar{\alpha}'=\bar{\alpha}}(\bar{\alpha}' - \bar{\alpha})^2 + \mathcal{O}\big[(\bar{\alpha}' - \bar{\alpha})^3\big]. \quad (2.26)$$

By combining the results, we have

$$(AB)(p, q) \simeq \int \frac{d\alpha d\bar{\alpha}}{2\pi\hbar}|\langle\alpha|\alpha'\rangle|^2\bigg\{A(\alpha)B(\alpha) + \frac{dA}{d\alpha}\frac{dB}{d\bar{\alpha}}(\alpha' - \alpha)(\bar{\alpha}' - \bar{\alpha}) + \mathcal{L}\bigg\}, \quad (2.27)$$

where $\mathcal{L}$ includes terms (up to quadratic order) that vanish after the integration. After computing the Gaussian integrals and keeping contributions up to first order in $\hbar$, we obtain

$$(AB)(p, q) \simeq A(p, q)B(p, q) + \frac{\hbar}{2}\frac{dA}{d\alpha}\frac{dB}{d\bar{\alpha}}. \quad (2.28)$$

In the $\hbar \to 0$ limit, we have

$$\lim_{\hbar\to 0}(AB)(p, q) = a(p, q)b(p, q), \quad (2.29)$$

where

$$a(p, q) \equiv \lim_{\hbar\to 0} A(p, q), \quad b(p, q) \equiv \lim_{\hbar\to 0} B(p, q). \quad (2.30)$$

Note that the functions $a(p, q)$ and $b(q, p)$ are assumed to remain finite in the $\hbar \to 0$ limit. They are the so-called *classical operators* [159], that resemble the operators $\hat{A}$ and $\hat{B}$ in the classical limit. The relation (2.29) gives the *factorization rule* for the expectation value of the product of two operators in the $\hbar \to 0$ limit.

Finally, let us replace $\hat{B}$ with the Hamiltonian operator $\hat{H}$ and consider the $\hbar \to 0$ limit of the expectation value of the right-hand side of the Heisenberg equation (HE) of motion:

$$\begin{aligned}\lim_{\hbar\to 0} -\frac{i}{\hbar}\big[A, H\big](p,q) &= -\lim_{\hbar\to 0}\left[\frac{\partial A}{\partial p}\frac{\partial H}{\partial q} - \frac{\partial A}{\partial q}\frac{\partial H}{\partial p}\right] \\ &= \frac{\partial a}{\partial q}\frac{\partial h}{\partial p} - \frac{\partial a}{\partial p}\frac{\partial h}{\partial q} \\ &= \big\{a(p,q), h(p,q)\big\}_{PB}, \end{aligned} \tag{2.31}$$

where $h(p,q) = \lim_{\hbar\to 0}\langle p,q|\hat{H}|p,q\rangle$ is the classical Hamiltonian. Note that in the above derivation, we have used the fact that for the complex variable $\alpha = p + iq$, $\mathrm{d}/\mathrm{d}\alpha = (\partial/\partial p - i\partial/\partial q)/2$. After taking the same expectation value of the left-hand side of the HE, we obtain

$$\lim_{\hbar\to 0}\langle p,q|\frac{d\hat{A}}{dt}|p,q\rangle = \frac{da(p,q)}{dt} = \big\{a(p,q), h(p,q)\big\}_{PB}. \tag{2.32}$$

This completes the proof of Dirac's conjecture. Here the coherent states of H_3 play an important role in linking the quantum and classical theories for a point particle. As we already mentioned, the coherent states of the Heisenberg-Weyl group can be generalized to any Lie group [121, 57], implying that we can take the classical limit of a given quantum theory by introducing a manifold of coherent states of an appropriate Lie group [159]. In the rest of this section, we focus our discussion on the classical limits of spin systems based on the coherent states of the SU(N) group for degenerate representations.

The local Hilbert space of a quantum spin-S system has dimension $N = 2S + 1$. Since the SU(N) group consists of all unitary basis transformations, with determinant equal to 1, of an N-level quantum-mechanical system, coherent states of SU(N) provide a natural platform to define the classical limit of a spin system. However, as we mentioned previously, the traditional approach has always been to use SU(2) coherent states to define a classical limit of spin systems. While the SU(N) Lie group is *not the only alternative*, the purpose of this section is to introduce this alternative path to illustrate the advantages of using Lie groups larger than SU(2).

As before, the first step is to take the $\hbar \to 0$ limit of the expectation value of a quantum operator for an SU(N) coherent state. As an example, let us consider the classical limit of

the *physical spin operator* $\hat{S}^z$ in the highest-weight state of SU(2):

$$\lim_{\hbar\to 0}\langle S^z = S|\hat{S}^z|S^z = S\rangle = \lim_{\hbar\to 0}\hbar S. \tag{2.33}$$

Note that we made $\hbar$ explicit in the above equation to indicate that the spin is an intrinsically quantum-mechanical object, i.e., the simple definition of the classical operator given in Eq. (2.30) does not exist for $\hat{S}^z$ in Eq. (2.33). However, we can still obtain a non-trivial classical limit by simultaneously sending $S = \lambda_1/2$ to infinity and $\hbar$ to zero, while keeping the product finite. This simple procedure can be easily generalized to any quantum operator $\hat{A}$, which is a polynomial function of the physical SU(N) generators. The classical limit of an operator is then defined by taking the expectation value on a coherent state

$$a(\{\alpha_\rho\}) = \langle\Omega(\{\alpha_\rho\})|\hat{A}|\Omega(\{\alpha_\rho\})\rangle, \tag{2.34}$$

where $\{\alpha_\rho\}$ is the set of $N-1$ complex parameters that parametrize the SU(N) coherent states, and simultaneously sending the eigenvalue λ_1, that labels the degenerate representations of SU(N), to infinity.

The second step is to consider the classical limit of the expectation value of the product of two operators. We ought to prove that the factorization rule holds in the classical limit

$$\langle\Omega(\{\alpha_\rho\})|\hat{A}\hat{B}|\Omega(\{\alpha_\rho\})\rangle \xrightarrow{\text{classical limit}} a(\{\alpha_\rho\})b(\{\alpha_\rho\}). \tag{2.35}$$

Indeed, the factorization rule holds for $\lambda_1 \to \infty$. Here we show the proof explicitly for SU(2). Consider the expectation value of the product of two on-site operators $\hat{A}$ and $\hat{B}$ for an SU(2) coherent state,

$$AB(\theta,\phi) = \langle\Omega(\theta,\phi)|\hat{A}\hat{B}|\Omega(\theta,\phi)\rangle = \frac{(2S+1)}{4\pi}\int \mathrm{d}\vec{\Omega}'|\langle\Omega|\Omega'\rangle|^2\frac{\langle\Omega|\hat{A}|\Omega'\rangle}{\langle\Omega|\Omega'\rangle}\frac{\langle\Omega'|\hat{B}|\Omega\rangle}{\langle\Omega'|\Omega\rangle}, \tag{2.36}$$

where we inserted the resolution of identity in terms of SU(2) coherent states, and

$$\frac{(2S+1)}{4\pi}d\vec{\Omega} = \frac{(2S+1)}{4\pi}d\phi d\theta\sin\theta \tag{2.37}$$

is the Haar measure of SU(2). The first term of the above integrand is the overlap between two SU(2) coherent states [16]

$$|\langle\Omega|\Omega'\rangle|^2 = \left(\frac{1+\vec{\Omega}\cdot\vec{\Omega}'}{2}\right)^{2S}, \tag{2.38}$$

where $\vec{\Omega} = (\sin\theta\cos\phi, \sin\theta\sin\phi, \cos\theta)$. In the large-$S$ limit [recall that $S = \lambda_1/2$ for SU(2)], the overlap becomes arbitrarily small except for $\vec{\Omega}' \simeq \vec{\Omega}$, i.e., the coherent states become asymptotically orthogonal for $S \to \infty$. The large value of S justifies a *saddle-point approximation* to evaluate the integral in Eq. (2.36). After expanding the term $\vec{\Omega}\cdot\vec{\Omega}'$ up to the quadratic order in $\delta\gamma = (\gamma' - \gamma)$, where $\gamma = \theta, \phi$,

$$\vec{\Omega}\cdot\vec{\Omega}' = \cos\theta\cos(\theta+\delta\theta) + \cos(\delta\phi)\sin(\theta)\sin(\theta+\delta\theta) = 1 - \frac{1}{2}(\delta\theta)^2 - \frac{1}{2}\sin^2\theta(\delta\phi)^2 + \mathcal{O}\big[(\delta\gamma)^3\big], \tag{2.39}$$

we rewrite the square of the overlap as

$$|\langle\Omega|\Omega'\rangle|^2 = e^{\ln|\langle\Omega|\Omega'\rangle|^2} \simeq e^{2S\ln\left[1-\frac{1}{4}(\delta\theta)^2-\frac{1}{4}\sin^2\theta(\delta\phi)^2\right]} \simeq e^{-S\left[(\theta'-\theta)^2/2+\sin^2\theta(\phi'-\phi)^2/2\right]}. \tag{2.40}$$

Since (for fixed θ and ϕ) the second factor and the third factor of the integrand in Eq. (2.36) are analytical functions of the complex variables $\alpha' = \sin\theta'\phi' + i\theta'$ and $\bar{\alpha}' = \sin\theta'\phi' - i\theta'$, respectively, we can expand the two terms as we did in Eqs. (2.25) and (2.26),

$$\begin{aligned} AB(\theta,\phi) \simeq{}& \frac{2S+1}{4\pi}\int_0^{2\pi} d\phi' \int_0^{\pi} d\theta' \sin\theta' \\ &\times e^{-S\left[(\theta'-\theta)^2/2+\sin^2\theta(\phi'-\phi)^2/2\right]}\Bigg\{A(\theta,\phi)B(\theta,\phi) \\ &- \frac{i}{2}\left[\frac{1}{\sin\theta}\frac{\partial A}{\partial\theta}\frac{\partial B}{\partial\phi}(\theta'-\theta)^2 - \frac{1}{\sin\theta}\frac{\partial A}{\partial\phi}\frac{\partial B}{\partial\theta}(\sin\theta'\phi' - \sin\theta\phi)^2\right] \\ &+ \frac{1}{2}\left[\frac{1}{\sin\theta}\frac{\partial A}{\partial\theta}\frac{\partial B}{\partial\theta}(\theta'-\theta)^2 + \frac{1}{\sin\theta}\frac{\partial A}{\partial\phi}\frac{\partial B}{\partial\phi}(\sin\theta'\phi' - \sin\theta\phi)^2\right] + \mathcal{L}\Bigg\}, \end{aligned} \tag{2.41}$$

where $\mathcal{L}$ includes terms (up to quadratic order) that vanish after the integration. Since the width of the Gaussian goes to zero in the large-S limit, we can extend the integration limits to infinity and set $\sin\theta' = \sin\theta$ to recover the familiar form of the Gaussian integration. In

summary, we have

$$\begin{aligned} AB(\theta,\phi) = A(\theta,\phi)B(\theta,\phi)\big(1+1/(2S)\big) \\ -\frac{i}{2}\frac{1}{S\sin\theta}\left[\frac{\partial A}{\partial\theta}\frac{\partial B}{\partial\phi}-\frac{\partial A}{\partial\phi}\frac{\partial B}{\partial\theta}\right] \\ +\frac{1}{2}\frac{1}{S\sin\theta}\left[\frac{\partial A}{\partial\theta}\frac{\partial B}{\partial\theta}+\frac{\partial A}{\partial\phi}\frac{\partial B}{\partial\phi}\right]+\mathcal{O}\big[(1/S)^2\big] \end{aligned} \tag{2.42}$$

By taking the large-S limit, we prove the factorization rule for SU(2)

$$AB(\theta,\phi) \xrightarrow{S\to\infty} A(\theta,\phi)B(\theta,\phi). \tag{2.43}$$

The above result also provides the definition of the Poisson bracket on the orbit of SU(2) coherent states

$$\big\{A(\theta,\phi),B(\theta,\phi)\big\}_{PB} = -i\lim_{S\to\infty} S\big[A,B\big](\theta,\phi) = \frac{1}{\sin\theta}\left(\frac{\partial A}{\partial\phi}\frac{\partial B}{\partial\theta}-\frac{\partial A}{\partial\theta}\frac{\partial B}{\partial\phi}\right). \tag{2.44}$$

Note that $\{\phi\sin\theta,\theta\}_{PB}=1$, implying that $\phi\sin\theta$ and θ play the role of canonical coordinate and momentum variables defined on the $S^2\simeq \mathrm{CP}^1$ manifold of SU(2) coherent states.

The general proof for SU(N) is non-trivial and can be found in Ref. [58]. The crucial observation is that two distinct SU(N) coherent states become orthogonal in the limit $\lambda_1\to\infty$. As a result, one can expand the integral associated with the expectation value in a similar manner as in Eq. (2.27), but now in powers of $1/\lambda_1$. Finally, by expanding the expectation value of the commutator between two operators up to the first order in $1/\lambda_1$ and then sending $\lambda_1\to\infty$, one can prove the generalization of Dirac's conjecture applied to the orbit of the SU(N) coherent states

$$\{a(\{\alpha_\rho\}),b(\{\alpha_\rho\})\}_{PB} = \sum_{\mu,\nu} g_{\mu\nu}\left(\frac{\partial a}{\partial\alpha^\nu}\frac{\partial b}{\partial\bar{\alpha}^\mu}-\frac{\partial a}{\partial\bar{\alpha}^\mu}\frac{\partial b}{\partial\alpha^\nu}\right) = \lim_{\lambda_1\to\infty} -i\lambda_1\langle\Omega(\{\alpha_\rho\})|[\hat{A},\hat{B}]|\Omega(\{\alpha_\rho\})\rangle, \tag{2.45}$$

where $g^{\mu\nu}$ is the Fubini-Study metric of CP^{N-1} (see Appendix B and Refs. [69, 58]).

For practical purposes, it is not always necessary to know *a priori* the exact form of the Poisson bracket in order to obtain the classical equations of motion. In most cases, it is

simpler to evaluate the right-hand side of Eq. (2.45). Namely, Eq. (2.45) provides us with a simple recipe to derive the classical dynamics on the manifold of SU(N) coherent states. We will follow this recipe in the next section to write down the generalized classical equations of motion for a quantum spin system.

2.3 Classical spin dynamics

In the previous section we saw that the classical SU(N) dynamics of a quantum spin system becomes exact for $\lambda_1 \to \infty$. However, for most systems of interest, the dimension of the local Hilbert space is finite and $\lambda_1 = 1$, implying that the classical dynamics is just an approximation of the exact quantum dynamics. The big advantage of this approximation is that the numerical cost of the simulations drops from an exponential to a linear dependence in the number of spins. The mathematical procedure of taking the classical limit can be physically represented as building a large SU(N) spin by ferromagnetically coupling M replicas of the original spin and then sending M to infinity. By replacing the SU(N) representation $[\lambda_1, \ldots, 0]$ with $[M\lambda_1, \ldots, 0]$, the spin—originally a microscopic object—becomes a macroscopic entity. *It is important to note that the "ferromagnetic" coupling between replicas corresponds to an SU(N) ferromagnetic Heisenberg interaction* [16]. In other words, the difference between alternative classical limits of a given spin system [e.g. SU(2) and SU(N)] is dictated by the *nature of the coupling* between different replicas. This raises the question about which classical limit better approximates the exact quantum dynamics. As we will explain in this section, the short answer to this question is that the choice of SU(N) coherent states with $N = 2S + 1$ guarantees that the dynamics will capture all the coherent low-energy modes that can appear for a general Hamiltonian. To appreciate this important point, we first derive two *different* classical dynamics based on SU(2) and SU(3) coherent states for a *common* quantum spin Hamiltonian and then we provide the general recipe to derive the classical dynamics for SU(N) coherent states.

2.3.1 Classical equations of motion for spins

SU(2) and SU(3) Landau-Lifshitz dynamics

Consider the following $S = 1$ spin Hamiltonian

$$\hat{\mathcal{H}} = \frac{1}{2}\sum_{\boldsymbol{r},\boldsymbol{\delta}}\sum_{\alpha,\beta}\hat{S}^{\alpha}_{\boldsymbol{r}}J^{\alpha\beta}_{\boldsymbol{\delta}}\hat{S}^{\beta}_{\boldsymbol{r}+\boldsymbol{\delta}} + D\sum_{\boldsymbol{r}}(\hat{S}^{z}_{\boldsymbol{r}})^2, \tag{2.46}$$

where $J^{\alpha\beta}_{\boldsymbol{\delta}}$ is the exchange tensor on the bond $\boldsymbol{\delta}$ and D is the strength of a single-ion anisotropy term. This $S = 1$ system admits two classical limits: one based on SU(2) coherent states (second representation with $\lambda_1 = 2$) and another one based on the SU(3) coherent states (fundamental representation with $\lambda_1 = 1$ and $\lambda_2 = 0$).

We will first consider the SU(2) classical limit. The time evolution of the spin components [generators of SU(2)] is dictated by the Heisenberg Equation (HE) of motion

$$\frac{d\hat{S}^{\alpha}_{\boldsymbol{r}}}{dt} = -\frac{i}{\hbar}\big[\hat{S}^{\alpha}_{\boldsymbol{r}},\hat{\mathcal{H}}\big] = \sum_{\boldsymbol{\delta}}\sum_{\mu,\nu,\beta}J^{\mu\nu}_{\boldsymbol{\delta}}\epsilon^{\alpha\mu\beta}\hat{S}^{\beta}_{\boldsymbol{r}}\hat{S}^{\nu}_{\boldsymbol{r}+\boldsymbol{\delta}} + D\sum_{\beta}\epsilon^{\alpha 3\beta}(\hat{S}^{\beta}_{\boldsymbol{r}}\hat{S}^{z}_{\boldsymbol{r}} + \hat{S}^{z}_{\boldsymbol{r}}\hat{S}^{\beta}_{\boldsymbol{r}}), \tag{2.47}$$

where $\epsilon^{\alpha\mu\beta}$ is the Levi-Civita symbol. The classical limit of the interaction term is given by

$$\hat{S}^{\beta}_{\boldsymbol{r}}\hat{S}^{\nu}_{\boldsymbol{r}+\boldsymbol{\delta}} \to \langle\Omega|\hat{S}^{\beta}_{\boldsymbol{r}}\hat{S}^{\nu}_{\boldsymbol{r}+\boldsymbol{\delta}}|\Omega\rangle = \langle\Omega_{\boldsymbol{r}}|\hat{S}^{\beta}_{\boldsymbol{r}}|\Omega_{\boldsymbol{r}}\rangle\langle\Omega_{\boldsymbol{r}+\boldsymbol{\delta}}|\hat{S}^{\nu}_{\boldsymbol{r}+\boldsymbol{\delta}}|\Omega_{\boldsymbol{r}+\boldsymbol{\delta}}\rangle = s^{\beta}_{\boldsymbol{r}}s^{\nu}_{\boldsymbol{r}+\boldsymbol{\delta}}$$

where we assumed that the coherent state of this system is a direct product of local coherent states, i.e., $|\Omega\rangle = \otimes_{\boldsymbol{r}}|\Omega_{\boldsymbol{r}}\rangle$. Since the single-ion anisotropy term is quadratic in the spin operators, we must use the factorization rule given in Eq. (2.35), which is only exact in the classical limit:

$$\hat{S}^{\beta}_{\boldsymbol{r}}\hat{S}^{z}_{\boldsymbol{r}} + \hat{S}^{z}_{\boldsymbol{r}}\hat{S}^{\beta}_{\boldsymbol{r}} \to \langle\Omega_{\boldsymbol{r}}|\hat{S}^{\beta}_{\boldsymbol{r}}\hat{S}^{z}_{\boldsymbol{r}} + \hat{S}^{z}_{\boldsymbol{r}}\hat{S}^{\beta}_{\boldsymbol{r}}|\Omega_{\boldsymbol{r}}\rangle \xrightarrow{\lambda_1\to\infty} 2s^{\beta}_{\boldsymbol{r}}s^{z}_{\boldsymbol{r}}. \tag{2.48}$$

As for the left-hand-side of the HE, the classical limit simply gives

$$d\hat{S}^{\alpha}_{\boldsymbol{r}}/dt \to \langle\Omega_{\boldsymbol{r}}|d\hat{S}^{\alpha}_{\boldsymbol{r}}/dt|\Omega_{\boldsymbol{r}}\rangle = ds^{\alpha}_{\boldsymbol{r}}/dt. \tag{2.49}$$

Consequently, the resulting classical equation of motion for SU(2) coherent states takes the form,

$$\frac{ds^{\alpha}_{\boldsymbol{r}}}{dt} = \sum_{\boldsymbol{\delta}} \sum_{\mu,\nu,\beta} J^{\mu\nu}_{\boldsymbol{\delta}} \epsilon^{\alpha\mu\beta} s^{\beta}_{\boldsymbol{r}} s^{\nu}_{\boldsymbol{r}+\boldsymbol{\delta}} + 2D \sum \beta \epsilon^{\alpha 3\beta} s^{\beta}_{\boldsymbol{r}} s^{z}_{\boldsymbol{r}}. \tag{2.50}$$

This is simply the well-known Landau-Lifshitz (LL) equation without the damping term,

$$\frac{ds^{\alpha}_{\boldsymbol{r}}}{dt} = \sum_{\mu\nu} \epsilon_{\alpha\mu\nu} s^{\mu}_{\boldsymbol{r}} b^{\nu}_{\boldsymbol{r}}, \quad \boldsymbol{b_r} = -\frac{dh}{d\boldsymbol{s_r}}, \tag{2.51}$$

where $h = \langle \Omega | \hat{\mathcal{H}} | \Omega \rangle$ is the classical Hamiltonian. Note that in terms of spherical coordinates θ and ϕ, Eq. (2.51) is equivalent to the Poisson bracket (2.45) on the orbit of SU(2):

$$\frac{d\theta}{dt} = -\frac{1}{\sin\theta}\frac{\partial h}{\partial \phi} = \{\theta, h\}_{PB}, \quad \frac{d\phi}{dt} = \frac{1}{\sin\theta}\frac{\partial h}{\partial \theta} = \{\phi, h\}_{PB}. \tag{2.52}$$

Let us consider now the classical limit based on SU(3) coherent states. In this case we need to compute the equation of motion of the eight generators of SU(3), $\hat{T}_{1-8}$, which can be regarded as the components of the SU(3) spin. For this purpose, we are going to use the basis of generators

$$\begin{pmatrix} \hat{T}^7 \\ \hat{T}^5 \\ \hat{T}^2 \end{pmatrix} = \begin{pmatrix} -\hat{S}^x \\ -\hat{S}^y \\ -\hat{S}^z \end{pmatrix}, \begin{pmatrix} \hat{T}^3 \\ \hat{T}^8 \\ \hat{T}^1 \\ \hat{T}^4 \\ \hat{T}^6 \end{pmatrix} = \begin{pmatrix} -\left(\hat{S}^x\right)^2 + \left(\hat{S}^y\right)^2 \\ \frac{1}{\sqrt{3}}\left[3\left(\hat{S}^z\right)^2 - \hat{\boldsymbol{S}}^2\right] \\ \hat{S}^x\hat{S}^y + \hat{S}^y\hat{S}^x \\ -\hat{S}^z\hat{S}^x - \hat{S}^x\hat{S}^z \\ \hat{S}^y\hat{S}^z + \hat{S}^z\hat{S}^y \end{pmatrix}. \tag{2.53}$$

These generators satisfy the commutation relation:

$$[\hat{T}^{\mu}, \hat{T}^{\nu}] = i \sum_{\eta} f_{\mu\nu\eta} \hat{T}^{\eta}. \tag{2.54}$$

The structure constants, $f_{\mu\nu\eta}$, satisfy the relation [see Appendix A for definitions],

$$f_{\eta\mu\nu} = -\frac{i}{2}\,\mathrm{Tr}\left(\lambda_\eta\left[\lambda_\mu, \lambda_\nu\right]\right), \tag{2.55}$$

where λ_μ are the Gell-Mann matrices. Note that, in the Cartesian basis

$$\left|x^1\right\rangle = \frac{i}{\sqrt{2}}(|+1\rangle - |-1\rangle), \left|x^2\right\rangle = \frac{1}{\sqrt{2}}(|+1\rangle + |-1\rangle), \left|x^3\right\rangle = -i|0\rangle, \tag{2.56}$$

the SU(3) generators $\hat{T}^\mu_j$ given in Eq. (2.53) are in fact represented by the Gell-Mann matrices themselves:

$$\hat{T}^\mu = \left(\hat{\lambda}_\mu\right)_{ab}\left|x^a\right\rangle\left\langle x^b\right| \quad \mu = 1, 2, \cdots, 8. \tag{2.57}$$

These generators are obtained by applying an SU(3) transformation (change of basis) to the standard basis presented in Eq. (2.3). The advantage of the new "physical" basis is that it is a direct sum of bases of irreps of the SO(3) group of rotations. The three elements, $-\hat{T}^{7,5,2}$, are the three spin operators $\hat{S}^\alpha$ which represent a local dipole moment and transform as vectors under rotations [three-dimensional irrep of SO(3)]. The remaining five elements of the basis, $\hat{T}^{3,8,1,4,6}$, are symmetric and traceless bilinear forms in the spin operators that represent a nematic or quadrupolar moment [five-dimensional irrep of SO(3)]. Each irrep of SO(3) corresponds to a different multipole, and the number of different irreps or multipoles for the more general SU(N) group is $N-1$. Importantly, the equations of motion that dictate the dynamics of the different multipolar components are coupled. For instance, as we will see below, the dynamics of the dipolar generators of SU(3), $-\hat{T}^{7,5,2}$, is coupled to the dynamics of the nematic generators $\hat{T}^{3,8,1,4,6}$. By adopting the SU(3) approach, we are treating the dipolar and the quadrupolar components on equal footing.

The first step is to rewrite the Hamiltonian in terms of the SU(3) generators:

$$\hat{\mathcal{H}} = \frac{1}{2}\sum_{\boldsymbol{r},\boldsymbol{\delta}}\sum_{\mu,\nu=7,5,2}\hat{T}^\mu_{\boldsymbol{r}} J^{\mu\nu}_{\boldsymbol{\delta}}\hat{T}^\nu_{\boldsymbol{r}+\boldsymbol{\delta}} + \frac{D}{\sqrt{3}}\sum_{\boldsymbol{r}}\left(\hat{T}^8_{\boldsymbol{r}} + \frac{2}{\sqrt{3}}\right), \tag{2.58}$$

where $J^{\mu\nu}_{\boldsymbol{\delta}}$ is the generalized exchange tensor for SU(3) spins that takes non-zero values only for interactions between the dipolar components. Note that the second term of the

above equation can be expressed in multiple ways. This ambiguity is removed by requiring that each Hamiltonian term *must be linear in the SU(3) generators* acting on a given site $\boldsymbol{r}$ [note that the generators of SU(N) together with the identity form a complete basis for the complex vector space of $N \times N$ matrices]. As shown in Eq. (2.54), the quadrupolar components $\hat{T}^{3,8,1,4,6}$ in general do not commute with the dipolar ones $-\hat{T}^{7,5,2}$. As a result, the eight Heisenberg equations of motion for the SU(3) spin components on each site turn out to be coupled:

$$\frac{d\hat{T}^{\mu}_{\boldsymbol{r}}}{dt} = \sum_{\boldsymbol{\delta}} \sum_{\nu,\eta=7,5,2} \sum_{\chi=1}^{8} J^{\nu\eta}_{\boldsymbol{\delta}} f_{\mu\nu\chi} \hat{T}^{\chi}_{\boldsymbol{r}} \hat{T}^{\eta}_{\boldsymbol{r}+\boldsymbol{\delta}} + \frac{D}{\sqrt{3}} \sum_{\chi=1}^{8} f_{\mu 8\chi} \hat{T}^{\chi}_{\boldsymbol{r}}. \tag{2.59}$$

As for the SU(2) case, the classical limit of the interaction term is again obtained by assuming that the coherent state is a direct product of coherent states on each site. An important difference, however, is that the classical limit of the single-ion term does not require the use of the factorization rule, which can be a strong approximation for finite values of λ_1, because each term of Eq. (2.59) is now linear in the generators of SU(3) acting on a given site $\boldsymbol{r}$. After taking the classical limit on the left-hand side of the above equation, we obtain the classical equations of motion for the SU(3) spins

$$\frac{dn^{\mu}_{\boldsymbol{r}}}{dt} = \sum_{\boldsymbol{\delta}} \sum_{\nu,\eta=7,5,2} \sum_{\chi=1}^{8} J^{\nu\eta}_{\boldsymbol{\delta}} f_{\mu\nu\chi} n^{\chi}_{\boldsymbol{r}} n^{\eta}_{\boldsymbol{r}+\boldsymbol{\delta}} + \frac{D}{\sqrt{3}} \sum_{\chi=1}^{8} f_{\mu 8\chi} n^{\chi}_{\boldsymbol{r}}. \tag{2.60}$$

or

$$\frac{dn^{\alpha}_{\boldsymbol{r}}}{dt} = \sum_{\mu\nu} f_{\alpha\mu\nu} n^{\mu}_{\boldsymbol{r}} b^{\nu}_{\boldsymbol{r}}, \quad \boldsymbol{b}_{\boldsymbol{r}} = -\frac{dh}{d\boldsymbol{n}_{\boldsymbol{r}}}, \tag{2.61}$$

where

$$n^{\alpha}_{\boldsymbol{r}} = \langle Z|\hat{T}^{\alpha}_{\boldsymbol{r}}|Z\rangle = (\hat{\lambda}^{\alpha})_{ab} \bar{Z}^{a}_{\boldsymbol{r}} Z^{b}_{\boldsymbol{r}} \tag{2.62}$$

is the expectation value of the SU(3) generator based on the SU(3) coherent states $|Z\rangle = \otimes \sum_a Z^a_{\boldsymbol{r}} |x^a\rangle$ [see Eq. (2.56) for definitions of $|x^a\rangle$]. These expectation values are known as the *color fields* in literature of high-energy physics [3]. We note that Eq. (2.61) can be regarded as a generalization of the LLD (2.51).

Clearly, the SU(3) approach becomes strictly necessary when the ground state of the Hamiltonian under consideration has some form of nematic ordering, $\langle \hat{T}^{2,5,7} \rangle = 0$ and $\langle \hat{T}^{\nu} \rangle \neq 0$ for some values of $\nu = 1, 3, 4, 5, 6$, which can be either spontaneous or induced by a large single-ion anisotropy term, such as the last term of $\hat{\mathcal{H}}$ for $D \gg |J_{\boldsymbol{\delta}}^{\alpha\beta}|$. The simple reason is that the SU(2) coherent states cannot describe a local quadrupolar moment. The need for the SU(3) dynamics becomes a bit more subtle when the ground state exhibits some form of magnetic (dipolar) ordering. Even in that case, nematic fluctuations can renormalize the magnitude of the dipole moment or produce coherent low-energy modes, which are different from the usual spin waves (dipolar fluctuations). These are the situations in which the SU(3) dynamics becomes more appropriate than the traditional SU(2) dynamics. Put succinctly, the SU(3) approach can faithfully represent all types of local fluctuations of a three-level system.

SU(N) Landau-Lifshitz dynamics

The SU(2) LLD can be straightforwardly generalized to SU(N) spins by following the same steps that we described for the SU(3) case. The classical equations of motion are obtained by: (i) expressing the Hamiltonian in terms of generators of SU(N) under the condition that each term must be linear in the SU(N) spin components acting on a given site; (ii) computing the Heisenberg equation of motion for each generator of SU(N); and (iii) replacing the operators with their expectation values for coherent states of SU(N). In general, the equations of motion for the SU(N) "color fields" take the form,

$$\frac{d\boldsymbol{n}_{\boldsymbol{r}}}{dt} = \boldsymbol{n}_{\boldsymbol{r}} \times \boldsymbol{b}_{\boldsymbol{r}}, \quad \boldsymbol{b}_{\boldsymbol{r}} = -\frac{dh}{d\boldsymbol{n}_{\boldsymbol{r}}}, \tag{2.63}$$

where we have defined the generalized cross product on the orbit of SU(N):

$$(\boldsymbol{a} \times \boldsymbol{b})_{\eta} \equiv \sum_{\alpha,\beta} f_{\alpha\beta\eta} a^{\alpha} b^{\beta}. \tag{2.64}$$

Eq. (2.63) is one of the key results of this dissertation.

Based on the above discussion, it is apparent that to faithfully describe all types fluctuations in a spin-S system, whose classical phase space is isomorphic to CP^{N-1}, we need to take the classical limit based on $\mathrm{SU}(N)$ coherent states with $N = 2S + 1$. We note however that for particular spin Hamiltonians, a subgroup of $\mathrm{SU}(N)$ may also provide a good approximation, as long as it incorporates the relevant components of the local order parameter. As an example, we can just consider the case of a pure isotropic Heisenberg model, the dynamics of which is well described by the traditional SU(2) LLD if the spin S is large enough. The key observation is that the local order parameter of these systems has a dominant dipolar character and the normal modes are coherent spin waves. Non-dipolar fluctuations "are buried" in continuum of multiple spin waves. The classical SU(2) dynamics breaks down when new modes associated with non-dipolar fluctuations emerge below the continuum of multiple spin waves.

2.3.2 Single-ion model

Consider the following integer spin-S single-ion Hamiltonian,

$$\hat{\mathcal{H}}_{\mathrm{SI}} = D(\hat{S}^z)^2, \tag{2.65}$$

with $D > 0$. This term controls the high-temperature dynamics of the Hamiltonian given in Eq. (2.46) if $|D| \gg |J^{ij}_{\boldsymbol{\delta}}|$. The non-degenerate ground state of $\hat{\mathcal{H}}_{\mathrm{SI}}$ is the eigenstate of S^z with eigenvalue $m = 0$: $|m = 0\rangle$. The excited states are the doublets $|\pm m\rangle$ with $1 \leq m \leq S$. The exact quantum dynamics can be solved in a closed form as there is no interaction term in the Hamiltonian. The transverse dynamical spin structure factor can be computed by using the Lehmann representation:

$$\begin{aligned}
\mathcal{S}^{+-}(\omega) &= \frac{1}{2\pi Z}\int_{-\infty}^{+\infty} dt e^{i\omega t}\mathrm{Tr}\left[e^{-\beta\hat{\mathcal{H}}_{\mathrm{SI}}}\hat{S}^{+}(t)\hat{S}^{-}(0)\right] \\
&= \frac{1}{Z}\sum_{m=0}^{S-1} e^{-\beta m^2 D}(S-m)(S+m+1)\delta[\omega-(2m+1)D] \\
&= \mathcal{S}^{-+}(\omega),
\end{aligned} \tag{2.66}$$

for $\omega \geq 0$, where

$$Z = 1 + 2\sum_{m=1}^{S} e^{-\beta m^2 D} \tag{2.67}$$

is the partition function. Similarly,

$$\begin{aligned}\mathcal{S}^{zz}(\omega) &= \frac{1}{2\pi Z}\int_{-\infty}^{+\infty} dt e^{i\omega t}\mathrm{Tr}\left[e^{-\beta\hat{\mathcal{H}}_{\mathrm{SI}}}\hat{S}^z(t)\hat{S}^z(0)\right] \\ &= -\frac{1}{Z\beta}\frac{\partial Z}{\partial D}\delta(\omega).\end{aligned} \tag{2.68}$$

The classical spin dynamics of this problem can also be solved analytically. Let us first consider the SU(2) LL equations:

$$\frac{ds^x}{dt} = -2Ds^y s^z, \quad \frac{ds^y}{dt} = 2Ds^x s^z, \quad \frac{ds^z}{dt} = 0. \tag{2.69}$$

The solution is given by

$$s^+(t) = s^+(0)e^{i\tilde{\omega}_- t}, \quad s^-(t) = s^-(0)e^{i\tilde{\omega}_+ t}, \quad s^z(t) = s^z(0), \tag{2.70}$$

with $\tilde{\omega}_\pm = \pm 2Ds_z(0)$. The corresponding transverse dynamical spin structure factor is computed by performing a thermal average over initial SU(2) coherent states (see discussions in the next section for details), which reads

$$\mathcal{S}^{+-}_{\mathrm{SU(2)}}(\omega) = \frac{S^2\sqrt{\beta D}\left(1-\frac{\omega^2}{4D^2S^2}\right)e^{-\beta\frac{\omega^2}{4D}}}{2D\sqrt{\pi}\mathrm{erf}(\sqrt{\beta D}S)}\Theta(2DS-|\omega|) = \mathcal{S}^{-+}_{\mathrm{SU(2)}}(\omega), \tag{2.71}$$

where $\mathrm{erf}(x)$ is the error function and $\Theta(x)$ is the Heaviside step function. Similarly,

$$\mathcal{S}^{zz}_{\mathrm{SU(2)}} = \delta(\omega)S^2\left[-\frac{e^{-\alpha}}{\sqrt{\alpha}}\frac{1}{\sqrt{\pi}\mathrm{erf}(\sqrt{\alpha})} + \frac{1}{2\alpha}\right], \tag{2.72}$$

where $\alpha = \beta DS^2$.

Figure (2.1) shows a comparison between the exact result for the transverse dynamical spin structure factor [see Eq. (2.66)] and the SU(2) classical approximation given in Eq. (2.71) for three different spin values. Clearly, the quantum mechanical spectrum consists of discrete

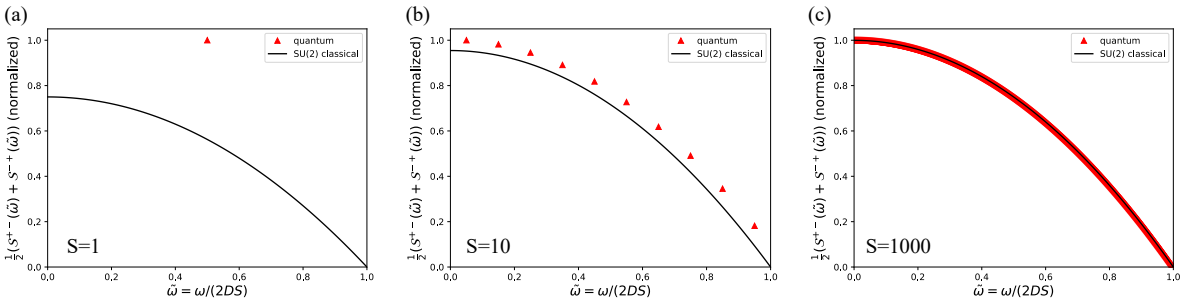


Figure 2.1: Comparisons of the transverse dynamical spin structure factor between the quantum (red triangle) and the SU(2) classical results (black line) for three different spin values: (a) $S = 1$, (b) $S = 10$, and (c) $S = 1000$. In all three panels, the inverse temperature $\beta DS^2 = 10^{-5}$, and the values of the dynamical structure factor are normalized to the maximum intensity of the exact result.

absorption peaks corresponding to $\Delta S_z = 1$ (for $\omega > 0$) transitions between discrete energy levels, whereas the SU(2) classical theory produces a broad continuum of spectral weight centered around $\omega = 0$. The continuous character of the distribution arises from the dependence of the spin precession frequency on the conserved quantity, $s^z(t) = s^z(0)$, which has a continuous distribution on the orbit of the SU(2) coherent states. For small values of S, such as $S = 1$, the classical result based on SU(2) coherent states deviates strongly from the exact quantum mechanical result [see Figs. (2.1)(a) and 1(b)]. Only for very large values of S [see Fig. (2.1) (c) for $S = 1000$] does the SU(2) classical result become a good approximation. The slow convergence of the quantum mechanical result to the large-S limit demonstrates the need of implementing an alternative classical limit for realistic Hamiltonians, such as $\hat{\mathcal{H}}_{\rm SI}$.

To illustrate the ideas discussed in Sec. 2.3.1, we now consider the classical limit of the single-ion model based on SU(3) coherent states as an approximation for the extreme $S = 1$ case. The generalized SU(3) LL equations take the form

$$\frac{dn_4}{dt} = -Dn_5, \quad \frac{dn_5}{dt} = Dn_4, \quad \frac{dn_6}{dt} = -Dn_7, \quad \frac{dn_7}{dt} = Dn_6, \tag{2.73}$$

$$\frac{dn_1}{dt} = \frac{dn_2}{dt} = \frac{dn_3}{dt} = \frac{dn_8}{dt} = 0. \tag{2.74}$$

The solution gives the time evolution of the classical dipole operators

$$\begin{aligned} s^{\pm}(t) = &\frac{1}{2}\big[s^{\pm}(0) \mp n_4(0) + in_6(0)\big]e^{iDt} \\ &+ \frac{1}{2}\big[s^{\pm}(0) \pm n_4(0) - in_6(0)\big]e^{-iDt}, \end{aligned} \tag{2.75}$$

where $s^{\pm} = -(n_7 \pm in_5)$, and

$$s^z(t) = s^z(0) = -n_2(0) \tag{2.76}$$

is a conserved quantity. By computing the thermal average over initial SU(3) coherent states of the Fourier transform of the spin-spin correlation function, we obtain the dynamical spin

structure factor for $\omega \geq 0$:

$$\mathcal{S}^{+-}_{\mathrm{SU}(3)}(\omega) = \delta_{\omega,D}\frac{6 + 2e^{\beta D}(\beta D - 3) + \beta D(\beta D + 4)}{\beta^2 D^2(e^{\beta D} - \beta D - 1)} = S^{-+}_{\mathrm{SU}(3)}(\omega), \tag{2.77}$$

and

$$\mathcal{S}^{zz}_{\mathrm{SU}(3)}(\omega) = \delta_{\omega,0}\frac{6e^{\beta D} - \beta D\left[6 + \beta D\left(3 + \beta D\right)\right] - 6}{3\beta^2 D^2(e^{\beta D} - \beta D - 1)}. \tag{2.78}$$

Figure (2.2) shows the comparison between the exact transverse dynamical spin structure factor of the $S = 1$ single-ion model and the results obtained with the SU(2) and SU(3) classical approximations for $\beta D S^2 = 0.1$. We can see that by working with the CP^2 classical phase space of the $S = 1$ system, we obtain a single transition at the correct frequency $\omega = D$, as opposed to the SU(2) classical approach. We also note that in the infinite temperature limit, $\beta D S^2 \to 0$, the intensity of the SU(3) classical result coincides with the exact quantum mechanical result if we renormalize the classical SU(3) spins $O^j_{\boldsymbol{r}} \to \kappa O^j_{\boldsymbol{r}}$ with $\kappa(N = 3, \lambda_1 = 1) = 2$. This renormalization factor is also required to satisfy the sum rule:

$$\sum_j \int d\omega \mathcal{O}^{jj}(\omega) = C_1(N = 3, \lambda_1 = 1) = \frac{16}{3}, \tag{2.79}$$

associated with the quadratic Casimir operator of SU(3) with eigenvalue $C_1(N = 3, \lambda_1 = 1)$, which holds for the SU(3) spin structure factor

$$\mathcal{O}^{jj}(\omega) = \frac{1}{2\pi Z}\int_{-\infty}^{+\infty} dt e^{i\omega t}\mathrm{Tr}\left[e^{-\beta\hat{\mathcal{H}}}\hat{O}^j(t)\hat{O}^j(0)\right]. \tag{2.80}$$

A similar renormalization factor $s^\alpha_{\boldsymbol{r}} \to \sqrt{1 + 1/S}s^\alpha_{\boldsymbol{r}}$ must be applied to the classical spins obtained from SU(2) coherent states to fulfill the sum rule in the infinite temperature limit [75]. In general, the renormalization factor that must be applied to recover the sum rule for arbitrary values of N and λ_1 is:

$$\kappa(N, \lambda_1) = \frac{\sqrt{C_1(N, \lambda_1)}}{\sqrt{(N-1)^3/(2N)\lambda_1}} = \sqrt{1 + N/\lambda_1}, \tag{2.81}$$

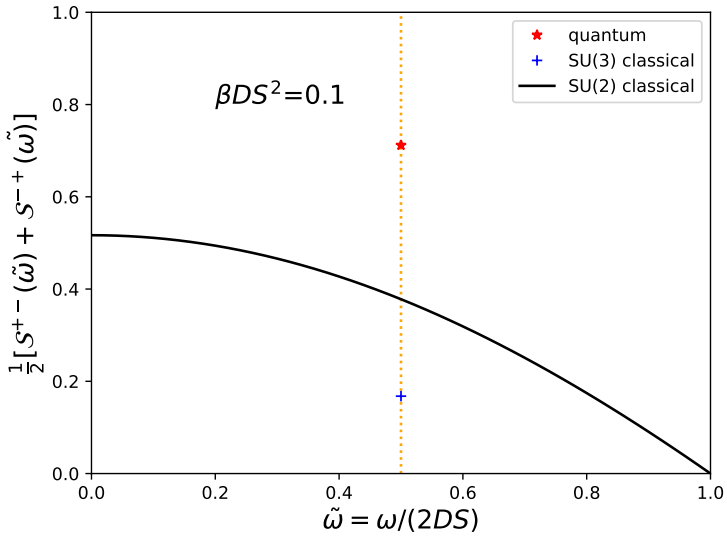


Figure 2.2: Comparison of the transverse dynamical spin structure factor for the $S = 1$ single-ion model as a function of the energy transfer at the inverse temperature $\beta DS^2 = 0.1$: quantum (red star), SU(3) classical (blue cross), and SU(2) classical (black line).

where $C_1(N, \lambda_1) = (N-1)^3\lambda_1^2/(2N) + (N-1)^3\lambda_1/2$ is the eigenvalue of the quadratic Casimir operator of SU(N) for the degenerate irrep $[\lambda_1, 0, \ldots, 0]$. The eigenvalues of the Casimir operators for semi-simple Lie groups were derived by Perelomov and Popov in [122]. Note that the eigenvalue of the quadratic Casimir operator of SU(N) in the physical basis considered in this work can be obtained by multiplying the eigenvalue in the basis adopted by Perelomov and Popov by a factor $(N-1)^2/2$.

In the low temperature limit, $\beta D S^2 \to \infty$, the dynamics is controlled by the normal modes of the quadratic fluctuations around the minimum energy classical state. The intensity of each excited mode is proportional to T because of the equipartition theorem. The exact quantum mechanical result can be recovered by multiplying the classical dynamical spin structure factor by $\beta\omega$, which is a well-known quantum-classical correspondence for the harmonic oscillator [169, 75] [see also Sec. 4.3.4 and Appendix C]. Note also that the ground state of $\hat{\mathcal{H}}_{\rm SI}$ has no net dipole moment, $\langle \hat{\boldsymbol{S}} \rangle = 0$, for $D > 0$. In other words, the state has only a net quadrupolar moment, implying that the orbit of SU(2) coherent states is incapable of representing the classical limit of this state. This is another clear indicator that one needs to use a bigger Lie algebra to define a classical limit of $\hat{\mathcal{H}}_{\rm SI}$ in order to capture the qualitative aspects of the exact quantum mechanical solution.

In summary, the spin dynamics of $\hat{\mathcal{H}}_{\rm SI}$ is well approximated by a classical LL dynamics based on SU(3) coherent states, but it is not well-described by the traditional SU(2) LL dynamics. Assuming that $|D|$ is comparable or bigger than zJ (z is the coordination number and J is the characteristic energy scale of the exchange tensor), this statement holds true for the full Hamiltonian $\hat{\mathcal{H}}$ [see Eq. (2.46)] for two simple reasons. In the high-T limit, the dynamics of $\hat{\mathcal{H}}$ is well approximated by the dynamics of $\hat{\mathcal{H}}_{\rm SI}$. The basic role of the interaction term of $\hat{\mathcal{H}}$ is to broaden the delta function shown in Fig. (2.2). In the low-T limit, the ground state of $\hat{\mathcal{H}}$ is a quantum paramagnet with no net dipolar moment for $D > 0$. As we already explained for the single-ion case, such a state has no classical counterpart within the orbit of SU(2) coherent states. We note that this statement remains true for the *magnetically ordered state* if the system is relatively close the to quantum critical point (QCP) that divides this phase from the quantum paramagnet [48] (see also Ch. 3), implying that it is still necessary to use SU(3) coherent states to approximate the spin dynamics of the ordered magnet in

the proximity of the QCP. Interestingly, this statement remains true for the easy-axis case $D < 0$ with $|D|$ comparable or bigger than zJ. In this limit, the ground state is an Ising-like magnetically ordered state, which certainly has a classical counterpart in SU(2) coherent states. However, the low-energy modes of this classical ground state include quadrupolar fluctuations [17], which are not captured by the traditional SU(2) LL dynamics.

2.3.3 Single-dimer problem

Consider the single-dimer problem introduced in Ch. 1

$$\hat{\mathcal{H}} = J\hat{\boldsymbol{S}}_1 \cdot \hat{\boldsymbol{S}}_2, \tag{2.82}$$

the eigenstates and eigenvalues of which are,

$$\begin{aligned} &|1\rangle = \frac{1}{\sqrt{2}}(|\uparrow\downarrow\rangle - |\downarrow\uparrow\rangle) \quad E_s = -\frac{3J}{4} \\ &\begin{cases} |2\rangle = |\uparrow\uparrow\rangle \\ |3\rangle = \frac{1}{\sqrt{2}}(|\uparrow\downarrow\rangle + |\downarrow\uparrow\rangle) \quad E_t = \frac{J}{4}\,. \\ |4\rangle = |\downarrow\downarrow\rangle \end{cases} \end{aligned} \tag{2.83}$$

The dynamical spin structure factor (DSSF) is computed by the Lehmann representation,

$$\mathcal{S}^{\mu\mu}_{\rm qm}(q,\omega) = \frac{1}{\mathcal{Z}}\sum_{i,j=1}^{4}\delta(\omega + E_i - E_j)e^{-\beta E_i}\langle i|\hat{S}^{\mu}_{q}|j\rangle\langle j|\hat{S}^{\mu}_{-q}|i\rangle, \tag{2.84}$$

where

$$\mathcal{Z} = e^{-\frac{\beta J}{4}}(3 + e^{\beta J}) \tag{2.85}$$

is the partition function. Due to the SU(2) invariance of the model Hamiltonian, we have

$$\mathcal{S}^{xx}_{\rm qm}(0,\omega) = \mathcal{S}^{yy}_{\rm qm}(0,\omega) = \mathcal{S}^{zz}_{\rm qm}(0,\omega) = \frac{\delta(\omega)}{3 + e^{\beta J}}, \tag{2.86}$$

and

$$\mathcal{S}^{xx}_{\rm qm}(\pi,\omega)=\mathcal{S}^{yy}_{\rm qm}(\pi,\omega)=\mathcal{S}^{zz}_{\rm qm}(\pi,\omega)=\frac{e^{\beta J}\delta(\omega-J)+\delta(\omega+J)}{2(3+e^{\beta J})}. \tag{2.87}$$

We can verify that the sum rule is satisfied,

$$\sum_{\alpha=x,y,z}\int d\omega\sum_{q}\mathcal{S}^{\alpha\alpha}_{\rm qm}(q,\omega)=\frac{3}{2}=2\times\frac{1}{2}\times\left(\frac{1}{2}+1\right)=N_sS(S+1), \tag{2.88}$$

where $N_s=2$ is the number of sites.

Now we consider the SU(2) classical limit of the dimer. The Landau-Lifshitz equation is written as

$$\frac{d\boldsymbol{S}_1}{dt}=J\boldsymbol{S}_2\times\boldsymbol{S}_1,\quad \frac{d\boldsymbol{S}_2}{dt}=J\boldsymbol{S}_1\times\boldsymbol{S}_2, \tag{2.89}$$

or equivalently,

$$\frac{d\boldsymbol{S}_t}{dt}=0\quad \frac{d\boldsymbol{S}_d}{dt}=J\boldsymbol{S}_t\times\boldsymbol{S}_d,\ \text{where}\ \boldsymbol{S}_t=\boldsymbol{S}_1+\boldsymbol{S}_2,\ \boldsymbol{S}_d=\boldsymbol{S}_1-\boldsymbol{S}_2. \tag{2.90}$$

As a result, we have a "single-spin" $\boldsymbol{S}_d$ precessing in an "external field" $\boldsymbol{S}_t$. The solution is

$$S^{\tilde{x}}_d(t)=S^{\tilde{x}}_d(0)\cos\omega t-S^{\tilde{y}}_d(0)\sin\omega t,\quad S^{\tilde{y}}_d(t)=S^{\tilde{y}}_d(0)\cos\omega t+S^{\tilde{x}}_d(0)\sin\omega t,\quad S^{\tilde{z}}_d(t)=S^{\tilde{z}}_d(0), \tag{2.91}$$

where $\check{\tilde{z}}=\boldsymbol{S}_t/|\boldsymbol{S}_t|$ is the unit vector in the direction of the total dipole moment, and $\check{\tilde{x}},\check{\tilde{y}}$ are unit vectors of the perpendicular plane of $\check{\tilde{z}}$. We note, however, that the characteristic precession frequency $\omega=J|\boldsymbol{S}_t|=\sqrt{2}SJ\sqrt{1+\cos\theta_{12}}$ is dictated by the initial angle θ_{12} between the two spin in the dimer (note that this angle is a conserved quantity because $\boldsymbol{S}_t$ is conserved). The spectrum is then continuous because θ_{12} is a continuous variable. Moreover, in the high-T limit, the excitation spectrum has a maximum at $\omega=2JS/\sqrt{3}$ (see Fig. 2.3). This is determined by maximizing $\sin^2(\theta_{12}/2)\sin\theta$, where the first factor corresponds to amplitude of the transition $(\boldsymbol{S}_1-\boldsymbol{S}_2)^2$, and the second factor represents the number of states in phase space that contributes to a given frequency $\omega=J|\boldsymbol{S}_t|$. This result is *qualitatively incorrect*! Nevertheless, for the purposes of comparison, we will still compute the corresponding DSSF. By choosing $\boldsymbol{S}_1(0)$ as the reference (to be fixed) and

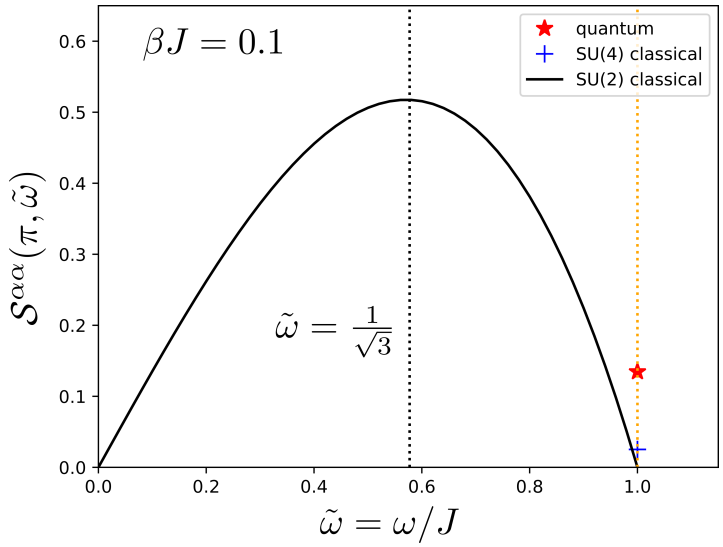


Figure 2.3: Comparisons of $\mathcal{S}^{\alpha\alpha}(\pi, \omega)$ for the single dimer as a function of the energy transfer at the inverse temperature $\beta J = 0.1$: quantum (red star), SU(4) classical (blue cross), and SU(2) classical (black line).

$\check{\tilde{y}} = \check{\tilde{z}} \times \boldsymbol{S}_1(0)/|\boldsymbol{S}_1(0)|$. We have (for $\omega \geq 0$)

$$\mathcal{S}^{\alpha\alpha}(0,\omega) = \frac{1}{6}\delta(\omega)\left[\frac{1}{2} + 2\left(\frac{1}{\beta J} - \frac{1}{4}\coth(\beta J/4)\right)\right], \tag{2.92}$$

and

$$\mathcal{S}^{\alpha\alpha}(\pi,\omega) = \frac{\exp\left[\frac{\beta(J^2-2\omega^2)}{4J}\right]\beta\omega(J^2-\omega^2)}{3J^2\sinh(J\beta/4)}\Theta(J-|\omega|). \tag{2.93}$$

Now we show that the correct classical limit for the dimer is based on the coherent states of SU(4). Instead of repeating the procedure outlined above and applying the Heisenberg equations (HE) of motion to (2.82), one can formulate an equivalent dynamics in the Schröodinger picture by explicitly introducing an SU(4) coherent state for the dimer. Because of the equivalence of the HE and Schrödinger pictures, together with the one-to-one correspondence between coherent states and expectation values, the resulting dynamics is entirely equivalent to the classical equations (2.63). In the "Schrödinger" picture, we have [46],

$$\frac{d}{dt}\boldsymbol{Z} = -i\mathfrak{h}\boldsymbol{Z}, \quad \text{where } \mathfrak{h} = \hat{\mathcal{H}}, \tag{2.94}$$

i.e. the dimer is treated as a single SU(4) spin. By choosing the eigen-basis [listed in Eq. (2.83)] of $\hat{\mathcal{H}}$ as the basis for $\boldsymbol{Z}$, the solution to Eq. (2.94) is given by

$$\boldsymbol{Z}(t) = z_1 e^{i\frac{3J}{4}t} + (z_2+z_3+z_4)e^{-i\frac{J}{4}t}, \tag{2.95}$$

where $z_{1,2,3,4}$ are complex variables depending on the initial condition. In the classical limit, the DSSF is computed as

$$\begin{aligned}\mathcal{S}^{\alpha\alpha}_{\mathrm{SU}(4)}(q,\omega) = \frac{1}{2\pi\mathcal{Z}_{\mathrm{SU}(4)}}\int_{-\infty}^{+\infty} dt e^{i\omega t}\int \mathcal{D}[\{\alpha_i\}]\langle \boldsymbol{Z}(\{\alpha_i\},t)|\hat{S}^{\alpha}_{q}|\boldsymbol{Z}(\{\alpha_i\},t)\rangle \\ \times \langle \boldsymbol{Z}(\{\alpha_i\},0)|\hat{S}^{\alpha}_{-q}|\boldsymbol{Z}(\{\alpha_i\},0)\rangle \exp\big[-\beta\langle \boldsymbol{Z}(\{\alpha_i\}|\hat{\mathcal{H}}|\boldsymbol{Z}(\{\alpha_i\}\rangle\big],\end{aligned} \tag{2.96}$$

where

$$\mathcal{Z}_{\mathrm{SU}(4)} = \int \mathcal{D}[\{\alpha_i\}]\exp\big[-\beta\langle \boldsymbol{Z}(\{\alpha_i\}|\hat{\mathcal{H}}|\boldsymbol{Z}(\{\alpha_i\}\rangle\big]. \tag{2.97}$$

We note that the above expression is obtained by applying the factorization rule, Eq. (2.35), to the quantum correlation function, $\langle \boldsymbol{Z}|\hat{S}^{\alpha}(t)\hat{S}^{\alpha}(0)e^{-\beta\hat{\mathcal{H}}}|\boldsymbol{Z}\rangle$. The integration $\int \mathcal{D}[\{\alpha_i\}]$ goes over the manifold of SU(4) coherent states with parameters $\{\alpha_i\}$. Here we use the angular parameterization for $\mathrm{CP}^3 \simeq S^7/S^1$ [113]. In this parameterization, an SU(4) coherent state is written as

$$|\boldsymbol{Z}\rangle = \cos\theta|1\rangle + e^{i\alpha_1}\sin\theta\cos\chi|2\rangle + e^{i\alpha_2}\sin\theta\sin\chi\cos\phi|3\rangle + e^{i\alpha_3}\sin\theta\sin\chi\sin\phi|4\rangle, \quad (2.98)$$

where $\alpha_{1,2,3} \in [0, 2\pi)$ and $\theta, \chi, \phi \in [0, \pi/2)$. The Haar measure for SU(4) [113] is

$$d\Omega_{\mathrm{SU}(4)} = \frac{6}{\pi^3} d\theta d\chi d\phi d\alpha_1 d\alpha_2 d\alpha_3 \sin^5\theta\cos\theta\sin^3\chi\cos\chi\sin\phi\cos\phi, \quad \text{where} \int d\Omega_{\mathrm{SU}(4)} = 1. \quad (2.99)$$

After integrating over these angular variables, we have (for $\omega \geq 0$)

$$\mathcal{S}^{\alpha\alpha}_{\mathrm{SU}(4)}(0,\omega) = -\frac{\beta J(\beta J(\beta J(\beta J+4)+12)+24)-24e^{\beta J}+24}{6\beta^2 J^2\left(\beta(-J)(\beta J+2)+2e^{\beta J}-2\right)}\delta(\omega), \quad \alpha = x, y, z \quad (2.100)$$

and

$$\mathcal{S}^{\alpha\alpha}_{\mathrm{SU}(4)}(\pi,\omega) = \frac{6e^{\beta J}(\beta J-4)+\beta J(\beta J(\beta J+6)+18)+24}{6\beta^2 J^2\left(\beta(-J)(\beta J+2)+2e^{\beta J}-2\right)}\delta(\omega - J) \quad \alpha = x, y, z, \quad (2.101)$$

implying that by taking the classical limit of Eq. (2.82) based on the SU(4) coherent states, we capture the correct discrete nature of the excitation spectrum for the dimer problem (see Fig. 2.3).

Finally, we have

$$\lim_{\beta\to\infty} \beta J \mathcal{S}^{\alpha\alpha}_{\mathrm{SU}(4)}(\pi,\omega) = \lim_{\beta\to\infty} \mathcal{S}^{\alpha\alpha}_{\mathrm{qm}}(\pi,\omega) = \frac{1}{2}, \quad (2.102)$$

which verifies the classical-to-quantum correspondence factor (see Sec. 4.3.4 and Appendix C) at $T = 0$, and

$$\lim_{\beta\to 0} \kappa^2_{\mathrm{SU}(4)} \mathcal{S}^{\alpha\alpha}_{\mathrm{SU}(4)}(\pi,\omega) = \lim_{\beta\to 0} \mathcal{S}^{\alpha\alpha}_{\mathrm{qm}}(\pi,\omega) = \frac{1}{8}, \quad (2.103)$$

which verifies the rescaling factor $\kappa_{\mathrm{SU}(4)} = \sqrt{5}$ [see Eq. (2.81)] for the fundamental representation of SU(4) in the infinite temperature limit.

As was the case for the single-ion model, we find that the exact quantum spin dynamics of the single dimer is well approximated by the classical LL dynamics based on SU(4) coherent states but is qualitatively different from the result obtained with the traditional SU(2) LL dynamics. By treating the single dimer as a whole, the intra-dimer exchange term becomes a generalized Zeeman term (linear coupling between an SU(4) "magnetic field" and the SU(4) spin). Systems where the dimers form a lattice connected by a relatively weak inter-dimer exchange interaction J' ($|J'| \lesssim J$), such as the spin ladder illustrated in Fig. 2.4**a**, become SU(4) spin lattices in the new language. The Hamiltonian of the spin ladder is written as

$$\hat{\mathcal{H}} = J \sum_i \hat{\boldsymbol{S}}_i^d \cdot \hat{\boldsymbol{S}}_i^u + J' \sum_i \sum_{m=d,u} \hat{\boldsymbol{S}}_i^m \cdot \hat{\boldsymbol{S}}_{i+1}^m, \tag{2.104}$$

where $m = d, u$ is the label of the two chains. By using the so-called bond-operator approach [131, 116], the Hamiltonian Eq. (2.104) reduces to a single chain of SU(4) spins (see Fig. 2.4**b**),

$$\hat{\mathcal{H}} = \sum_i \sum_\mu \mathcal{B}^\mu(J) \hat{T}_i^\mu + \sum_i \sum_{\mu,\nu} \hat{T}_i^\mu \mathcal{J}^{\mu\nu}(J') \hat{T}_{i+1}^\nu, \tag{2.105}$$

where $\hat{T}_i^\mu$ denotes the μ-th SU(4) generator [1] at "site" (rung of the ladder) i. The intra-dimer interaction J determines the "Zeeman energy" that splits the singlet and the triplet states of the i^{th} dimer, where the magnitude of the SU(4) "magnetic field" $\mathcal{B}^\mu$ is equal to J and its direction is parallel to the SU(4) generator $\hat{\boldsymbol{S}}_i^d \cdot \hat{\boldsymbol{S}}_i^u$. While the inter-dimer exchange interaction J' leads to an anisotropic exchange interaction between SU(4) spins, where the exchange tensor $\mathcal{J}^{\mu\nu}$ is a linear function of J' [116]. Large experimental [118, 155, 152] and numerical efforts [21, 149, 157] (just to name a few) have been dedicated to study the spin-ladder problem because it is one of the most fundamental problems in low-dimensional quantum magnetism. One drawback of these numerical techniques (such as the quantum Monte Carlo method [149]) is that they cannot handle finite-temperature dynamics for quantum spin lattice problems. Although the bond-operator method [131, 116] provides an alternative analytical approach to study the the finite-temperature dynamics, it only considers the Boltzmann distribution of the normal modes (harmonic approximation),

[1] Bilinear in bond operators that create singlet and triplet excitations at rung i.

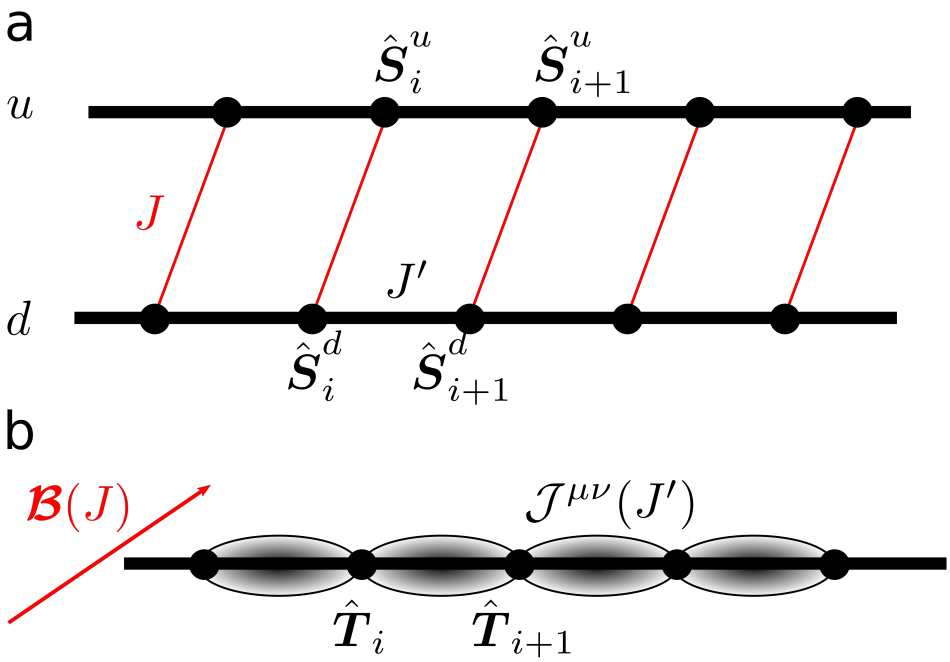


Figure 2.4: The spin ladder problem. **a.** The original problem: J denotes the exchange interactions between the dimers (rungs of the ladder) and J' labels the inter-dimer exchange interactions (along the legs of the ladder); $m = d, u$ is the label of the two chains. **b.** The SU(4) representation: The anisotropic "exchange" model with an exchange tensor $\mathcal{J}^{\mu\nu}(J')$ in a "magnetic field" $\boldsymbol{\mathcal{B}}(J)$.

i.e. any kind of *non-linear effect* is missed in this treatment. We conjecture that the classical SU(4) spin dynamics of the ladder problem for weakly coupled dimers provides a good approximation to the exact result at any temperature after properly rescaling the temperature axis. To the best of our knowledge, the application of the classical SU(N) dynamics to weakly coupled multi-spin unit systems (such as the spin ladder problem) has not been discussed in literature and it is an interesting topic for future studies.

2.4 Numerical methods

In this section, we explain the elementary numerical methods for the classical SU(N) LLD. More advanced and efficient numerical methods are discussed in detail in Ref. [46] and implemented in the open-source code `Sunny.jl` [22].

Here we explain how to compute the thermodynamic properties of an N_s-site quantum spin-S system in the classical limit based on SU(N) coherent states. Let us assume that the spin system is described by the Hamiltonian $\hat{\mathcal{H}}$. By exploiting the factorization rule given in Eq. (2.35), the expectation value of a thermodynamic observable $\hat{O}$ is given by,

$$\begin{aligned}\langle \hat{O} \rangle &= \frac{1}{Z}\mathrm{Tr}[e^{-\beta\hat{\mathcal{H}}}\hat{O}] = \frac{1}{Z}\int \mathcal{D}[\{\alpha_{\boldsymbol{r}}^{\rho}\}]\langle\Omega|e^{-\beta\hat{\mathcal{H}}}\hat{O}|\Omega\rangle \\ &\xrightarrow{\text{classical limit}} \frac{1}{Z}\int \mathcal{D}[\{\alpha_{\boldsymbol{r}}^{\rho}\}]e^{-\beta h[\{\alpha_{\boldsymbol{r}}^{\rho}\}]}o[\{\alpha_{\boldsymbol{r}}^{\rho}\}], \quad Z = \int \mathcal{D}[\{\alpha_{\rho}\}]e^{-\beta h[\{\alpha_{\boldsymbol{r}}^{\rho}\}]}, \end{aligned} \tag{2.106}$$

where $\mathcal{D}[\{\alpha_{\boldsymbol{r}}^{\rho}\}]$ is the integration measure over the set of $N_s(N-1)$ complex parameters $\{\alpha_{\boldsymbol{r}}^{\rho}\}$ of the SU(N) coherent states, and h and o are the classical limits defined in Eq. (2.34) for $\hat{H}$ and $\hat{O}$, respectively. Here $\hat{O}$ can be any static observables, such as the energy, the magnetization, the static structure factor $\mathcal{S}^{\mu\nu}(\boldsymbol{q}) = 1/N_s \sum_{\boldsymbol{r}} e^{-i\boldsymbol{q}\cdot\boldsymbol{r}}\hat{S}_{\boldsymbol{r}}^{\mu}\hat{S}_{\boldsymbol{0}}^{\mu}$, etc. It can also be a dynamical observable, such as the dynamical spin structure factor [see Eq. (2.66) for the definition of the single-ion model]. Unlike the results of the single-ion problem given in Eqs. (2.71) and (2.77), for most systems of interest it is difficult to find analytical expressions for integrals in Eq. (2.106). In Sec. 2.4.1, we explain how to use the Monte Carlo method to evaluate these high-dimensional integrals. Moreover, we need the numerical solution of the

classical equations of motion to be able to compute dynamical quantities. The algorithms are presented in Sec. 2.4.2.

2.4.1 Monte Carlo sampling on CP^{N-1}

An ensemble of states that follows the Boltzmann distribution (2.106) can be generated by the standard Metropolis-Hastings Monte Carlo algorithm [103, 66]. Here we provide the details of this algorithm for classical SU(3) spins, whose coherent states form the CP^2 manifold. This example will allow us to illustrate the general scheme for classical SU(N) spins with coherent states in a CP^{N-1} manifold. As we will demonstrate below, knowing the integration measure of the CP^{N-1} manifold [see Ref. [113]] in terms of $2(N-1)$ real parameters (angles) is enough to propose a Monte Carlo move.

The classical limit for a spin-1 system is based on direct products of SU(3) coherent states,

$$|Z\rangle = \otimes_{\boldsymbol{r}} |Z_{\boldsymbol{r}}\rangle, \tag{2.107}$$

where the coherent state on a particular site $\boldsymbol{r}$ is parameterized with four angles,

$$|Z_{\boldsymbol{r}}\rangle = \cos\theta_{\boldsymbol{r}}|0\rangle + e^{i\alpha_{1,\boldsymbol{r}}}\sin\theta_{\boldsymbol{r}}\cos\phi_{\boldsymbol{r}}|1\rangle + e^{i\alpha_{2,\boldsymbol{r}}}\sin\theta_{\boldsymbol{r}}\sin\phi_{\boldsymbol{r}}|-1\rangle. \tag{2.108}$$

The resulting manifold of coherent states is $S^5/S^1 \sim \mathrm{CP}^2$. The "local MC move" must be uniformly distributed on S^5/S^1, the integration measure of which is given by

$$\mathrm{d}\Omega_4 = \frac{2}{\pi^2}\mathrm{d}\theta\mathrm{d}\phi\mathrm{d}\alpha_1\mathrm{d}\alpha_2 \sin^3\theta\cos\theta\sin\phi\cos\phi, \tag{2.109}$$

with

$$\int_0^{\pi/2}\mathrm{d}\theta\int_0^{\pi/2}\mathrm{d}\phi\int_0^{2\pi}\mathrm{d}\alpha_1\int_0^{2\pi}\mathrm{d}\alpha_2 f(\theta,\phi,\alpha_1,\alpha_2) = 1, \tag{2.110}$$

where $f(\theta,\phi,\alpha_1,\alpha_2)$ is known as the joint distribution function. By integrating the joint distribution function over the other variables, we obtain the distribution function for θ, ϕ, and $\alpha_{1,2}$:

$$f(\theta) = 4\sin^3\theta\cos\theta,\ \ f(\phi) = \sin(2\phi),\ \ f(\alpha_{1,2}) = \frac{1}{2\pi}. \tag{2.111}$$

To generate random numbers that follow the above distribution functions, we apply the inverse transform sampling method by generating a local random move from the cumulative distribution function of the f's given in the above equation:

$$\theta = \sin^{-1}(U_1^{1/4}), \phi = \sin^{-1}(U_2^{1/2}), \alpha_{1,2} = 2\pi U_{3,4}, \tag{2.112}$$

where $U_{1,2,3,4}$ are pseudo-random numbers uniformly distributed between zero and one. Once the system is thermalized, we save the angle snapshots or take measurements every every N_{mes} MC sweeps, where the interval N_{mes} sweeps should be greater than the autocorrelation time.

2.4.2 Dynamical spin structure factor (classical)

The Fourier transform of the spin-spin correlation function is known as the dynamical spin structure factor,

$$\mathcal{S}^{\mu\nu}(\boldsymbol{q},\omega) = \frac{1}{2\pi N}\int_{-\infty}^{+\infty} dt e^{i\omega t}\sum_{i,j} e^{-i\boldsymbol{q}\cdot(\boldsymbol{r}_i-\boldsymbol{r}_j)}\langle \hat{S}_i^{\mu}(t)\hat{S}_j^{\nu}(0)\rangle. \tag{2.113}$$

Neutron scattering experiments provide a direct probe of the dynamical structure factor, where the neutron scattering intensity $I(\boldsymbol{q},\omega)$ is related to the dynamical structure factor through

$$I(\boldsymbol{q},\omega) \propto f^2(\boldsymbol{q})\sum_{\mu,\nu}\left(\delta_{\mu\nu} - \frac{q_\mu q_\nu}{q^2}\right)\mathcal{S}^{\mu\nu}(\boldsymbol{q},\omega), \tag{2.114}$$

where $f(\boldsymbol{q})$ is the magnetic form factor of the magnetic ion and the factor in the bracket is known as the neutron polarization factor [87]. By taking the classical limit as shown in Eq. (2.106), the (classical) dynamical spin structure factor is computed as

$$\mathcal{S}^{\mu\nu}(\boldsymbol{q},\omega) = \frac{\tau}{2\pi}\sum_{\text{IC}} s^{\mu}(\boldsymbol{q},\omega)s^{\nu}(-\boldsymbol{q},-\omega), \tag{2.115}$$

where the sum runs over the ensemble of initial conditions obtained from the MC procedure discussed in the previous section, and τ is time interval of the evolution, which should be

longer than any characteristic time of the system. The quantity

$$s^{\mu}(\boldsymbol{q},\omega) = \frac{1}{\sqrt{N_s}} \sum_{\boldsymbol{r}} \frac{1}{\tau} \sum_{t} e^{-i\boldsymbol{q}\cdot\boldsymbol{r}+i\omega t} s^{\mu}(\boldsymbol{r},t) \tag{2.116}$$

is the Fourier transform of the classical dipolar operator $s^{\mu}(\boldsymbol{r},t)$, which is obtained by numerically solving the generalized Landau-Lifshitz equation Eq. (2.63) with the fourth order Runge-Kutta (RK4) method and N_s is the total number of sites in the finite lattice system.

Chapter 3

Applications of the classical spin dynamics

3.1 Motivation

In this chapter we seek to test the hypothesis proposed in Ch. 2, i.e., that the low-energy excitations of large classes of spin systems are better described by classical limit based on SU(N) coherent states. To this end, we consider the case of the effective spin-1 antiferromagnet $Ba_2FeSi_2O_7$.

3.2 The $Ba_2FeSi_2O_7$ compound

Figure 3.1 (a) illustrates the crystal structure of $Ba_2FeSi_2O_7$ comprising layers of $FeSi_2O_7$ separated by Ba atoms. As shown in Fig. 3.1 (b), the FeO_4 tetrahedra of the $FeSi_2O_7$ layer are connected via SiO_4 polyhedra and the two adjacent Fe^{2+} (magnetic) atoms are coupled through the super-exchange interaction, J, that is mediated by the two oxygen ligands (red dashed line in Fig. 3.1 (b)). The magnetic ions of each layer from square lattices that are vertically stacked along the c-axis, leading to a quasi-two-dimensional simple tetragonal spin-lattice.

The single-ion state of the Fe^{2+} ion is illustrated in Fig. 3.2. Due to the combined effects of the crystal field and spin orbit coupling, the five $S = 2$ energy levels of the Fe^{2+} split into

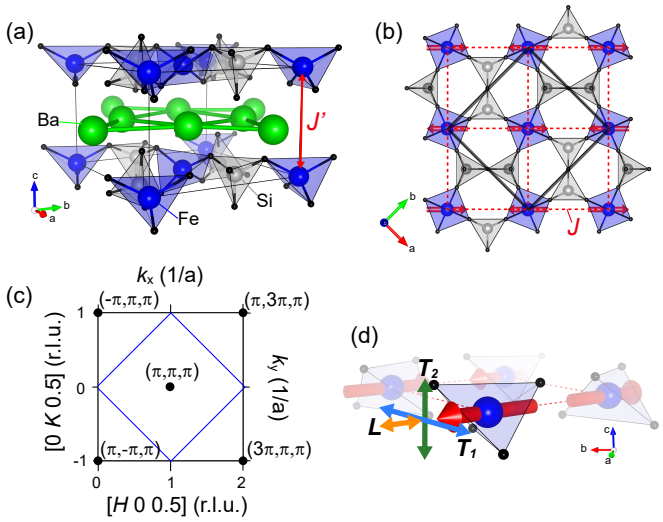


Figure 3.1: (a) Crystal structure of $Ba_2FeSi_2O_7$. Ba atoms separate layers (with exchange interaction J') composed of $FeSi_2O_7$, resulting in a quasi-two-dimensional structure. (b) In-plane magnetic unit cell formed by Fe^{2+} with exchange interaction J. (c) The Brillouin zone. The coordinates $(H\ K\ L)$ of the reciprocal lattice of the origin lattice are related to $(k_x\ k_y\ k_z)$ of the magnetic lattice formed by the Fe^{2+} atoms through $k_x = 2\pi(H-K)$, $k_y = 2\pi(H+K)$, and $k_z = 2\pi L$. (d) Illustration of the spin fluctuation modes. T_1 and T_2 indicate transverse fluctuation in the ab-plane and out-of the plane, respectively. L indicates longitudinal fluctuation of spin.

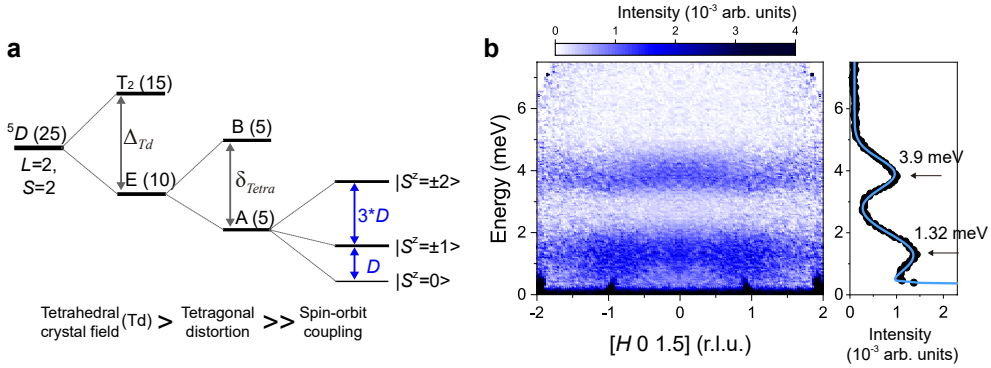


Figure 3.2: (a) Orbital energy states of Fe^{2+} with a tetrahedral crystal field (Δ_{Td}), tetragonal distortion (δ_{Tetra}), and spin orbit coupling (λ). (b) The left panel shows inelastic neutron scattering data measured at T=90 K, symmetrized over negative and positive H and integrated over L=[0.9, 2.1] and K=[-0.1,0.1]. The integrated scattering intensity over H=[-2, 2] is shown in the right panel. The two peaks were fitted with Gaussian functions (solid blue line). Arrows indicate the peak centers at 1.32 meV and 3.2 meV.

a singlet S^z=0 ground state and two excited $S^z = \pm 1$ and $S^z = \pm 2$ doublets with energies D and $4D$, respectively (see Fig. 3.2 (a)). As a result, the spin excitations of $Ba_2FeSi_2O_7$ are generically described by an antiferromagnetic $S = 2$ spin Hamiltonian on a simple tetragonal lattice:

$$\begin{aligned}\hat{\mathcal{H}} = & J \sum_{\langle \boldsymbol{r}, \boldsymbol{r}' \rangle} \left[\hat{S}^x_{\boldsymbol{r}} \hat{S}^x_{\boldsymbol{r}'} + \hat{S}^y_{\boldsymbol{r}} \hat{S}^y_{\boldsymbol{r}'} + \Delta \hat{S}^z_{\boldsymbol{r}} \hat{S}^z_{\boldsymbol{r}'} \right] \\ & + J' \sum_{\langle\langle \boldsymbol{r}, \boldsymbol{r}' \rangle\rangle} \left[\hat{S}^x_{\boldsymbol{r}} \hat{S}^x_{\boldsymbol{r}'} + \hat{S}^y_{\boldsymbol{r}} \hat{S}^y_{\boldsymbol{r}'} + \Delta' \hat{S}^z_{\boldsymbol{r}} \hat{S}^z_{\boldsymbol{r}'} \right] \\ & + D \sum_{\boldsymbol{r}} (\hat{S}^z_{\boldsymbol{r}})^2. \end{aligned} \tag{3.1}$$

Because the gap D of the $S^z = \pm 1$ doublet is four times smaller than the gap of the $S^z = \pm 2$ doublet and the dominant super-exchange interaction J is smaller than $D/4$ in $Ba_2FeSi_2O_7$, the low-energy spectrum is well captured by projecting the $S = 2$ spin Hamiltonian into the $S^z = 0$ and $S^z = \pm 1$ low-energy states. The resulting effective $S = 1$ model is written as

$$\begin{aligned}\hat{\mathcal{H}}_{\text{eff}} = & \tilde{J} \sum_{\langle \boldsymbol{r}, \boldsymbol{r}' \rangle} \left[\hat{S}^x_{\boldsymbol{r}} \hat{S}^x_{\boldsymbol{r}'} + \hat{S}^y_{\boldsymbol{r}} \hat{S}^y_{\boldsymbol{r}'} + \tilde{\Delta} \hat{S}^z_{\boldsymbol{r}} \hat{S}^z_{\boldsymbol{r}'} \right] \\ & + \tilde{J}' \sum_{\langle\langle \boldsymbol{r}, \boldsymbol{r}' \rangle\rangle} \left[\hat{S}^x_{\boldsymbol{r}} \hat{S}^x_{\boldsymbol{r}'} + \hat{S}^y_{\boldsymbol{r}} \hat{S}^y_{\boldsymbol{r}'} + \tilde{\Delta}' \hat{S}^z_{\boldsymbol{r}} \hat{S}^z_{\boldsymbol{r}'} \right] \\ & + \tilde{D} \sum_{\boldsymbol{r}} (\hat{S}^z_{\boldsymbol{r}})^2. \end{aligned} \tag{3.2}$$

with $\tilde{J} = 3J$, $\tilde{J}' = 3J'$, $\tilde{\Delta} = \Delta/3$, $\tilde{\Delta}' = \Delta'/3$ and $\tilde{D} = D$.

3.3 Inelastic neutron scattering data

Figure 3.3(a) shows the temperature dependence of the unpolarized neutron scattering intensity $I(\boldsymbol{Q}, E)$ [see Eq. (2.114)] of $Ba_2FeSi_2O_7$. Below T_N, the spectrum exhibits sharp spin waves corresponding to acoustic (T_1) and optical (T_2) transverse modes at the zone center (ZC), $\boldsymbol{Q}_m = (1, 0, 0.5)$. The longitudinal mode is observed as a broad continuum above the T_1-mode throughout the entire Brillouin zone (BZ) due to decay into a pair of transverse modes Ref. [48]. While the sharp spin waves disappear above T_N, a broad dispersion with a finite gap emerges at the ZC. With increasing temperature, the gap size increases up to an

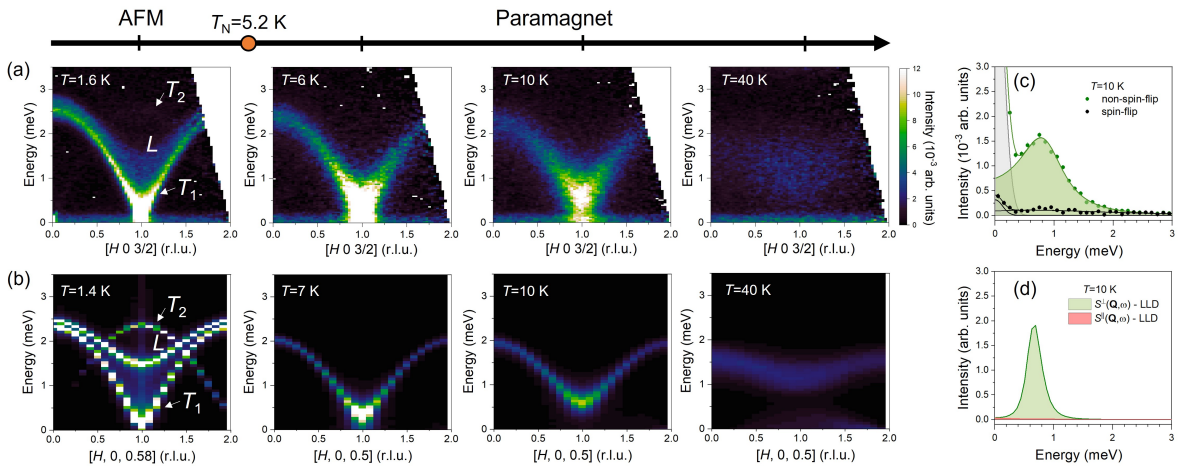


Figure 3.3: (a) Contour maps of the INS data as a function of energy and momentum transfer along the $[H, 0, 1.5]$ direction measured at $T = 1.6$ K, 6 K, 10 K, and 40 K. The T_1, T_1, and L indicate the acoustic and optical transverse modes, and the longitudinal mode in the spectra. (b) Resolution convoluted INS intensities calculated by the LLD method at the temperatures indicated in each subpanel. (c) Polarized neutron scattering at $\boldsymbol{Q} = (1, 0, 0)$ measured at 10 K ($T > T_{\rm N}$). The Non-spin-flip (spin-flip) channel for the z-polarization response correspond to the transverse (longitudinal) component of $I(\boldsymbol{Q}, E)$. The green-shaded region indicates the magnetic INS response extracted by fitting a DLDHO function to data. (d) Green (red) shaded region indicates the transverse (longitudinal) component of $I(\boldsymbol{Q}, E)$ calculated by LLD.

energy approximately equal to D (gap of the single-ion problem) and the bandwidth becomes narrower. To understand the diffusive spectra above $T_{\rm N}$, our experimental collaborators performed a polarized neutron scattering experiment. Fig. 3.3 (c) shows the neutron spin polarization dependence of the $I(E)$ at $\boldsymbol{Q} = (1, 0, 0)$. The neutron spin-flip and non-spin-flip dependence are coupled to the sample magnetization and the wave-vector, allowing us to extract the directional dependence of the dynamical spin structure factor [see Eq. (2.113)]. For this polarization geometry, the neutron spin polarization along $[0, 1, 0]$ provides separate in-plane ($\mathcal{S}^{\perp} = \mathcal{S}^{xx}(\boldsymbol{Q}, E) + S^{yy}(\boldsymbol{Q}, E)$) and out-of plane ($\mathcal{S}^{\parallel} = \mathcal{S}^{zz}(\boldsymbol{Q}, E)$) components of $S(\boldsymbol{Q}, E)$, for the non spin-flip and spin-flip channels, respectively. The resulting spectra exhibits dominant scattering intensity for the non spin-flip channel, indicating the diffusive spectra at 10 K mainly comes from the in-plane components of $\mathcal{S}(\boldsymbol{Q}, E)$.

3.4 Simulation details

The model parameters of this calculation are listed in Table 5.1 by fitting the GSWT calculation with the INS data that will be discussed in Sec. 5.1. The simulations are done on finite lattices of $24 \times 24 \times 12$ sites. The spin snapshots are saved every 100 MC sweeps (the interval of 100 sweeps is greater than the autocorrelation time of $\simeq 60$ MC sweeps). Finally, we have verified that the sum rule, $\int d\omega \mathcal{S}^{\mu\nu}(\boldsymbol{Q}, \omega) = \mathcal{S}^{\mu\nu}(\boldsymbol{Q})$, which relates the integration of the dynamical spin structure factor and the static spin structure factor obtained from MC, is satisfied to a good approximation for the number of initial conditions that we are using. For the results shown in this work, we used 200 and 2000 initial conditions for temperatures below and above $T_{\rm N}$, respectively.

3.5 Comparison with experiments

The resulting $I(\boldsymbol{Q}, E)$ is compared to the experimental data in Fig. 3.3(b). Because the classical approximation underestimates the value of Néel temperature $T_{\rm N}$ by a factor of ~ 3, $T_{\rm N} \simeq 3T_{\rm N}^{\rm cl}$, we compare the measured and calculated spectra at the same values of $T/T_{\rm N}$ and $T^{\rm cl}/T_{\rm N}^{\rm cl}$, respectively. Below the $T_{\rm N}$, the calculated spectrum exhibits the two

transverse modes, T_1 and T_2, and the longitudinal mode, L. Since the LLD calculation at low temperatures coincides with the generalized *linear* spin wave calculation [48] [see also, Ch. 5], the decay and renormalization of the T_2 and L-modes observed at 2 K [Fig. 3.4(a)] are not captured by this classical approximation. Above $T_{\rm N}$, the LLD calculation reproduces the gapped nature of the spectrum, representing an excitation between the $|S^z = 0\rangle$ and $|\pm 1\rangle$ states with a finite dispersion due to the exchange interaction. As the temperature increases, the mode becomes a less-dispersive broad peak centered around an energy $E_p \simeq D$. In the classical description, this diffusive mode originates from the combined effect of the "external SU(3) field," D, which induces a precession of each SU(3) moment with frequency $D/\hbar$ (center of the peak), and the random molecular field generated by the exchange interaction between the fluctuating neighboring moments, which determines the width of the peak. We note that the traditional LL dynamics based on SU(2) coherent states cannot capture this gapped diffusive mode and gives a qualitatively incorrect result in the high-temperature limit.

The computed spectra reproduce the main characteristics of the observed dispersions and bandwidth. Since the $|S^z = 0\rangle$ and $|\pm 1\rangle$ states are connected by the components that are transverse to the z-axis, $S^{\pm}{=}S^x \pm iS^y$, the corresponding intensity of $I(\boldsymbol{Q}, E)$ should appear in the channel $\mathcal{S}^{\perp}{=}\mathcal{S}^{xx}(\boldsymbol{Q},\omega) + \mathcal{S}^{yy}(\boldsymbol{Q},\omega)$ [see Fig. 3.3(d)], which is in good agreement with the polarization dependence of the measured $\mathcal{S}(\boldsymbol{Q},\omega)$. However, it is also clear from the comparison that the calculated spectrum underestimates the width of the mode at temperatures $T \gtrsim T_N$. As was mentioned in Sec. 2.3.2, this discrepancy arises from an inadequate normalization of the SU(3) spins at $T \gtrsim T_N$, an issue which we pursue further now.

To explore the origin of this disagreement, Fig. 3.4 compares the measured and calculated energy scans at ZC with varying temperature. We consider a wave vector $\boldsymbol{Q} = (1, 0, 0.2)$ that is close, but not exactly equal, to the ordering wave vector $\boldsymbol{Q}_{\rm m}$ in order to avoid the tail of the Bragg reflection below $T_{\rm N}$ and the technical challenges associated with calculating the spectrum at ZC. The three modes discussed above are visible in the spectrum shown in Fig. 3.4(a). In particular, the Goldstone mode becomes visible because of its finite energy at $\boldsymbol{Q} = (1, 0, 0.2)$ generated by the L-dispersion produced by the small inter-layer coupling J'.

While the T_1 and T_2 transverse modes remain nearly unchanged with increasing temperature, the frequency of the L-mode decreases and the model becomes broader and indistinguishable from the quasi-elastic scattering near $T_{\rm N}$. Above $T_{\rm N}$, the quasi-elastic scattering continuously evolves into a broad peak centered at finite energy, the energy of which increases gradually with the temperature (see Fig. 3.4(c)).

Figure 3.4(b)-(c) shows a comparison between the LLD calculation and the INS data across $T_{\rm N}$. Remarkably, the spectral weight for the longitudinal mode (indicated by arrow) is enhanced and shifts to low-energy with decreasing temperature, which is consistent with the data. Above $T_{\rm N}$, the LLD calculation gives a diffusive peak-shaped spectrum centered at a energy E_p that approaches D for $T \gg T_N$, as expected from the single-ion result [see Sec. 2.3.2]. It is important to note that the usual LL dynamics based on SU(2) coherent states predicts a qualitatively different behavior in the entire temperature range. The longitudinal mode is not captured below $T_{\rm N}$ and the diffusive peak remains centered around $E_p = 0$ for $T > T_{\rm N}$.

As it is clear from 3.4(c), the main shortcoming of the SU(3) LL dynamics is that it underestimates the width of the diffusive peak. This discrepancy can be removed in the high-temperature limit by applying an adequate renormalization of the SU(3) spins $n^\eta_{\boldsymbol{r}} \to \kappa n^\eta_{\boldsymbol{r}}$, with $\kappa = 2$ in the high-temperature ($T \gg T_{\rm N}$) limit [see Sec. 2.3.2]. This renormalization guarantees that the SU(3) spin dynamical structure factor satisfies the exact sum rule in the high-T limit, and it increases the theoretical Néel temperature to $T^{\rm cl}_{\rm N} \simeq 7.5$ K, which is approximately 2.3 K higher than the experimental value. Fig. 3.5 (a) shows comparison between the new results obtained after applying this renormalization factor and the experimental data measured at the same temperature $T^{\rm cl} = T^{\rm exp}$. The comparison reveals an excellent agreement at the highest temperatures. As expected, significant deviations are observed at the lowest two temperatures, $T = 12$ K and $T = 10$ K, because they are relatively close to the theoretical Néel temperature $T^{\rm cl}_{\rm N} \simeq 7.5$ K of the classical simulation with $\kappa = 2$. In other words, since the energy E_p of the diffusive peak goes to zero at the Néel temperature, its position is shifted to the left relative to the measured peak at $T = 10$ K. The emergence of a quasielastic peak (centered at $E = 0$) in the theoretical calculation is the clear indicator of proximity to the Néel temperature $T^{\rm cl}_{\rm N}$. Figures 3.5 (b) and (c) show a comparison of

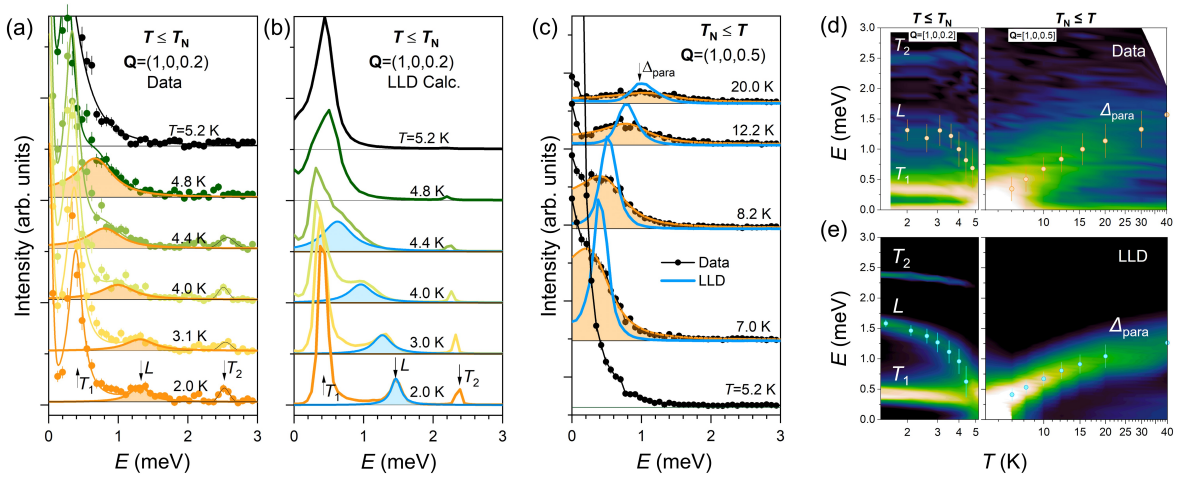


Figure 3.4: (a) Measured constant momentum scans at the ZC with temperatures below T_N and (b) corresponding calculated spectra from LLD. The transverse and longitudinal modes are indicated with labels 'T_1', 'T_2', and 'L'. (c) Comparison of the measured and calculated momentum scans above T_N. The spectral weight for the resonant excitation (longitudinal mode) arising above T_N (below T_N) was fitted with DLDHO function, and the fitting results are indicated by the shaded regions. The extracted spectral shapes of the resonant modes are compared with the LLD calculations shown by the blue solid line in (c). (d)(e) Comparison of contour plots of the constant momentum scans between data and LLD calculation across T_N.

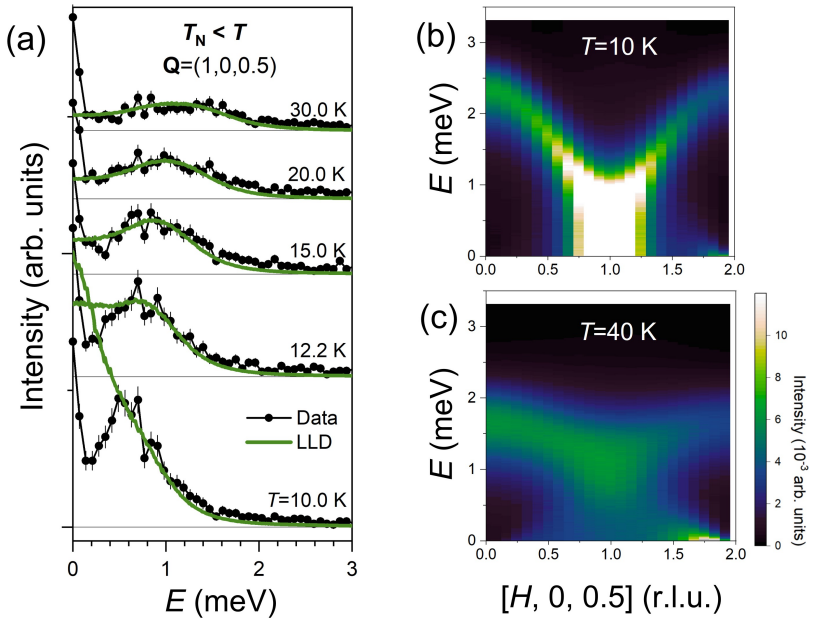


Figure 3.5: (a) Comparison of the measured energy scans at the ZC above T_N and $I(\boldsymbol{Q}, E)$ (b) At T=10 K and (c) at T=40 K, with the results obtained from LLD simulations with renormalized SU(3) spins ($n^{\eta}_{\boldsymbol{r}} \to \kappa n^{\eta}_{\boldsymbol{r}}$).

the dispersion and intensity of the mode, $I(\boldsymbol{Q}, E)$, along the same direction in reciprocal space that is presented in Fig. 3.3. As it is clear from these figures, the agreement between experiment and theory also exhibits a significant improvement away from the ZC.

3.6 Conclusions

In summary, the generalized classical LL dynamics based on SU(3) spins reproduces to a good approximation the measured INS cross section over the full temperature range from $T \ll T_{\rm N}$ to $T \gg T_{\rm N}$. The most significant quantitative deviations are observed at very low temperatures $T \ll T_{\rm N}$ and very close to $T_{\rm N}$. As we have demonstrated in Ref. [48], the former are due to quantum corrections that account for the decay of the longitudinal mode into two transverse modes. The latter are due to an expected discrepancy between the measured value of of the Néel temperature $T_{\rm N} = 5.2$ K and the value $T_{\rm N}^{\rm cl} \simeq 7.5$ K that is obtained from the simulations after applying the rescaling factor $\kappa = 2$ to the classical SU(3) spins. This rescaling factor arises from enforcing the sum rule in the infinite T limit. Similarly, the LL dynamics of unrenormalized classical SU(3) ($\kappa = 1$) leads to the correct sum rule in the zero temperature limit after quantizing the normal modes. Therefore, the correct scaling factor should be a function $\kappa(T)$ that monotonically interpolates between the two limiting cases $\kappa(0) = 1$ and $\kappa(\infty) = 2$. Clearly, this interpolation should produce a more accurate estimate of the Néel temperature and the dynamical spin structure factor near $T_{\rm N}$. Finding the optimal interpolation function $\kappa(T)$ is also a challenge for the traditional SU(2) LL dynamics and is a topic worthy of further study.

Chapter 4

Generalized spin wave theory

4.1 Introduction

In Ch. 3, we saw that experimental data of the high-temperature dynamics of the effective $S = 1$ system $Ba_2FeSi_2O_7$ is well reproduced by the SU(3) classical spin dynamics introduced in Ch. 2. Quantum fluctuations become increasingly important below the classical-to-quantum cross-over temperature, i.e., when k_BT is smaller than, or comparable to, the characteristic energy, $\hbar\omega$, of a given mode. Genuine many-body effects induced by quantum fluctuations —such as the decay and renormalization of the spectra— cannot be explained with the classical spin dynamics. In this chapter, we present a semiclassical approach to incorporating such quantum effects that is applicable to a large class of realistic spin systems. In particular, the approach is appropriate when a spin system has a ground state that *still admits a classical limit*, while the transitions into the excited states must be described quantum mechanically. In general, these classical ground states break translational symmetry and are written as direct products of coherent states. Each coherent state can either represent the quantum mechanical state of a single spin — as in the examples of $Ba_2FeSi_2O_7$ and FeI_2, discussed in Chpts. 3 and 5, respectively — or a locally entangled state of a multi-spin unit, such a the singlet ground state of a spin dimer [131, 100].

At low temperatures, the normal (collective) modes associated with small fluctuations of the classical ground state are known as *spin waves*. Following the conventional paradigm, we introduce bosonic operators that satisfy $[b_i, b_j^\dagger] = \delta_{ij}$ in order to quantize these spin waves.

The corresponding bosonic particle is known as a *magnon*. We briefly review the conventional SU(2) spin wave theory (SWT) in Sec. 4.2. Similar to the SU(N) generalization of the Landau-Lifshitz dynamics discussed in previous chapters, the conventional SWT must also be generalized. In Sec. 4.3, we present the formalism for the SU(N) SWT. In particular, we will see that the integer parameter M, which labels the different *degenerate* irreps of SU(N) (see Sec. 2.3) plays the role of $1/\hbar$, i.e. it is the control parameter for the semiclassical expansion of the SU(N) spin wave theory. For this reason, we will call it "$1/M$-expansion" [110, 17, 48], which is a generalization of the well-known $1/S$ expansion. The formalism introduced in this chapter will be applied in Ch. 5.

4.2 SU(2) spin wave theory

As mentioned above, the starting point of SWT is the classical ground state configuration. To describe small fluctuations of the spins around the ground state, Holstein and Primakoff [71] introduced a bosonic representation of the spin operators [SU(2) generators] in the *local* reference frame whose z-axis is aligned with the direction of the ordered moment $\boldsymbol{s}_j \equiv \langle\Omega_j|\hat{\boldsymbol{S}}|\Omega_j\rangle = S(\sin\theta_j\cos\phi_j, \sin\theta_j\sin\phi_j, \cos\theta_j)$, where θ_j, ϕ_j are the parameters of the local SU(2) coherent state $|\Omega_j\rangle$. The Holstein-Primakoff representation of the spin operators is:

$$\hat{\tilde{S}}_j^+ = \sqrt{2S - b_j^\dagger b_j} b_j, \quad \hat{\tilde{S}}_j^- = b_j^\dagger \sqrt{2S - b_j^\dagger b_j}, \quad \hat{\tilde{S}}_j^z = S - b_j^\dagger b_j. \tag{4.1}$$

where $\hat{\tilde{S}}^\mu$ represents the component of the spin operator in the local reference frame. Using the canonical commutation relations for the bosonic operators, $[b_j, b_j^\dagger] = 1$, we recover the SU(2) spin operator commutation relations: $[\hat{\tilde{S}}^\mu, \hat{\tilde{S}}^\nu] = i\epsilon^{\mu\nu\rho}\hat{\tilde{S}}^\rho$,

The well-known $1/S$ expansion is obtained by expanding the square roots in Eq. (4.1) in powers of $1/S$ [10, 83, 97, 39, 101, 16]. In Appendix C, we use a square lattice antiferromagnet (SLAFM) as an example to illustrate the application of conventional SWT in the harmonic approximation. The theoretical framework for higher order quantum corrections in $1/S$ has been discussed thoroughly in Refs. [38, 174, 108] and used to explain many-body quantum effects observed in a large number of $S = 1/2$ systems [141, 72, 95, 98, 124]. However,

as we explained in Ch. 2, the SU(2) approach must be generalized to study the dynamical properties of $S \geq 1$ systems under general conditions. This will be the main topic of the remaining sections of this chapter.

4.3 SU(N) spin wave theory

4.3.1 SU(N) Schwinger boson representation

The SU(N) generators introduced in Eq. (2.3) can be written as bilinear forms in terms of N "flavors" of Schwinger boson (SB) operators [16],

$$\hat{g}_{mm'} = b_m^\dagger b_{m'}, \tag{4.2}$$

where $1 \leq m(m') \leq N$ is the flavor index of the SB. The SB operators satisfy an additional local constraint

$$\sum_{m=1}^{N} b_{\boldsymbol{r},m}^\dagger b_{\boldsymbol{r},m} = M, \tag{4.3}$$

which determines the finite-dimensional local Hilbert space of a spin system. Here $M = \lambda_1$ is an integer equal to the maximum eigenvalue of the Cartan subalgebra generator $\hat{H}_1$ defined in Eq. (2.9) (note that $\lambda_j = 0$ for $2 \leq j \leq N-1$), that labels different degenerate irreps of SU(N). The dimension $\mathcal{D}$ of the representation (i.e. of the local Hilbert space) is $\binom{M+N-1}{N-1}$. Note that $\mathcal{D} = N$ for the fundamental $M = 1$ representation. In other words, the finite dimensional space of the spin system under consideration is obtained as a projection of the Fock space of the canonical bosons [16].

By combining the canonical commutation relations and the constraint, $[b_m, b_{m'}^\dagger] = \delta_{mm'}$, we can demonstrate that bilinear forms given in (4.2) obey the SU(N) commutation relations given in Eq. (2.6). The number of bosons is $M = 1$ for the fundamental representation of SU(N) and it is higher than one for other irreducible representations. For instance, as it is illustrated in Figure 4.1, $M = 2$ for the spin one representation of SU(2) and $N = 2$ (two flavors needed to get the generators of SU(2)).

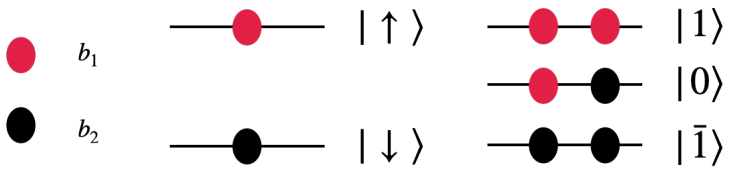


Figure 4.1: In terms of the SU(2) Schwinger bosons (SBs), we have $\hat{S}^z = (b_1^\dagger b_1 - b_2^\dagger b_2)/2$. Left panel: the total number of SBs is $M = 1$ in the fundamental representation of SU(2). Right panel: $M = 2$ for the $S = 1$ representation of SU(2).

The SU(N) Schwinger boson representation of the spin operators should not be confused with the Schwinger boson approximation [14, 16, 56, 170], which is qualitatively different from the semi-classical approach that we describe below.

4.3.2 Choice of N

As mentioned in Sec. 4.1, the SWT is a semi-classical theory, the starting point of which is the classical limit. Since there is more than one way of taking the classical limit of a quantum spin system, there are multiple choices of spin wave theories that can be used to describe them. However, as is the case of the classical limit of a spin-S system (see Ch. 2), by using the SU(N) SWT with $N = 2S + 1$ flavors of SBs, all unitary transformations among the N levels are faithfully represented, i.e., all local low-energy excitations (fluctuations of the classical state) can be captured by using generators of SU(N). In contrast, for $N' < 2S + 1$ (i.e. $M > 1$), multipolar excitations associated with generators of SU(N), which are not generators of SU(N'), can only be recovered by including corrections up to infinite order, which can account for the formation of bound states between the quasiparticles that are obtained at the quadratic level [110]. For instance, quadrupolar modes of $S = 1$ systems can only be obtained in the conventional SU(2) SWT by summing ladder diagrams up to infinite order in the $1/S$ (or loop) expansion, but they can be captured at the quadratic level by using the SU(3) SWT [17].

4.3.3 $1/M$-expansion

Let us work with the fundamental representation of SU(N). To make connection with realistic spin Hamiltonians, we will work with a hermitian basis (physical basis) of SU(N) generators [see Sec. 2.3.1 for definitions]:

$$\hat{T}^{\mu}_{\boldsymbol{r}} = \boldsymbol{b}^{\dagger}_{\boldsymbol{r}} \mathcal{T}^{\mu}_{\boldsymbol{r}} \boldsymbol{b}_{\boldsymbol{r}}, \quad \mu = 1, 2, \ldots, N^2 - 1, \tag{4.4}$$

where $\boldsymbol{b}_{\boldsymbol{r}} = (b_{\boldsymbol{r}1}, b_{\boldsymbol{r}2}, \ldots, b_{\boldsymbol{r}N})^T$ and $\mathcal{T}^{\mu}_{\boldsymbol{r}}$ is an $N \times N$ hermitian matrix. Let us consider a general spin Hamiltonian

$$\hat{\mathcal{H}} = \frac{1}{2} \sum_{\boldsymbol{r},\boldsymbol{\delta}} \sum_{\mu,\nu=1}^{N^2-1} \mathcal{J}^{\mu\nu}_{\boldsymbol{\delta}} \hat{T}^{\mu}_{\boldsymbol{r}} \hat{T}^{\nu}_{\boldsymbol{r}+\boldsymbol{\delta}} + \sum_{\boldsymbol{r}} \sum_{\mu=1}^{N^2-1} \mathcal{D}_{\mu} \hat{T}^{\mu}. \tag{4.5}$$

The first term of $\hat{\mathcal{H}}$ corresponds to an anisotropic exchange interaction between two SU(N) spins connected by the bond $\boldsymbol{\delta}$. In most cases, the exchange tensor $\mathcal{J}^{\mu\nu}_{\boldsymbol{\delta}}$ has non-zero matrix elements connecting dipolar components (anisotropic Heisenberg model). In some cases, biquadratic spin interactions of the form $K_{ij}(\hat{\boldsymbol{S}}_i \cdot \hat{\boldsymbol{S}}_j)^2$ are also present and the SU(3) exchange tensor has finite matrix elements connecting quadrupolar components [104, 24]. The second term of $\hat{\mathcal{H}}$ represents any arbitrary on-site term that can be interpreted as generalized Zeeman coupling between the SU(N) spin and an external SU(N) field. For instance, the sum of the usual Zeeman term $-\hat{\boldsymbol{S}} \cdot \boldsymbol{h}$ and the single-ion anisotropy $D(\hat{S}^z)^2$.

We assume that the ground state $|\psi_{\mathrm{mf}}\rangle$ of $\hat{\mathcal{H}}$ admits a classical limit, i.e., it is well approximated by a direct product of local SU(N) coherent states: $|\psi_{\mathrm{mf}}\rangle = \otimes_{\boldsymbol{r}} |\psi_{\boldsymbol{r}}\rangle$. Given N_s sites, the resulting $2(N-1)N_s$ variational parameters are determined by minimizing the classical energy $E_{\mathrm{mf}} = \langle \psi_{\mathrm{mf}} | \hat{\mathcal{H}} | \psi_{\mathrm{mf}} \rangle$. If $|\psi_{\mathrm{mf}}\rangle$ breaks the translation symmetry, which is the case for most systems of interest, N_s reduces to the number of different sublattices of the ordered state.

Now we associate the local state $|\psi_{\boldsymbol{r}}\rangle$ that minimizes E_{mf} with a single-particle state of a local Schwinger boson $\tilde{b}^{\dagger}_{\boldsymbol{r}1}$

$$|\psi_{\boldsymbol{r}}\rangle = \tilde{b}^{\dagger}_{\boldsymbol{r}1} |\varnothing\rangle, \tag{4.6}$$

where $|\varnothing\rangle$ is the common vacuum of the local Schwinger bosons $\tilde{b}^{\dagger}_{\boldsymbol{r}m}$, $m = 1, \ldots, N$. We can introduce an SU(N) transformation $\tilde{\boldsymbol{b}}^{\dagger}_{\boldsymbol{r}} = \boldsymbol{b}^{\dagger}_{\boldsymbol{r}} U^{\dagger}_{\boldsymbol{r}}$ that maps the original Schwinger bosons $\boldsymbol{b}^{\dagger}_{\boldsymbol{r}}$ into a new set of Schwinger bosons $\tilde{\boldsymbol{b}}^{\dagger}_{\boldsymbol{r}}$ containing the boson $\tilde{b}^{\dagger}_{\boldsymbol{r}1}$ that creates the lowest energy state. Clearly, the new bosons satisfy the same commutation relations and their single-particle states span the local Hilbert space of the system. We note that this transformation aligns the quantization axis along the direction of the ordered SU(N) spin[1], as it is done in the

[1]The transformation $U_{\boldsymbol{r}}$ is the same as Eq. (2.21) if the "highest-weight" boson is chosen to be condensed.

traditional SWT with the SU(2) Holstein-Primakoff representation [110] [see Eq. (4.1)], where the $m = 1$ SB operator corresponds to the "↑" boson. In this way, fluctuations generated by $\hat{T}^{\mu}_{\boldsymbol{r}}$ above $|\psi_{\rm mf}\rangle$ are represented by the boson number fluctuations of the remaining $N-1$ (non-condensed) bosons.

The classical or mean field ground state $|\psi_{\boldsymbol{r}}\rangle$ can then be expressed as a condensation of the boson $\tilde{b}^{\dagger}_{\boldsymbol{r}1}$:

$$\tilde{b}^{\dagger}_{\boldsymbol{r}1} = \tilde{b}_{\boldsymbol{r}1} = \sqrt{M}\sqrt{1 - \frac{1}{M}\sum_{m=2}^{N} \tilde{b}^{\dagger}_{\boldsymbol{r}m}\tilde{b}_{\boldsymbol{r}1}}. \tag{4.7}$$

This leads to the generalized Holstein-Primakoff transformation for the SU(N) generators

$$\begin{aligned}\hat{T}^{\mu}_{\boldsymbol{r}} = [\tilde{\mathcal{T}}^{\mu}_{\boldsymbol{r}}]_{11}\left(M - \sum_{m=2}^{N}\tilde{b}^{\dagger}_{\boldsymbol{r}m}\tilde{b}_{\boldsymbol{r}m}\right) + \sum_{m=2}^{N}\left(\tilde{b}^{\dagger}_{\boldsymbol{r}m}[\tilde{\mathcal{T}}^{\mu}_{\boldsymbol{r}}]_{m1}\sqrt{1 - \frac{1}{M}\sum_{m=2}^{N}\tilde{b}^{\dagger}_{\boldsymbol{r}m}\tilde{b}_{\boldsymbol{r}m}} + h.c.\right) \\ + \sum_{m,m'=2}^{N}[\tilde{\mathcal{T}}^{\mu}_{\boldsymbol{r}}]_{mm'}\tilde{b}^{\dagger}_{\boldsymbol{r}m}\tilde{b}_{\boldsymbol{r}m'},\end{aligned} \tag{4.8}$$

where $\tilde{\mathcal{T}}^{\mu}_{\boldsymbol{r}} = U_{\boldsymbol{r}}\mathcal{T}^{\mu}_{\boldsymbol{r}}U^{\dagger}_{\boldsymbol{r}}$. As in the case of the $1/S$-expansion, we implement a Taylor expansion of the square-root that appears in the above equation. This is justified by assuming $\sum_{m=2}^{N}\langle\tilde{b}^{\dagger}_{\boldsymbol{r}m}\tilde{b}_{\boldsymbol{r}m}\rangle \ll M$. After plugging Eq. (4.8) into the general Hamiltonian Eq. (4.5) and expanding the square root, we obtain

$$\hat{\mathcal{H}} = M^2\mathcal{H}^{(0)} + M\hat{\mathcal{H}}^{(2)} + M^{1/2}\hat{\mathcal{H}}^{(3)} + M^0\hat{\mathcal{H}}^{(4)} + \mathcal{O}(M^{-1}), \tag{4.9}$$

where $\hat{\mathcal{H}}^{(n)}$ denotes the terms of the n-th power in the $N-1$ uncondensed SB operators $\tilde{b}^{\dagger}_{\boldsymbol{r}m}$ and $\tilde{b}_{\boldsymbol{r}m}$ with $m \neq 1$. We note that $M^2\mathcal{H}^{(0)} = \langle\psi_{\rm mf}|\hat{\mathcal{H}}|\psi_{\rm mf}\rangle$ corresponds to the classical Hamiltonian of the spin system, which is the only term that survives in the infinite M limit (*classical limit* of the system). As discussed in Sec. 4.3.1, the value of M sets the representation of SU(N). We have again reached the same conclusion presented in Ch. 2—the classical limit $\hbar \to 0$ for a quantum spin system is equivalent to sending the dimension of the representation M to infinity. For this reason, we will refer to Eq. (4.9) as a $1/M$-expansion [110]. Quantum effects can be taken into account order by order in $1/M$. The well-known $1/S$-expansion is recovered for the particular case $N = 2$ and $M = 2S$. The

linear term $\hat{\mathcal{H}}^{(1)}$ is absent in Eq. (4.9) because $|\psi_{\rm mf}\rangle$ corresponds to the state with minimal classical energy. Below we present a general scheme for doing calculations with the $1/M$ expansion.

Linear spin wave theory

The quadratic bosonic Hamiltonian $\hat{\mathcal{H}}^{(2)}$ corresponds to a theory of non-interacting bosons. After Fourier transforming into the momentum space, $\hat{\mathcal{H}}^{(2)}$ can be diagonalized by means of the standard Bogoliubov transformation for bosons [43]

$$\hat{\mathcal{H}}^{(2)} = \sum_{\boldsymbol{k},n} \omega_{\boldsymbol{k},n} \left(\beta^\dagger_{\boldsymbol{k},n} \beta_{\boldsymbol{k},n} + \frac{1}{2} \right), \tag{4.10}$$

where $\beta^\dagger_{\boldsymbol{k},n}$ creates a quasi-(Bogoliubov-) particle with momentum $\boldsymbol{k}$ in band n [2], that is related to $\tilde{b}_{\boldsymbol{k},\alpha}$ and $\tilde{b}^\dagger_{\boldsymbol{k},\alpha}$ through a para-unitary transformation [43]. The explicit expressions for the transformation are given in Appendix D.

We note that the quasi-particle dispersion relation $\omega_{\boldsymbol{k},n}$ obtained above is *identical* to that of the *linearized* SU(N) Landau-Lifshitz dynamics, where we consider small fluctuations of the SU(N) color field near its "mean-field" value $\boldsymbol{n}^{(0)}_{\boldsymbol{r}}$:

$$\boldsymbol{n}_{\boldsymbol{r}}(t) = \boldsymbol{n}^{(0)}_{\boldsymbol{r}} + \delta \boldsymbol{n}_{\boldsymbol{r}}(t). \tag{4.11}$$

The SU(N) Landau-Lifshitz equation Eq. (2.63) becomes

$$\frac{d\delta \boldsymbol{n}_{\boldsymbol{r}}}{dt} = \delta \boldsymbol{n}_{\boldsymbol{r}} \times \boldsymbol{b}^{(0)}_{\boldsymbol{r}} + \boldsymbol{n}^{(0)}_{\boldsymbol{r}} \times \delta \boldsymbol{b}_{\boldsymbol{r}}, \tag{4.12}$$

where $\boldsymbol{b}^{(0)}_{\boldsymbol{r}}$ is the "mean-field" value of the molecular field and $\delta \boldsymbol{b}_{\boldsymbol{r}}$ is its fluctuation. As we show in Appendix C with the example of the SLAFM, the corresponding Hamiltonian $\mathcal{H}^{\rm LLLD}$ of the linearized equations of motion has the same structure as $\hat{\mathcal{H}}^{(2)}$ by recalling that $\delta \boldsymbol{n}_{\boldsymbol{r}}$ is parameterized by $N-1$ complex numbers $z_{\boldsymbol{r},2} \dots z_{\boldsymbol{r},N}$ in the fundamental representation, i.e. $\mathcal{H}^{\rm LLLD}$ can be obtained from $\hat{\mathcal{H}}^{(2)}$ (before the Fourier and Bogoliubov transforms) by replacing $\tilde{b}_{\boldsymbol{r},\alpha}$ ($\tilde{b}^\dagger_{\boldsymbol{r},\alpha}$) with $z_{\boldsymbol{r},\alpha}$ ($z^*_{\boldsymbol{r},\alpha}$). After applying Fourier and para-unitary

[2] The number of bands is equal to $(N-1)N_s$, where N_s is the number of sublattices.

(Bogoliubov) transformations (or a canonical transformation that preserves the form of Hamilton's equation) to the complex variables $z_{\boldsymbol{r},\alpha}$, we have

$$\mathcal{H}^{\mathrm{LLLD}} = \sum_{\boldsymbol{k},n} \omega_{\boldsymbol{k},n} \tilde{z}^*_{\boldsymbol{k},n} \tilde{z}_{\boldsymbol{k},n}, \tag{4.13}$$

where $\tilde{z}^*_{\boldsymbol{k},n}$ ($\tilde{z}_{\boldsymbol{k},n}$) is the amplitude of the normal-mode with the frequency $\pm\omega_{\boldsymbol{k},n}$. In summary, in both approaches, the normal modes of the small oscillations of SU(N) spins around the ordered state are described by a collection of decoupled harmonic oscillators with labels $\boldsymbol{k}$ and n.

The connection between the two approaches becomes more evident by recalling the process of the canonical quantization. Begin by associating $\sqrt{2}\Re(\tilde{z}_{\boldsymbol{k},n}) = x_{\boldsymbol{k},n}$ with the canonical coordinate and $\sqrt{2}\Im(\tilde{z}_{\boldsymbol{k},n}) = p_{\boldsymbol{k},n}$ with the canonical momentum. Then promote x and p to be operators while enforcing $[\hat{x}, \hat{p}] = i$ ($\hbar \equiv 1$). The quasi-particle operator then corresponds to the "ladder operator," $\beta^\dagger_{\boldsymbol{k},n} = 1/\sqrt{2}(\hat{x}_{\boldsymbol{k},n} + i\hat{p}_{\boldsymbol{k},n})$. Finally, we should keep in mind that a quantum harmonic oscillator has a non-vanishing zero-point energy [see Eq. (4.10)] whereas the amplitude of a classical harmonic oscillator is continuous. This difference leads to different results for the dynamical correlation functions. We discuss this in Sec. 4.3.4.

The harmonic approximation [3] becomes insufficient in presence of strong fluctuations. If the strong fluctuations are predominantly of thermal origin, we must solve the full (non-linear) LL equations by using the numerical techniques introduced in Sec. 2.4. Whereas if the fluctuations are of quantum origin, we must take into account the higher order corrections of $\hat{\mathcal{H}}$ in powers of $1/M$, which can be significant for low enough values of M.

Loop expansion

The higher order corrections in the $1/M$ expansion ($n \geq 3$-particle terms) correspond to interactions between quasiparticles of the linear spin wave theory. These terms account for many-body effects in the spin system, such as the decay and renormalization of the quasiparticle dispersion relation and the existence of the multi-magnon bound states. After

[3] It is also known as the random phase or Gaussian approximation, depending on the context.

Fourier transforming into the reciprocal space and applying a Bogoliubov transformation that diagonalizes the quadratic Hamiltonian $\hat{\mathcal{H}}^{(2)}$, the higher order terms, $\hat{\mathcal{H}}^{(n)}$ $n \geq 3$, can be expressed as

$$\hat{\mathcal{H}}^{(n)} = \sum_{\boldsymbol{q}_1,\boldsymbol{q}_2\ldots\boldsymbol{q}_n} \sum_{n_1,n_2,\ldots n_n} \delta(\boldsymbol{q}_1+\boldsymbol{q}_2+\ldots+\boldsymbol{q}_n) \times \Bigg[\frac{1}{n!}V_0^{(n)}(\{\boldsymbol{q}_i\},\{n_i\})\beta_{\boldsymbol{q}_1 n_1}\beta_{\boldsymbol{q}_2 n_2}\ldots\beta_{\boldsymbol{q}_n n_n} + \frac{V_1^{(n)}(\{\boldsymbol{q}_i\},\{n_i\})}{1!(n-1)!}\beta^\dagger_{\bar{\boldsymbol{q}}_1 n_1}\beta_{\boldsymbol{q}_2 n_2}\ldots\beta_{\boldsymbol{q}_n n_n} + \frac{V_2^{(n)}(\{\boldsymbol{q}_i\},\{n_i\})}{2!(n-2)!}\beta^\dagger_{\bar{\boldsymbol{q}}_1 n_1}\beta^\dagger_{\bar{\boldsymbol{q}}_2 n_2}\ldots\beta_{\boldsymbol{q}_n n_n} + \ldots + h.c.\Bigg], \tag{4.14}$$

where $V_i^{(n)}$ is the *vertex function* of order n, with i "outgoing" particles ($\beta^\dagger$) and $n-i$ "incoming particles" (β). The above expression has been put into normal-order. For order n terms, there are Quotient$[n/2]+1$ types (and their hermitian conjugates) of vertex functions because each function $V_i^{(n)}$ is fully symmetric with respect to the band and momentum indices of the i "outgoing" particles and $n-i$ "incoming particles", respectively [see Fig. 4.2(a)]. See Appendix E for derivation of the vertex functions for SU(3).

After determining the vertex functions, $V^{(n)}$, we are ready to construct a systematic perturbation theory that is controlled by $1/M$. We will first demonstrate that the $1/M$ expansion is just a particular example of the loop expansion commonly used to describe spontaneous symmetry breaking in particle theory [138]. The connection is more evident after noticing that M becomes an overall prefactor of the rescaled Hamiltonian (4.9), $\bar{H} = \hat{\mathcal{H}}/M$, after we have rescaled the bosonic fields according to $\bar{b}_{\boldsymbol{r},\nu} = \tilde{b}_{\boldsymbol{r},\nu}/\sqrt{M}$. Since the original interaction vertices $V^{(n)}$ ($n \geq 3$) scale as $V^{(n)} \sim (M)^{2-\frac{n}{2}}$, all vertices of the rescaled Hamiltonian $\bar{\mathcal{H}}(\{\bar{b}_{\boldsymbol{r},\nu}, \bar{b}^\dagger_{\boldsymbol{r},\nu}\})$ become of order M, while the propagator is still of order $1/M$. Thus, the order p of a particular one-particle irreducible diagram is $V-I$, where V is the number of vertices and I is the number of internal lines. (Note that the frequency ω is of order M^0 because the quadratic contribution $\langle\bar{\mathcal{H}}^{(2)}\rangle$ is independent of M.) Since the number of loops is $L = I - V + 1$, [4] we obtain the desired result: $p = 1 - L$.

Let us rederive this result without rescaling the fields and the Hamiltonian. As we already mentioned, Eq. (4.9) tells us that the interaction vertices $V^{(n)}$ ($n \geq 3$) scale as

[4] Every vertex introduces a delta function that reduces the number of independent momenta by one, except for one delta function that is left over for overall energy momentum conservation.

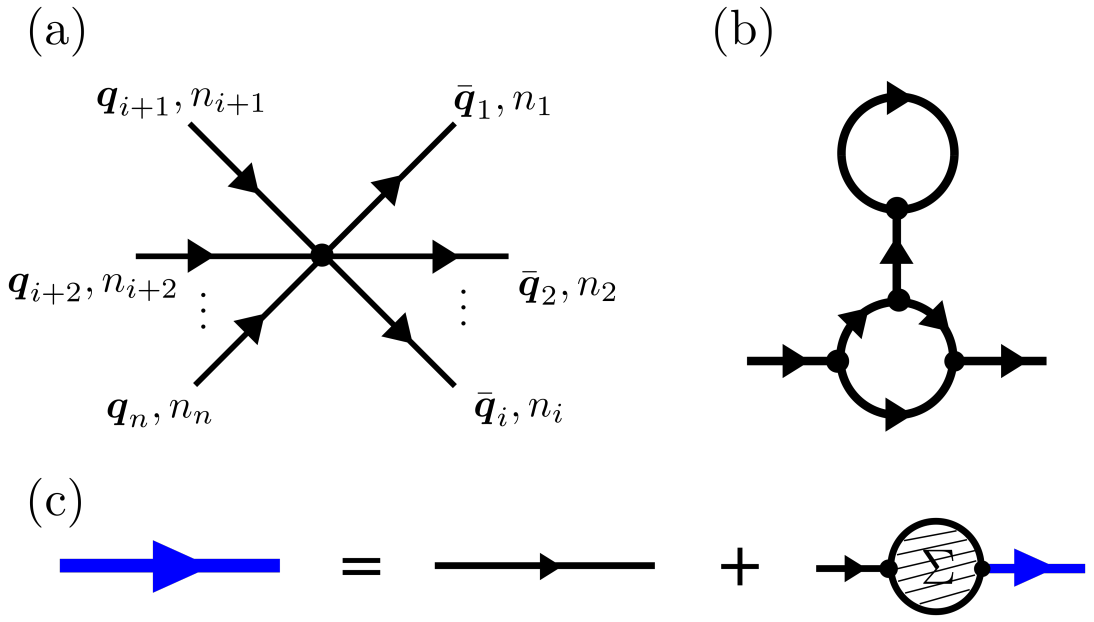


Figure 4.2: (a) The interaction vertex $V_i^{(n)}$. (b) An example diagram that contributes to the self-energy Σ with $L = 2$ loops, $I = 5$ internal lines, and $n = 4$ cubic vertices $V^{(3)}$. (c) Diagrammatic representation of the Dyson equation $\mathcal{G} = \mathcal{G}_0 + \mathcal{G}_0\Sigma\mathcal{G}$ [equivalent to (4.16)]: the blue bold line denotes the dressed (interacting) quasi-particle propagator $\mathcal{G}$ and the thin line denotes the bare (non-interacting) propagator $\mathcal{G}_0$.

$V^{(n)} \sim (M)^{2-\frac{n}{2}}$. The quasi-particle propagator,

$$\mathcal{G}_{0,\alpha}(\boldsymbol{k}, i\omega) = (-i\omega + \omega_{\boldsymbol{k},\alpha})^{-1}, \tag{4.15}$$

where ω is the Matsubara frequency, scales as $\mathcal{G}_{0,\alpha}(k) \sim M^{-1}$ because $\omega_{\boldsymbol{k},\alpha}$ is of order M [see Eq. (4.9)]. The *dressed* single-particle propagator is obtained from the Dyson equation,

$$\mathcal{G}^{-1}(\boldsymbol{k}, i\omega) = \mathcal{G}_0^{-1}(\boldsymbol{k}, i\omega) - \Sigma(\boldsymbol{k}, i\omega), \tag{4.16}$$

where $\Sigma(\boldsymbol{k}, i\omega)$ is the single-particle self-energy. Fig. 4.2(c) gives the diagrammatic representation of the Dyson equation. At a given order in M, the dressed propagator includes two external legs, L independent loops, I internal lines (bare propagators $\mathcal{G}_0$) and V_n interaction vertices of the type $V^{(n)}$ [see Fig. 4.2(b) for an example]. After a summation over the Matsubara frequency $\omega \sim M^1$, each loop gives a contribution of order M^1. Hence, the order p of a particular one-particle irreducible diagram contributing to $\Sigma(\boldsymbol{k}, i\omega)$ is

$$p = L - I + \sum_{n\geq 3} V_n \left[2 - \frac{n}{2}\right]. \tag{4.17}$$

Since each internal line connects a pair of vertices, we have

$$\sum_{n\geq 3} nV_n = 2I + 2, \tag{4.18}$$

where $\sum_{n\geq 3} nV_n$ is the total number of lines. Furthermore, the number of loops is equal to the number of independent momentum integrals. From the conservation of momentum at each vertex, we have

$$L = I - \big(\sum_{n\geq 3} V_n - 1\big). \tag{4.19}$$

By combining the above results, we obtain

$$p = 1 + \sum_{n\geq 3} V_n - \sum_{n\geq 3} \frac{nV_n}{2} = 1 - L, \tag{4.20}$$

implying again that the order of a given diagram is determined by the number of loops.

We note that the Dyson equation (4.16) is a self-consistent equation for ω. Quite often, to simplify the calculation, the so-called *on-shell approximation*: $\Sigma(\boldsymbol{k},\omega) \to \Sigma(\boldsymbol{k},\omega_{\boldsymbol{k}})$ is adopted after making the analytical continuation $\omega \pm i0^+ \to i\omega$. In this way, the renormalized poles of the dressed propagator $\mathcal{G}$ are calculated as

$$\tilde{\omega}_{\boldsymbol{q},n} - i\tilde{\Gamma}_{\boldsymbol{q},\alpha} = \omega_{\boldsymbol{q},n} + \Sigma_n(\boldsymbol{k},\omega_{\boldsymbol{k},n}), \tag{4.21}$$

where $\Re[\Sigma_n(\boldsymbol{k},\omega_{\boldsymbol{k},n}]$ gives the renormalization of the quasi-particle dispersion relation $\omega_{\boldsymbol{q},n}$ obtained from the LSWT and $\Im[\Sigma_n(\boldsymbol{k},\omega_{\boldsymbol{k},n}]$ gives the inverse of life time of the dressed particles [recall that the lifetime for non-interacting quasi-particle is infinity].

4.3.4 Dynamical spin structure factor (quantum)

As mentioned in Sec. 2.4.2, neutron scattering experiments provide a direct probe for the dynamical spin structure factor (DSSF) [see Eq. (2.113)]. We have also provided the numerical recipes (see Sec. 2.4.2) for computing the DSSF in the classical limit. In this section, we sketch the calculation of the DSSF by using the $1/M$ expansion to incorporate quantum effects at $T = 0$. In general, one can extend the definition of the DSSF to the correlation function between any two SU(N) generators given in Eq. (4.4). Although the correlation function between non-dipolar generators cannot be directly probed by neutron scattering experiments, part of the spectral weight of the DSSF will be transferred to non-dipolar quasiparticle excitations in the presence of terms that hybridize the different modes. In these cases, neutron scattering experiments can still reveal the presence and the dispersion of quasiparticle excitations with a predominant non-dipolar character. Therefore, for the sake of completeness, we consider the generalized dynamical structure factor between two SU(N) generators:

$$\mathcal{O}^{\mu\nu}(\boldsymbol{q},\omega) = \frac{1}{2\pi N_s}\int_{-\infty}^{+\infty} dt e^{i\omega t}\sum_{i,j} e^{-i\boldsymbol{q}\cdot(\boldsymbol{r}_i-\boldsymbol{r}_j)}\langle \hat{T}_i^{\mu}(t)\hat{T}_j^{\nu}(0)\rangle, \tag{4.22}$$

where N_s is the number of sites and $\langle\ldots\rangle$ denotes the expectation value in the state of thermodynamic equilibrium (ground state at $T = 0$). In practice, it is more convenient to

compute the imaginary-time dynamical spin susceptibility,

$$\chi^{\mu\nu}(\boldsymbol{q}, i\omega) = -\frac{1}{2\pi N_s}\int_0^\beta d\tau e^{i\omega\tau}\sum_{i,j} e^{-i\boldsymbol{q}\cdot(\boldsymbol{r}_i-\boldsymbol{r}_j)}\langle T_\tau\big[\hat{T}_i^\mu(\tau)\hat{T}_j^\nu(0)\big]\rangle, \tag{4.23}$$

where T_τ denotes time-ordering in imaginary time and ω is the Matsubara frequency [4]. Eq. (4.22) can be obtained by applying the fluctuation-dissipation theorem at $T = 0$ after the analytic continuation $i\omega \to \omega + i0^+$:

$$\mathcal{O}^{\mu\nu}(\boldsymbol{q}, \omega) = -2\Im\big[\chi^{\mu\nu}(\boldsymbol{q}, \omega + i0^+)\big]. \tag{4.24}$$

Below we consider the leading order contributions to Eq. (4.22) up to $\mathcal{O}[M^{-1}]$. To achieve this goal, we expand the square root in Eq. (4.8)

$$\begin{aligned}\hat{T}^\mu = M\tilde{\mathcal{T}}_{11}^\mu + \sqrt{M}\sum_{\alpha=2}^N\big(\tilde{\mathcal{T}}_{\alpha1}^\mu\tilde{b}_\alpha^\dagger + \tilde{\mathcal{T}}_{1\alpha}^\mu\tilde{b}_\alpha\big) + \sum_{\alpha,\beta=2}^N\big(\tilde{\mathcal{T}}_{\alpha\beta}^\mu - \tilde{\mathcal{T}}_{11}^\mu\delta_{\alpha\beta}\big)\tilde{b}_\alpha^\dagger\tilde{b}_\beta \\ - \frac{1}{2\sqrt{M}}\sum_{\alpha,\beta=2}^N\big(\tilde{\mathcal{T}}_{\alpha1}^\mu\tilde{b}_\alpha^\dagger\tilde{b}_\beta^\dagger\tilde{b}_\beta + \tilde{\mathcal{T}}_{1\alpha}^\mu\tilde{b}_\beta^\dagger\tilde{b}_\beta\tilde{b}_\alpha\big) + \mathcal{O}(M^{-3/2}).\end{aligned} \tag{4.25}$$

After expressing these cubic contributions in terms of the Bogoliubov quasiparticle operators [38, 174, 108] and imposing normal ordering, we obtain the following corrections to terms that are linear and quadratic in the bosonic operators:

$$\hat{T}^\mu \simeq M\tilde{\mathcal{T}}_{11}^\mu + \sqrt{M}\sum_{\alpha=2}^N\Big(\Lambda_\alpha^\mu\tilde{b}_\alpha^\dagger + h.c.\Big) + \sum_{\alpha,\beta=2}^N\big(\tilde{\mathcal{T}}_{\alpha\beta}^\mu - \tilde{\mathcal{T}}_{11}^\mu\delta_{\alpha\beta}\big)\tilde{b}_\alpha^\dagger\tilde{b}_\beta, \tag{4.26}$$

where

$$\Lambda_\alpha^\mu = \tilde{\mathcal{T}}_{\alpha1}^\mu\left[1 - \frac{1}{2M}\sum_{\beta=2}^N\big(\bar{N}^{\beta\alpha} + \bar{N}^{\beta\beta}\big)\right] - \frac{1}{2M}\tilde{\mathcal{T}}_{1\alpha}^\mu\sum_{\beta=2}^N\Delta^{\alpha\beta}. \tag{4.27}$$

In the above expression, we have introduced short-handed notations for the vacuum expectations between the uncondensed SBs

$$\bar{N}^{\alpha\beta} = \langle\tilde{b}_\alpha^\dagger\tilde{b}_\beta\rangle \quad \Delta^{\alpha\beta} = \langle\tilde{b}_\alpha\tilde{b}_\beta\rangle. \tag{4.28}$$

After plugging Eq. (4.26) into Eq. (4.23) and Fourier transforming in space, $\chi^{\mu\nu}$ acquires three contributions of $\mathcal{O}[1/M]$,

$$\chi^{\mu\nu}(\boldsymbol{q}, i\omega) = \chi^{\mu\nu}_{\text{elastic}}(\boldsymbol{0}, 0) + \chi^{\mu\nu}_{\text{qp}}(\boldsymbol{q}, i\omega) + \chi^{\mu\nu}_{\text{tc}}(\boldsymbol{q}, i\omega), \tag{4.29}$$

where $\chi^{\mu\nu}_{\text{elastic}}$, $\chi^{\mu\nu}_{\text{qp}}$ and $\chi^{\mu\nu}_{\text{tc}}$ are elastic, one-particle and two-particle corrections, respectively. The elastic contribution includes the square of the first term of Eq. (4.26), $\mathcal{T}^{\mu}_{11}\mathcal{T}^{\nu}_{11}M^2$, and the quantum correction arising from the product of the first and third terms of Eq. (4.26):

$$-2M\tilde{\mathcal{T}}^{\mu}_{11}\sum_{\alpha,\beta=2}^{N}\left(\tilde{\mathcal{T}}^{\nu}_{\alpha\beta} - \tilde{\mathcal{T}}^{\nu}_{11}\delta_{\alpha\beta}\right)\bar{N}_{\alpha\beta}.$$

$\chi^{\mu\nu}_{\text{qp}}$ includes contributions from the quasi-particle channel associated with "transverse fluctuations" of the SU(N) order parameter, while $\chi^{\mu\nu}_{\text{tc}}$ includes two-particle contributions associated with "longitudinal fluctuations" of the SU(N) order parameter [108]. Below we consider the latter two contributions separately.

Transverse fluctuations

The quasi-particle channel is written as

$$\chi^{\mu\nu}(\boldsymbol{q}, i\omega) = \frac{MN_u}{N_s}\sum_{m,n}\sum_{\alpha,\beta=2}^{N}\begin{pmatrix}(\Lambda^{\mu}_{n,\alpha})^*\\ \Lambda^{\mu}_{n,\alpha}\end{pmatrix}^{T}\begin{pmatrix}[G_{11}(\boldsymbol{q}, i\omega)] & [G_{12}(\boldsymbol{q}, i\omega)]\\ [G_{21}(\boldsymbol{q}, i\omega)] & [G_{22}(\boldsymbol{q}, i\omega)]\end{pmatrix}_{(n,\alpha),(m,\beta)}\begin{pmatrix}(\Lambda^{\nu}_{m,\beta})^*\\ \Lambda^{\nu}_{m,\beta}\end{pmatrix}, \tag{4.30}$$

where we have explicitly recovered the sublattice indices m and n for the boson operators. Fourier transform of these operators is given by

$$\tilde{b}_{\boldsymbol{r},(m,\alpha)} = \frac{1}{\sqrt{N_u}}\sum_{\boldsymbol{k}} e^{i\boldsymbol{k}\cdot\boldsymbol{r}}\tilde{b}_{\boldsymbol{k},(m,\alpha)}. \tag{4.31}$$

Here N_u is the number of magnetic unit cells and the ratio N_s/N_u is the number of nonequivalent sublattices. The 2×2 block matrix in Eq. (4.30) is the interacting single-particle Green's function for the uncondensed SBs,

$$G(\boldsymbol{q}, i\omega) = -\frac{1}{2\pi} \int_0^\beta d\tau e^{i\omega\tau} \langle T_\tau \big[\vec{b}_{\boldsymbol{q}}(\tau) \vec{b}^\dagger_{\boldsymbol{q}}(0) \big] \rangle, \tag{4.32}$$

where $\vec{b}_{\boldsymbol{q}} = (\tilde{b}_{\boldsymbol{q},(m,\alpha)}, \tilde{b}^\dagger_{-\boldsymbol{q},(m,\alpha)})^T$ is a $2N_s/N_u(N-1)$-component vector [5]. We note that the poles of $G(\boldsymbol{q}, i\omega)$ are the same as those of $\mathcal{G}(\boldsymbol{q}, i\omega)$ [see Eq. (4.16)]. The difference is that the numerator of $G(\boldsymbol{q}, i\omega)$ contains the "matrix elements" that connects the vacuum of the quasi-particles with the excited states created by $\vec{b}^\dagger_{\boldsymbol{q}}$ [see Appendix D for details], whereas the numerator of $\mathcal{G}(\boldsymbol{q}, i\omega)$ is one.

In the harmonic approximation, $\Lambda^\mu_\alpha \simeq \tilde{\mathcal{T}}^\mu_{\alpha 1}$, $G(\boldsymbol{q}, i\omega)$ reduces to the non-interacting single-particle Green's function

$$G_0(\boldsymbol{q}, i\omega) = \frac{1}{-i\omega A + \hat{\mathcal{H}}^{(2)}}, \tag{4.33}$$

where

$$A = \begin{pmatrix} \mathbb{I}_{[N_s/N_u(N-1)] \times [N_s/N_u(N-1)]} & 0 \\ 0 & -\mathbb{I}_{[N_s/N_u(N-1)] \times [N_s/N_u(N-1)]} \end{pmatrix}. \tag{4.34}$$

Since the poles of G_0 and $\mathcal{G}_0$ are the same, the inelastic part of $\mathcal{O}^{\mu\nu}(\boldsymbol{q}, \omega)$ is given by $-2\Im\big[\chi^{\mu\nu}_{\rm qp}(\boldsymbol{q}, \omega + i0^+)\big] \sim M\delta(\omega - \omega_{\boldsymbol{q},n})$, which is $\mathcal{O}[M^0]$ because the quasi-particle dispersion relation $\omega_{\boldsymbol{q},n}$ is $\mathcal{O}[M]$ [see Eq. (4.10)], implying that the delta function $\delta(\omega - \omega_{\boldsymbol{q},n})$ is $\mathcal{O}[M^{-1}]$. Since $\omega_{\boldsymbol{q},n}$ (frequency of the normal modes) is the same as the dispersion relation that is obtained from the linearized SU(N) Landau-Lifshitz dynamics (see Sec. 2.3), the two approaches give identical pole positions in the harmonic approximation. However, as illustrated in Appendix C, the spectral weight of the quantum result at $T = 0$ is obtained by multiplying the classical result by $\beta\omega$. This is so because a quantum harmonic oscillator has finite zero-point energy, whereas a classical harmonic oscillator has solutions with arbitrarily small amplitude/energy [see Appendix C].

[5] The label m goes over the N_s/N_u sublattice indices and α goes over the $N-1$ uncondensed SBs flavor indices.

Now we consider the $1/M$ quantum correction to $\chi^{\mu\nu}_{\rm qp}$ beyond the harmonic approximation. From the normal ordering of the cubic terms in the full expression of Λ^{μ}_{α} given in Eq. (4.27), we obtain the $1/M$ correction to the coefficients of the linear terms in $\tilde{b}(\tilde{b}^{\dagger})$. By using Eq. (4.21), we include the $1/M$ (one-loop) self-energy corrections $\Sigma^{\text{one-loop}}$ to the poles of the quasi-particle propagator, where $\Re[\Sigma^{\text{one-loop}}]$ changes the pole positions relative to the harmonic approximation and $\Im[\Sigma^{\text{one-loop}}]$ accounts for the broadening of the delta function peaks.

Longitudinal fluctuations

The two-particle continuum channel is written as

$$\chi^{\mu\nu}_{\rm tc}(\boldsymbol{q}, i\omega) = -\frac{1}{2\pi N_u}\sum_{\boldsymbol{k},\boldsymbol{k}'}\sum_{m,n}\sum_{\{\alpha_i\}}\Xi^{\mu}_{m,(\alpha_1,\alpha_2)}\Xi^{\nu}_{n,(\alpha_3,\alpha_4)} \times\int_0^{\beta} d\tau e^{i\omega\tau}\left\langle T_{\tau}\left[\tilde{b}^{\dagger}_{\boldsymbol{k},(m,\alpha_1)}(\tau)\tilde{b}_{\boldsymbol{k}+\boldsymbol{q},(m,\alpha_2)}(\tau)\tilde{b}^{\dagger}_{\boldsymbol{k}',(n,\alpha_3)}(0)\tilde{b}_{\boldsymbol{k}'-\boldsymbol{q},(n,\alpha_4)}(0)\right]\right\rangle, \tag{4.35}$$

where

$$\Xi^{\mu}_{m,(\alpha,\beta)} = \tilde{T}^{\mu}_{m,(\alpha,\beta)} - \delta_{\alpha,\beta}\tilde{T}^{\mu}_{m,(1,1)}. \tag{4.36}$$

By using the Wick's theorem [4], we have

$$\begin{aligned}\chi^{\mu\nu}_{\rm tc}(\boldsymbol{q}, i\omega) = \frac{1}{N_u\beta}\sum_{\boldsymbol{k}}\sum_{\omega'}\sum_{\{m_i\}}\sum_{\{\alpha_i\}}\Xi^{\mu}_{m,(\alpha_1,\alpha_2)}\Xi^{\nu}_{n,(\alpha_3,\alpha_4)} \\ \times\Big([G_{21}(\boldsymbol{k}, i\omega')]_{(m,\alpha_1),(n,\alpha_3)}[G_{12}(\boldsymbol{k}+\boldsymbol{q}, i\omega'+i\omega)]_{(m,\alpha_2),(n,\alpha_4)} \\ + [G_{22}(\boldsymbol{k}, i\omega')]_{(m,\alpha_1),(n,\alpha_4)}[G_{11}(\boldsymbol{k}+\boldsymbol{q}, i\omega'+i\omega)]_{(m,\alpha_2),(n,\alpha_3)}\Big).\end{aligned} \tag{4.37}$$

We note that in the spirit of $1/M$ correction, we should replace the Green's function in the above equation with the non-interacting Green's function given in Eq. (4.33). This is because the leading terms of the longitudinal channel is already $1/M$ smaller than the leading terms in the transverse channel [108].

After summing over the Matsubara frequency ω' and taking the analytic continuation, we have

$$\mathcal{O}^{\mu\nu}_{\mathrm{tc}}(\boldsymbol{q},\omega) \sim \sum_{\boldsymbol{k}} \sum_{n,n'} \delta(\omega - \omega_{\boldsymbol{k},n} - \omega_{\boldsymbol{k}+\boldsymbol{q},n'}), \tag{4.38}$$

where the details of the calculation are given in Appendix D. We note that the above result is explicitly of the order $\mathcal{O}[M^{-1}]$.

Chapter 5

Applications of the generalized spin wave theory

In this chapter we will apply the generalized SU(3) spin wave theory introduced in Ch. 4 to two realistic effective $S = 1$ systems. Our goal is to study their low-temperature dynamics, which in both cases can be modeled by a Hamiltonian of the form (2.58). Since the magnitude of the single-ion anisotropy $|D|$ in both systems is bigger than zJ, where z is the coordination number and J is the characteristic energy scale of the exchange tensor, we must use the SU(3) description to capture their low-temperature dynamics. In Sec. 5.1, we first consider the easy-plane system ($D > 0$) $Ba_2FeSi_2O_7$ introduced in Ch. 3, the ground state of which has no traditional SU(2) counterpart, i.e. it is not an SU(2) coherent state. By applying the $1/M$ expansion introduced in Ch. 4 (up to one-loop correction), we capture the decay and renormalization of a longitudinal mode revealed by the INS experiments [48]. In Sec. 5.2, we consider the easy-axis system ($D < 0$) FeI_2, the ground state of which is an Ising-like ordered state. This ground state certainly has a classical counterpart in SU(2) coherent states. However, as we will show in Sec. 5.2, we still need to use the SU(3) spin wave theory to capture various many-body effects revealed by the INS and THz experiments [17, 18, 91].

5.1 Decay and renormalization of a longitudinal mode in $Ba_2FeSi_2O_7$

5.1.1 Introduction: longitudinal mode in spin-1 magnets

In easy-plane quantum magnets like $Ba_2FeSi_2O_7$, phase transitions can be driven by either fluctuations of the phase or the amplitude of the order parameter [119]. The phase fluctuations are the transverse modes of the order parameter (Goldstone modes in the long-wavelength limit), whereas amplitude fluctuations correspond to the longitudinal modes. Due to the gapless nature of the Goldstone transverse modes, the longitudinal or "Higgs" mode is kinematically allowed to decay into two transverse modes. This decay becomes more significant in low-dimensional systems. Indeed, the longitudinal mode in two-dimensional (2D) antiferromagnets was originally assumed to be overdamped due to an infrared divergence of the imaginary part of the longitudinal susceptibility [40, 130]. However, more recent theoretical work has predicted that the longitudinal peak should remain visible even in 2D [125, 126, 54, 129]. One aspect of this problem, which has not been emphasized in previous works, is that the rather strong decay of the longitudinal mode is accompanied by a significant renormalization of the gap and dispersion of the modes. As noted above, this additional many-body effect provides a hard test for theories that attempt to reproduce the measured decay of the Higgs mode.

As a starting point to understand the physics described above, we focus on the quasi-2D Heisenberg square lattice material $Ba_2FeSi_2O_7$ (introduced in Ch. 3) with effective $S = 1$, an antiferromagnetic exchange coupling ($\tilde{J}$) and a strong easy-plane single-ion anisotropy ($\tilde{D}$). In this case, $\alpha = \tilde{J}/\tilde{D}$ can be viewed as a tuning parameter that can be used to drive a system from a quantum paramagnet (QPM) to an antiferromagnet (AFM) with an intervening quantum critial point (QCP), as shown in Fig. 5.1. Near the QCP, spontaneous symmetry breaking produces two transverse modes (one a Goldstone mode) and a longitudinal Higgs mode. The longitudinal mode is unstable with respect to decay into a pair of transverse modes, resulting in an intrinsic line broadening [174, 76].

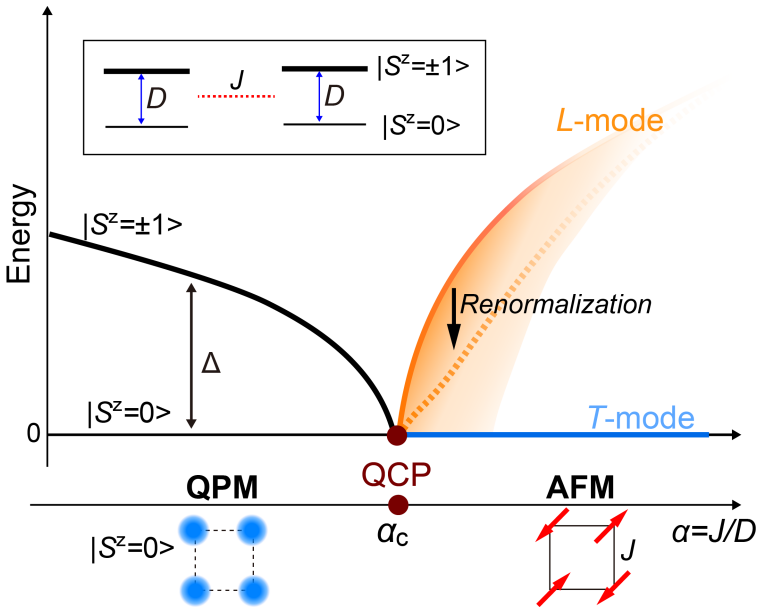


Figure 5.1: Schematic phase diagram illustrating the O(2) quantum critical point (QCP) between the antiferromagnetic (AFM) state and the quantum paramagnet (QPM) as a function of J/D (J is a Heisenberg exchange and D is a easy-plane single-ion anisotropy). The low-energy excitations of the QPM are two degenerate $S^z{=}\pm1$ modes (black line) with a gap, Δ, which closes at the QCP. The spontaneous U(1) symmetry breaking leads to a gapless magnon or transverse mode ($T-$mode), indicated with a blue line, which is accompanied by a gapped longitudinal mode ($L-$mode) indicated with the orange line. Near the QCP, the energy and the lifetime of the $L-$mode are strongly renormalized (dashed orange line) due to the decay into the continuum of two transverse modes (shaded orange region).

The high-quality neutron-scattering data of $Ba_2FeSi_2O_7$ provided by our collaborators reveals a complex spectrum where transverse modes are resolution limited, while a longitudinal mode displays significant $\boldsymbol{Q}$-dependent broadening throughout the Brillouin zone (BZ), demonstrating the importance of quasi-particle decay even away from the long-wavelength limit. The neutron-scattering results further show that the longitudinal mode has a very small gap, indicating that $Ba_2FeSi_2O_7$ is relatively close to a QCP. To understand the inelastic neutron-scattering data, we performed a generalized SU(3) spin-wave calculation, as introduced in Ch. 4, and compute the low-energy excitation spectrum of an effective low-energy spin $S = 1$ model. In particular, we show that the one-loop correction is enough to account for the broadening of the longitudinal mode and the large renormalization of the gap and the dispersion of this mode. We further show that not including the one-loop correction results in Hamiltonian parameters that place the exact ground state of the spin Hamiltonian for $Ba_2FeSi_2O_7$ on the nonmagnetic side of the QCP — contrary to experimental fact. This provides a dramatic demonstration of the importance of including renormalization effects, where the linear spin-wave calculation overestimates the stability range of the magnetically ordered state. The fact that the one-loop correction can simultaneously account for the real and imaginary part of the self-energy of the longitudinal mode, as well as of the renormalization of the transverse mode dispersion, confirms that the easy-plane quantum magnet $Ba_2FeSi_2O_7$ is an ideal platform for studying many-body effects in the proximity of the O(2) QCP.

5.1.2 Inelastic neutron scattering data

An overview of the inelastic neutron-scattering data is presented in Fig. 5.2 through contour maps of the neutron-scattering intensity, $I(\boldsymbol{Q}, \omega)$, along $[H, H, 0.5]$ and $[H, 0, 0.5]$. For both spectra, strongly dispersive spin excitations extending up to energy ~ 2.7 meV are observed.

There are several distinct features in the inelastic neutron-scattering data. An intense spin-wave excitation emanates from the magnetic zone center (ZC), $\boldsymbol{Q} = (1, 0, 0.5)$, which arises due to the in-phase oscillation between Fe^{2+} spins in the plane. We refer to this mode as T_1. Along the $[H, 0, 0.5]$ direction toward the zone boundary (ZB) at $\boldsymbol{Q} = (0, 0, 0.5)$, the T_1-mode reaches its maximum energy of ~ 2.5 meV. Another weak, but sharp mode, is visible

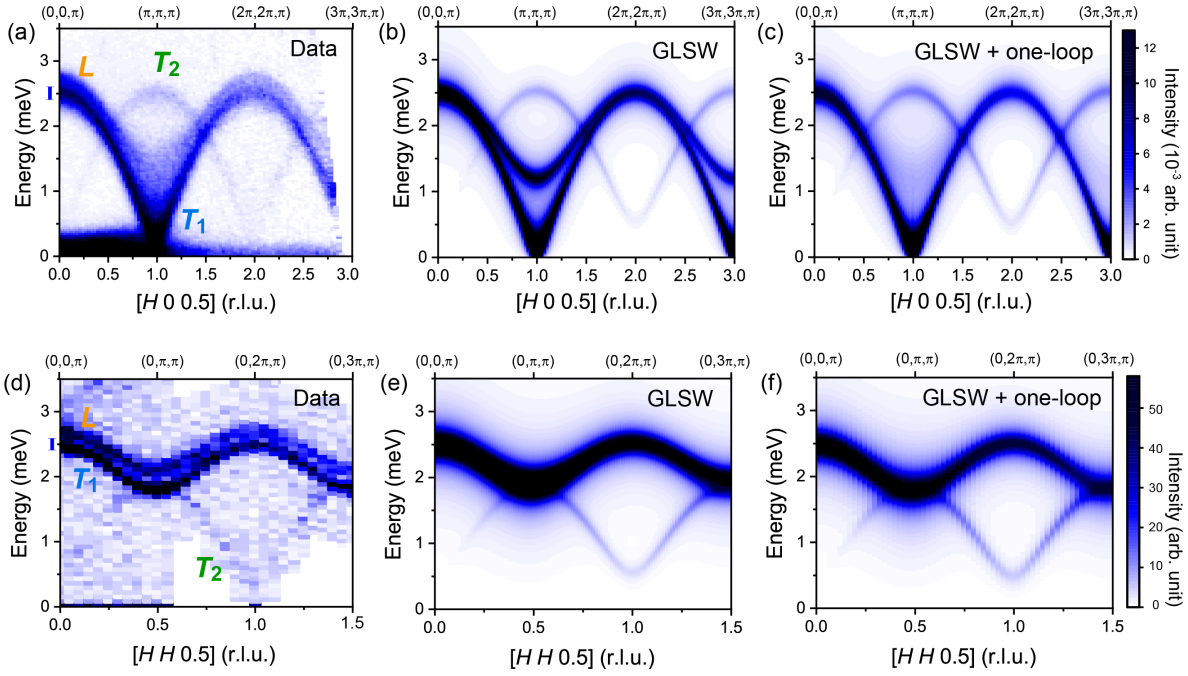


Figure 5.2: (a) Contour map of the inelastic neutron scattering (INS) data as a function of energy and momentum transfer along the $[H,0,0.5]$ direction measured at T=1.6 K ($< T_{\rm N}$) using the HYSPEC time-of-flight spectrometer at SNS. (d) Contour map of the INS data as a function of energy and momentum transfer along $[H,H,0.5]$ direction measured at T=1.4 K ($< T_{\rm N}$) using the cold Neutron Triple-Axis spectrometer (CTAX) at HFIR. The instrumental resolutions at dE=2.5 meV for each instrument are indicated with blue bars along the y-axis in (a) and (d). The two transverse modes and the longitudinal mode are labeled with T_1, T_2, and L, respectively. (b),(c),(e), and (f) INS intensities calculated by the generalized linear spin wave theory (GLSWT) and GLSWT plus one-loop corrections (GLSWT+one-loop) with the parameter sets $\mathcal{A}$ and $\mathcal{B}$ given in Table 5.1, respectively. The instrumental resolution of HYSPEC and CTAX was modeled in the calculated spectra using a Lorentzian function.

along $[H, 0, 0.5]$ with an energy of 2.5 meV at the ZC. We refer to this mode as T_2. These two modes are expected for a strong easy-plane antiferromagnet, where transverse magnons split into gapless in-plane fluctuations (T_1-mode) and gapped out-of-plane fluctuations (T_2-mode). The finite value of the energy gap of the out-of-plane fluctuation at the ZC is associated with the strength of the easy-plane single-ion anisotropy [128].

The T_1 and T_2 transverse magnon modes are also observed along the $[H, H, 0.5]$ direction in Fig. 5.2 (d). Noticeably, an additional sharp mode is observed at the top of the T_1-mode. This mode is visible along the entire Brillouin zone boundary. We refer to this additional mode as "L"-mode. The L-mode is visible in the spectra along $[H, 0, 0.5]$ as well, however, it exhibits dramatic line broadening near the ZC. The experimental analysis reveals that the L-mode is three times broader than the instrumental resolution at the ZC, whereas it has comparable line width to instrumental resolution near the ZB (see Ref. [48] for details of the analysis).

5.1.3 Generalized spin wave theory calculations

The magnetically ordered (AFM) state of $Ba_2FeSi_2O_7$ (see the bottom right of Fig. 3.1) can be approximated by a product (mean-field) state of normalized SU(3) coherent states,

$$|\psi_{\boldsymbol{r}}\rangle = \cos\theta|0\rangle + \big(\sin\theta\cos\phi|1\rangle + \sin\theta\sin\phi|-1\rangle\big)e^{i\boldsymbol{Q}_m\cdot\boldsymbol{r}}, \tag{5.1}$$

where $\boldsymbol{Q}_m = (\pi, \pi, \pi)$ [(1, 0, 0.5) in the chemical lattice] is the AFM ordering wave vector. Although a general SU(3) coherent state is a parameterized by 4 independent parameters [see Eq. (2.54)], the two independent parameters θ and ϕ are enough to describe the collinear order under consideration. The three basis states $|m\rangle$ ($m = 0, \pm 1$) are represented by creating a boson with quantum number m from the vacuum: $|m\rangle = b^\dagger_{\boldsymbol{r},m}|\varnothing\rangle$. As discussed in Ch. 4, the next step is to align the quantization axis with the direction of the local SU(3) order parameter. The spatial dependence of the transformation $U_{\boldsymbol{r}}$ can be removed by working in a twisted frame, where the original AFM order becomes a FM one. This can be done by rotating the spin reference frame of one of the two sublattices of the tetragonal lattice by an angle π along the z-axis: $S^z_{\boldsymbol{r}} \to S^z_{\boldsymbol{r}}$, and $S^{x,y}_{\boldsymbol{r}} \to -S^{x,y}_{\boldsymbol{r}}$. In the new reference frame, the

effective $S = 1$ model for $Ba_2FeSi_2O_7$ given in Eq. (3.2) becomes

$$\tilde{\mathcal{H}}_{\text{eff}} = \tilde{J} \sum_{\langle \boldsymbol{r},\boldsymbol{r}'\rangle,\nu} a_\nu S^\nu_{\boldsymbol{r}} S^\nu_{\boldsymbol{r}'} + \tilde{J}' \sum_{\langle \boldsymbol{r},\boldsymbol{r}'\rangle,\nu} b_\nu S^\nu_{\boldsymbol{r}} S^\nu_{\boldsymbol{r}'} + \tilde{D} \sum_{\boldsymbol{r}} (S^z_{\boldsymbol{r}})^2, \tag{5.2}$$

where $a_x = a_y = b_x = b_y = -1$, $a_z = \tilde{\Delta}$ and $b_z = \tilde{\Delta}'$. Then we write $\tilde{\mathcal{H}}_{\text{eff}}$ in terms of SU(3) SBs. In this calculation, we choose the local "0" boson to be condensed and perform the $1/M$ expansion (see Eq. (4.9)) for (5.2). The classical Hamiltonian is given by

$$\begin{aligned} \mathcal{H}^{(0)} &= (2\tilde{J}\tilde{\Delta} + \tilde{J}'\tilde{\Delta}') \sin^4\theta \cos^2 2\phi \\ &\quad - \frac{1}{2}(2\tilde{J} + \tilde{J}') \sin^2 2\theta (1 + \sin 2\phi) + \tilde{D} \sin^2\theta. \end{aligned} \tag{5.3}$$

Since the AFM order is invariant under time reversal followed by one lattice translation, the states $|S_z = \pm 1\rangle$ must have equal weight in the mean field state (5.1), implying that $\phi = \pi/4$. By minimizing $\mathcal{H}^{(0)}$ with respect to θ, we obtain

$$x \equiv \sin^2\theta = \frac{1}{2} - \frac{\tilde{D}}{8(2\tilde{J} + \tilde{J}')}. \tag{5.4}$$

The quadratic (GLSWT) Hamiltonian is written in terms of the two uncondensed SBs,

$$\mathcal{H}^{(2)} = \sum_{\boldsymbol{k},\alpha=\pm 1} \left[A_{\boldsymbol{k},\alpha} \tilde{b}^\dagger_{\boldsymbol{k},\alpha} \tilde{b}_{\boldsymbol{k},\alpha} - \frac{B_{\boldsymbol{k},\alpha}}{2} \left(\tilde{b}_{-\boldsymbol{k},\alpha} \tilde{b}_{\boldsymbol{k},\alpha} + \tilde{b}^\dagger_{\boldsymbol{k},\alpha} \tilde{b}^\dagger_{-\boldsymbol{k},\alpha} \right) \right], \tag{5.5}$$

where $\gamma^{xy}_{\boldsymbol{k}} = \cos(k_x) + \cos(k_y)$, $\gamma^z_{\boldsymbol{k}} = \cos(k_z)$ and the expressions for $A_{\boldsymbol{k},\alpha}$ and $B_{\boldsymbol{k},\alpha}$ are given in Appendix E. We note that the two uncondensed SBs are decoupled in (5.5), which is not true for a generic system. Note that the collinear mean-field state (5.1) has a residual Z_2 symmetry associated with a π-rotation along the direction of the ordered moments (local $\tilde{z}$-axis). The bosonic operator $\tilde{b}^\dagger_{+1}$ picks up minus sign under this Z_2 symmetry because it creates the state with $\tilde{S}^z = -1$. In contrast, the bosonic operator $\tilde{b}^\dagger_{-1}$ remains invariant because it creates the state with $\tilde{S}^z = 0$. This symmetry analysis implies that the $\tilde{b}_{+1}$ and $\tilde{b}_{-1}$ bosons must be decoupled in $\mathcal{H}^{(2)}$ because a non-vanishing hybridization term would otherwise break this Z_2 symmetry.

The diagonal form of $\mathcal{H}^{(2)}$,

$$\mathcal{H}^{(2)} = \sum_{\boldsymbol{k},\alpha=\pm1} \omega_{\boldsymbol{k},\alpha} \left(\beta^{\dagger}_{\boldsymbol{k},\alpha} \beta_{\boldsymbol{k},\alpha} + \frac{1}{2} \right), \tag{5.6}$$

is then obtained by applying an independent Bogoliubov transformation for each bosonic flavor,

$$\tilde{b}_{\boldsymbol{k},\pm1} = u_{\boldsymbol{k},\pm1} \beta_{\boldsymbol{k},\pm1} + v_{\boldsymbol{k},\pm1} \beta^{\dagger}_{-\boldsymbol{k},\pm1}, \tag{5.7}$$

with

$$u_{\boldsymbol{k},\pm1} = \sqrt{\frac{1}{2}\left(\frac{|A_{\boldsymbol{k},\pm1}|}{\omega_{\boldsymbol{k},\pm1}} + 1 \right)}, \; v_{\boldsymbol{k},\pm1} = \frac{B_{\boldsymbol{k},\pm}}{|B_{\boldsymbol{k},\pm}|} \sqrt{\frac{1}{2}\left(\frac{|A_{\boldsymbol{k},\pm1}|}{\omega_{\boldsymbol{k},\pm1}} - 1 \right)}. \tag{5.8}$$

The operators $\beta^{\dagger}_{\boldsymbol{k},\pm1}$ create quasi-particles with energy

$$\omega_{\boldsymbol{k},\pm1} = \sqrt{A^2_{\boldsymbol{k},\pm1} - B^2_{\boldsymbol{k},\pm1}}, \tag{5.9}$$

where $\omega_{\boldsymbol{k},+1}(\omega_{\boldsymbol{k},-1})$ is the dispersion relation of the transverse (longitudinal) modes.

In the Sec. 5.1.4, we will show that although the GLSW approach discussed above can reproduce the dispersion relations of all observed low-energy modes in $Ba_2FeSi_2O_7$, it cannot account for various interaction effects that are revealed by the INS experiments. To capture these effects, we must then include the next order terms in the $1/M$-expansion.

After Fourier transforming and applying a Bogoliubov transformation, the cubic contributions to the generalized spin wave theory become

$$\mathcal{H}^{(3)} = \mathcal{H}^{(3)}_c + \mathcal{H}^{(3)}_l, \tag{5.10}$$

where

$$\begin{aligned} \mathcal{H}^{(3)}_c = & \frac{1}{\sqrt{N_s}} \sum_{\boldsymbol{q}_i} \sum_{\alpha_i=\pm1} \delta(\boldsymbol{q}_1 + \boldsymbol{q}_2 + \boldsymbol{q}_3) \\ & \times \Big[\frac{1}{3!} V^{(3)}_s(\boldsymbol{q}_{1,2,3}, \alpha_{1,2,3}) \beta_{\boldsymbol{q}_1,\alpha_1} \beta_{\boldsymbol{q}_2,\alpha_2} \beta_{\boldsymbol{q}_3,\alpha_3} \\ & + \frac{1}{2!} V^{(3)}_d(\boldsymbol{q}_{1,2,3}, \alpha_{1,2,3}) \beta^{\dagger}_{\bar{\boldsymbol{q}}_1,\alpha_1} \beta^{\dagger}_{\bar{\boldsymbol{q}}_2,\alpha_2} \beta_{\boldsymbol{q}_3,\alpha_3} + h.c. \Big], \end{aligned} \tag{5.11}$$

and

$$\mathcal{H}_l^{(3)} = \frac{1}{\sqrt{N_s}} \sum_{\boldsymbol{q}} \sum_{\alpha=\pm 1} \left[V_l^{(3)}(\boldsymbol{q}, \boldsymbol{0}, \boldsymbol{q}; \alpha, -1, \alpha) \beta^\dagger_{\boldsymbol{0},-1} + h.c. \right]$$
$$= \sqrt{N_s} \sum_{\alpha=\pm 1} \left[V_{L,\alpha} \beta^\dagger_{\boldsymbol{0},-1} + h.c. \right]. \tag{5.12}$$

Here $V_d^{(3)}$ and $V_s^{(3)}$ are the decay and sink vertices, respectively. The symmetry allowed cubic vertices are depicted in the second and third lines of Fig. 5.3. Note that, unlike the SU(2) case, collinear magnetic ordering does not preclude cubic terms in the expansion (4.9) of the generalized SU(N) spin wave theory with $N > 2$. For the SU(3) case under consideration, the residual Z_2 symmetry only requires that the $\tilde{b}_{+1}$ boson must appear an even number of times (e.g., $\tilde{b}_{+1}\tilde{b}_{+1}$ or $\tilde{b}^\dagger_{+1}\tilde{b}^\dagger_{+1}$) in the cubic terms. $\mathcal{H}_l^{(3)}$ is a linear term that originates from the normal-ordering of the cubic term. This term renormalizes the optimal value θ that was obtained from the minimization of $\mathcal{H}^{(0)}$. The integral of $V_l^{(3)}(\boldsymbol{q}; \alpha, -1)$ over the entire Brillouin zone is the so-called *cubic-linear* vertex, which is non-zero only for the longitudinal boson at the ordering wave vector $\boldsymbol{q} = \boldsymbol{0}$ (in the twisted frame). The explicit forms of $V_{d,s}^{(3)}$ and $V_l^{(3)}$ are derived in Appendix E.

Knowing the interaction vertices, as discussed in Sec. 4.3.3, we compute the self-energy diagrams up to a certain order in M to include the many-body effects. Here we consider the lowest-order (one-loop) $\mathcal{O}[M^0]$ Feynman diagrams [see Fig. 5.4]. Since the inverse of the bare boson propagator is of order $\mathcal{O}(M^1)$, the remaining diagrams of order $\mathcal{O}(M^0)$ give a relative $1/M$ correction to the poles of the bare propagators.

The contributions to the self-energy from the decay and from the source diagrams shown in Fig. 5.4 are

$$\Sigma_\alpha^d(\boldsymbol{q}, i\omega) = \frac{1}{2N_s} \sum_{\boldsymbol{k},\alpha_1,\alpha_2=\pm 1} \frac{|V_d^{(3)}(\bar{\boldsymbol{k}}, \boldsymbol{k}+\bar{\boldsymbol{q}}, \boldsymbol{q}; \alpha_1, \alpha_2, \alpha)|^2}{i\omega - \omega_{\boldsymbol{k},\alpha_1} - \omega_{\boldsymbol{q}+\bar{\boldsymbol{k}},\alpha_2}}, \tag{5.13}$$

and

$$\Sigma_\alpha^s(\boldsymbol{q}, i\omega) = -\frac{1}{2N_s} \sum_{\boldsymbol{k},\alpha_1,\alpha_2=\pm 1} \frac{|V_s^{(3)}(\boldsymbol{k}, \bar{\boldsymbol{k}}+\bar{\boldsymbol{q}}, \boldsymbol{q}; \alpha_1, \alpha_2, \alpha)|^2}{i\omega + \omega_{\boldsymbol{k},\alpha_1} + \omega_{\boldsymbol{q}+\bar{\boldsymbol{k}},\alpha_2}}, \tag{5.14}$$

respectively.

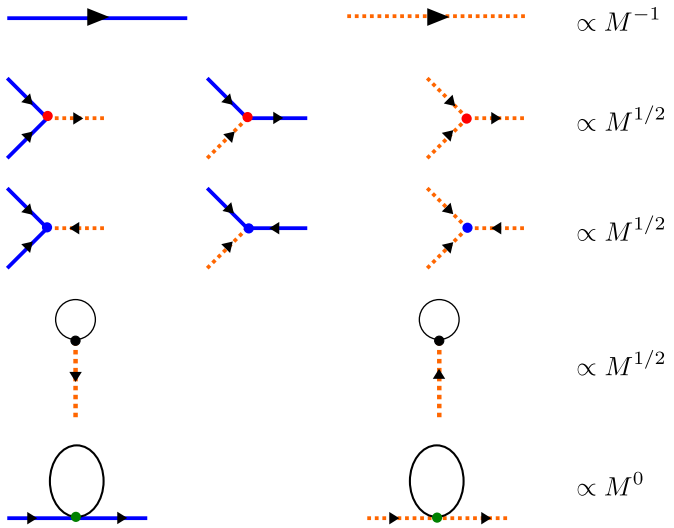


Figure 5.3: Basic ingredients of the perturbative field theory in $1/M$ for $Ba_2FeSi_2O_7$. Solid (dash) lines represent the bare propagator of the transverse (longitudinal) boson. The symmetry-allowed cubic vertices are shown on the second and third lines. The red (blue) dot represents a decay (sink) vertex. The cubic-linear vertices are listed on the fourth line. The last line represents the normal vertex $V^{(4,N)}_{\alpha\alpha}$ from $\mathcal{H}^{(4)}$.

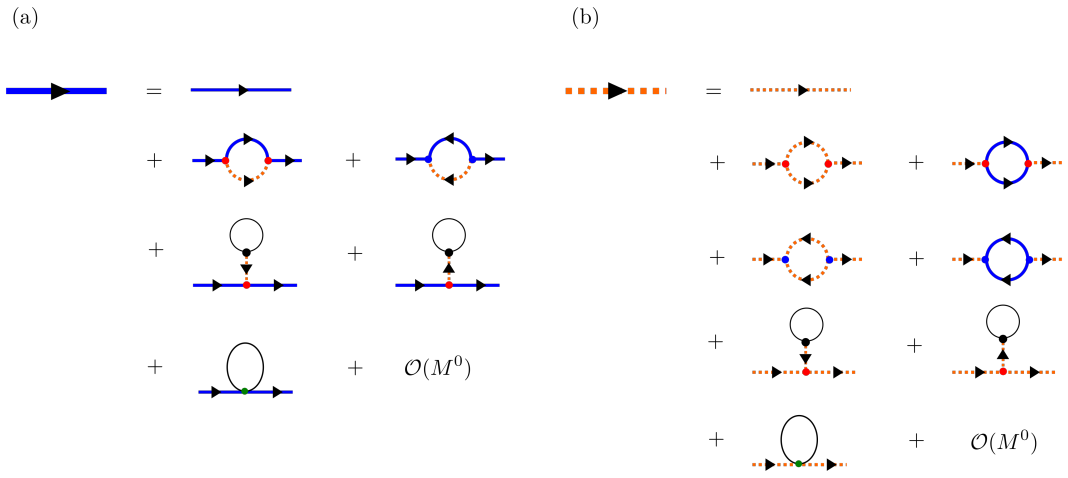


Figure 5.4: Diagrammatic representation of the Dyson equation for $Ba_2FeSi_2O_7$. (a) One-loop diagrams that contribute up to the order M^0 for the transverse boson. (b) One-loop diagrams that contribute up to the order M^0 for the longitudinal boson. The dressed propagator is denoted by a thick line, whereas the bare propagator is denoted by a thin line.

Finally, the diagrams that appear in the last line for both panels of Fig. 5.4 arise from the *normal ordering* of the quartic term $\mathcal{H}^{(4)}$ in Eq. (4.9). These contributions simply renormalize the quadratic Hamiltonian:

$$\mathcal{H}^{(4)}_{NO} = \sum_{\boldsymbol{q},\alpha,\alpha'} \left[V^{(4,N)}_{\alpha\alpha'} \beta^\dagger_{\boldsymbol{q},\alpha} \beta_{\boldsymbol{q},\alpha'} + (V^{(4,A)}_{\alpha\alpha'} \beta_{-\boldsymbol{q},\alpha} \beta_{\boldsymbol{q},\alpha'} + h.c.) \right], \tag{5.15}$$

where $V^{(4,N)}_{\alpha\alpha'}(V^{(4,A)}_{\alpha\alpha'})$ represents the normal (anomalous) contributions. Since $\mathcal{H}^{(4)}_{NO}$ is of order M^0, only the diagonal normal contribution arising from the normal vertex $V^{(4,N)}_{\alpha\alpha'}\delta_{\alpha,\alpha'}$ gives a relative correction of order $1/M$ to the bare single-particle energy given in Eq. (5.9) (the anomalous terms in Eq. (5.15) give a relative correction contribution order $1/M^2$). The derivation of $V^{(4,N)}_{\alpha\alpha}$ is included in Appendix E.

We note the parallel between the decay, sink, and quartic diagrams that give the $1/M$ correction to the single-particle self-energy and the ones that appear in the $1/S$ expansion of the standard SU(2) spin wave theory of *non-collinear* Heisenberg magnets [38]. The main difference is that the SU(3) theory includes an extra bosonic flavor that enables more symmetry-allowed decay channels. In addition, the cubic-linear diagram exists even in absence of magnetic field because the magnitude of the ordered magnetic moment can be renormalized by changing the variational parameter θ. These diagrams, shown in the third line of Fig. 5.4 (a) and the fourth line of Fig. 5.4 (b), are obtained by contracting one of the legs of the decay vertex with the cubic-linear vertex shown in Fig. 5.3. By using the Feynman rules, the cubic-linear diagrams are calculated as

$$\Sigma^{cl}_\alpha(\boldsymbol{q}) = -\frac{1}{\omega_{\boldsymbol{0},-1}} \left(\left[V^{(3)}_d(\boldsymbol{0}, \bar{\boldsymbol{q}}, \boldsymbol{q}; \alpha, -1, \alpha) \right]^* V_{L,\alpha} + h.c. \right). \tag{5.16}$$

After the analytical continuation $\omega \pm i0^+ \to i\omega$, we adopt the on-shell approximation Eq. 4.21 discussed in Sec. 4.3.3 for Eq. (5.13) and Eq. (5.14). The renormalized pole of the dressed propagator $\mathcal{G}$ is then calculated as $\tilde{\omega}_{\boldsymbol{q},\alpha} - i\tilde{\Gamma}_{\boldsymbol{q},\alpha} = \omega_{\boldsymbol{q},\alpha} + V^{(4,N)}_{\boldsymbol{q},\alpha\alpha} + \Sigma^{cl}_\alpha(\boldsymbol{q}) + \Sigma^s_\alpha(\boldsymbol{q}, \omega_{\boldsymbol{q},\alpha}) + \Sigma^d_\alpha(\boldsymbol{q}, \omega_{\boldsymbol{q},\alpha})$, where the imaginary part of the pole $\tilde{\Gamma}_{\boldsymbol{k},\alpha}$ arises from the decay term Σ^d_α. This accounts for the observed broadening of the the longitudinal mode in most regions of the BZ [see Fig. 5.2 (c)(f)]. The calculation of the dynamical spin structure factor is already summarized in Sec. 4.3.4. We note that $\mathcal{S}^{\mu\nu}_{\text{tc}}$ in Eq. (4.29) is not analyzed in comparison

with experiments, as it only contributes to the continuum. Moreover, the shift in the real part of the pole implies a corresponding renormalization in the model parameters. By fitting the neutron-scattering data with the renormalized dispersion peaks $\omega_L(\boldsymbol{Q}_m)$ at the ZC, we obtain the set of optimal Hamiltonian parameters listed as set $\mathcal{B}$ in Table 5.1 and discussed further below.

5.1.4 Comparison with INS experiments

To understand the spin excitation spectrum of $Ba_2FeSi_2O_7$ and demonstrate the importance of using the one-loop corrections, we start the comparison between experiment and theory with the GLSWT (i.e. without one-loop corrections). Figure 5.2 (b) and (e) shows contour plots of $I(\boldsymbol{Q}, \omega)$ calculated with the GLSWT along the $[H, 0, 0.5]$ and $[H, H, 0.5]$ directions, respectively. The Hamiltonian parameters (see set $\mathcal{A}$ in Table 5.1) are extracted by fitting the measured positions of the quasi-particle peaks (Gaussian-fitted peak centers of the experimental data) at the ZC. The GLSWT reproduces the dispersion of the two observed transverse modes, T_1 and T_2, along the $[H, 0, 0.5]$ and $[H, H, 0.5]$ directions [Fig. 5.2 (b) ,(e)]. Noticeably, the calculated longitudinal mode closely reproduces the experimental dispersion of the "L"-mode, which demonstrates that the SU(3) spin-wave theory describes the quasi-particles in $Ba_2FeSi_2O_7$.

Notably, the GLSWT does not reproduce the broadening and renormalization of the longitudinal modes observed in the inelastic neutron-scattering data. This is because the effect arises from the decay of a longitudinal mode into two transverse modes, which is induced by the cubic term $\hat{\mathcal{H}}$ of the expansion Eq. (4.9). To capture this effect, the $1/M$-correction from the one-loop expansion (see Sec. 4.3) must be included. The GLSWT+one-loop correction can then describe the broadened spectrum of the longitudinal mode. The new Hamiltonian parameters, which are determined via the same procedure that is described above [see set $\mathcal{B}$ in Table 5.1], allow us to reproduce the observed spectrum [Fig. 5.2 (c), (f)].

A more in-depth comparison between theory and experiment is shown in Fig. 5.5 (a) and (b). These figures show the quasi-particle dispersions along the $[H, 0, 0.5]$ direction calculated with the GLSWT and GLSWT plus one-loop corrections compared to the measured dispersion. Near the ZC, $\boldsymbol{Q}_m = (1, 0, 0.5)$, the energy of longitudinal mode

Table 5.1: The parameters of the effective $S = 1$ model extracted by fitting the Gaussian-peak centers of the experimental dispersion with the GLSWT and GLSWT + one loop calculated energies at the zone center $\boldsymbol{Q}_m = (1, 0, 0.5)$. In both cases, we assume $\tilde{J}' = 0.1\tilde{J}$, and $\tilde{\Delta} = \tilde{\Delta}' = 1/3$, i.e. $\Delta = \Delta' = 1$ for the $S = 2$ model (Heisenberg model without exchange anisotropy). The parameter set is referred to by its label ($\mathcal{A}$ or $\mathcal{B}$) in the text.

Theory	Label	$\tilde{J}$ (meV)	$\tilde{D}$ (meV)
GLSWT	$\mathcal{A}$	0.242	1.630
GLSWT + one-loop	$\mathcal{B}$	0.263	1.432

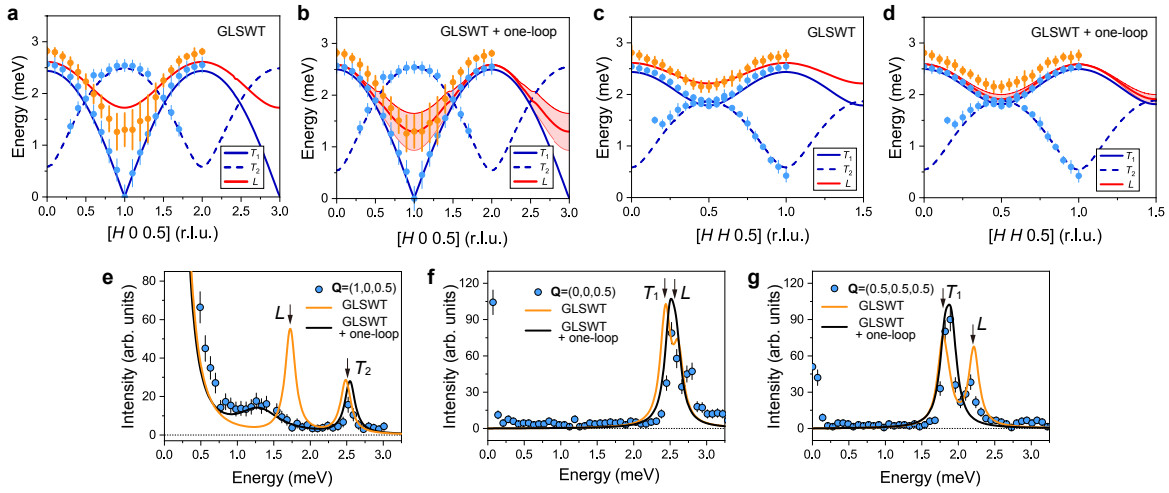


Figure 5.5: Comparison of the measured and calculated dispersion along the $[H, 0, 0.5]$ (a, b) and $[H, H, 0.5]$ (c, d) directions. In all panels of this figure, the theoretical results are obtained for the parameter set $\mathcal{B}$ in Table 5.1. a–d Blue and orange filled circles indicate the measured transverse and longitudinal modes. Dots and error bars indicate peak centers and full width at half maxima (FWHM) of the observed modes, respectively. Lines indicate the calculated dispersions obtained from the GLSWT and GLSWT+one-loop corrections. The red-shaded region in b and d depict the decay (line broadening) of the longitudinal mode given by the one-loop corrections. e–g Comparison between the measured (blue dots) and calculated (orange and black lines) INS intensities at three high-symmetric $\boldsymbol{Q}$-points at (1, 0, 0.5), (0, 0, 0.5), and (0.5, 0.5, 0.5). For GLSWT, two transverse and longitudinal modes are denoted with T_1, T_2, and L.

obtained from the GLSWT is noticeably higher than the peak center of the measured "L"-mode (orange dots). The discrepancy in the dispersion is resolved by introducing the one-loop corrections. The real part of the self-energy renormalizes the energy of the longitudinal mode, leading to a better agreement with the observed peak positions near the ZC. At the same time, the imaginary part of the self-energy obtained from the decay diagrams, Σ_α^d, leads to an intrinsic line broadening of the longitudinal mode that is missing in the GLSWT. In Fig. 5.5 b and d, the lower (upper) boundary of the red-shaded region is given by $\tilde{\omega}_{\boldsymbol{k},-1}(\mp)\tilde{\Gamma}_{\boldsymbol{k},-1}$, representing theoretical line broadening of the longitudinal mode that is compared against the experimental FWHM (orange error bars). In particular, the effects mentioned above are most striking at $\boldsymbol{Q}_m = (1, 0, 0.5)$, therefore we present a comparison of the intensity line-cut at this momentum transfer in Fig. 5.5 (e). It is interesting to note that the energy shift of the transverse mode is also captured by the one-loop corrections.

After verifying that the one-loop corrections can simultaneously capture the broadening of the longitudinal mode and the energy shift of both the transverse and the longitudinal modes at the magnetic ZC, it is natural to ask if this also holds true far away from the ZC. Figure 5.5f and g show the intensity cuts for two representative points on the ZB. At a first glance, the peak centers of both modes are reasonably reproduced by the one-loop corrections. A more detailed analysis reveals that the experimental FWHM of both peaks is equal to the instrumental resolution. However, as illustrated in Fig. 5.6a, since the longitudinal modes are still inside the two-magnon continuum, the one-loop correction predicts an intrinsic broadening (black curves) in Fig. 5.5f, g.

To understand the origin of this discrepancy, we trace back the decay channel of the longitudinal mode on the zone boundaries. The two-magnon continuum at the zone edge starts at an energy equal to the sum of the single-magnon energies at the zone center and the zone boundary. Due to the U(1) symmetry of the effective Hamiltonian, the magnons are gapless at the zone center, implying that the onset of the two-magnon continuum coincides with the single-magnon branch (see Fig. 5.6).

In absence of U(1) symmetry, the magnon modes become gapped and the longitudinal mode does not need to lie inside the two-magnon continuum for arbitrary values of the wave vector (see Fig. 5.6**b**). A small magnon gap pushes the onset of the two-magnon

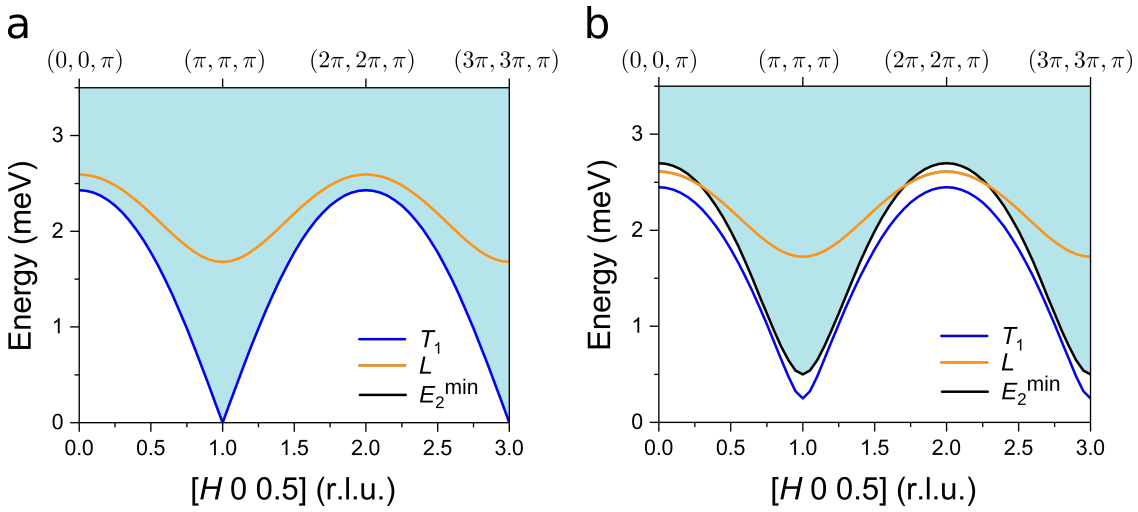


Figure 5.6: Kinematic constraints for the decay of the longitudinal mode. The blue (orange) curve shows the calculated transverse (longitudinal) band dispersions along $[H, 0, 0.5]$ with the GLSWT (using parameters set $\mathcal{B}$ in Table 5.1). The light blue-shaded areas indicate the two-transverse mode continuum, whose lower edge is indicated with a black solid line ($E_2^{\mathbf{min}}$). **a** Results of the effective $S = 1$ model. **b** Same as **a** but for a gapped branch of transverse modes (an ad hoc gap has been added to Eq. (5.5)).

continuum to be above the energy of the longitudinal mode at the zone boundaries. This modification of the two-magnon spectrum precludes the decay of the longitudinal mode near the zone boundary and explains the experimental observation. We therefore conjecture that the single-magnon dispersion is indeed gapped.

Unfortunately, it is difficult to extract the size of this gap from our INS data because of the large quasi-elastic scattering. We note that the gap can be captured by working with the original spin $S = 2$ Hamiltonian (Eq. (3.1)). The tetragonal symmetry allows for a single-ion anisotropy term of the form $\mathcal{H}_A = A\sum_i[(S_i^x)^4 + (S_i^y)^4]$, which breaks the global U(1) symmetry, generating a finite gap for the transverse mode. However, when we project the original $S = 2$ Hamiltonian onto the low-energy space to obtain the effective spin $S = 1$ Hamiltonian (Eq. (3.2)), the term $\mathcal{H}_A$ simply renormalizes the single-ion anisotropy, implying that the low-energy model acquires an "emergent" U(1) symmetry that is absent in the original high-energy model. Lastly, we note that the energies of the longitudinal mode on the zone boundaries after the one-loop corrections are slightly lower than the measured values. This level of discrepancy can be attributed to the missing second-order corrections $\mathcal{O}[J^2/(3D)]$ to the low-energy model Eq. (3.2) or to missing terms in the original Hamiltonian (3.1). A simple analysis shows that a second nearest-neighbor AFM interaction with $\tilde{J}_2 \sim 0.2\tilde{J}$ can account for this discrepancy. For simplicity, $\tilde{J}_2$ is not included in our calculation. Except for the discrepancy near the zone boundaries, the effective $S = 1$ model with one-loop corrections successfully captures most features of the INS data inside the BZ.

Finally, we emphasize that the loop expansion preserves the Goldstone mode that results from the spontaneous breaking of the emergent U(1) symmetry group of $\tilde{\mathcal{H}}_{\text{eff}}$. More specifically, as it is shown in Appendix E, the $\mathcal{O}(M^0)$ correction to the real part of the self-energy vanishes for the Goldstone mode, although the *individual* contributions from the diagrams shown in Fig. 5.4 diverge as $1/q$ in the long-wavelength limit. We note that previous attempts to computie the decay of the longitudinal mode [76] have not accounted for the renormalization of the single-particle dispersion arising from the $1/M$ correction to the*real part* of the self-energy. This correction leads to a significant change in the extracted ratio $\alpha = \tilde{J}/\tilde{D}$ of $Ba_2FeSi_2O_7$, cf. $\alpha_{\text{GLSW}} = 0.152$, and $\alpha_{\text{GLSW+one loop}} = 0.187$. This change is a direct consequence of the substantial renormalization of the energy $\omega_L(\boldsymbol{Q}_m)$ of

the longitudinal mode at the ZC. In fact, an accurate calculation that goes beyond the one-loop approximation estimates that the critical α_c required to close the gap $\omega_L(\boldsymbol{Q}_m)$ for $\tilde{J}' = 0.1\tilde{J}$, and $\tilde{\Delta} = \tilde{\Delta}' = 1/3$ is around 0.158 [See Appendix E]. In other words, the Hamiltonian parameters extracted from fitting the experiment with GLSWT place Ba2FeSi2O7 on the quantum paramagnetic side of the phase diagram shown in Fig. 5.1, which obviously contradicts the experimental evidence. In contrast, the set of parameters obtained from GLSWT+one-loop correction ($\alpha_{\text{GLSW+one loop}} = 0.152$) place the material at the magnetically ordered phase of the exact phase diagram. Furthermore, the calculated ordered moment is very close to the measured value 2.95 μ_B (see Supplement Note 12 of Ref. [48] for discussion of the reduction of the ordered moment). In general, nonlinear corrections become increasingly important upon approaching the QCP, and logarithmic corrections due to multi-loop vertex renormalizations become relevant very close to this point [125, 84, 2, 115]. The fact that a one-loop correction is enough to reproduce the spectrum of $Ba_2FeSi_2O_7$ indicates that this material is still far enough from that critical regime.

5.1.5 Conclusions

In summary, $Ba_2FeSi_2O_7$ provides a natural realization of a quasi-2D easy-plane antiferromagnet in proximity to the QCP, which signals the transition into the QPM phase. Previous examples of low-dimensional easy-plane quantum magnets in the proximity of this QCP were typically located on the quantum paramagnetic side of the quantum phase transition [81, 164, 165, 175]. $Ba_2FeSi_2O_7$ then allows us to explain the strong decay and renormalization effects of the low-energy transverse and longitudinal modes of the AFM state. Furthermore, the distance to the O(2) QCP could be in principle controlled by chemical substitution, while the application of an in-plane magnetic field, that gaps out the transverse modes, can be used to control the decay rate of the longitudinal mode.

Here, we have used the INS data of $Ba_2FeSi_2O_7$ as a platform to test a loop expansion based on an SU(3) spin-wave theory, that captures the longitudinal and the transverse modes at the linear level. This loop expansion, which generalizes the well-known $1/S$-expansion of the SU(2) spin-wave theory, allows us to reproduce the measured width and renormalization

of the longitudinal and transverse modes near the zone center by just including a one-loop correction. Small discrepancies near the zone boundary are attributed to limitations of the effective low-energy $S = 1$ model that we adopted for this work.

5.2 Many-body effects observed in FeI_2

5.2.1 Introduction: two magnon bound state in spin-1 magnets

Depending on spin-space anisotropies and the range of magnetic interactions, single-magnon quasiparticles in a quantum magnet can interact attractively, generating multi-magnon bound states (BS). The existence of such BS was first predicted in the 1930s by Bethe [27] in 1D quantum magnets, using a spin-1/2 Heisenberg model. These exchange-driven BS are usually observed in 1D ferromagnetic spin chains with $S \leq 1$ [146, 73, 36]: two magnons in such a system can bind on adjacent sites because the proximity of two spin-flips reduces the energy via the ferromagnetic exchange interaction. In this section, we demonstrate that the effective spin-1 triangular lattice antiferromagnet FeI_2 supports similar BS physics. One distinctive feature for the BS in FeI_2 is that the two spin-flips preferably happen on the same site, known as the single-ion two-magnon bound state (TMBS). As mentioned in the beginning of this chapter, the low-temperature dynamics of FeI_2 can be modeled by an anisotropic Heisenberg model with a strong easy-axis anisotropy $D < 0$. Moreover, the nearest-neighbor exchange interaction J_1 of FeI_2 is ferromagnetic. Although the exchange anisotropies and competing further-neighbor exchange interactions are necessary to explain the complex magnetic structure [see Fig. 5.7**a** for the magnetic order in the triangular plane] and details of the excitation spectrum, the balance between D and J_1 is sufficient to understand the TMBS physics in FeI_2. For this reason, let us ignore the exchange anisotropies and further-neighbor exchange interactions for a moment. The energy cost of a single-magnon excitation [Fig. 5.7**b**] with respect to the ground state [Fig. 5.7**a**] is $2|J_1|+|D|$ whereas the energy cost of two spin flips on the same site is $4|J_1|$. In addition, the energy cost of two single spin flips on adjacent sites is $3|J_1|+2|D|$. As a result, the TMBS becomes the lowest energy excitation given strong enough easy-axis anisotropy (c.f. $|J_1/D| \sim 0.1$ for

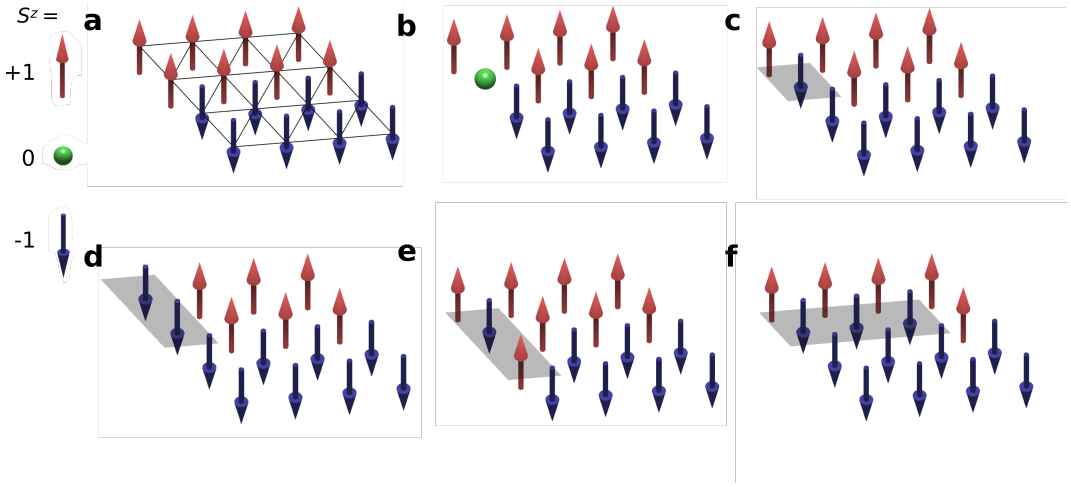


Figure 5.7: Single-ion states of Fe^{2+} ions accessible at low energy correspond to $S = 1$ magnetic moments with uniaxial anisotropy. The sketches represent a plane of spins in the **a** ground state configuration, and examples of **b** a one-magnon elementary excitation, **c** a two-magnon bound-state (TMBS), **d** a 4-magnon bound-state, **e** a 4-magnon anti-bound-state, and **f** a 6-magnon bound-state. The grey shadows represent the particular spins that are deviated as compared to the ground state. Reprinted from Fig. 1 of Ref. [91].

FeI_2). We note that the TMBS with $|\Delta S^z| = 2$ is quadrupolar in nature, which calls for the SU(3) representation. As mentioned already in Ch. 4, quadrupolar modes of $S = 1$ systems can only be obtained in the conventional SU(2) SWT by summing ladder diagrams up to infinite order in the $1/S$ (or loop) expansion, but they can be captured at the quadratic level by using the SU(3) SWT.

In Sec. 5.2.2, we first present a complete description of FeI_2. Then in Sec. 5.2.3, we apply the SU(3) LSWT to study the low-energy excitations of FeI_2, as revealed by INS experiments. In particular, we demonstrate that the observed spectral weight of the TMBS, which in principle should be invisible to neutrons due to its quadrupolar nature (dipole selection rule), originates from a hybridization with the single-magnon band through off-diagonal exchange interactions. Given the rich spectrum of quasi-particles in FeI_2, we also apply the one-loop corrections to investigate the decay of these quasi-particles in Sec. 5.2.4. In contrast with $Ba_2FeSi_2O_7$, which admits spontaneous decay of the longitudinal mode, the decay of quasi-particles in FeI_2 is induced by an external magnetic field applied perpendicularly to the triangular plane, which tunes the kinematic conditions for decay. As we will show in Sec. 5.2.4, most experimental features are captured by the GLSWT+one-loop [or the generalized non-linear spin wave theory (GNLSWT) up to the one-loop order] calculations, except the phenomenon at 3T. While the GLSWT+one-loop calculation predicts strong decay for one particular band, no visible broadening is observed in the experimental results. Remarkably, this qualitative discrepancy can be resolved by taking into account 4 magnon bound states [see Fig. 5.7 **d-e**], which are observed in the terahertz (THz) spectroscopy measurement by our collaborators [91]. Including this distinct quasiparticle in our GNLSWT calculations is impractical (non-perturbative) as it requires to sum ladder diagrams to infinite order in a perturbative loop expansion. We avoid this problem by performing an exact diagonalization (ED) of the SU(3) spin-wave Hamiltonian at quartic order on a finite lattice. The results are summarized in Sec. 5.2.5.

5.2.2 The FeI_2 compound

The FeI_2 compound has spatially-complex exchange pathways between magnetic Fe^{2+} ions residing on perfect triangular-lattice layers and spin-orbit effects within the weakly-distorted

trigonal environment of I^- ligands [Fig. 5.8**a**]. At the single-ion level, a well-isolated triplet is stabilized below 10 meV [Fig. 5.8**b**] and maps onto an effective $S=1$ model with an easy-axis single-ion anisotropy D [19], where D is estimated to lie between 1.9 and 2.2 meV from bulk suceptibility and Mössbauer measurements [53, 26]. The magnetic exchange interactions are an order of magnitude smaller [123] and stabilize a collinear c-axis magnetic order [55, 158, 52] below $T_N = 9.5$ K [148] through a first order transition with no apparent lattice distortion [55]. The magnetic structure features an up-up-down-down stripe configuration in the ab-plane that shifts by one unit along the a-axis between subsequent triangular layers [Fig. 5.8**c**]. With a propagation vector $\mathbf{k}_m = (1/4, 0, 1/4)$, this yields three magnetic domains in the material, related by 120° rotations.

The minimal model which explains the observed magnetic structure at low temperature [Fig. 5.8**c**] is a Heisenberg model with easy-axis single-ion anisotropy:

$$\hat{\mathcal{H}} = \sum_{\langle i,j \rangle} J_{ij} \hat{\boldsymbol{S}}_i \cdot \hat{\boldsymbol{S}}_j - D \sum_i (\hat{S}_i^z)^2. \tag{5.17}$$

Within the triangular plane, the up-up-down-down stripe structure requires competing exchange interactions between first, second and third neighbors [144], with $J_1 < 0$ ferromagnetic, $J_2 > 0$ antiferromagnetic, and J_3 such that $J_1 - 2J_3 < 0$ and $J_1 + 2J_2 + 2J_3 > 0$.

5.2.3 Non-interacting theory: The hybridization mechanism

Fig. 5.9**a** displays the INS data of FeI_2 along the high-symmetry path indicated in the figure. The data contain two separate excitation bands, corresponding to TMBS and one-magnon excitations, indicated by white arrows. To capture the TMBS, we must employ the SU(3) SWT for the effective $S = 1$ system FeI_2. For the magnetically ordered ground state [see Fig. 5.8**c**], we choose $\tilde{b}^\dagger_{i,+1}$ to be condensed bosons in the local frame, while $\tilde{b}^\dagger_{i,0}$ will be taken to create a single magnon and $\tilde{b}^\dagger_{i,-1}$ a TMBS. Although the SU(3) SWT is sufficient to capture both dipolar and quadrupolar excitations at the linear level, they remain decoupled for the minimal model (5.17), which is purely diagonal (Heisenberg), because they carry different quantum numbers. This implies that the TMBS excitation is completely flat, localized and *invisible* in neutron-scattering experiments. Thus, an unexplained aspect of the INS data is

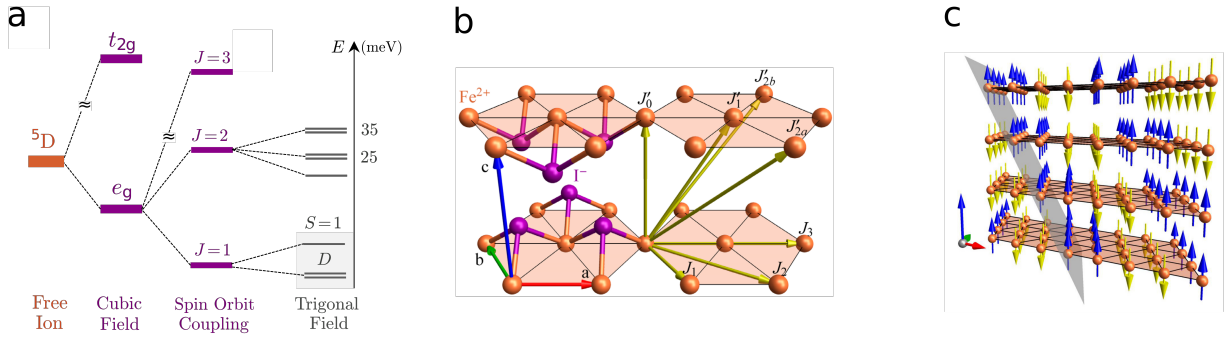


Figure 5.8: **a.** Local coordination environment of Fe^{2+} ions and hierarchy of single-ion energy-scales. **b.** Trigonal crystal structure of FeI_2, showing triangular layers of Fe^{2+} ions and resulting symmetry-inequivalent magnetic exchange pathways, mediated by I^- ligands, up to third nearest neighbors in-plane (J_1, J_2, J_3) and fourth nearest neighbors out-of-plane ($J_0^{'}, J_1^{'}, J_{2a}^{'}, J_{2b}^{'}$). **c.** Magnetic structure of FeI_2, showing ferromagnetic planes (gray) arranged in a up-up-down-down (blue-blue-green-green) sequence.

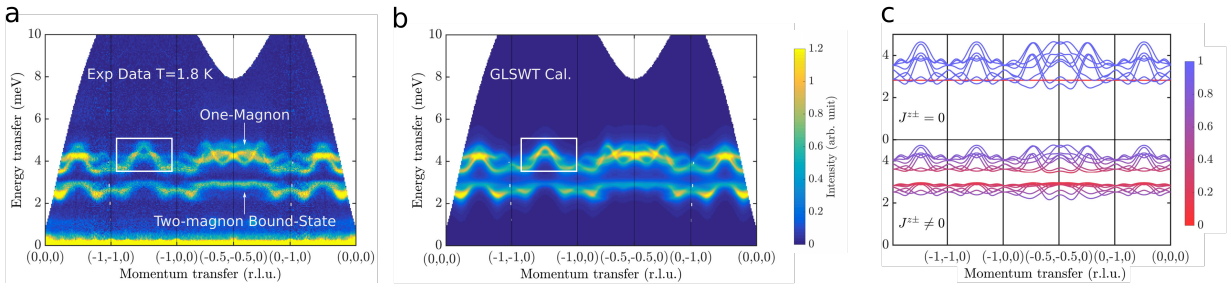


Figure 5.9: **a.** Energy-resolved neutron-scattering intensity collected at $T = 1.8$ K. White boxes indicate symmetry-equivalent positions in reciprocal space with large intensity disparities that are predicted by a Heisenberg model with the usual Fe^{2+} form factor. **b.** Generalized spin-wave theory fit to the data using the anisotropic model. **c.** Hybridization effect from anisotropic exchange interaction $J^{z\pm}$ represented through the relative weight of $b_{i,-1}^{\dagger}$ (TMBS, red) and b_{i0} (one-magnon, blue) in a given excitation eigenvector.

the dispersive nature of the TMBS excitation wherever it approaches the one-magnon band (Fig. 5.9**a**). Given the overlap between the calculated TMBS energy and LSWT magnon dispersion, the INS data suggest that a strong hybridization occurs between dipolar and quadrupolar fluctuations.

A symmetry analysis of spin-space anisotropy for nearest-neighbor bonds yields four independent parameters such that the corresponding exchange Hamiltonian can be written

$$\mathcal{H}_{\text{n.n.}} = \sum_{\langle i,j \rangle} \Big\{ J_1^{zz} S_i^z S_j^z + J_1^{\pm} \left(S_i^+ S_j^- + S_i^- S_j^+ \right) + J_1^{\pm\pm} \left(\gamma_{ij} S_i^+ S_j^+ + \gamma_{ij}^* S_i^- S_j^- \right) - \frac{i J_1^{z\pm}}{2} \left[(\gamma_{ij}^* S_i^+ - \gamma_{ij} S_i^-) S_j^z + S_i^z (\gamma_{ij}^* S_j^+ - \gamma_{ij} S_j^-) \right] \Big\},$$

where $\gamma_{ij} = 1$, $e^{-i2\pi/3}$, and $e^{i2\pi/3}$ for bond $\boldsymbol{a}_1$, $\boldsymbol{a}_2$, and $\boldsymbol{a}_1 + \boldsymbol{a}_2$ [see Fig. 5.8**a**], respectively. Before proceeding to the details of the calculation, we note that the nearest-neighbor symmetric off-diagonal exchange interaction $J_1^{z\pm}$ is responsible for hybridizing the overlapping one-magnon and TMBS bands. At quadratic order in the SU(3) Schwinger boson representation [see Sec.4.3], $S_i^z S_j^+$ maps onto $(\tilde{b}_{i,-1}^\dagger \tilde{b}_{i,0} + \tilde{b}_{j,-1}^\dagger \tilde{b}_{j,0})$, introducing an on-site coupling transforming a single magnon into a TMBS. As a result, these overlapping bands (excitations) acquire a mixed dipolar-quadupolar character.

To progress, we introduce a 15-parameter (*minimal* to explain various features of the INS data) model that includes all four anisotropic exchange parameters on nearest-neighbor bonds, diagonal XXZ anisotropy for the five non-negligible further-neighbor interactions, and single-ion anisotropy. Since the magnetic unit cell contains four nonequivalent sites (see Fig. 5.8**c**), we must introduce $4 \times 2 = 8$ uncondensed SBs to account for all coherent low-energy excitations. The quadratic Hamiltonian is written as

$$\hat{\mathcal{H}}^{(2)} = \frac{1}{2} \sum_{\boldsymbol{q}\alpha\beta} \sum_{m,n\neq 1} \begin{pmatrix} \tilde{b}_{(\alpha,\boldsymbol{q})m}^\dagger \\ \tilde{b}_{(\beta,\boldsymbol{q})m}^\dagger \\ \tilde{b}_{(\alpha,\bar{\boldsymbol{q}})m} \\ \tilde{b}_{(\beta,\bar{\boldsymbol{q}})m} \end{pmatrix}^T \begin{pmatrix} \Delta_{mn}^\alpha & \Theta_{mn;\boldsymbol{q}}^{\alpha\beta} & 0 & \Xi_{mn;\boldsymbol{q}}^{\alpha\beta} \\ \Theta_{nm;\boldsymbol{q}}^{\alpha\beta *} & \Delta_{mn}^\beta & \Xi_{nm;\bar{\boldsymbol{q}}}^{\alpha\beta} & 0 \\ 0 & \Xi_{mn;\bar{\boldsymbol{q}}}^{\alpha\beta *} & \Delta_{nm}^\alpha & \Theta_{mn;\bar{\boldsymbol{q}}}^{\alpha\beta *} \\ \Xi_{nm;\boldsymbol{q}}^{\alpha\beta *} & 0 & \Theta_{nm;\bar{\boldsymbol{q}}}^{\alpha\beta} & \Delta_{nm}^\beta \end{pmatrix} \begin{pmatrix} \tilde{b}_{(\alpha,\boldsymbol{q})n} \\ \tilde{b}_{(\beta,\boldsymbol{q})n} \\ \tilde{b}_{(\alpha,\bar{\boldsymbol{q}})n}^\dagger \\ \tilde{b}_{(\beta,\bar{\boldsymbol{q}})n}^\dagger \end{pmatrix} - \sum_{m\neq 1} \sum_i \Delta_{mm}^i, \tag{5.18}$$

where $\bar{\boldsymbol{q}} \equiv -\boldsymbol{q}$, $\alpha = 1, ..., 4$ is the sublattice index, and $\tilde{b}_{(\alpha,\boldsymbol{q})\sigma} = N_{uc}^{-1/2} \sum_{\boldsymbol{r}} e^{-i\boldsymbol{q}\cdot\boldsymbol{r}} \tilde{b}_{(\alpha,\boldsymbol{r})\sigma}$. N_{uc} is the total number of the magnetic unit cells and $\boldsymbol{r}$ the coordinates of lattice sites. The following quantities originate from expanding Eq. (4.8):

$$\Delta^{\alpha}_{mn} = M \sum_{\beta} \sum_{\boldsymbol{\delta}_{\alpha\beta}>0} \sum_{\mu\nu} \tilde{\mathcal{S}}^{\mu}_{11}(\beta) \mathcal{J}^{\mu\nu}_{\boldsymbol{\delta}_{\alpha\beta}} \tilde{\mathcal{S}}^{\nu}_{mn}(\alpha) - \frac{D}{2} \tilde{\mathcal{Q}}^{zz}_{mn}(\alpha), \tag{5.19}$$

$$\Theta^{\alpha\beta}_{mn;\boldsymbol{q}} = M \sum_{\boldsymbol{\delta}_{\alpha\beta}>0} \sum_{\mu\nu} \tilde{\mathcal{S}}^{\mu*}_{1m}(\alpha) \mathcal{J}^{\mu\nu}_{\boldsymbol{\delta}_{\alpha\beta}} \tilde{\mathcal{S}}^{\nu}_{1n}(\beta) e^{i\boldsymbol{q}\cdot\boldsymbol{\delta}_{\alpha\beta}}, \tag{5.20}$$

$$\Xi^{\alpha\beta}_{mn;\boldsymbol{q}} = M \sum_{\boldsymbol{\delta}_{\alpha\beta}>0} \sum_{\mu\nu} \tilde{\mathcal{S}}^{\mu*}_{1m}(\alpha) \mathcal{J}^{\mu\nu}_{\boldsymbol{\delta}_{\alpha\beta}} \tilde{\mathcal{S}}^{\nu*}_{1n}(\beta) e^{i\boldsymbol{q}\cdot\boldsymbol{\delta}_{\alpha\beta}}, \tag{5.21}$$

where $\boldsymbol{\delta}_{\alpha\beta}$ are the bond vectors connecting sublattices α and β and the summation over $\boldsymbol{\delta}_{\alpha\beta} > 0$ avoids double-counting of each bond. The calligraphic letters in the above equation denote the corresponding operators in the local reference frame [see Eq. (4.8)],

$$\tilde{\mathcal{S}}^{\mu}_{\boldsymbol{r}} = U_{\boldsymbol{r}} \mathcal{S}^{\mu}_{\boldsymbol{r}} U^{\dagger}_{\boldsymbol{r}} \quad \tilde{\mathcal{Q}}^{zz}_{\boldsymbol{r}} = U_{\boldsymbol{r}} (\mathcal{S}^{z}_{\boldsymbol{r}})^2 U^{\dagger}_{\boldsymbol{r}}. \tag{5.22}$$

After diagonalizing $\hat{\mathcal{H}}^{(2)}$ by means of the Bogoliubov transform (numerically for the case of FeI_2), we have eight distinctive bands with hybridized dipolar (one-magnon) and quadrupolar (TMBS) characters:

$$\hat{\mathcal{H}}^{(2)} = \sum_{\boldsymbol{q}} \sum_{n=1}^{8} \omega_{\boldsymbol{q},n} \left(\beta^{\dagger}_{\boldsymbol{q},n} \beta_{\boldsymbol{q},n} + \frac{1}{2} \right). \tag{5.23}$$

As we mentioned in Sec. 5.2.2, the FeI_2 compound has three equivalent magnetic domains related by 120° rotations. To account for this effect, we applied the 120° rotations to the results (wave vectors) of one of the three magnetic domains. The resulting dispersion relations without (with) $J_{z\pm}$ are depicted in the upper (lower) panel Fig. 5.9**c**. The relative weight of the $\tilde{b}_{i,0}$ and $\tilde{b}_{i,-1}$ bosons is shown in blue and red colors, respectively. As expected, the two modes are strongly hybridized in the region where the dipolar and quadrupolar excitations have practically the same energy. The model parameters are extracted by performing a fit to data with the calculated neutron intensity in the harmonic approximation [see Sec. 4.3.4] along high-symmetry paths in the $(h, k, 0)$-plane and for selected cuts in the

l-direction. The remaining data are used to check the fit [see the Supplementary Info of Ref. [17] for more details]. The fitted results are in remarkable agreement with the data [Fig. 5.9**c**]. The best-fit model parameters are summarized in Table 5.2.

5.2.4 Perturbative approach: The field-induced decay of quasiparticles

As shown in Fig. 5.9**b**,**d**, the microscopic interactions in FeI_2 allow bands of distinct elementary quasiparticles to overlap and strongly hybridize. Consequently, it is natural to wonder if decays are possible for these excitations. Although kinematic conditions for decay are not met in FeI_2 in the absence of a magnetic field, we conjecture that the relative Zeeman shift between initial and final states with different quantum spin numbers can compensate for this discrepancy [see right panel of Fig. 5.10] and activate decay processes for an adequate magnetic field. To search for magnon decay processes in FeI_2, our experimental collaborators applied a magnetic field perpendicular to the triangular planes to tune the relative position of magnetic excitations, and performed the corresponding INS experiments. Interestingly, a slight misalignment between the magnetic field direction and the c-axis of the FeI_2 crystal selects a single magnetic domain out of the three, which dramatically simplifies interpretation of the results.

In Fig. 5.11, we compare the SU(3) GLSW calculations by using the model parameters listed in Table 5.2 and $g = 3.8(5)$ with the INS data for $\mu_0 H = 0, 1, 2, 3$ and 4 T. For $\mu_0 H \leq 2$ T, the number, dispersion, intensity, linewidth, and field-dependence of all the observed modes are in excellent agreement with GLSW predictions for all measured momenta (Fig. 5.11**A**). However, there are noticeable discrepancies between the INS data and GLSW predictions for $\mu_0 H = 3$ T and $\mu_0 H = 4$ T. For instance, as indicated by the white box in Fig. 5.11**A**, the INS intensities of one of the excitations are broadened, implying the decay of the corresponding quasiparticles, which cannot be explained with the GLSW calculation. Therefore, we performed GNLSW calculations up to the one-loop order to take into account the decay. We note that the steps to derive the interacting vertex functions for FeI_2 are the same as $Ba_2FeSi_2O_7$ [see Appendix E], so we do not repeat the calculations here. In

Table 5.2: The best GLSWT fitting parameters in units of **Kelvin** (K) of inelastic neutron-scattering data for FeI_2.

	$J_1^{\pm}$	$J_1^{\pm\pm}$	$J_1^{z\pm}$	$J_2^{\pm}$	$J_3^{\pm}$	$J_0'^{\pm}$	$J_1'^{\pm}$	$J_{2a}'^{\pm}$	D
Mean	-1.385	-1.010	-3.017	0.136	0.977	0.167	0.085	0.360	25.729
SD	0.009	0.005	0.006	0.009	0.006	0.005	0.002	0.004	0.020

	J_1^{zz}	J_2^{zz}	J_3^{zz}	$J_0'^{zz}$	$J_1'^{zz}$	$J_{2a}'^{zz}$	E_{TMBS}
Mean	-2.461	0.719	4.720	0.000	0.000	0.143	2.822
SD	0.895	0.993	0.990	-	-	0.396	0.001

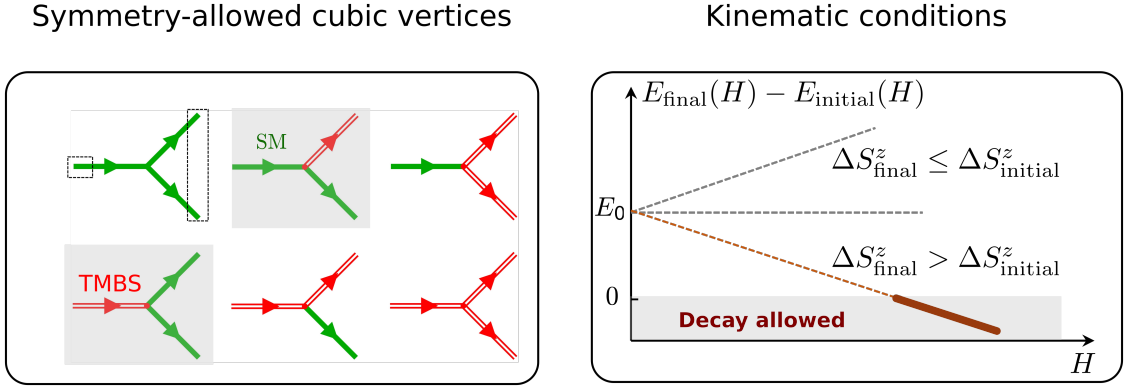


Figure 5.10: (Left). All symmetry-allowed cubic interaction vertices between initial single-quasiparticle and final two-quasiparticle states for a $S=1$ system. The green and red lines represent propagators for the SM and TMBS quasiparticles, respectively. The processes highlighted in gray are the relevant magnon decay channels in FeI_2. (Right). Effect of a magnetic field on the kinematic condition underlying decay processes. The Zeeman shift of a given (initial or final) state α depends on the total spin quantum number $[\Delta S^z]_\alpha$ as $E_\alpha(H) = -g\mu_B\mu_0 H[\Delta S^z]_\alpha$ where $g=3.8$. Decays are kinematically allowed if $E_{\text{final}}(H) - E_{\text{inital}}(H) \leq 0$.

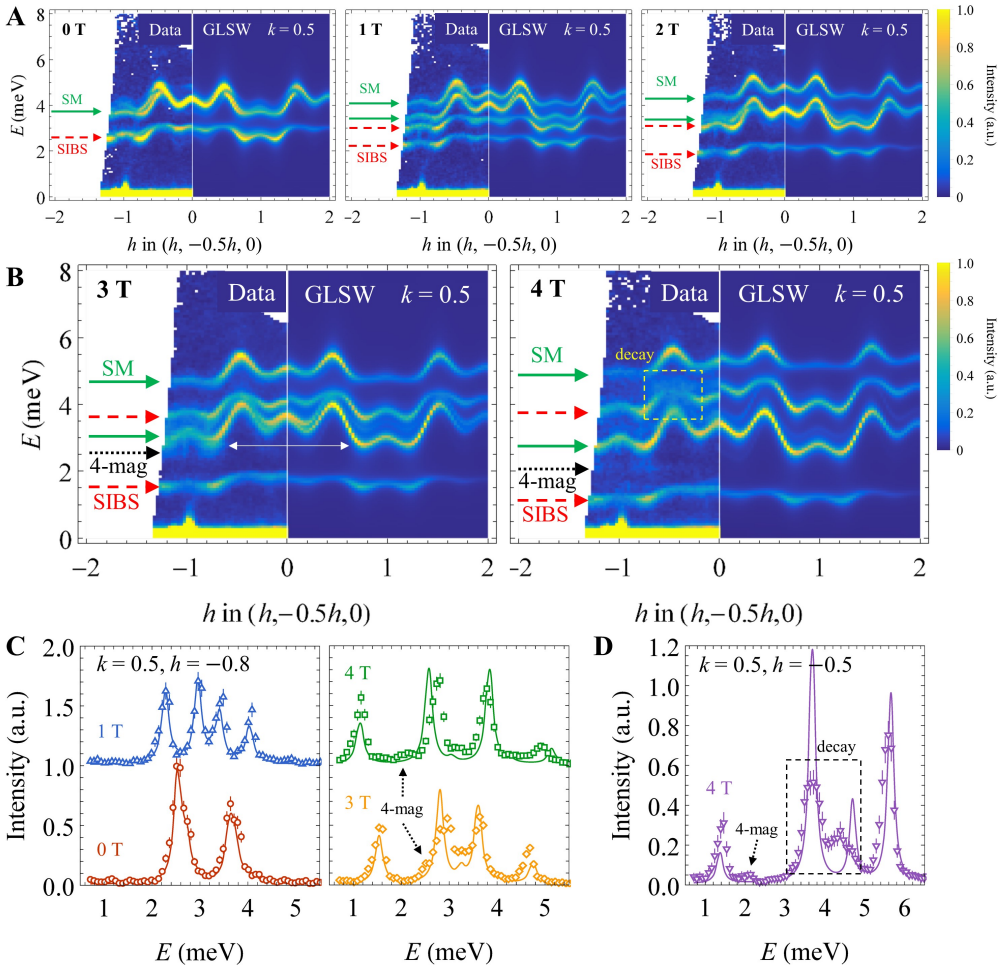


Figure 5.11: Magnetic field dependence of neutron scattering spectra of FeI_2 and comparison with SU(3)-generalized linear spin-wave (GLSW) calculations. **a**, Momentum- and energy-dependence of the neutron-scattering intensity at $T = 1.8$ K and $\mu_0 H = 0$, 1 and 2 T (AF phase). Momenta perpendicular to the $(h, -0.5h, 0)$ cut direction are integrated over $|\Delta k| \leq 0.05$ and $|\Delta l| \leq 0.05$. The arrows mark and track the dominant character of the corresponding bands: solid green for single-magnon (SM) and dashed red for single-ion two-magnon bound-states (TMBS). **b**, Same cuts at $\mu_0 H = 3$ and 4 T revealing departures from GLSW calculations. The black arrows mark the energy of a 4-magnon excitation, originating from the binding of two single-ion bound-states by exchange interactions, and effect not accounted for by GLSW calculations as highlighted by the white double-sided arrow. The yellow dashed box indicates regions of momentum-energy where excitations lineshape are dramatically broadened, indicating strong magnon decay. **c-d**, Constant-**Q** cuts through the data (open symbols) and GLSW predictions (lines) for various magnetic fields highlighting: **c**, the 4-magnon bound-state as an extra peak shoulders around $E \approx 2.5$ meV for $h = -0.8$ and $\mu_0 H = 3$ and 4 T (dashed arrows), and **d**, magnon decay around $E \approx 3.5$-4.5 meV for $h = -0.5$ and $\mu_0 H = 3$ T (dashed box).

addition, the contributing one-loop self-energy diagrams for FeI_2 are also parallel to those of $Ba_2FeSi_2O_7$ [see Fig. 5.4]. The only difference is that the intermediate processes involve only two quasiparticles for $Ba_2FeSi_2O_7$ but eight for FeI_2. Due to the strong single-ion anisotropy, $D/J_1 \sim 18.6$, the cubic-linear and quartic diagrams [corresponding to the diagrams shown on the last two lines of Fig. 5.4 (a)(b)] give negligible contribution ($10^{-3}|J_1|$) to the self-energy. We therefore neglect these contributions in our calculation.

For $\mu_0 H = 4$ T, Fig. 5.12**b**, the GNLSWT calculations predict large decay rates for the top of the E_4 and E_6 bands (see band labeling in Fig. 5.12). This yields a broadened neutron-scattering response highlighted by the dashed yellow box in Fig. 5.12**b**, in excellent agreement with the experimental observations. While the hybrid character of all the bands is fully accounted for in our quantitative decay rate calculations, it is instructive to focus on their dominant character at a given wave-vector to elucidate their decay mechanism. The broadening of band E_4 around 3.7 meV stems from the emission of a $\Delta S^z = +2$ single-ion bound-state on branch E_2 by a $\Delta S^z = +1$ single-magnon, which correspondingly loses energy and momentum. The broadening observed around 4.4 meV for band E_6 corresponds to a $\Delta S^z = -2$ single-ion bound state decaying into two single-magnon excitations: one at the bottom of the E_2 band with $\Delta S^z = +1$ and one at a different wave-vector of the E_6 band, where the $\Delta S^z = -1$ character dominates. These decay processes correspond to the spontaneous creation and annihilation of a single-ion bound-state through a net change of two units of angular momentum, implying that the relevant interaction vertices are mediated by the anisotropic, *spin-non-conserving* term $J^{\pm\pm} S_i^+ S_j^+$. See vertices enclosed by black boxes in Fig. 5.10**b**.

Surprisingly, a qualitatively different phenomenon occurs for $\mu_0 H = 3$ T, Fig. 5.12**B**. While the GLSWT+one-loop calculations predict strong decay for excitations at the bottom of the E_4 band, no visible broadening is observed in the experimental results of Fig. 5.11**B**. We note that this branch lies proximate to a four-magnon bound-state (4MBS) that been revealed by the THz experiments [91] [see also, the black dashed arrow in Fig. 5.11**B**]. As we will show in the next subsection, including the 4MBS in the calculation can explain the lack of observed decay.

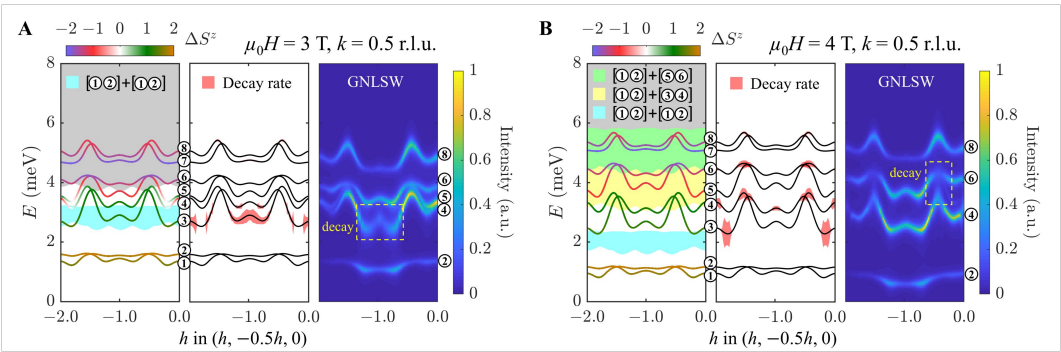


Figure 5.12: SU(3)-generalized non-linear spin-wave (GNLSW) calculations at the one-loop order for in the $(h, -0.5h, 0)$ cut direction showing in turn: the renormalized spectra + kinematic conditions for decay, decay rate, and realistic neutron scattering intensity. **A** 3 T. **B** 4 T. In the left-most panels for both **A** and **B**, The eight hybridized bands are numbered and color-coded to reflect the value of ΔS^z they carry as a function of momentum-transfer. Shaded regions indicate two-particle continua.

5.2.5 Non-perturbative approach: The effects of 4-magnon bound states

As shown in Fig. 5.9, the single-ion TMBS have an almost flat dispersion throughout the Brillouin Zone, and given J_1 is ferromagnetic (attractive interaction), the TMBS display a strong propensity to form bound states with themselves, leading to the so-called 4MBS. Just as with the inclusion of the TMBS with the conventional SU(2) SWT, the inclusion of the 4MBS with the SU(3) SWT is also a non-perturbative calculation, i.e., it requires the summation of ladder diagrams to infinite order in a perturbative loop expansion. However, here we show that we can avoid this problem by performing an exact diagonalization (ED) study in the *truncated subspace* $\mathcal{S}_{1,2}$, with the number of quasiparticles ≤ 2 on a finite lattice. In this section, we briefly review the ED calculation. The detailed comparisons of the ED calculation with INS and THz data can be found in Refs. [18, 91].

As the Hilbert space dimension becomes prohibitively large for ED if we include states with three quasiparticles, our calculation only accounts for 1-, 2- and 4-magnon excitations. The excluded states have only perturbative effects because of their higher energy scales compared to that of a single quasiparticle. The subspace $\mathcal{S}_{1,2}$ is spanned by the basis $\{|i\rangle, |i \leq j\rangle\}$ with $|i\rangle = \beta_i^\dagger|\emptyset\rangle$ and $|i \leq j\rangle = \zeta_{ij}\beta_i^\dagger\beta_j^\dagger|\emptyset\rangle$, where i stands for the dictionary index of $(n_i, \boldsymbol{q}_i)$, $|\emptyset\rangle$ refers to the vacuum of the β (Bogoliubov)-quasiparticles [see Eq. (5.23)], and $\zeta_{i\neq j} = 1$ and $\zeta_{i=j} = 1/\sqrt{2!}$ are normalization factors. Introducing the projector $\mathcal{P}_{1,2}$ to the subspace $\mathcal{S}_{1,2}$, the restricted Hamiltonian is obtained by the projection

$$\mathcal{P}_{1,2}\mathcal{H}\mathcal{P}_{1,2} = \begin{pmatrix} \mathcal{H}_{11} & \mathcal{H}_{12} \\ h.c. & \mathcal{H}_{22} \end{pmatrix}, \tag{5.24}$$

with matrix elements

$$\begin{aligned} \mathcal{H}_{11}^{i,j} &= \delta_{ij}\varepsilon_{n_i,\boldsymbol{q}_i}, \quad \mathcal{H}_{12}^{i,j\leq k} = \frac{1}{\sqrt{N_{uc}}} V^{(S1)}_{n_i,n_j,n_k}(\boldsymbol{q}_i,\boldsymbol{q}_j,\boldsymbol{q}_k)\zeta_{j,k}, \\ \mathcal{H}_{22}^{i\leq j,k\leq l} &= \delta_{ik}\delta_{jl}(\varepsilon_{n_i,\boldsymbol{q}_i} + \varepsilon_{n_j,\boldsymbol{q}_j})\zeta_{ij}^2 + \frac{1}{N_{uc}} U_{n_i,n_j,n_k,n_l}(\boldsymbol{q}_i,\boldsymbol{q}_j,\boldsymbol{q}_k,\boldsymbol{q}_l)\zeta_{ij}\zeta_{kl}. \end{aligned} \tag{5.25}$$

Here the function $U_{n_i,n_j,n_k,n_l}(\boldsymbol{q}_{i,j,k,l})$ accounts for the interaction between β-quasiparticles,

$$\mathcal{H}^{(4)} = \frac{1}{2!2!N_{uc}}\sum_{ijkl}\delta(\boldsymbol{q}_i+\boldsymbol{q}_j+\boldsymbol{q}_k+\boldsymbol{q}_l-\boldsymbol{G})U_{n_i,n_j,n_k,n_l}(\boldsymbol{q}_i,\boldsymbol{q}_j,\boldsymbol{q}_k,\boldsymbol{q}_l)\beta^\dagger_{n_i,\bar{\boldsymbol{q}}_i}\beta^\dagger_{n_j,\bar{\boldsymbol{q}}_j}\beta_{n_k,\boldsymbol{q}_k}\beta_{n_l,\boldsymbol{q}_l}, \quad (5.26)$$

where $\boldsymbol{G}$ is the reciprocal lattice vector. The diagonalization of $\mathcal{P}_{1,2}\mathcal{H}\mathcal{P}_{1,2}$ is done for a fixed center of mass momentum. It reveals that the spectrum includes four energy levels below the two-particle continuum with a strong 4-magnon character (see Ref. [18]), which are identified as the 4-magnon bound states. After the inclusion of the 4MBS, we explain the strong suppression of decays observed in the experiments at 3 T [18], which stems from the finite probability that the decay products of the corresponding decay channel will form a four-magnon bound-state instead of propagating independently in the system.

5.2.6 Conclusions

In summary, we have applied the generalized SU(3) spin wave theory introduced in Ch. 4 to account for the rich quantum many-body effects observed in FeI_2. Interestingly, these intriguing many-body phenomena are captured at different complexity levels of the $1/M$ expansion based on the SU(3) classical theory: the non-interacting theory for the hybridization mechanism, the GLSWT + one-loop (perturbative) calculation for the field induced decay, and the exact diagonalization (non-perturbative) calculation for the suppression of one of the decay channels. The excellent agreement between the experimental data and the theoretical prediction confirms that the generalized SU(N) dynamics is an adequate framework to model quantum magnets with strong single-ion anisotropy.

Finally, we note that FeI_2 provides an outstanding example of a spin one system with a classical (Ising-like) ground state, the excitation spectrum of which still exhibits rich quantum many-body effects. This simple example illustrates the need to consider alternative semi-classical theories that can capture the many-body quantum effects of general quantum magnets.

Chapter 6

CP^2 Skyrmions and Skyrmion crystals

In Ch. 4 – Ch. 5 we focused on the collective modes of a general quantum magnet. In particular, we demonstrated that these quasi-particles can be obtained by *linearizing* the generalized classical equation of motion (2.63) and applying the canonical quantization procedure (see Sec. 4.3.3). In this chapter, we will consider a different category of "particles" that arise as stationary solutions of the equations of motion (they correspond to local minima of the classical Hamiltonian). These solutions of the *non-linear* field equations are generically known as topological solitons and they appear in different areas of physics [29]. Their topological character (intrinsic stability against continuous deformations) makes them behave as emergent mesoscale particles that can be used for different applications [51]. Here we will focus on one particular example of magnetic soliton — the *magnetic skyrmions* — that corresponds to some localized vortex-like inhomogeneous spin textures and carries an integer topological charge.

6.1 Introduction: magnetic skyrmions and their generalization

Lord Kelvin's vision of the atom as a vortex in ether [145] inspired Skyrme [139, 140] to explain the origin of nucleons as emergent, topologically non-trivial configurations of a pion field described by a 3+1 dimensional O(4) non-linear σ-model. In modern language,

these "skyrmions" are examples of topological solitons, and Skyrme's model has become the prototype of a classical theory that supports these solutions. Besides its important role in high-energy physics and cosmology, Skyrme's model also led to important developments in other areas of physics. For instance, the baby Skyrme model [30, 31, 90] (planar reduction of the non-linear σ-model), which is as an extension of the Heisenberg model [30, 31, 127], has baby skyrmion solutions in the presence of a chiral symmetry breaking Dzyaloshinskii-Moriya (DM) interaction [49, 107, 106, 28].

Periodic arrays of magnetic skyrmions and single skyrmion metastable states were originally observed in chiral magnets, such as MnSi, $Fe_{1-x}Co_xSi$, FeGe and Cu_2OSeO_3 [109, 162, 161, 136, 1]. This discovery sparked the interest of the community at large and spawned efforts in multiple directions. Identifying realistic conditions for the emergence of novel magnetic skyrmions is one of the main goals of modern condensed matter physics. Novel mechanisms are usually accompanied by new properties. For instance, while skyrmions of chiral magnets have a fixed vector chirality, this is still a degree of freedom in centrosymmetric materials, such as $BaFe_{1-x-0.05}Sc_xMg_{0.05}O_{19}$, $La_{2-2x}Sr_{1+2x}Mn_2O_7$, Gd_2PdSi_3 and $Gd_3Ru_4Al_{12}$ [160, 163, 96, 132, 86, 35, 70], where skyrmions arise from frustration, i.e., from competing exchange or dipolar interactions [117, 92, 94, 67, 23, 153, 68].

The target manifold of the above-mentioned planar baby skyrmions is $S^2 \cong \mathrm{CP}^1$, i.e., the usual 2D sphere, corresponding to normalized dipoles or the conventional classical limit of a quantum spin system based on SU(2) coherent states. In Ch. 2, we have demonstrated that there is more than one way of taking the classical limit for a quantum spin system. As a result, we should now consider the more general target complex projective space CP^{N-1} that represents the normalized N-component complex vectors, up to an irrelevant complex phase, i.e., the generalized classical limit based on SU(N) coherent states. The topologically distinct, smooth mappings from the base manifold S^2 (2D sphere $\cong$ compactified plane) to the target manifold CP^{N-1} can be labeled by the integers: $\Pi_2(\mathrm{CP}^{N-1}) = \mathbb{Z}$. This homotopy group suggests generalizations of the planar Skyrme's model to $N > 2$, such as the CP^2 nonlinear σ-model [63, 45, 47] and in the Faddeev-Skyrme type model [50, 6]. In recent work, Akagi et al. considered the SU(3) version of the Heisenberg model with a DM interaction, whose continuum limit becomes a gauged CP^2 nonlinear σ-model with a background uniform

gauge field [3]. An attractive aspect of this model is that it admits analytical solution by the application of techniques developed for the gauged non-linear σ-model. However, it may be challenging to find materials described by this model because SU(3) can only be an accidental symmetry of spin-spin interactions of real quantum magnets.

The main purpose of this chapter is to demonstrate that exotic CP^2 skyrmions readily emerge in simple and realistic spin-1 ($N = 3$) models and their higher-spin generalizations. Remarkably, isolated CP^2 skyrmions can either be metastable states of a quantum paramagnet (QPM) or of a fully polarized (FP) ferromagnet. Unlike the "usual" CP^1 magnetic skyrmions, the dipolar field of the metastable CP^2 skyrmions of quantum paramagnets vanishes away from the skyrmion core. Moreover, the application of an external magnetic field to the QPM induces stable triangular crystals of CP^2 skyrmions in the field interval that separates the QPM from the FP state.

6.2 Spin-1 model

To illustrate the basic ideas we consider a minimal spin-1 model defined on the triangular lattice (TL):

$$\hat{\mathcal{H}} = \sum_{\langle i,j \rangle} J_{ij} \left(\hat{S}_i^x \hat{S}_j^x + \hat{S}_i^y \hat{S}_j^y + \Delta \hat{S}_i^z \hat{S}_j^z \right) - h \sum_i \hat{S}_i^z + D \sum_i \left(\hat{S}_i^z \right)^2 . \tag{6.1}$$

The first term includes an easy-axis ferromagnetic (FM) nearest-neighbor exchange interaction $J_1 < 0$ and a second-nearest-neighbor antiferromagnetic (AFM) exchange $J_2 > 0$. For simplicity, we assume that the exchange anisotropy, defined by the dimensionless parameter $\Delta > 1$, is the same for both interactions. The second and third terms represent the Zeeman coupling to an external field and an easy-plane single-ion anisotropy ($D > 0$), respectively. $\hat{\mathcal{H}}$ is invariant under the space-group of the TL and the U(1) group of global spin rotations along the field-axis. We will adopt $|J_1|$ as the unit of energy (i.e. $J_1 = -1$).

The first step is to take the classical limit of $\hat{\mathcal{H}}$, where multiple approaches are possible [62, 167] (see also, Ch. 2). To correctly capture low-energy excitations of this spin-1 model, it is important to retain more information about spin fluctuations in the ($N = 3$)-dimensional

local Hilbert space. Therefore, we will take the classical limit of Eq. (6.1) based on coherent states of SU(3) by following procedures discussed in Sec. 2.3.1. To begin with, we rewrite $\hat{\mathcal{H}}$ in terms of SU(3) spin components defined in (2.53),

$$\hat{\mathcal{H}} = \sum_{\langle i,j \rangle} I_{ij}^{\mu} \hat{T}_i^{\mu} \hat{T}_j^{\mu} - \sum_i B^{\mu} \hat{T}_i^{\mu}, \tag{6.2}$$

where $I_{ij}^{\mu} = J_{ij}(\Delta\delta_{\mu,2} + \delta_{\mu,5} + \delta_{\mu,7})$ and $B^{\mu} = (-h\delta_{\mu,2} - D\delta_{\mu,8}/\sqrt{3})$. Then we evaluate the expectation value of $\hat{\mathcal{H}}$ in SU(3) coherent states $|\boldsymbol{Z}\rangle$:

$$\mathcal{H} \equiv \langle \boldsymbol{Z}|\hat{\mathcal{H}}|\boldsymbol{Z}\rangle. \tag{6.3}$$

By using the definition (2.62) of the SU(3) color field (classical limit of SU(3) spin operators), we can express

$$\mathcal{H} = \sum_{\langle i,j \rangle} I_{ij}^{\mu} n_i^{\mu} n_j^{\mu} - \sum_i B^{\mu} n_i^{\mu}. \tag{6.4}$$

To avoid an explicit use of the structure constants of SU(3), we introduce the operator field $\mathfrak{n}_j = n_j^{\mu}\lambda_{\mu}$. Topological soliton solutions of the color field become well-defined in the continuum (long wavelength) limit, where the Hamiltonian can be approximated by

$$\mathcal{H} \simeq \int \mathrm{d}r^2 \left[-\frac{\mathcal{I}_1^{\mu}}{2} \partial_a n^{\mu} \partial_a n^{\mu} + \frac{\mathcal{I}_2^{\mu}}{2} \left(\nabla^2 n^{\mu}\right)^2 - \mathcal{B}^{\mu} n^{\mu} \right]. \tag{6.5}$$

Here ∂_a denotes the spatial derivatives and there is an implicit summation over the repeated a index. The coupling constants can be expressed in terms of the parameters of the lattice model (6.2):

$$\begin{aligned} \mathcal{I}_1^{\mu} &= \frac{3}{2}(I_1^{\mu} + 3I_2^{\mu}), \quad \mathcal{I}_2^{\mu} = \frac{3}{32}(I_1^{\mu} + 9I_2^{\mu}), \\ \mathcal{B}^{\mu} &= B^{\mu} - 3(\Delta - 1)(J_1 + J_2)\delta_{\mu,8}. \end{aligned} \tag{6.6}$$

Eq. (6.5) corresponds to an anisotropic *non-linear* CP^2 sigma-model. For skyrmion solutions the base plane $\mathbb{R}^2$ can be compactified to S^2 because the color field takes a constant value, n_{∞}, at spatial infinity. These spin textures can then be characterized by the topological

charge of the mapping $\mathfrak{n} : \mathbb{R}^2 \sim S^2 \mapsto CP^2$:

$$C = -\frac{i}{32\pi} \int \mathrm{d}x\mathrm{d}y \varepsilon_{jk} \,\mathrm{Tr}\left(\mathfrak{n}\left[\partial_j \mathfrak{n}, \partial_k \mathfrak{n}\right]\right). \tag{6.7}$$

For the lattice systems of interest, the CP^2 skyrmion charge can be computed after interpolating the color fields on nearest-neighbor sites, $\mathfrak{n}_j$ and $\mathfrak{n}_k$, along the CP^2 geodesic:

$$C = \sum_{\triangle_{jkl}} \rho_{jkl} = \frac{1}{2\pi} \sum_{\triangle_{jkl}} \left(\gamma_{jl} + \gamma_{lk} + \gamma_{kj}\right), \tag{6.8}$$

where $\triangle_{jkl}$ denotes each oriented triangular plaquette of nearest-neighbor sites $j \to k \to l$ and $\gamma_{kj} = \arg\left[\langle \boldsymbol{Z}_k \mid \boldsymbol{Z}_j \rangle\right]$ is the Berry connection on the bond $j \to k$. The explicit derivations of Eq. (6.7), (6.8) are given in Appendix F.

6.3 Methods and simulation details

The $T = 0$ phase diagram Fig. 6.1 is obtained by numerically minimizing the classical spin Hamiltonian $\mathcal{H}$ (6.4) on a finite lattice. Two crucial steps are useful to improve the efficiency of the local gradient-based minimization algorithms [77]. In the first step, we set multiple random initial conditions $|\boldsymbol{Z}\rangle$ (~ 50 for our case), where $|\boldsymbol{Z}_j\rangle$ on *every* site j is uniformly sampled on the $\mathrm{CP}^2 \simeq S^5/S^1$ manifold. After running the minimization algorithm, we keep the solution with the lowest energy for a given set of Hamiltonian parameters. In the next step, half of the initial conditions are randomly generated, while the other half correspond to the lowest-energy solutions obtained in the first step within a predefined neighborhood of the Hamiltonian parameters. This procedure is iterated until the phase diagram converges. The shape and size of this unit cell is dictated by the symmetry-related magnetic ordering wave vectors $\boldsymbol{Q}_\nu$ ($\nu = 1, 2, 3$) [see Figs. 6.2**a** and **b**], which are determined by minimizing the exchange interaction in momentum space: $J(\boldsymbol{q}) = \sum_{jl} J_{jl} e^{i\boldsymbol{q}\cdot(\boldsymbol{r}_j - \boldsymbol{r}_l)}$. The ratio between both exchange interactions, $J_2/|J_1| = 2/(1+\sqrt{5})$, is tuned to fix the magnitude of the ordering wave vectors, $|\boldsymbol{Q}_\nu| = |\boldsymbol{b}_1|/5$ [67], corresponding to a magnetic unit cell of linear size $L = 5$. The numerical minimization for the phase diagram Fig. 6.1 is done in a cell of 10×10 spins

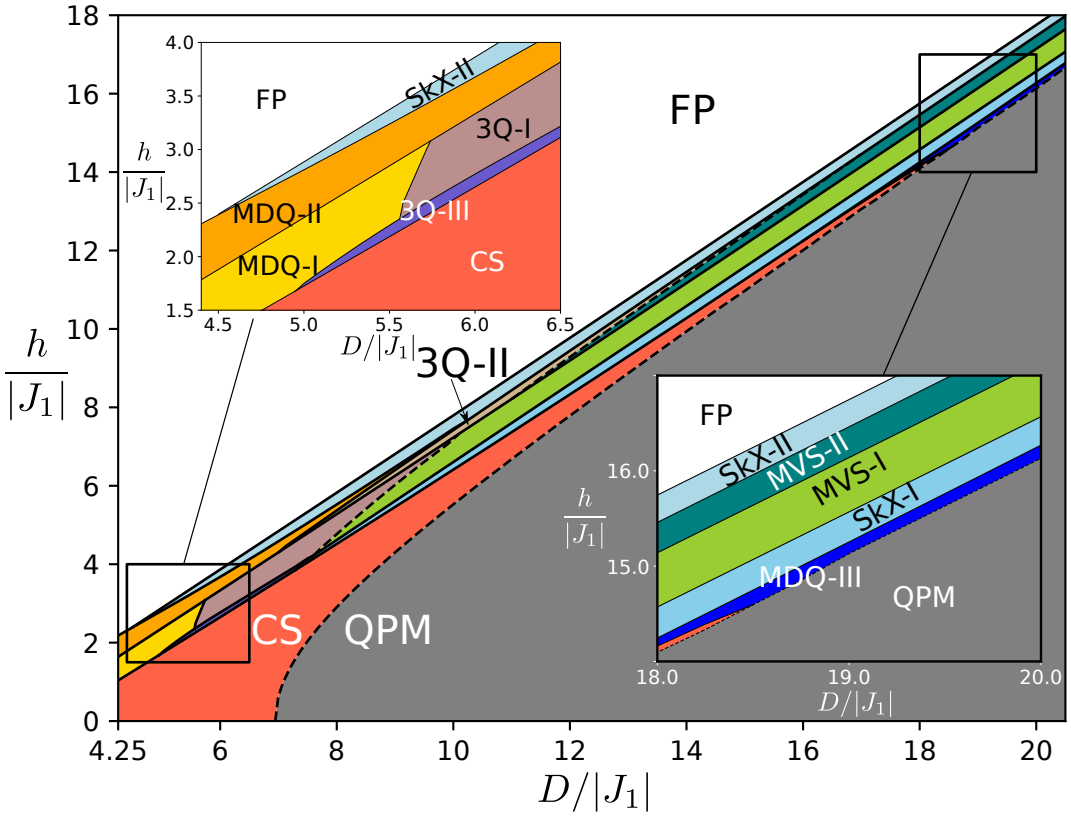


Figure 6.1: $T = 0$ phase diagram of the classical Hamiltonian $\mathcal{H}$ as a function of the single-ion anisotropy D and the external field h, for $J_2/|J_1| = 2/(1+\sqrt{5})$ and $\Delta = 2.6$. The two insets show the phases for small-D and large-D, respectively. The solid (dashed) lines indicate 1st- (2nd-) order phase transitions.

containing four magnetic unit cells ($L = 5$). A we will see later, the relevant qualitative aspects of the phase diagram do not depend on the particular choice of the model. The three ordering wave vectors, which are related by the C_6 symmetry of the TL, are parallel to the Γ-M_ν directions (denoted in Fig. 6.2).

6.4 Phase diagram

The resulting phase diagram shown in Fig. 6.1 includes multiple magnetically ordered phases between the FP phase and the QPM phase, where every spin is in the $|0\rangle$ state. Below we include a complete characterization for all remaining phases that appear in Fig. 6.1.

6.4.1 SkX phases

Two field-induced CP^2 skyrmion crystals (SkX-I and SkX-II) appear in the region $D \gg |J_1|$. As shown in Fig. 6.2**a**, the CP^2 skyrmions of the SkX-I crystal have dipole moments that evolve continuously into the purely nematic state ($|0\rangle$) as they move away from the core. Conversely, Fig. 6.2**b** shows that the spins in the SkX-II phase have a strong quadrupolar character at the skyrmion core (the small dipolar moment is in fact completely suppressed in the large $D/|J_1|$ limit), and they evolve continuously into the magnetic state $|1\rangle$ as they move away from the core. The CP^2 skyrmion density distribution ρ_{jkl} is also indicated with colored triangular plaquettes in Fig. 6.2**a**, **b** for SkX-I and SkX-II, respectively. As shown in the inset of Fig. 6.1, the phase SkX-II extends down to $D/|J_1| \simeq 5$, while the phase SkX-I disappears near $D/|J_1| \simeq 8$.

6.4.2 Single-Q orderings

New competing orderings appear in intermediate $D/|J_1|$ region. In particular, a significant fraction of the phase diagram is occupied by the so-called canted spiral (CS) phase,

$$|\boldsymbol{Z}_j\rangle = \cos\theta|0\rangle_j + e^{i\boldsymbol{Q}\cdot\boldsymbol{r}_j}\sin\theta\cos\phi|1\rangle_j + e^{-i\boldsymbol{Q}\cdot\boldsymbol{r}_j}\sin\theta\sin\phi|\bar{1}\rangle_j, \tag{6.9}$$

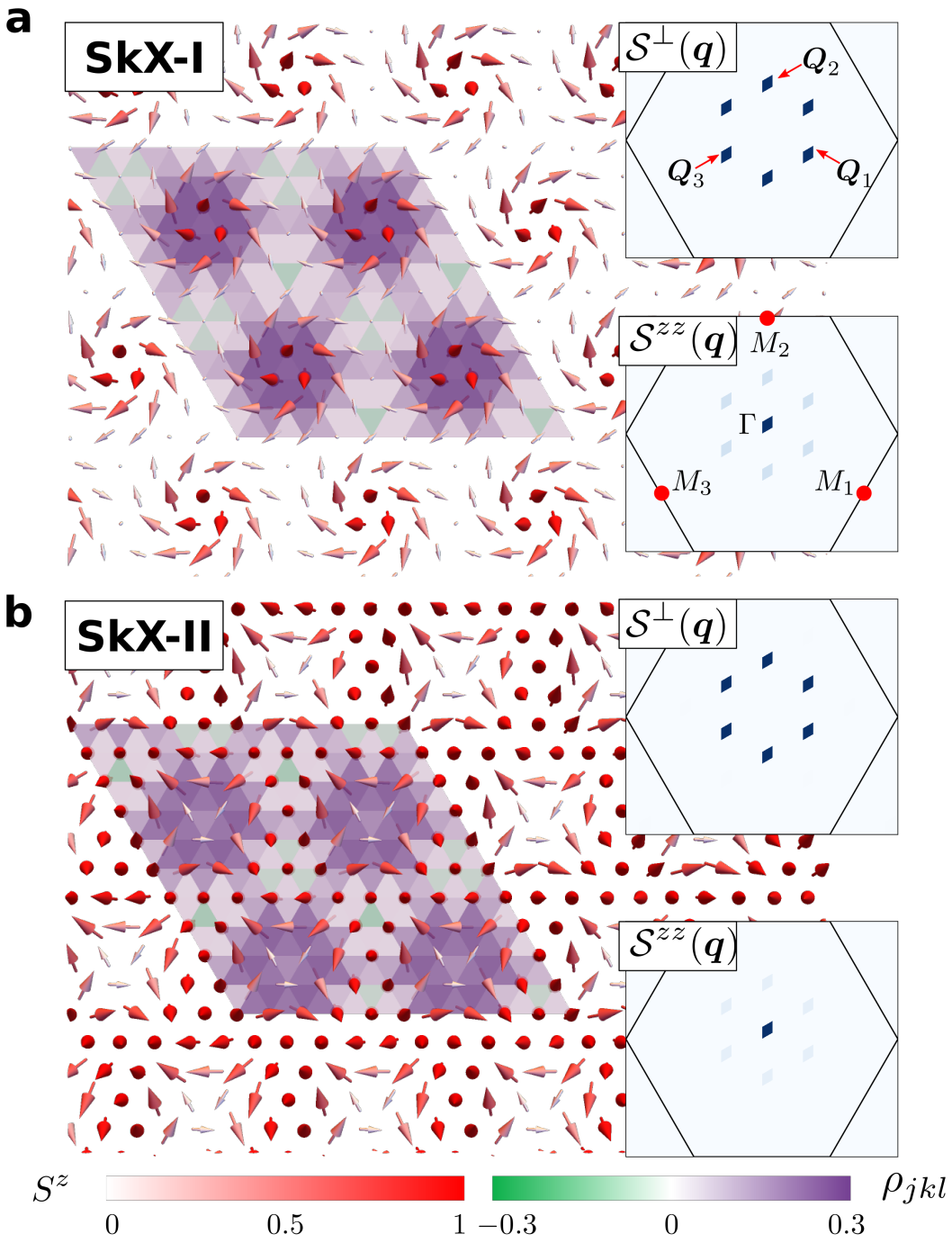


Figure 6.2: **a**, **b** Real space distribution of the dipolar sector of the CP^2 skyrmion crystals SkX-I and SkX-II. The length of the arrow represents the magnitude of the dipole moment of the color field $|\langle \hat{\boldsymbol{S}}_j \rangle| = \sqrt{(n_j^7)^2 + (n_j^5)^2 + (n_j^2)^2}$. The color scale of the arrows indicates $\langle \hat{S}_j^z \rangle = -n_j^2$. The insets display the static spin structure factors $\mathcal{S}^{\perp}(\boldsymbol{q}) = n_{\boldsymbol{q}}^7 n_{\bar{\boldsymbol{q}}}^7 + n_{\boldsymbol{q}}^5 n_{\bar{\boldsymbol{q}}}^5$ and $\mathcal{S}^{zz}(\boldsymbol{q}) = n_{\boldsymbol{q}}^2 n_{\bar{\boldsymbol{q}}}^2$, with $\boldsymbol{n}_{\boldsymbol{q}} = \sum_j e^{i\boldsymbol{q}\cdot\boldsymbol{r}_j} \boldsymbol{n}_j / L$. The CP^2 skyrmion density distribution ρ_{jkl} [see Eq. (6.8)] is indicated by the color of the triangular plaquettes

.

where θ and ϕ are variational parameters, and $\boldsymbol{Q}$ can take any values among $\{\boldsymbol{Q}_1, \boldsymbol{Q}_2, \boldsymbol{Q}_3\}$. Upon increasing D, the magnitude of the dipole moment of each spin, $|\langle \hat{\boldsymbol{S}}_j \rangle|$, is continuously suppressed to zero at the boundary,

$$D_c = h\sqrt{1 - \frac{4J^2(\boldsymbol{Q})}{h^2 + 4J^2(\boldsymbol{Q})}} - 2J(\boldsymbol{Q})\left(1 - \frac{2J(\boldsymbol{Q})}{\sqrt{h^2 + 4J^2(\boldsymbol{Q})}}\right), \tag{6.10}$$

which signals the second order transition into the QPM phase. In between the two Skyrmion crystal phases, there are two modulated vertical spiral phases MVS-I and MVS-II with a polarization plane parallel to the $\hat{\boldsymbol{z}}$-axis. Unlike the case of spirals described by SU(2) coherent states, the magnitude of the dipole moment is continuously modulated as the dipole moment rotates along the $\hat{\boldsymbol{z}}$ axis [see Fig. 6.3**a** **b**]. In the large-$D/|J_1|$ limit, the two spirals become vertical spiral states in the pseudo-spin variables.

6.4.3 Modulated double-Q orderings

There are three different modulated double-$\boldsymbol{Q}$ (MDQ I-III) orderings in the phase diagram [see Fig. 6.4]. Similar to the relation between MVS-I and MVS-II, the MDQ-I and MDQ-II phases appearing in the small $D/|J_1|$ region have the same symmetry and are separated by a first order metamagnetic transition. The MDQ-III phase, which occupies a small region above the QPM phase in the large $D/|J_1|$ region, is the pseudospin counterpart of the 2-q' phase reported in Ref. [92]. Since we have chosen a strong enough easy-axis exchange anisotropy Δ [see Eq. (1) of the main text], which translates into an effective single-ion easy-axis anisotropy $\tilde{\mathcal{D}}$ (K term of Ref. [92]) upon taking the long wavelength limit of the effective pseudospin model [see Eq. (22) of the main text], the MDQ-III phase eventually disappears for $D/|J_1| \gtrsim 25$. The existence of the MDQ-III phase for moderately large values of $D/|J_1|$ results from higher order terms in J_{ij}/D not included in the effective pseudospin model (19) of the main text. As shown in Fig. 6.4, the CP^2 skyrmion charge distribution of these MDQ orderings displays a stripe structure.

6.4.4 3Q spiral orderings

There are three triple-$\boldsymbol{Q}$ spiral orderings [3$\boldsymbol{Q}$S I-III] whose transverse spin structure factor exhibits dominant weight in one of the three ordering wave vectors $\boldsymbol{Q}_\nu$ ($\nu = 1, 2, 3$)

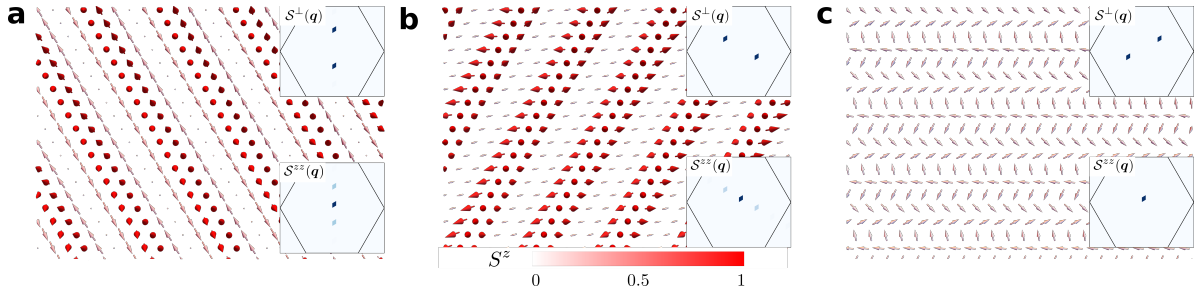


Figure 6.3: Real space distribution of the dipolar sector of the color fields for the three single-$\boldsymbol{Q}$ orderings. **a** MVS-I. **b** MVS-II. **c** CS. The length of the arrow represents the magnitude of the dipole moment of the color field $|\langle \hat{\boldsymbol{S}}_j \rangle| = \sqrt{(n_j^7)^2 + (n_j^5)^2 + (n_j^2)^2}$. The color scale of the arrows indicates $\langle \hat{S}_j^z \rangle = -n_j^2$. The insets display the static spin structure factors $\mathcal{S}^{\perp}(\boldsymbol{q}) = \langle n_{\boldsymbol{q}}^7 n_{\bar{\boldsymbol{q}}}^7 + n_{\boldsymbol{q}}^5 n_{\bar{\boldsymbol{q}}}^5 \rangle$ and $\mathcal{S}^{zz}(\boldsymbol{q}) = \langle n_{\boldsymbol{q}}^2 n_{\bar{\boldsymbol{q}}}^2 \rangle$, with $\boldsymbol{n}_{\boldsymbol{q}} = \sum_j e^{i\boldsymbol{q}\cdot\boldsymbol{r}_j} \boldsymbol{n}_j / \sqrt{N}$.

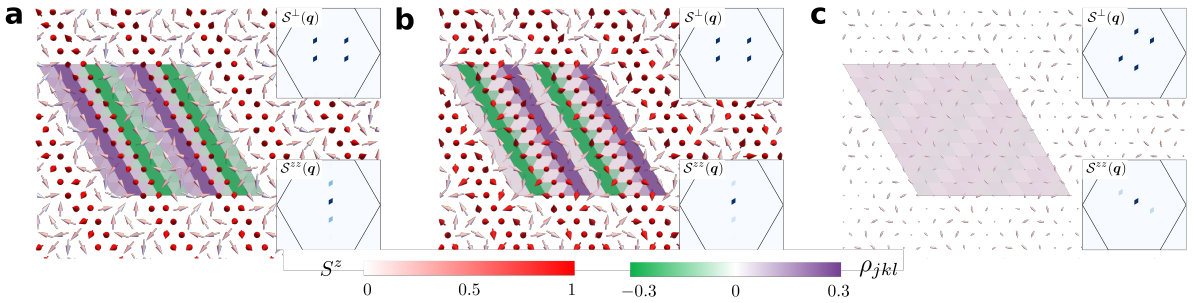


Figure 6.4: Real space distribution of the dipolar sector of the color fields for the three modulated double-$\boldsymbol{Q}$ orderings: **a** MDQ-I, **b** MDQ-II, and **c** MDQ-III. The length of the arrow represents the magnitude of the dipole moment of the color field $|\langle \hat{\boldsymbol{S}}_j \rangle| = \sqrt{(n_j^7)^2 + (n_j^5)^2 + (n_j^2)^2}$. The color scale of the arrows indicates $\langle \hat{S}_j^z \rangle = -n_j^2$. The insets display the static spin structure factors $\mathcal{S}^{\perp}(\boldsymbol{q}) = \langle n_{\boldsymbol{q}}^7 n_{\bar{\boldsymbol{q}}}^7 + n_{\boldsymbol{q}}^5 n_{\bar{\boldsymbol{q}}}^5 \rangle$ and $\mathcal{S}^{zz}(\boldsymbol{q}) = \langle n_{\boldsymbol{q}}^2 n_{\bar{\boldsymbol{q}}}^2 \rangle$, with $\boldsymbol{n}_{\boldsymbol{q}} = \sum_j e^{i\boldsymbol{q}\cdot\boldsymbol{r}_j} \boldsymbol{n}_j / \sqrt{N}$. The CP^2 skyrmion density distribution ρ_{jkl} [see Eq. (16) of the main text] is indicated by the color of the triangular plaquettes in all three panels.

[see Fig. 6.5 **a**-**c**]. The CP^2 Skyrmion density of these 3$\boldsymbol{Q}$S phases displays a staggered distribution. Upon increasing D for a fixed value of h, the subdominant weights are continuously suppressed for the 3$\boldsymbol{Q}$S-I and 3$\boldsymbol{Q}$S-II states, leading to a second order phase transition into MVS-I, and MVS-II, respectively. The additional characteristic of the 3$\boldsymbol{Q}$S-III state is that the longitudinal spin structure factor has a equal weights on the three ordering wave vectors $\boldsymbol{Q}_\nu$.

6.5 Large-D limit

In the remaining sections of this chapter, we will focus on the SkX phases and the single-skyrmion metastable solutions that emerge in their proximity. The origin of the CP^2 skyrmion crystals can be understood by analyzing the small $|J_{ij}|/D$ regime, where $\hat{\mathcal{H}}$ can be reduced via first order degenerate perturbation theory in J_{ij}/D to an effective pseudo-spin-1/2 low-energy Hamiltonian,

$$\hat{\mathcal{H}}_{\text{eff}} = \sum_{\langle i,j \rangle} \tilde{J}_{ij} (\hat{s}_i^x \hat{s}_j^x + \hat{s}_i^y \hat{s}_j^y + \tilde{\Delta} \hat{s}_i^z \hat{s}_j^z) - \tilde{h} \sum_i \hat{s}_i^z. \tag{6.11}$$

The pseudo-spin-1/2 operators are the projection of the original spin operators into the low-energy subspace $\mathcal{S}_0$ generated by the quasi-degenerate doublet $\{|0\rangle_j, |1\rangle_j\}$ (see Fig. 6.6):

$$\hat{s}_j^z = \mathcal{P}_0 \hat{S}_j^z \mathcal{P}_0 - \frac{1}{2}, \quad \hat{s}_j^\pm = \frac{\mathcal{P}_0 \hat{S}_j^\pm \mathcal{P}_0}{\sqrt{2}}, \tag{6.12}$$

where $\mathcal{P}_0$ is the projection operator of the low-energy subspace.

Importantly, the first state of the doublet has a net quadrupolar moment but no net dipole moment, $\langle 0|\hat{\boldsymbol{S}}_j|0\rangle_j = 0$, while the second state maximizes the dipole moment along the $\hat{\boldsymbol{z}}$-direction $\langle 1|\hat{\boldsymbol{S}}_j|1\rangle_j = \hat{\boldsymbol{z}}$. This means that three pseudo-spin operators generate an SU(2) subgroup of SU(3) different from the SU(2) subgroup of spin rotations.

$\hat{\mathcal{H}}_{\text{eff}}$ represents an effective triangular easy-axis XXZ model with effective exchange, anisotropy and field parameters $\tilde{J}_{ij} = 2J_{ij}$, $\tilde{\Delta} = \frac{\Delta}{2}$ and $\tilde{h} = h - D - 3\Delta(J_1 + J_2)$, respectively. This model is known to exhibit a field-induced CP^1 SkX phase [92, 67] that survives in the

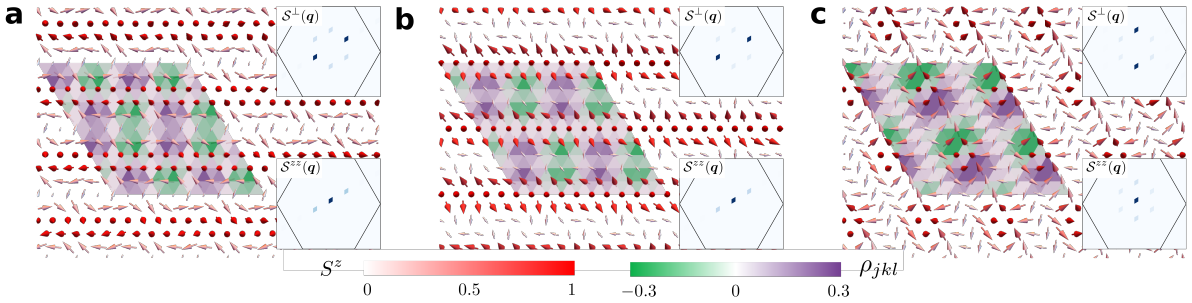


Figure 6.5: Real space distribution of the dipolar sector of the color fields for the three $3\boldsymbol{Q}$ spiral orderings: **a** $3\boldsymbol{Q}$S-I, **b** $3\boldsymbol{Q}$S-II, and **c** $3\boldsymbol{Q}$S-III. The length of the arrow represents the magnitude of the dipole moment of the color field $|\langle \hat{\boldsymbol{S}}_j \rangle| = \sqrt{(n_j^7)^2 + (n_j^5)^2 + (n_j^2)^2}$. The color scale of the arrows indicates $\langle \hat{S}_j^z \rangle = -n_j^2$. The insets display the static spin structure factors $\mathcal{S}^{\perp}(\boldsymbol{q}) = \langle n_{\boldsymbol{q}}^7 n_{\bar{\boldsymbol{q}}}^7 + n_{\boldsymbol{q}}^5 n_{\bar{\boldsymbol{q}}}^5 \rangle$ and $\mathcal{S}^{zz}(\boldsymbol{q}) = \langle n_{\boldsymbol{q}}^2 n_{\bar{\boldsymbol{q}}}^2 \rangle$, with $\boldsymbol{n}_{\boldsymbol{q}} = \sum_j e^{i\boldsymbol{q}\cdot\boldsymbol{r}_j} \boldsymbol{n}_j / \sqrt{N}$. The CP^2 skyrmion density distribution ρ_{jkl} [see Eq. (16) of the main text] is indicated by the color of the triangular plaquettes in all three panels.

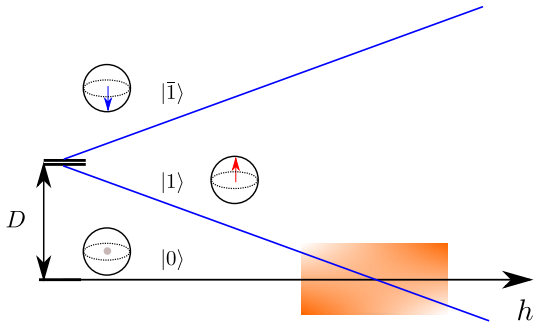


Figure 6.6: Spectrum of the single-ion model $\hat{\mathcal{H}}_{\mathrm{SI}} = D(\hat{S}^z)^2 - h\hat{S}^z$. The shaded region denotes the effective regime with a quasi-degenerate doublet: $\{|0\rangle, |1\rangle\}$.

long-wavelength limit [94]:

$$\mathcal{H}_{\text{eff}} \simeq \int \mathrm{d}r^2 \left[-\frac{\mathcal{J}_1^\eta}{2} \partial_a \tilde{n}^\eta \cdot \partial_a \tilde{n}^\eta + \frac{\mathcal{J}_2^\eta}{2} \left(\nabla^2 \tilde{n}^\eta \right)^2 - \tilde{\mathcal{B}} \tilde{n}_z + \tilde{\mathcal{D}} \tilde{n}_z^2 \right], \tag{6.13}$$

where $\eta = x, y, z$ denotes the three components of the unit vector field $\tilde{\boldsymbol{n}}$ ($|\tilde{\boldsymbol{n}}| = 1$), and

$$\begin{aligned} \mathcal{J}_1^\eta &= \frac{3s^2}{2}(\tilde{J}_1 + 3\tilde{J}_2)[1 + (\tilde{\Delta} - 1)\delta_{\eta z}], \\ \mathcal{J}_2^\eta &= \frac{3s^2}{32}(\tilde{J}_1 + 9\tilde{J}_2)[1 + (\tilde{\Delta} - 1)\delta_{\eta z}] \\ \tilde{\mathcal{B}} &= s\tilde{h}, \quad \tilde{\mathcal{D}} = 3s^2(\tilde{\Delta} - 1)(\tilde{J}_1 + \tilde{J}_2), \end{aligned} \tag{6.14}$$

with $s = 1/2$. Although the target manifold of this theory is CP^1 (orbit of SU(2) coherent states that belong $\mathcal{S}_0$), we must keep in mind that $\hat{\mathcal{H}}_{\text{eff}}$ describes the large $D/|J_1|$ limit where the CP^2 skyrmions of the original spin-1 model become asymptotically close to CP^1 *pseudo-spin* skyrmions. In other words, the SkXs include a finite $|\bar{1}\rangle$ component for finite $D/|J_1|$, which increases upon decreasing D. This component, which only appears in the low-energy model when second order corrections in J_{ij} are included, is responsible for the metamagnetic transition between the MVS-I and MVS-II phases (the transition disappears in the $D \to \infty$ limit).

Since $\hat{\mathcal{H}}_{\text{eff}}(h)$ and $\hat{\mathcal{H}}_{\text{eff}}(-h)$ are related by a pseudo-time-reversal (PTR) transformation ($\hat{s}_j \to -\hat{s}_j$ on the lattice and $\tilde{n} \to -\tilde{n}$ in the continuum) their corresponding ground states are related by the same transformation. In particular, the ground state ($\tilde{\boldsymbol{n}} = \hat{\boldsymbol{z}}$) that is obtained above the saturation field ($\tilde{\mathcal{B}} > \tilde{\mathcal{B}}_{\text{sat}}$) corresponds to the FP state ($\langle \hat{\boldsymbol{S}}_j \rangle = \hat{\boldsymbol{z}}$) in the original spin-1 variables, while the ground state ($\tilde{\boldsymbol{n}} = -\hat{\boldsymbol{z}}$) below the negative saturation field ($\tilde{\mathcal{B}} < -\tilde{\mathcal{B}}_{\text{sat}}$) corresponds to the QPM phase ($|\boldsymbol{Z}_j\rangle = |0\rangle_j$). Correspondingly, the SkX induced by a positive h has pseudo-spins polarized along the quadrupolar direction ($|0\rangle$) near the core of the skyrmions and parallel to the dipolar one ($|1\rangle$) at the midpoints between two cores. This explains the origin of the SkX-II crystals depicted in Fig. 6.2 **b**. The negative $\mathcal{B}$ counterpart of this phase, which is obtained by applying the PTR transformation, corresponds to the SkX-I crystal shown in Fig. 6.2**a**. In this case the skyrmion cores are magnetic, while the midpoints are practically quadrupolar (they become purely quadrupolar

in the large $D/|J_1|$ limit). This simple reasoning explains the origin of the novel SkX phases included in the $T = 0$ phase diagram of $\mathcal{H}$ shown in Fig. 6.1. The intermediate phase between the SkX-I and SkX-II ground state of $\mathcal{H}$ induced by positive and negative values of h is a single-$\boldsymbol{Q}$ spiral with a polarization plane parallel to the c-axis, known as vertical spiral (VS). This explains the origin of the MVS-I and MVS-II phases in between the two SkX phases (the first order transition between both phases disappears in the large-D limit [92]).

Single-skyrmion solutions. Besides the SkX phases shown in Fig. 6.7, the effective field theory (6.13) is known to support metastable CP^1 single-skyrmion solutions beyond the saturation fields $|\tilde{\mathcal{B}}| > \tilde{\mathcal{B}}_{\rm sat}$. The pseudo-spin variable is anti-parallel to the external field at the core, and it gradually rotates towards the direction parallel to the field upon moving away from the center. Interestingly, this pseudo-spin texture translates into metastable single-skyrmion solutions of the QPM phase that have a magnetic core and a nematic periphery, as it is shown in Figs. 6.7**a** and **b** for different sets of Hamiltonian parameters. The CP^2 skyrmions are metastable solutions in the QPM phase for $D \gtrsim 14$, implying that these exotic magnetic-nematic textures should emerge in real magnets under quite general conditions.

Similarly, the metastable pseudo-spin single-skyrmion solutions of the FP phase ($\tilde{\mathcal{B}} > \tilde{\mathcal{B}}_{\rm sat}$) lead to a spin texture with a nematic (non-magnetic) core and a magnetic (FP) periphery, like the one shown in Fig. 6.7**c**. Interestingly, this exotic CP^2 skyrmion solution remains metastable down to $D \simeq 4|J_1|$, and it coexists with regular (CP^1) metastable skyrmion solutions, like the one shown Fig. 6.7**d**, which emerge below $D \simeq 4.25|J_1|$.

6.6 Discussion

In summary, we have demonstrated that CP^2 skyrmion textures emerge in realistic models of hexagonal magnets out of the combination of geometric frustration with competing exchange and single-ion anisotropies. It is important to note that the skyrmion crystals and metastable solutions reported in this work survive in the long wavelength limit [94], implying that the above described CP^2 skyrmion phases should also exist in extensions of the model to honeycomb and Kagome lattice geometries. The generic spin-1 model considered in this work describes a series of triangular antiferromagnets in the form of ABX_3, BX_2, and

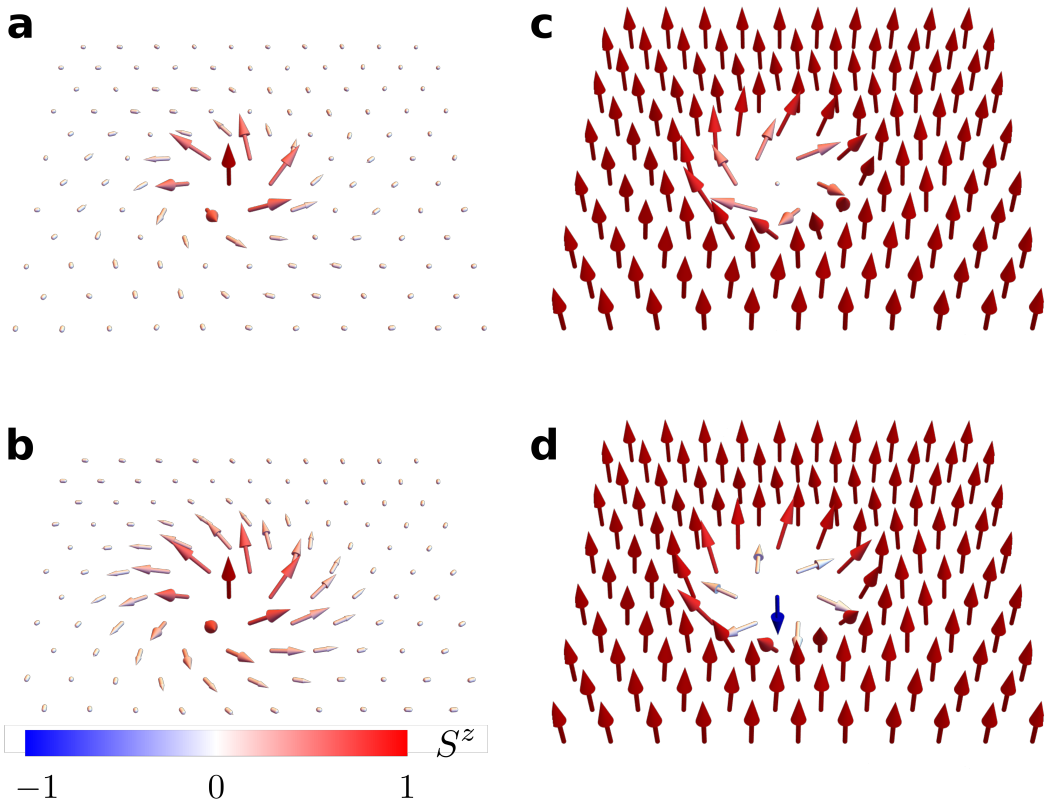


Figure 6.7: Dipolar sector of CP^2 skyrmions. The color scale indicates the value of n_j^2 ($\langle \hat{S}_j^z \rangle$). **a**, **b** Skyrmion excitation on top of a QPM background. **c**, **d** Skyrmion excitation on top of a fully polarized background. $J_2/|J_1| = 2/(1+\sqrt{5})$ and $\Delta = 2.6$ in (a), (c), and (d). $J_2/|J_1| = 2/(3+\sqrt{5})$ and $\Delta = 2.2$ in **b**. In these panels, **a**. $D = 17.1|J_1|$, $H = 13|J_1|$. **b**. $D = 18.3|J_1|$, $H = 14|J_1|$. **c**. $D = 7|J_1|$, $H = 5|J_1|$. **d**. $D = 4|J_1|$, $H = 2|J_1|$.

ABO_2 [42, 102, 32], where A is a an alkali metal, B is a transition metal, and X is a halogen atom. Several Ni-based compounds, including $NiGa_2S_4$ [112], $Ba_3NiSb_2O_9$ [37], $Na_2BaNi(PO_4)_2$ [93], are also found to be realizations of spin-1 models on TLs. Some of these compounds have been already identified as candidates to host crystals of CP^1 magnetic skyrmions that are stabilized by the combination of frustration and exchange anisotropy [8]. Others, such as FeI_2 [17, 91], are described by the the Hamiltonian (6.1), but the sign of the single-ion and exchange anisotropies is opposite to the case of interest in this work. Related compounds, such as $CsFeCl_3$, are known to be quantum paramagnets described by the Hamiltonian (6.1) [85] with a dominant easy-plane single-ion anisotropy $D/J_1 \simeq 10$. An alternative route to find realizations of our spin-1 Hamiltonian is to consider hexagonal materials comprising $4f$ magnetic ions with a singlet single-ion ground state and an excited Ising-like doublet (the effective easy-plane single-ion anisotropy D is equal to the singlet-doublet gap). Ultracold atoms are also powerful platforms to realize spin-1 models with *tunable* single-ion anisotropy [41].

Our results demonstrate that magnetic field induced CP^2 skyrmion crystals should emerge in the presence of a dominant single-ion easy-plane anisotropy D that is strong enough to stabilize a QPM at $T = 0$. In terms of SU(3) spins, the single-ion anisotropy acts as an external SU(3) field that couples linearly to one component ($\hat{T}_j^8$) of the quadrupolar moment. Correspondingly, the QPM can be regarded as a uniform quadrupolar state induced by a strong enough $\hat{T}_j^8$ component of the SU(3) field. The field-induced quantum phase transition between this uniform quadrupolar state and the skyrmion crystals is presaged by the emergence of metastable CP^2 single-skyrmion solutions consisting of a magnetic skyrmion core that decays continuously into a quadrupolar periphery. These novel skyrmions can be induced by increasing the strength of the magnetic field in the neighborhood of a given magnetic ion of a frustrated quantum paramagnet with competing exchange and single-ion anisotropies.

Chapter 7

Conclusions and outlooks

In this dissertation we have generalized three important notions in the field of quantum magnetism: (I) classical or Landau-Lifshitz dynamics, (II) spin wave theory, and (III) magnetic topological solitons, in particular magnetic solitons that may emerge in real materials. Some approaches, which bear different names in literature, such as the "multi-flavor" linear spin wave theory [79] or the "bond-operator method" [131], are particular examples that can now unified through an important observation: there is more than one way of taking the classical limit for a quantum spin system. By applying these generalized tools and concepts to realistic finite-spin ($S \geq 1$) systems, we have uncovered a number of physical phenomena that cannot be captured with the traditional approaches: the temperature evolution of a coherent mode in a spin-1 magnet; the existence of multi-magnon bound states; the spontaneous/field-induced decay of quasi-particles of mixed dipolar and quarupolar characters; and the emergence of the unconventional CP^2 skyrmions. These examples illustrate the important point that systems that are well-described by a generalized semi-classical approach can still exhibit *unconventional behaviors* that are rooted in the quantum mechanical origin of spin degrees of freedom.

The first step of solving the dynamics of a quantum spin system is to choose an adequate Lie algebra to describe the problem. A given spin Hamiltonian can be expressed as a function of generators of different Lie algebras [24]. These different representations should in principle lead to the same exact solution. However, except for very particular cases, it is impossible to solve the problem posed by an interacting quantum spin system without making any

approximation. As a result, the "optimal choice" of the representation should lead to a classical or "mean-field" state that best captures the qualitative properties of the system under consideration.

We note that similar arguments hold for other topics in condensed matter physics. For instance, in the plasmon theory of the interacting electron gas [4], one can predict the RPA free energy by including the leading order fluctuations in the mean-field value of the (bosonic) auxiliary Hubbard-Stratonovich field, which, in the canonical formalism, would require the summation of a subset of ring diagrams to infinite order. Another example can be found in the mean-field BCS Hamiltonian, which explains the superconducting transition temperature for conventional superconductors [4]. This model was obtained by performing a mean-field decoupling on the full BCS Hamiltonian by introducing the order parameter (that corresponds to the creation/annihilation of Cooper pairs) and assuming the order parameter is static [20].

Returning to the problem of spin dynamics, we first choose a representation (Lie group) and express the spin Hamiltonian as a function the generators of the corresponding Lie algebra. We then make the "classical" approximation by replacing the quantum spin Hamiltonian with its expectation value for a coherent states of the Lie group. Here we have used two realistic spin systems to illustrate how the coherent states of SU($2S+1$) better estimate the ground state energy and the excitations of a quantum spin-S system with large single-ion anisotropy. In Ch. 2, we briefly sketched the necessity of using the SU(N) representation for another large class of spin systems comprising weakly coupled multi-spin units (e.g., weakly coupled spin dimers, trimers, or quadrumers) [131, 116, 46]. We saw that the classical Hamiltonian based on SU(4) coherent states, i.e., the states that span the local Hilbert space of a spin-1/2 single bond unit, provides an adequate classical limit for treating such quantum spin systems. The classical approximations made in this dissertation can only account for very short-ranged quantum entanglement, such as the singlet character of the ground state of an antiferromagnetic Heisenberg model for a single dimer system. It is interesting to ask if an even more general "classical" approach based on groups, which are not necessarily Lie groups, can account for the highly entangled nature of the ground states of certain spin systems.

In Ch. 6 and Ref. [168], we reported the emergence of CP^2 skyrmions and skyrmion crystals in a *realistic* spin-1 model. An important conclusion that can be drawn from our study, as compared to other proposals to realize CP^2 skyrmions in quantum magnets [3, 5], is that the spin-1 Hamiltonian does *not* need to be SU(3) invariant. A result from homotopy theory, that $\pi_2(CP^2) = \mathbb{Z}$, was one of the most important motivations that led to the discussions presented in Ch. 6. Here $CP^2 \simeq SU(3)/[SU(2) \times U(1)]$ is the manifold of the SU(3) coherent states in the fundamental representation (see Ch. 2). Given that the (target) manifold of SU(3) coherent states depends on the representation, we may also ask if new types of topological solitons can emerge in real materials by working with other representations of SU(3). Indeed, as it has been explored recently in a series of studies [150, 7, 143], the flag manifold $SU(3)/[U(1) \times U(1)]$, which corresponds to the first non-degenerate representation of SU(3) [62], supports an exotic type of topological solitons with two charge labels, given by $\pi_2(SU(3)/[U(1) \times U(1)]) = \mathbb{Z} \times \mathbb{Z}$. However, as in Refs. [3, 5], the starting point of all these studies is an SU(3) invariant Hamiltonian, which can be challenging to realize in magnetic systems. We are instead interested in exploring the possibility of finding physically realizable spin Hamiltonians that support these new types of topological solitons.

In Ch. 6, we also showed that the CP^2 SkXs, which emerged from Eq. (6.1) in the large-D limit, are reminiscent of the field-induced CP^1 SkXs reported in Ref. [92], although the relevant doublet leading to the SkXs in our study is the non-magnetic state $|S^z = 0\rangle$ and the "spin-up" state $|S^z = 1\rangle$. On the other hand, it is also worth reinvestigating the spin-1 model that gives rise to the field-induced CP^1 SkX phases because they were obtained using the traditional SU(2) representation in Ref. [92], whereas the SU(3) approach is obviously more appropriate.

Another thrilling aspect of a topologically non-trivial spin texture (e.g., a SkX) is that it may be relevant to our understanding of the spontaneous topological Hall effect in itinerant electron systems. As it was pointed out in Ref. [171], the "real-space Berry curvature" (emergent gauge field) acting on itinerant electrons can have two sources: the non-trivial topological texture of localized (dipolar) spin fields, or spin-orbit coupling. The resulting Berry curvature provides an unified explanation for the spontaneous topological Hall effect observed in systems with various (non-collinear/collinear) (dipolar) spin structures. Based

on the results presented in this dissertation, we can begin asking questions about the consequences of the Berry curvature generated by more general *multipolar* fields, as in the case of CP^2 SkXs, where we found smooth topological textures in which the dipolar field is continuously transformed into a quadrupolar field. Finally, it is also interesting to study the spin dynamics of CP^2 skyrmions and their interactions with external currents and applied magnetic and strain fields. In contrast to spin wave excitations, skyrmions usually move very slowly and have a long lifetime, owing to the fact that discontinuous changes in spin configurations have large energy costs [135]. Langevin dynamics (also known as stochastic Landau-Lishitz-Gilbert dynamics) offer an approach that allows description of the motion of skyrmion systems that are in contact with a thermal bath (see Ref. [111] for a complete discussion in the context of the (CP^1) magnetic skyrmion dynamics). It consists of the LLD discussed in this dissertation with the addition of damping and noise terms that mimic the effect of a thermal bath. Like the SU(N) generalization of the LLD, it also necessary to generalize the traditional Langevin dynamics in order to describe the motion of CP^{N-1} skyrmions.

Bibliography

[1] Adams, T., Chacon, A., Wagner, M., Bauer, A., Brandl, G., Pedersen, B., Berger, H., Lemmens, P., and Pfleiderer, C. (2012). Long-wavelength helimagnetic order and skyrmion lattice phase in Cu_2OSeO_3. *Phys. Rev. Lett.*, 108(23):237204.

[2] Affleck, I. and Wellman, G. F. (1992). Longitudinal modes in quasi-one-dimensional antiferromagnets. *Physical Review B*, 46(14):8934.

[3] Akagi, Y., Amari, Y., Sawado, N., and Shnir, Y. (2021). Isolated skyrmions in the CP^2 nonlinear sigma model with a dzyaloshinskii-moriya type interaction. *Phys. Rev. D*, 103:065008.

[4] Altland, A. and Simons, B. D. (2010). *Condensed matter field theory.* Cambridge university press.

[5] Amari, Y., Akagi, Y., Gudnason, S. B., Nitta, M., and Shnir, Y. (2022). $\mathbb{C}p^2$ skyrmion crystals in an su(3) magnet with a generalized dzyaloshinskii-moriya interaction.

[6] Amari, Y., Klimas, P., Sawado, N., and Tamaki, Y. (2015). Potentials and the vortex solutions in the CP^N Skyrme-Faddeev model. *Phys. Rev. D*, 92(4):045007.

[7] Amari, Y. and Sawado, N. (2018). Bps sphalerons in the F_2 nonlinear sigma model. *Phys. Rev. D*, 97:065012.

[8] Amoroso, D., Barone, P., and Picozzi, S. (2020). Spontaneous skyrmionic lattice from anisotropic symmetric exchange in a ni-halide monolayer. *Nature Communications*, 11(1):5784.

[9] Anderson, P. W. (1950). Antiferromagnetism. theory of superexchange interaction. *Physical Review*, 79(2):350.

[10] Anderson, P. W. (1952). An approximate quantum theory of the antiferromagnetic ground state. *Phys. Rev.*, 86:694–701.

[11] Anderson, P. W. (1973). Resonating valence bonds: A new kind of insulator? *Materials Research Bulletin*, 8(2):153–160.

[12] Arnol'd, V. I. (2013). *Mathematical methods of classical mechanics*, volume 60. Springer Science & Business Media.

[13] Arovas, D. (2021). Lecture notes on group theory in physics (a work in progress).

[14] Arovas, D. P. and Auerbach, A. (1988). Functional integral theories of low-dimensional quantum heisenberg models. *Phys. Rev. B*, 38:316–332.

[15] Ashcroft, N. and Mermin, N. (2011). *Solid State Physics*. Cengage Learning.

[16] Auerbach, A. (2012). *Interacting electrons and quantum magnetism*. Springer Science & Business Media.

[17] Bai, X., Zhang, S.-S., Dun, Z., Zhang, H., Huang, Q., Zhou, H., Stone, M. B., Kolesnikov, A. I., Ye, F., Batista, C. D., and Mourigal, M. (2021a). Hybridized quadrupolar excitations in the spin-anisotropic frustrated magnet FeI_2. *Nature Physics*, 17(4):467–472.

[18] Bai, X., Zhang, S.-S., Zhang, H., Dun, Z., Phelan, W. A., Garlea, V. O., Mourigal, M., and Batista, C. D. (2021b). Instabilities of heavy magnons in an anisotropic magnet.

[19] Balucani, U. and Stasch, A. (1985). Hybrid excitations in layered iron halides. *Physical Review B*, 32(1):182.

[20] Bardeen, J., Cooper, L. N., and Schrieffer, J. R. (1957). Theory of superconductivity. *Phys. Rev.*, 108:1175–1204.

[21] Barnes, T., Dagotto, E., Riera, J., and Swanson, E. S. (1993). Excitation spectrum of heisenberg spin ladders. *Phys. Rev. B*, 47:3196–3203.

[22] Barros, K. (2022). A general-purpose library for performing generalized SU(N) classical spin simulations, https://github.com/SunnySuite/Sunny.jl/.

[23] Batista, C. D., Lin, S.-Z., Hayami, S., and Kamiya, Y. (2016). Frustration and chiral orderings in correlated electron systems. *Reports on Progress in Physics*, 79(8):084504.

[24] Batista, C. D. and Ortiz, G. (2004). Algebraic approach to interacting quantum systems. *Advances in Physics*, 53(1):1–82.

[25] Bernu, B., Lhuillier, C., and Pierre, L. (1992). Signature of néel order in exact spectra of quantum antiferromagnets on finite lattices. *Physical review letters*, 69(17):2590.

[26] Bertrand, Y., Fert, A., and Gelard, J. (1974). Susceptibilité magnétique des halogénures ferreux fecl2, febr2, fel2. *Journal de Physique*, 35(4):385–391.

[27] Bethe, H. (1931). Zur theorie der metalle. *Zeitschrift für Physik*, 71(3-4):205–226.

[28] Bogdanov, A. and Hubert, A. (1994). Thermodynamically stable magnetic vortex states in magnetic crystals. *Journal of Magnetism and Magnetic Materials*, 138(3):255 – 269.

[29] Bogdanov, A. N. and Panagopoulos, C. (2020). Physical foundations and basic properties of magnetic skyrmions. *Nature Reviews Physics*, 2(9):492–498.

[30] Bogolubskaya, A. and Bogolubsky, I. (1989). Stationary topological solitons in the two-dimensional anisotropic heisenberg model with a skyrme term. *Physics Letters A*, 136:485–488.

[31] Bogolyubskaya, A. A. and Bogolyubsky, I. L. (1990). ON STATIONARY TOPOLOGICAL SOLITONS IN TWO-DIMENSIONAL ANISOTROPIC HEISENBERG MODEL. *Lett. Math. Phys.*, 19:171–177.

[32] Botana, A. S. and Norman, M. R. (2019). Electronic structure and magnetism of transition metal dihalides: Bulk to monolayer. *Phys. Rev. Materials*, 3:044001.

[33] Capriotti, L., Trumper, A. E., and Sorella, S. (1999). Long-range néel order in the triangular heisenberg model. *Phys. Rev. Lett.*, 82:3899–3902.

[34] Chalker, J. T., Holdsworth, P. C., and Shender, E. (1992). Hidden order in a frustrated system: Properties of the heisenberg kagomé antiferromagnet. *Physical review letters*, 68(6):855.

[35] Chandragiri, V., Iyer, K. K., and Sampathkumaran, E. V. (2016). Magnetic behavior of $Gd_3Ru_4Al_{12}$, a layered compound with distorted kagomé net. *Journal of Physics: Condensed Matter*, 28(28):286002.

[36] Chauhan, P., Mahmood, F., Changlani, H. J., Koohpayeh, S. M., and Armitage, N. P. (2020). Tunable magnon interactions in a ferromagnetic spin-1 chain. *Phys. Rev. Lett.*, 124(3):037203.

[37] Cheng, J. G., Li, G., Balicas, L., Zhou, J. S., Goodenough, J. B., Xu, C., and Zhou, H. D. (2011). High-Pressure Sequence of $Ba_3NiSb_2O_9$ Structural Phases: New $S = 1$ Quantum Spin Liquids Based on Ni^{2+}. *Phys. Rev. Lett.*, 107(19):197204.

[38] Chernyshev, A. L. and Zhitomirsky, M. E. (2009). Spin waves in a triangular lattice antiferromagnet: Decays, spectrum renormalization, and singularities. *Phys. Rev. B*, 79:144416.

[39] Chubukov, A., Sachdev, S., and Senthil, T. (1994a). Large-s expansion for quantum antiferromagnets on a triangular lattice. *Journal of Physics: Condensed Matter*, 6(42):8891.

[40] Chubukov, A. V., Sachdev, S., and Ye, J. (1994b). Theory of two-dimensional quantum heisenberg antiferromagnets with a nearly critical ground state. *Physical Review B*, 49(17):11919.

[41] Chung, W. C., de Hond, J., Xiang, J., Cruz-Colón, E., and Ketterle, W. (2021). Tunable Single-Ion Anisotropy in Spin-1 Models Realized with Ultracold Atoms. *Phys. Rev. Lett.*, 126(16):163203.

[42] Collins, M. F. and Petrenko, O. A. (1997). Review/Synthèse: Triangular antiferromagnets. *Can. J. Phys.*, 75(9):605–655.

[43] Colpa, J. (1978). Diagonalization of the quadratic boson hamiltonian. *Physica A: Statistical Mechanics and its Applications*, 93(3):327–353.

[44] Cornwell, J. (1997). *Group Theory in Physics: An Introduction*. ISSN. Elsevier Science.

[45] D'Adda, A., Luscher, M., and Di Vecchia, P. (1978). A 1/n Expandable Series of Nonlinear Sigma Models with Instantons. *Nucl. Phys. B*, 146:63–76.

[46] Dahlbom, D., Zhang, H., Miles, C., Bai, X., Batista, C. D., and Barros, K. (2022). Geometric integration of classical spin dynamics via a mean-field schrödinger equation.

[47] Din, A. M. and Zakrzewski, W. (1980). General classical solutions in the $cp^n - 1$ model. *Nuclear Physics*, 174:397–406.

[48] Do, S.-H., Zhang, H., Williams, T. J., Hong, T., Garlea, V. O., Rodriguez-Rivera, J. A., Jang, T.-H., Cheong, S.-W., Park, J.-H., Batista, C. D., and Christianson, A. D. (2021). Decay and renormalization of a longitudinal mode in a quasi-two-dimensional antiferromagnet. *Nature Communications*, 12(1):5331.

[49] Dzyaloshinsky, I. (1958). A thermodynamic theory of weak ferromagnetism of antiferromagnetics. *J. Phys. Chem. Solids*, 4:241.

[50] Ferreira, L. A. and Klimas, P. (2010). Exact vortex solutions in a cpnskyrme-faddeev type model. *Journal of High Energy Physics*, 2010(10):8.

[51] Fert, A., Reyren, N., and Cros, V. (2017). Magnetic skyrmions: advances in physics and potential applications. *Nature Reviews Materials*, 2(7):17031.

[52] Friedt, J., Sanchez, J., and Shenoy, G. (1976). Electronic and magnetic properties of metal diiodides mi2 (m= v, cr, mn, fe, co, ni, and cd) from ^{129}i mössbauer spectroscopy. *The Journal of Chemical Physics*, 65(12):5093–5102.

[53] Fujita, T., Ito, A., and Ôno, K. (1966). The mössbauer study of the ferrous ion in fei2. *Journal of the Physical Society of Japan*, 21(9):1734–1736.

[54] Gazit, S., Podolsky, D., and Auerbach, A. (2013). Fate of the Higgs Mode Near Quantum Criticality. *Phys. Rev. Lett.*, 110:140401.

[55] Gelard, J., Fert, A., Meriel, P., and Allain, Y. (1974). Magnetic structure of fei2 by neutron diffraction experiments. *Solid State Communications*, 14(2):187–189.

[56] Ghioldi, E. A., Gonzalez, M. G., Zhang, S.-S., Kamiya, Y., Manuel, L. O., Trumper, A. E., and Batista, C. D. (2018). Dynamical structure factor of the triangular antiferromagnet: Schwinger boson theory beyond mean field. *Phys. Rev. B*, 98:184403.

[57] Gilmore, R. (1972). Geometry of symmetrized states. *Annals of Physics*, 74(2):391–463.

[58] Gitman, D. M. and Shelepin, A. L. (1993). Coherent states of SU(n) groups. *Journal of Physics A: Mathematical and General*, 26(2):313–327.

[59] Glauber, R. J. (1963a). Coherent and incoherent states of the radiation field. *Phys. Rev.*, 131:2766–2788.

[60] Glauber, R. J. (1963b). Photon correlations. *Physical Review Letters*, 10(3):84.

[61] Glauber, R. J. (1963c). The quantum theory of optical coherence. *Physical Review*, 130(6):2529.

[62] Gnutzmann, S. and Kus, M. (1998). Coherent states and the classical limit on irreducible representations. *Journal of Physics A: Mathematical and General*, 31(49):9871–9896.

[63] Golo, V. L. and Perelomov, A. M. (1978). Solution of the Duality Equations for the Two-Dimensional SU(N) Invariant Chiral Model. *Phys. Lett. B*, 79:112–113.

[64] Goodenough, J. B. (1955). Theory of the role of covalence in the perovskite-type manganites [la, m (ii)] mn o 3. *Physical Review*, 100(2):564.

[65] Hall, B. (2015). *Lie Groups, Lie Algebras, and Representations: An Elementary Introduction*. Graduate Texts in Mathematics. Springer International Publishing.

[66] Hastings, W. K. (1970). Monte carlo sampling methods using markov chains and their applications. *Biometrika*, 57(1):97–109.

[67] Hayami, S., Lin, S.-Z., and Batista, C. D. (2016). Bubble and skyrmion crystals in frustrated magnets with easy-axis anisotropy. *Phys. Rev. B*, 93:184413.

[68] Hayami, S. and Motome, Y. (2021). Topological spin crystals by itinerant frustration. *J. Phys.: Condens. Matter*, 33(44):443001.

[69] Helgason, S. (2001). *Differential Geometry, Lie Groups, and Symmetric Spaces*. Crm Proceedings & Lecture Notes. American Mathematical Society.

[70] Hirschberger, M., Nakajima, T., Gao, S., Peng, L., Kikkawa, A., Kurumaji, T., Kriener, M., Yamasaki, Y., Sagayama, H., Nakao, H., Ohishi, K., Kakurai, K., Taguchi, Y., Yu, X., Arima, T.-h., and Tokura, Y. (2019). Skyrmion phase and competing magnetic orders on a breathing kagomé lattice. *Nature Communications*, 10(1):5831.

[71] Holstein, T. and Primakoff, H. (1940). Field dependence of the intrinsic domain magnetization of a ferromagnet. *Phys. Rev.*, 58:1098–1113.

[72] Hong, T., Qiu, Y., Matsumoto, M., Tennant, D. A., Coester, K., Schmidt, K. P., Awwadi, F. F., Turnbull, M. M., Agrawal, H., and Chernyshev, A. L. (2017). Field induced spontaneous quasiparticle decay and renormalization of quasiparticle dispersion in a quantum antiferromagnet. *Nature Communications*, 8(1):15148.

[73] Hoogerbeets, R., Duyneveldt, A. J. v., Phaff, A. C., Swuste, C. H. W., and Jonge, W. J. M. d. (1984). Evidence for magnon bound-state excitations in the quantum chain system $(C_6H_{11}N_3)CuCl_3$. *J. Phys. C: Solid State Phys.*, 17(14):2595–2608.

[74] Hubbard, J. (1963). Electron correlations in narrow energy bands. *Proceedings of the Royal Society of London. Series A. Mathematical and Physical Sciences*, 276(1365):238–257.

[75] Huberman, T., Tennant, D. A., Cowley, R. A., Coldea, R., and Frost, C. D. (2008). A study of the quantum classical crossover in the spin dynamics of the 2ds= 5/2 antiferromagnet rb2mnf4: neutron scattering, computer simulations and analytic theories. *Journal of Statistical Mechanics: Theory and Experiment*, 2008(05):P05017.

[76] Jain, A., Krautloher, M., Porras, J., Ryu, G. H., Chen, D. P., Abernathy, D. L., Park, J. T., Ivanov, A., Chaloupka, J., Khaliullin, G., Keimer, B., and Kim, B. J. (2017). Higgs mode and its decay in a two dimensional antiferromagnet. *Nat. Phys.*, 13:633–637.

[77] Johnson, S. G. (2011). The NLopt nonlinear-optimization package, http://github.com/stevengj/nlopt.

[78] Kanamori, J. (1957). Theory of the magnetic properties of ferrous and cobaltous oxides, ii. *Progress of Theoretical Physics*, 17(2):197–222.

[79] Kim, F. H., Penc, K., Nataf, P., and Mila, F. (2017). Linear flavor-wave theory for fully antisymmetric su(n) irreducible representations. *Phys. Rev. B*, 96:205142.

[80] Klauder, J. and Skagerstam, B. (1985). *Coherent States: Applications in Physics and Mathematical Physics*. World Scientific.

[81] Kohama, Y., Sologubenko, A. V., Dilley, N. R., Zapf, V. S., Jaime, M., Mydosh, J. A., Paduan-Filho, A., Al-Hassanieh, K. A., Sengupta, P., Gangadharaiah, S., Chernyshev, A. L., and Batista, C. D. (2011). Thermal transport and strong mass renormalization in $\mathrm{nicl_2{-}4SC(nh_2)_2}$. *Phys. Rev. Lett.*, 106:037203.

[82] Kramers, H. (1934). L'interaction entre les atomes magnétogènes dans un cristal paramagnétique. *Physica*, 1(1-6):182–192.

[83] Kubo, R. (1952). The spin-wave theory of antiferromagnetics. *Phys. Rev.*, 87:568–580.

[84] Kulik, Y. and Sushkov, O. P. (2011). Width of the longitudinal magnon in the vicinity of the o (3) quantum critical point. *Physical Review B*, 84(13):134418.

[85] Kurita, N. and Tanaka, H. (2016). Magnetic-field- and pressure-induced quantum phase transition in $CsFeCl_3$ proved via magnetization measurements. *Phys. Rev. B*, 94:104409.

[86] Kurumaji, T., Nakajima, T., Hirschberger, M., Kikkawa, A., Yamasaki, Y., Sagayama, H., Nakao, H., Taguchi, Y., Arima, T.-h., and Tokura, Y. (2019). Skyrmion lattice with a giant topological hall effect in a frustrated triangular-lattice magnet. *Science*, 365(6456):914–918.

[87] Lacroix, C., Mendels, P., and Mila, F. (2011). *Introduction to frustrated magnetism: materials, experiments, theory*, volume 164. Springer Science & Business Media.

[88] Landau, L. D. and Lifshitz, E. (1935). On the theory of the dispersion of magnetic permeability in ferromagnetic bodies. *Phys. Z. Sowjet.*, 8:153.

[89] Lee, J. M. (2006). *Riemannian manifolds: an introduction to curvature*. Springer Science & Business Media.

[90] Leese, R., Peyrard, M., and Zakrzewski, W. (1990). Soliton scatterings in some relativistic models in (2+1) dimensions. *Nonlinearity*, 3:773–807.

[91] Legros, A., Zhang, S.-S., Bai, X., Zhang, H., Dun, Z., Phelan, W. A., Batista, C. D., Mourigal, M., and Armitage, N. P. (2021). Observation of 4- and 6-magnon bound states in the spin-anisotropic frustrated antiferromagnet FeI_2. *Phys. Rev. Lett.*, 127:267201.

[92] Leonov, A. O. and Mostovoy, M. (2015). Multiply periodic states and isolated skyrmions in an anisotropic frustrated magnet. *Nature Communications*, 6(1):8275.

[93] Li, N., Huang, Q., Brassington, A., Yue, X. Y., Chu, W. J., Guang, S. K., Zhou, X. H., Gao, P., Feng, E. X., Cao, H. B., Choi, E. S., Sun, Y., Li, Q. J., Zhao, X., Zhou, H. D., and Sun, X. F. (2021). Quantum spin state transitions in the spin-1 equilateral triangular lattice antiferromagnet $Na_2BaNi(PO_4)_2$. *Phys. Rev. B*, 104:104403.

[94] Lin, S.-Z. and Hayami, S. (2016). Ginzburg-landau theory for skyrmions in inversion-symmetric magnets with competing interactions. *Phys. Rev. B*, 93:064430.

[95] Ma, J., Kamiya, Y., Hong, T., Cao, H. B., Ehlers, G., Tian, W., Batista, C. D., Dun, Z. L., Zhou, H. D., and Matsuda, M. (2016). Static and dynamical properties of the spin-1/2 equilateral triangular-lattice antiferromagnet $ba_3cosb_2o_9$. *Phys. Rev. Lett.*, 116:087201.

[96] Mallik, R., Sampathkumaran, E. V., Paulose, P. L., Sugawara, H., and Sato, H. (1998). Magnetic anomalies in gd_2pdsi_3. *Pramana - J. Phys.*, 51:505.

[97] Manousakis, E. (1991). The spin-$\frac{1}{2}$ heisenberg antiferromagnet on a square lattice and its application to the cuprous oxides. *Rev. Mod. Phys.*, 63:1–62.

[98] Masuda, T., Zheludev, A., Manaka, H., Regnault, L.-P., Chung, J.-H., and Qiu, Y. (2006). Dynamics of composite haldane spin chains in IPA$-cucl_3$. *Phys. Rev. Lett.*, 96:047210.

[99] Mathur, M. and Sen, D. (2001). Coherent states for su(3). *Journal of Mathematical Physics*, 42(9):4181–4196.

[100] Matsumoto, M., Normand, B., Rice, T. M., and Sigrist, M. (2004). Field- and pressure-induced magnetic quantum phase transitions in tlcucl$_3$. *Phys. Rev. B*, 69:054423.

[101] Mattis, D. C. (2012). *The theory of magnetism I: Statics and Dynamics*, volume 17. Springer Science & Business Media.

[102] McGuire, M. A. (2017). Crystal and magnetic structures in layered, transition metal dihalides and trihalides. *Crystals*, 7(5).

[103] Metropolis, N. and Ulam, S. (1949). The monte carlo method. *Journal of the American Statistical Association*, 44(247):335–341. PMID: 18139350.

[104] Millet, P., Mila, F., Zhang, F. C., Mambrini, M., Van Oosten, A. B., Pashchenko, V. A., Sulpice, A., and Stepanov, A. (1999). Biquadratic interactions and spin-peierls transition in the spin-1 chain livge$_2O_6$. *Phys. Rev. Lett.*, 83:4176–4179.

[105] Moriya, T. (1960a). Anisotropic superexchange interaction and weak ferromagnetism. *Physical review*, 120(1):91.

[106] Moriya, T. (1960b). Anisotropic superexchange interaction and weak ferromagnetism. *Phys. Rev.*, 120:91–98.

[107] Moriya, T. (1960c). New mechanism of anisotropic superexchange interaction. *Phys. Rev. Lett.*, 4:228–230.

[108] Mourigal, M., Fuhrman, W. T., Chernyshev, A. L., and Zhitomirsky, M. E. (2013). Dynamical structure factor of the triangular-lattice antiferromagnet. *Phys. Rev. B*, 88:094407.

[109] Mühlbauer, S., Binz, B., Jonietz, F., Pfleiderer, C., Rosch, A., Neubauer, A., Georgii, R., and Böni, P. (2009). Skyrmion lattice in a chiral magnet. *Science*, 323(5916):915.

[110] Muniz, R. A., Kato, Y., and Batista, C. D. (2014). Generalized spin-wave theory: Application to the bilinear-biquadratic model. *Progress of Theoretical and Experimental Physics*, 2014(8).

[111] Nagaosa, N. and Tokura, Y. (2013). Topological properties and dynamics of magnetic skyrmions. *Nature Nanotechnology*, 8:899.

[112] Nakatsuji, S., Nambu, Y., Tonomura, H., Sakai, O., Jonas, S., Broholm, C., Tsunetsugu, H., Qiu, Y., and Maeno, Y. (2005). Spin Disorder on a Triangular Lattice. *Science*, 309(5741):1697–1700.

[113] Nemoto, K. (2000). Generalized coherent states forSU(n) systems. *Journal of Physics A: Mathematical and General*, 33(17):3493–3506.

[114] Niggemann, N., Hering, M., and Reuther, J. (2019). Classical spiral spin liquids as a possible route to quantum spin liquids. *Journal of Physics: Condensed Matter*, 32(2):024001.

[115] Nohadani, O., Wessel, S., and Haas, S. (2005). Quantum phase transitions in coupled dimer compounds. *Physical Review B*, 72(2):024440.

[116] Normand, B. and Rüegg, C. (2011). Complete bond-operator theory of the two-chain spin ladder. *Phys. Rev. B*, 83:054415.

[117] Okubo, T., Chung, S., and Kawamura, H. (2012). Multiple-q states and the skyrmion lattice of the triangular-lattice heisenberg antiferromagnet under magnetic fields. *Phys. Rev. Lett.*, 108:017206.

[118] Patyal, B. R., Scott, B. L., and Willett, R. D. (1990). Crystal-structure, magnetic-susceptibility, and epr studies of bis(piperidinium)tetrabromocuprate(ii): A novel monomer system showing spin diffusion. *Phys. Rev. B*, 41:1657–1663.

[119] Pekker, D. and Varma, C. (2015). Amplitude/higgs modes in condensed matter physics. *Annu. Rev. Condens. Matter Phys.*, 6(1):269–297.

[120] Perelomov, A. (2012). *Generalized Coherent States and Their Applications*. Theoretical and Mathematical Physics. Springer Berlin Heidelberg.

[121] Perelomov, A. M. (1972). Coherent states for arbitrary lie group. *Comm. Math. Phys.*, 26(3):222–236.

[122] Perelomov, A. M. and Popov, V. S. (1968). CASIMIR OPERATORS FOR SEMISIMPLE LIE GROUPS. *Mathematics of the USSR-Izvestiya*, 2(6):1313–1335.

[123] Petitgrand, D., Brun, A., and Meyer, P. (1980). Magnetic field dependence of spin waves and two magnon bound states in fei2. *Journal of Magnetism and Magnetic Materials*, 15:381–382.

[124] Plumb, K. W., Hwang, K., Qiu, Y., Harriger, L. W., Granroth, G. E., Kolesnikov, A. I., Shu, G. J., Chou, F. C., Rüegg, C., Kim, Y. B., and Kim, Y.-J. (2016). Quasiparticle-continuum level repulsion in a quantum magnet. *Nature Physics*, 12(3):224–229.

[125] Podolsky, D., Auerbach, A., and Arovas, D. P. (2011). Visibility of the amplitude (Higgs) mode in condensed matter. *Phys. Rev. B*, 84:174522.

[126] Podolsky, D. and Sachdev, S. (2012). Spectral functions of the Higgs mode near two-dimensional quantum critical points. *Phys. Rev. B*, 86:054508.

[127] Polyakov, A. M. and Belavin, A. A. (1975). Metastable States of Two-Dimensional Isotropic Ferromagnets. *JETP Lett.*, 22:245–248.

[128] Romhányi, J. and Penc, K. (2012). Multiboson spin-wave theory for ba 2 coge 2 o 7: a spin-3/2 easy-plane néel antiferromagnet with strong single-ion anisotropy. *Physical Review B*, 86(17):174428.

[129] Rose, F., Léonard, F., and Dupuis, N. (2015). Higgs amplitude mode in the vicinity of a $(2 + 1)$-dimensional quantum critical point: A nonperturbative renormalization-group approach. *Phys. Rev. B*, 91:224501.

[130] Sachdev, S. (1999). Universal relaxational dynamics near two-dimensional quantum critical points. *Physical Review B*, 59(21):14054.

[131] Sachdev, S. and Bhatt, R. N. (1990). Bond-operator representation of quantum spins: Mean-field theory of frustrated quantum heisenberg antiferromagnets. *Phys. Rev. B*, 41:9323–9329.

[132] Saha, S. R., Sugawara, H., Matsuda, T. D., Sato, H., Mallik, R., and Sampathkumaran, E. V. (1999). Magnetic anisotropy, first-order-like metamagnetic transitions, and large negative magnetoresistance in single-crystal Gd_2PdSi_3. *Phys. Rev. B*, 60:12162–12165.

[133] Savary, L. and Balents, L. (2016). Quantum spin liquids: a review. *Reports on Progress in Physics*, 80(1):016502.

[134] Schrödinger, E. (1926). Der stetige Übergang von der Mikro- zur Makromechanik. *Naturwissenschaften*, 14(28):664–666.

[135] Schütte, C., Iwasaki, J., Rosch, A., and Nagaosa, N. (2014). Inertia, diffusion, and dynamics of a driven skyrmion. *Phys. Rev. B*, 90:174434.

[136] Seki, S., Yu, X. Z., Ishiwata, S., and Tokura, Y. (2012). Observation of skyrmions in a multiferroic material. *Science*, 336(6078):198.

[137] Shender, E. and Holdsworth, P. (1996). Order by disorder and topology in frustrated magnetic systems. In *Fluctuations and Order*, pages 259–279. Springer.

[138] Sidney, C. (1985). *Aspects of Symmetry*. Cambridge.

[139] Skyrme, T. H. R. (1961). A non-linear field theory. *Proc. R. Soc. A*, 260(1300):127–138.

[140] Skyrme, T. H. R. (1988). The origins of skymions. *International Journal of Modern Physics A*, 3(12):2745–2751.

[141] Stone, M. B., Zaliznyak, I. A., Hong, T., Broholm, C. L., and Reich, D. H. (2006). Quasiparticle breakdown in a quantum spin liquid. *Nature*, 440(7081):187–190.

[142] Sudarshan, E. (1963). Equivalence of semiclassical and quantum mechanical descriptions of statistical light beams. *Physical Review Letters*, 10(7):277.

[143] Takahashi, I. and Tanizaki, Y. (2021). Sigma-model analysis of su(3) antiferromagnetic spins on the triangular lattice. *Phys. Rev. B*, 104:235152.

[144] Tanaka, Y. and Uryû, N. (1975). Ground state spin configurations of the triangular ising net with the nearest and next nearest neighbor interactions. *Journal of the Physical Society of Japan*, 39(3):825–826.

[145] Thomson, W. (1867). Ii. on vortex atoms. *London, Edinburgh, Dublin Philos. Mag. J. Sci.*, 34(227):15–24.

[146] Torrance, J. B. and Tinkham, M. (1969). Excitation of multiple-magnon bound states in $CoCl_2{\cdot}2H_2O$. *Phys. Rev.*, 187(2):595–606.

[147] Toth, S. and Lake, B. (2015). Linear spin wave theory for single-q incommensurate magnetic structures. *Journal of Physics: Condensed Matter*, 27(16):166002.

[148] Trooster, J. and de Valk, W. (1978). Spin ordering in febr2 and fei2. evidence for first order phase transition in fei2. *Hyperfine Interactions*, 4(1-2):457–459.

[149] Troyer, M., Tsunetsugu, H., and Würtz, D. (1994). Thermodynamics and spin gap of the heisenberg ladder calculated by the look-ahead lanczos algorithm. *Phys. Rev. B*, 50:13515–13527.

[150] Ueda, H. T., Akagi, Y., and Shannon, N. (2016). Quantum solitons with emergent interactions in a model of cold atoms on the triangular lattice. *Phys. Rev. A*, 93:021606.

[151] Villain, J., Bidaux, R., Carton, J.-P., and Conte, R. (1980). Order as an effect of disorder. *Journal de Physique*, 41(11):1263–1272.

[152] Vuletić, T., Korin-Hamzić, B., Ivek, T., Tomić, S., Gorshunov, B., Dressel, M., and Akimitsu, J. (2006). The spin-ladder and spin-chain system (la, y, sr, ca) 14cu24o41: Electronic phases, charge and spin dynamics. *Physics reports*, 428(4):169–258.

[153] Wang, Z., Su, Y., Lin, S.-Z., and Batista, C. D. (2020). Skyrmion crystal from RKKY interaction mediated by 2D electron gas. *Phys. Rev. Lett.*, 124(20):207201.

[154] Wannier, G. H. (1950). Antiferromagnetism. the triangular ising net. *Phys. Rev.*, 79:357–364.

[155] Watson, B. C., Kotov, V. N., Meisel, M. W., Hall, D. W., Granroth, G. E., Montfrooij, W. T., Nagler, S. E., Jensen, D. A., Backov, R., Petruska, M. A., Fanucci, G. E., and Talham, D. R. (2001). Magnetic spin ladder $(C_5H_{12}n)_2$Cubr$_4$: High-field magnetization and scaling near quantum criticality. *Phys. Rev. Lett.*, 86:5168–5171.

[156] White, S. R. and Chernyshev, A. L. (2007). Neél order in square and triangular lattice heisenberg models. *Phys. Rev. Lett.*, 99:127004.

[157] White, S. R., Noack, R. M., and Scalapino, D. J. (1994). Resonating valence bond theory of coupled heisenberg chains. *Phys. Rev. Lett.*, 73:886–889.

[158] Wiedenmann, A., Regnault, L., Burlet, P., Rossat-Mignod, J., Koundé, O., and Billerey, D. (1988). A neutron scattering investigation of the magnetic phase diagram of fei2. *Journal of magnetism and magnetic materials*, 74(1):7–21.

[159] Yaffe, L. G. (1982). Large N limits as classical mechanics. *Rev. Mod. Phys.*, 54:407–435.

[160] Yu, X., Mostovoy, M., Tokunaga, Y., Zhang, W., Kimoto, K., Matsui, Y., Kaneko, Y., Nagaosa, N., and Tokura, Y. (2012). Magnetic stripes and skyrmions with helicity reversals. *Proceedings of the National Academy of Sciences*, 109(23):8856–8860.

[161] Yu, X. Z., Kanazawa, N., Onose, Y., Kimoto, K., Zhang, W. Z., Ishiwata, S., Matsui, Y., and Tokura, Y. (2011). Near room-temperature formation of a skyrmion crystal in thin-films of the helimagnet FeGe. *Nature Materials*, 10(2):106.

[162] Yu, X. Z., Onose, Y., Kanazawa, N., Park, J. H., Han, J. H., Matsui, Y., Nagaosa, N., and Tokura, Y. (2010). Real-space observation of a two-dimensional skyrmion crystal. *Nature*, 465(7300):901.

[163] Yu, X. Z., Tokunaga, Y., Kaneko, Y., Zhang, W. Z., Kimoto, K., Matsui, Y., Taguchi, Y., and Tokura, Y. (2014). Biskyrmion states and their current-driven motion in a layered manganite. *Nature Communications*, 5(1):3198.

[164] Zapf, V., Jaime, M., and Batista, C. D. (2014). Bose-einstein condensation in quantum magnets. *Rev. Mod. Phys.*, 86:563–614.

[165] Zapf, V. S., Zocco, D., Hansen, B. R., Jaime, M., Harrison, N., Batista, C. D., Kenzelmann, M., Niedermayer, C., Lacerda, A., and Paduan-Filho, A. (2006). Bose-einstein condensation of $s = 1$ nickel spin degrees of freedom in $NiCl_2{-}4SC(NH_2)_2$. *Phys. Rev. Lett.*, 96:077204.

[166] Zener, C. (1951). Interaction between the d-shells in the transition metals. ii. ferromagnetic compounds of manganese with perovskite structure. *Physical Review*, 82(3):403.

[167] Zhang, H. and Batista, C. D. (2021). Classical spin dynamics based on SU(N) coherent states. *Phys. Rev. B*, 104:104409.

[168] Zhang, H., Wang, Z., Dahlbom, D., Barros, K., and Batista, C. D. (2022). Cp^2 skyrmions and skyrmion crystals in realistic quantum magnets.

[169] Zhang, S., Changlani, H. J., Plumb, K. W., Tchernyshyov, O., and Moessner, R. (2019a). Dynamical structure factor of the three-dimensional quantum spin liquid candidate $nacani_2f_7$. *Phys. Rev. Lett.*, 122:167203.

[170] Zhang, S.-S., Ghioldi, E. A., Kamiya, Y., Manuel, L. O., Trumper, A. E., and Batista, C. D. (2019b). Large-s limit of the large-n theory for the triangular antiferromagnet. *Phys. Rev. B*, 100:104431.

[171] Zhang, S.-S., Ishizuka, H., Zhang, H., Halász, G. B., and Batista, C. D. (2020). Real-space berry curvature of itinerant electron systems with spin-orbit interaction. *Phys. Rev. B*, 101:024420.

[172] Zhang, W.-M., Feng, D. H., and Gilmore, R. (1990). Coherent states: Theory and some applications. *Rev. Mod. Phys.*, 62:867–927.

[173] Zhang, Z., Wierschem, K., Yap, I., Kato, Y., Batista, C. D., and Sengupta, P. (2013). Phase diagram and magnetic excitations of anisotropic spin-one magnets. *Phys. Rev. B*, 87:174405.

[174] Zhitomirsky, M. E. and Chernyshev, A. L. (2013). Colloquium: Spontaneous magnon decays. *Rev. Mod. Phys.*, 85:219–242.

[175] Zvyagin, S., Wosnitza, J., Batista, C., Tsukamoto, M., Kawashima, N., Krzystek, J., Zapf, V., Jaime, M., Oliveira Jr, N., and Paduan-Filho, A. (2007). Magnetic excitations in the spin-1 anisotropic heisenberg antiferromagnetic chain system nicl 2- 4 sc (nh 2) 2. *Physical review letters*, 98(4):047205.

Appendices

A Representation of SU(3)

In this appendix, we present some discussions about the representation of SU(3).

A.1 Fundamental representation

In Gell-Mann's quark model, he introduced eight 3×3 traceless and Hermitian matrices as the generators of $\mathfrak{su}(3)$ in the fundamental representation [the $[1,0]$-representation, see Eq. (2.10)]:

$$\hat{\lambda}_1 = \begin{pmatrix} 0 & 1 & 0 \\ 1 & 0 & 0 \\ 0 & 0 & 0 \end{pmatrix}, \quad \hat{\lambda}_2 = \begin{pmatrix} 0 & -i & 0 \\ i & 0 & 0 \\ 0 & 0 & 0 \end{pmatrix}, \quad \hat{\lambda}_3 = \begin{pmatrix} 1 & 0 & 0 \\ 0 & -1 & 0 \\ 0 & 0 & 0 \end{pmatrix},$$

$$\hat{\lambda}_4 = \begin{pmatrix} 0 & 0 & 1 \\ 0 & 0 & 0 \\ 1 & 0 & 0 \end{pmatrix}, \quad \hat{\lambda}_5 = \begin{pmatrix} 0 & 0 & -i \\ 0 & 0 & 0 \\ i & 0 & 0 \end{pmatrix}, \quad \hat{\lambda}_6 = \begin{pmatrix} 0 & 0 & 0 \\ 0 & 0 & 1 \\ 0 & 1 & 0 \end{pmatrix},$$

$$\hat{\lambda}_7 = \begin{pmatrix} 0 & 0 & 0 \\ 0 & 0 & -i \\ 0 & i & 0 \end{pmatrix}, \quad \hat{\lambda}_8 = \frac{1}{\sqrt{3}} \begin{pmatrix} 1 & 0 & 0 \\ 0 & 1 & 0 \\ 0 & 0 & -2 \end{pmatrix}.$$

The eight matrices, which formed a basis for the quark model, are direct generalizations of the Pauli matrices of $\mathfrak{su}(2)$. Note that the Gell-Mann matrices are written in the basis of eigenstates of $\hat{S}^z$ of $S = 1$: $\{|+1\rangle, |-1\rangle, |0\rangle\}$. In this dissertation, to make connections with realistic spin Hamiltonians, we consider a change of basis and write the eight generators in

terms of SU(2) spin operators in the $S = 1$ representation:

$$\begin{pmatrix} \hat{T}^7 \\ \hat{T}^5 \\ \hat{T}^2 \end{pmatrix} = \begin{pmatrix} -\hat{S}^x \\ -\hat{S}^y \\ -\hat{S}^z \end{pmatrix}, \begin{pmatrix} \hat{T}^3 \\ \hat{T}^8 \\ \hat{T}^1 \\ \hat{T}^4 \\ \hat{T}^6 \end{pmatrix} = \begin{pmatrix} -\left(\hat{S}^x\right)^2 + \left(\hat{S}^y\right)^2 \\ \frac{1}{\sqrt{3}}\left[3\left(\hat{S}^z\right)^2 - \hat{\boldsymbol{S}}^2\right] \\ \hat{S}^x\hat{S}^y + \hat{S}^y\hat{S}^x \\ -\hat{S}^z\hat{S}^x - \hat{S}^x\hat{S}^z \\ \hat{S}^y\hat{S}^z + \hat{S}^z\hat{S}^y \end{pmatrix} \tag{1}$$

These generators satisfy the commutation relation:

$$[\hat{T}^\mu, \hat{T}^\nu] = i f_{\mu\nu\eta} \hat{T}^\eta, \tag{2}$$

where the structure constants are related to the Gell-Mann matrices through

$$f_{\eta\mu\nu} = -\frac{i}{2} \operatorname{Tr}\left(\hat{\lambda}_\eta \left[\hat{\lambda}_\mu, \hat{\lambda}_\nu\right]\right). \tag{3}$$

Interestingly, in the Cartesian basis

$$\left|x^1\right\rangle = \frac{i}{\sqrt{2}}(|+1\rangle - |-1\rangle), \left|x^2\right\rangle = \frac{1}{\sqrt{2}}(|+1\rangle + |-1\rangle), \left|x^3\right\rangle = -i|0\rangle, \tag{4}$$

the SU(3) generators given in Eq. (1), $\hat{T}^\mu_j$, are again represented by the Gell-Mann matrices:

$$\hat{T}^\mu = \left(\hat{\lambda}_\mu\right)_{ab} \left|x^a\right\rangle\left\langle x^b\right| \quad \mu = 1, 2, \cdots, 8. \tag{5}$$

A.2 Adjoint representation

The *adjoint representation* of a Lie algebra is a linear map from the Lie algebra to itself: $\mathrm{ad}_X(Y) : \mathfrak{g} \to \mathfrak{g}, X, Y \in \mathfrak{g}$:

$$\mathrm{ad}_{\hat{T}^\mu}(\hat{T}^\nu) \equiv [\hat{T}^\mu, \hat{T}^\nu] = i f_{\mu\nu\eta} \hat{T}^\eta. \tag{6}$$

Since the underlying vector space of representation is the Lie algebra itself, the dimension of the adjoint representation is equal to the dimension of the Lie algebra. In particular, the dimension of the adjoint representation of $\mathfrak{su}(3)$ is $3^2 - 1 = 8$, which has the same dimension as the $[1, 1]$-representation [see Eq. (2.10)]. The matrix form of the μ-th generator is written as

$$[\mathrm{ad}_{\hat{T}_\mu}]_{\eta\nu} = i f_{\mu\nu\eta}, \;\; \mu, \nu, \eta = 1 \cdots 8. \tag{7}$$

In summary, there are in total eight 8×8 matrices in the adjoint representation of $\mathfrak{su}(3)$.

B Symplectic structure on the manifold of coherent states

In this appendix, we will illustrate that the manifold of coherent states possesses a natural symplectic structure, which can be used to define the classical equations of motion, i.e. the *Poisson bracket*. To achieve this goal, we will first review some basic concepts from differential geometry. Then we will apply these concepts to the manifold of coherent states of the Heisenberg-Weyl group and SU(N). The discussions presented here can be sketchy for some mathematical-oriented readers. We guide those readers to refer to textbooks for differential geometry [69, 89], the standard textbook for mathematical methods in classical mechanics [12], and these research articles [159, 58, 62].

B.1 Some concepts from differential geometry

Manifold. Here we skip the formal definition of a manifold by saying that a manifold is a topological space (a set of points, along with a set of neighborhoods for each point, satisfying a set of axioms relating points and neighborhoods) that resembles (so-called homeomorphic to) Euclidean space near each point. Examples of manifold include a plane, a sphere, a torus, etc. A general manifold may have addition structures. For example, a Riemannian metric on a manifold allows distances and angles to be defined. As another example, a symplectic manifold with a symplectic structure serve as the phase spaces in the Hamiltonian formalism of classical mechanics, which is discussed in the next subsection of this appendix.

1-forms. Consider the Euclidean space $\mathbb{R}^n$. Let $\boldsymbol{v} \in \mathbb{R}^n$ be a vector in this space. A one-form is a linear map ω: $\mathbb{R}^n \to \mathbb{R}$, such that:

$$\omega(a_1\boldsymbol{v}_1 + a_2\boldsymbol{v}_2) = a_1\omega(\boldsymbol{v}_1) + a_2\omega(\boldsymbol{v}_2),\ \forall\ a_{1,2} \in \mathbb{R},\ \forall\ \boldsymbol{v}_{1,2} \in \mathbb{R}^n. \tag{8}$$

Note that the space of 1-forms on $\mathbb{R}^n$ is itself n-dimensional, which is called the dual space $[\mathbb{R}^n]^*$. In differential geometry, the basis of $\mathbb{R}^n$ is denoted with the subscript $\{e_i\}$, whereas that of the dual $[\mathbb{R}^n]^*$ is denoted with the superscript $\{e^j\}$ with $e^j(e_i) = \delta_i^j \in \mathbb{R}$, i.e. e^j acting on e_i gives us the Kronecker delta. [**Warning**: We distinguish the subscript/superscript only

in this appendix of this dissertation. In other chapters, we use subscripts/superscripts freely. This is because: 1. The dual space of $\mathbb{R}^n$ is itself. 2. In most cases, we work with a fixed basis of a vector space. 3. We are lazy.] Now we consider a concrete example of 1-form. Let $\boldsymbol{u} = u_i e^i \in [\mathbb{R}^n]^*$ and $\boldsymbol{v} = v^i e_i \in \mathbb{R}^n$ [v^i (contravariant) and u_i (covariant) is called the component of the vector with respect to the basis vector e_i and e^j, respectively]. Now let us act $\boldsymbol{u}$ on $\boldsymbol{v}$:

$$\boldsymbol{u}(\boldsymbol{v}) = u_i e^i(v^j e_j) = u_i v^j e^i(e_j) = u_i v^j \delta^i_j = u_j v^j. \tag{9}$$

If we identify $\boldsymbol{u}$ as a force in $\mathbb{R}^3$ (more precisely $[\mathbb{R}^3]^*$), its work on the displacement $\boldsymbol{v}$ is a 1-form acting on $\boldsymbol{v}$.

Differential 1-forms. Consider a differentiable function f that maps elements of an n-dimensional manifold $\mathcal{M}$ to $\mathbb{R}$: $f(\boldsymbol{v}) \in \mathbb{R}, \forall\ \boldsymbol{v} \in \mathcal{M}$. Note that f is not necessarily a 1-form (see an example below). However, we claim that the differentiation of f at $\boldsymbol{v}$, $df(\boldsymbol{v})$: $T(\mathcal{M}_{\boldsymbol{v}}) \to \mathbb{R}$, is a 1-form, where $T(\mathcal{M}_{\boldsymbol{v}})$ is the tangent space of $\mathcal{M}$ at $\boldsymbol{v}$, which is also n-dimensional and locally like $\mathbb{R}^n$. To see this, let us notice that the differentiation of a function at $\boldsymbol{v}$ is written as

$$df(\boldsymbol{v}) = \frac{\partial f}{\partial v^i} dv^i. \tag{10}$$

Given a fixed point $\boldsymbol{v} \in \mathcal{M}$, we have the information of $\frac{\partial f}{\partial v^i}$. As a result, we can identify the set $\{\frac{\partial f}{\partial v^i}\}$ as the basis of the tangent vectors and dv^i as the components. Therefore, we call $df(\boldsymbol{v})$ a *differential 1-form*, because it satisfies the definition of a 1-form. Finally, the differential 1-forms also form the dual space $[T(\mathcal{M}_{\boldsymbol{v}})]^*$, and is called the *cotangent space* at $\boldsymbol{v}$. As an example, consider a function f defined on $\mathbb{R}^2$:

$$f(x, y) = x^2 + y^2. \tag{11}$$

Apparently, f is not a 1-form because it is not a linear function. But at a particular point in $\mathbb{R}^2$, for instance $(x, y) = (1, 1)$, $df = 2dx + 2dy$ is a 1-form because it is now a linear function. Consider if $(dx, dy) = (2, 1)$, then $df = 6$, and if $(dx, dy) = (3, 2)$, then $df = 10$.

Bilinear maps. The motivation to define the bilinear map is to introduce the concept of tensors. A map ω: $\mathbb{R}^n \times \mathbb{R}^n \to \mathbb{R}$ is called a *bilinear map*, if it is linear on each slot, i.e.

$\forall\ \boldsymbol{v}_i \in \mathbb{R}^n, a_i \in \mathbb{R}$:

$$\begin{aligned}\omega(a_1\boldsymbol{v}_1 + a_2\boldsymbol{v}_2, \boldsymbol{v}_3) &= a_1\omega(\boldsymbol{v}_1, \boldsymbol{v}_2) + a_2\omega(\boldsymbol{v}_2, \boldsymbol{v}_3)\\ \omega(\boldsymbol{v}_1, a_1\boldsymbol{v}_2 + a_2\boldsymbol{v}_3) &= a_1\omega(\boldsymbol{v}_1, \boldsymbol{v}_2) + a_2\omega(\boldsymbol{v}_2, \boldsymbol{v}_3).\end{aligned} \tag{12}$$

Tensor products. The tensor product of two 1-forms ω_1 and ω_2 is defined as the bilinear map $\omega_1 \otimes \omega_2$ such that

$$(\omega_1 \otimes \omega_2)(\boldsymbol{v}_1, \boldsymbol{v}_2) = \omega_1(\boldsymbol{v}_1)\omega_2(\boldsymbol{v}_2). \tag{13}$$

In the component form, we have $\omega_1 = (\omega_1)_i e^i$, $\omega_2 = (\omega_2)_j e^j$, and let $\boldsymbol{v}_1 = 1e_k$ and $\boldsymbol{v}_2 = 1e_l$:

$$\begin{aligned}(\omega_1 \otimes \omega_2)(\boldsymbol{v}_1, \boldsymbol{v}_2) &= \omega_1(\boldsymbol{v}_1) + \omega_2(\boldsymbol{v}_2)\\ &= (\omega_1)_i e^i(e_k)(\omega_2)_j e^j(e_l)\\ &= (\omega_1)_i \delta^i_k (\omega_2)_j \delta^j_l\\ &= (\omega_1)_k (\omega_2)_l.\end{aligned} \tag{14}$$

Inner product and metric tensor. The *inner product* $g(\boldsymbol{v}_1, \boldsymbol{v}_2)$ is a bilinear map with the following additional properties:

- $g(\boldsymbol{v}_1, \boldsymbol{v}_2) = g(\boldsymbol{v}_2, \boldsymbol{v}_1)$,
- $g(\boldsymbol{v}, \boldsymbol{v}) \geq 0,\ \forall\ \boldsymbol{v}$,
- $g(\boldsymbol{v}, \boldsymbol{v}) = 0$ if and only if $\boldsymbol{v} = \boldsymbol{0}$.

Notice that the inner product can be viewed as a generalization of a dot product [a 1-form, see Eq. (9)], if we define

$$u_i = g_{ij} u^j. \tag{15}$$

The dot product is then written as

$$u^i v_j = g_{ij} u^i v^j, \tag{16}$$

where for this particular case, $g_{ij} = \delta_{ij}$. Furthermore, note that the action of the inner product gives the square of the norm of a vector $g(\boldsymbol{v}, \boldsymbol{v}) = |\boldsymbol{v}|^2$. Therefore, the inner product g is called a *metric tensor* and the "component" g_{ij} is called a *metric*. The inner product can also act on the product space of the tangent space of a manifold $\mathcal{M}$ at $\boldsymbol{v}$: $T(\mathcal{M}_{\boldsymbol{v}}) \times T(\mathcal{M}_{\boldsymbol{v}}) \to \mathbb{R}$, which gives us the infinitesimal distance on the manifold. For example, in the spherical coordinates of $\mathbb{R}^3$

$$ds^2 = dr \otimes dr + r d\theta \otimes d\theta + r^2 \sin^2\theta d\phi \otimes d\phi, \tag{17}$$

where the metric is written as

$$g_{ij} = \begin{pmatrix} 1 & 0 & 0 \\ 0 & r^2 & 0 \\ 0 & 0 & r^2 \sin^2\theta \end{pmatrix} \tag{18}$$

in the basis of $(dr, d\theta, d\phi)^T$.

2-forms. A *2-form* is a map $\omega : \mathbb{R}^n \times \mathbb{R}^n \to \mathbb{R}^n$, which is bilinear and antisymmetric:

$$\begin{aligned} \omega^2(a_1\boldsymbol{v}_1 + a_2\boldsymbol{v}_2, \boldsymbol{v}_3) &= a_1\omega(\boldsymbol{v}_1, \boldsymbol{v}) \\ \omega^2(\boldsymbol{v}_1, \boldsymbol{v}_2) &= -\omega(\boldsymbol{v}_2, \boldsymbol{v}_1) \\ \forall\ a_{1,2} \in \mathbb{R},\ \boldsymbol{v}_{1,2,3} &\in \mathbb{R}^n. \end{aligned} \tag{19}$$

Note that a 2-form is the *exterior (wedge) product* of two 1-forms: $\omega^2 = \omega_1 \wedge \omega_2$, where the exterior product is defined as

$$\omega_1 \wedge \omega_2 \equiv \omega_1 \otimes \omega_2 - \omega_2 \otimes \omega_1, \tag{20}$$

satisfying $\omega_1 \wedge \omega_2 = -\omega_2 \wedge \omega_1$, and $\omega \wedge \omega = 0$. The exterior product is closely related to the cross product in $\mathbb{R}^3$. Consider the exterior product of two 1-forms:

$$\boldsymbol{u} = u_i e^i,\ \boldsymbol{v} = v_j e^j,\ i = 1, \ldots 3. \tag{21}$$

$$\boldsymbol{u} \wedge \boldsymbol{v} = (u_1 v_2 - u_2 v_1) e^1 \wedge e^2 + (u_2 v_3 - u_3 v_2)(e^2 \wedge e^3) + (u_3 v_1 - u_1 v_3)(e^3 \wedge e^1). \tag{22}$$

The coefficients in the basis $\{e^1 \wedge e^2, e^2 \wedge e^3, e^3 \wedge e^1\}$ of the exterior space $\wedge^2[\mathbb{R}^3]$ are the same as those of the cross product of two vectors. However, it is important to notice that the exterior is a bi-vector, instead of a vector as the case of the cross product. Based on the definition Eq. (20), the value of a 2-form $\omega = \omega_1 \wedge \omega_2$ on two vectors in $\mathbb{R}^n$ is given by

$$\omega_1 \wedge \omega_2(\boldsymbol{v}_1, \boldsymbol{v}_2) = \begin{vmatrix} \omega_1(\boldsymbol{v}_1) & \omega_2(\boldsymbol{v}_1) \\ \omega_1(\boldsymbol{v}_2) & \omega_2(\boldsymbol{v}_2) \end{vmatrix}. \tag{23}$$

Let us view $\omega_{1,2}$ as the coordinate functions along the $\omega_{1,2}$ axes. This leads to the geometric interpretation of a 2-form: it is the oriented area of the image of the parallelogram with sides $\omega(\boldsymbol{v}_1)$ and $\omega(\boldsymbol{v}_2)$ on the ω_1-ω_2 plane [12]. In general, the value of a *k-form* acting on k vectors is given by

$$\omega_1 \wedge \omega_2 \ldots \wedge \omega_k(\boldsymbol{v}_1, \boldsymbol{v}_2, \ldots, \boldsymbol{v}_k) = \begin{vmatrix} \omega_1(\boldsymbol{v}_1) & \ldots & \omega_k(\boldsymbol{v}_1) \\ \vdots & & \vdots \\ \omega_1(\boldsymbol{v}_k) & \ldots & \omega_k(\boldsymbol{v}_k). \end{vmatrix} \tag{24}$$

A *differential 2-form* is a two-form: $T(\mathcal{M}_{\boldsymbol{v}}) \times T(\mathcal{M}_{\boldsymbol{v}}) \to \mathbb{R}$, where $T(\mathcal{M}_{\boldsymbol{v}})$ is the tangent space of a manifold at $\boldsymbol{v} \in \mathcal{M}$. Consider two differential 1-form on $\mathbb{R}^2$

$$\begin{aligned} df &= \frac{\partial f}{\partial x^1} dx^1 + \frac{\partial f}{\partial x^2} dx^2 \\ dg &= \frac{\partial g}{\partial x^1} dx^1 + \frac{\partial g}{\partial x^2} dx^2. \end{aligned} \tag{25}$$

Their exterior product leads to a differential 2-form:

$$\begin{aligned}(df \wedge dg) &= (\frac{\partial f}{\partial x^1}dx^1 + \frac{\partial f}{\partial x^2}dx^2) \wedge (\frac{\partial g}{\partial x^1}dx^1 + \frac{\partial g}{\partial x^2}dx^2) \\ &= (\frac{\partial f}{\partial x^1}\frac{\partial g}{\partial x^1}dx^1 \wedge dx^1) + (\frac{\partial f}{\partial x^2}\frac{\partial g}{\partial x^2}dx^2 \wedge dx^2) \\ &+ (\frac{\partial f}{\partial x^1}\frac{\partial g}{\partial x^2}dx^1 \wedge dx^2) + (\frac{\partial f}{\partial x^2}\frac{\partial g}{\partial x^1}dx^2 \wedge dx^1) \\ &= (\frac{\partial f}{\partial x^1}\frac{\partial g}{\partial x^2} - \frac{\partial f}{\partial x^2}\frac{\partial g}{\partial x^1})dx^1 \wedge dx^2 \\ &= \mathcal{J}(f, g; \boldsymbol{x})dx^1 \wedge dx^2, \end{aligned} \tag{26}$$

where $\mathcal{J}(f, g; \boldsymbol{x})$ is the Jacobian determinant. If we treat f and g as some non-linear maps: $\mathbb{R}^2 \to \mathbb{R}^2$, the value of the differential 2-form gives the oriented area of a distorted parallelogram, whose sides are the images of the maps.

Exterior derivatives and integrations of differential forms. Consider a differential k-form ω^k on the manifold $\mathcal{M}$

$$\omega^k = a_{i_1,i_2,\ldots,i_k}dx^{i_i} \wedge dx^{i_2} \ldots \wedge dx^{i_k}. \tag{27}$$

The exterior derivative of ω^k is a $k+1$ form [12]:

$$d\omega^k = da_{i_1,i_2,\ldots,i_k} \wedge dx^{i_i} \wedge dx^{i_2} \ldots \wedge dx^{i_k}. \tag{28}$$

Note that $d\omega^k$ generalizes the concepts of a curl operator, a divergence operator, etc. Recall that the curl of a vector field is introduced when considering the integration of the vector field along a closed loop, whose value is equal to the integration of the curl of the vector field over the surface enclosed by the loop, known as the Stokes theorem. Whereas the divergence of a vector field is introduced when considering the integration of the vector field over a closed surface, whose value is equal to the integration of the divergence of the vector field over the volume enclosed by the surface, known as the Gauss theorem. Similarly, $d\omega^k$ and ω^k are related to each other through the *generalized Stokes theorem*:

$$\int_{\partial\Sigma} \omega^k = \int_{\Sigma} d\omega^k, \tag{29}$$

where Σ is called a $k+1$ chain on the manifold $\mathcal{M}$ [12]. Finally, we provide a proof for Eq. (28) by considering a 1-form $\omega = a(x_1, x_2)dx^1$ on the $\mathbb{R}^2$-plane, which is the tangent space of some manifold $\mathcal{M}$. Let us compute the loop integral of $\omega(\boldsymbol{v}(t))$, where $\boldsymbol{v}(t) \in \mathbb{R}^2$, and $t \in [0, 1]$ is a continuous "time" variable such that $\boldsymbol{v}(0) = \boldsymbol{v}(1)$. Without loss of generality, we choose the loop to be a parallelogram with sides $\boldsymbol{\eta}$ and $\boldsymbol{\chi}$. The loop integral is given by

$$\begin{aligned} I(\boldsymbol{\eta}, \boldsymbol{\chi}) &= \int_0^1 dt \left\{ [a(\boldsymbol{\eta}t) - a(\boldsymbol{\eta}t + \boldsymbol{\chi})]\, dx^1(\boldsymbol{\eta}) - [a(\boldsymbol{\chi}t) - a(\boldsymbol{\chi}t + \boldsymbol{\eta})] dx^1(\boldsymbol{\chi}) \right\} \\ &= \int_0^1 dt \left\{ [a(\boldsymbol{\eta}t) - a(\boldsymbol{\eta}t + \boldsymbol{\chi})]\, \eta^1 - [a(\boldsymbol{\chi}t) - a(\boldsymbol{\chi}t + \boldsymbol{\eta})] \chi^1 \right\}, \end{aligned} \tag{30}$$

where η^1 and χ^1 are the components of $\boldsymbol{\eta}$ and $\boldsymbol{\chi}$, respectively. At the same time,

$$a(\boldsymbol{\eta}t + \boldsymbol{\chi}) - a(\boldsymbol{\eta}t) = \frac{\partial a}{\partial x^1}\chi^1 + \frac{\partial a}{\partial x^2}\chi^2 + \mathcal{O}[\boldsymbol{\eta}^2, \boldsymbol{\chi}^2], \tag{31}$$

and

$$a(\boldsymbol{\chi}t + \boldsymbol{\eta}) - a(\boldsymbol{\chi}t) = \frac{\partial a}{\partial x^1}\eta^1 + \frac{\partial a}{\partial x^2}\eta^2 + \mathcal{O}[\boldsymbol{\eta}^2, \boldsymbol{\chi}^2]. \tag{32}$$

As a result,

$$I(\boldsymbol{\eta}, \boldsymbol{\chi}) = \int_{\partial\Sigma} \omega = \frac{\partial a}{\partial x^2}(\chi^1\eta^2 - \chi^2\eta^1) + \mathcal{O}[\boldsymbol{\eta}^2, \boldsymbol{\chi}^2]. \tag{33}$$

By using Eq. (28), we have

$$\begin{aligned} d\omega &= da(x_1, x_2) \wedge dx^1 \\ &= \left(\frac{\partial a}{\partial x^1} dx^1 + \frac{\partial a}{\partial x^2} dx^2 \right) \wedge dx^1 \\ &= \frac{\partial a}{\partial x^1} dx^1 \wedge dx^1 + \frac{\partial a}{\partial x^2} dx^2 \wedge dx^2 \\ &= \frac{\partial a}{\partial x^2} dx^2 \wedge dx^1. \end{aligned} \tag{34}$$

The corresponding integral $d\omega(\boldsymbol{\eta}, \boldsymbol{\chi})$ over the oriented surface enclosed by $\boldsymbol{\eta}$ and $\boldsymbol{\chi}$ is then given by

$$\int_\Sigma d\omega = \int_\Sigma \frac{\partial a}{\partial x^2} dx^2 \wedge dx^1(\boldsymbol{\eta}, \boldsymbol{\chi}) = \frac{\partial a}{\partial x^2}(\chi^1\eta^2 - \chi^2\eta^1) + \mathcal{O}[\boldsymbol{\eta}^2, \boldsymbol{\chi}^2]. \tag{35}$$

This concludes the proof for Eq. (28).

B.2 Classical phase space

Classical mechanics for point particles

In the Hamiltonian formalism of the classical mechanics, the state of an n-particle system lives in a $2n$-dimensional phase space (a manifold $\mathcal{M}^{2n}$) with coordinates $\boldsymbol{q} = (q^1, q^2, \ldots, q^n)$ (canonical positions) and $\boldsymbol{p} = (p^1, p^2, \ldots, p^n)$ (canonical momenta). A function $f(\boldsymbol{q}, \boldsymbol{p})$ defined on the classical phase space is a map $\mathcal{M}^{2n} \to \mathbb{R}$. If f has no explicit time dependence, its time evolution is dictated by the Hamiltonian equation of motion

$$\frac{df(\boldsymbol{q},\boldsymbol{p})}{dt} = \sum_i \left(\frac{\partial f}{\partial q^i}\frac{\partial h}{\partial p^i} - \frac{\partial f}{\partial p^i}\frac{\partial h}{\partial q^i} \right) \equiv \{f(\boldsymbol{p},\boldsymbol{q}), h(\boldsymbol{p},\boldsymbol{q})\}_{PB}, \tag{36}$$

where $h(\boldsymbol{p}, \boldsymbol{q})$ is the classical Hamiltonian function of the system and $\{\cdot,\cdot\}$ is the so-called *Poisson bracket*. Based on the discussions in the previous section, given a particular point $\boldsymbol{v}_0 = (\boldsymbol{q}_0, \boldsymbol{p}_0)$ in phase space, df and dh are differential 1-forms acting on $T(\mathcal{M}^{2n}_{\boldsymbol{v}_0})$, i.e. the tangent space of $\mathcal{M}_{2n}$ at $\boldsymbol{v}_0$. Correspondingly, $\partial f(h)/\partial q(p)^i \in T(\mathcal{M}^{2n}_{\boldsymbol{v}_0})$ are tangent vectors at $\boldsymbol{v}_0$. The Poisson bracket in Eq. (36), which is antisymmetric, can then be viewed as the action of a differential 2-form on $T(\mathcal{M}^{2n}_{\boldsymbol{v}_0}) \otimes T(\mathcal{M}^{2n}_{\boldsymbol{v}_0})$, where the 2-form is written as

$$\omega = \omega_{ij} dq^i \wedge dp^j, \quad \omega_{ij} = \delta_{ij}. \tag{37}$$

Note that the differential 2-form given in Eq. (37) satisfies the following properties: 1. The exterior derivative [see Eq. (28) for definition] $d\omega = d\delta_{ij} \wedge dq^i \wedge dp^j = 0$. The form ω is then called *closed* because according to the Stokes theorem Eq. (29), the integration of ω over a closed surface also vanishes. 2. The form is *non-degenerate*, i.e. if there $\exists\ \boldsymbol{v}_1 \in T(\mathcal{M}^{2n}_{\boldsymbol{v}_0})$, $\omega(\boldsymbol{v}_1, \boldsymbol{v}_2) = 0,\ \forall\ \boldsymbol{v}_2 \in T(\mathcal{M}^{2n}_{\boldsymbol{v}_0})$, then $\boldsymbol{v}_1 = \boldsymbol{0}$. A differential 2-form satisfies these two properties is called *symplectic* and the manifold with such a 2-form is said to have a symplectic structure.

Manifold of coherent states

We have seen that the Poisson bracket of point particles is closely related to the symplectic structure on the classical phase space. Now we will see that the manifold of coherent states

of a Lie group inherently possesses a symplectic structure, which provides a natural platform to define the classical mechanics for a general system, e.g. a spin system. (write later, say about when it is difficult to define the classical limit, then we can use the coherent states)

Consider a Lie group G. The Lie algebra $\mathfrak{g}$ of G is a vector space. Correspondingly, the dual vector space $\mathfrak{g}^*$ consists of 1-forms of $\mathfrak{g}$. The dot product [see Eq. (9)] defines the action of 1-forms on the vectors

$$\langle u, v\rangle \equiv u_i v^i, \quad u \in \mathfrak{g}^*,\ v \in \mathfrak{g}, \tag{38}$$

where u_i and v^i are the components of the 1-form and vectors, respectively. To discuss the coherent states, we first fix the representation for G. One natural choice for the space of representation [see Chapter 2.1] is the Lie algebra $\mathfrak{g}$, known as the *adjoint representation*. The representation is given by

$$\mathrm{Ad}_g(\lambda) \equiv g\lambda g^{-1}, \quad g \in G,\ \lambda \in \mathfrak{g}. \tag{39}$$

Correspondingly, the adjoint representation of a Lie algebra element [see the example for $\mathfrak{su}(3)$ in Appendix A] is given by

$$\mathrm{ad}_\lambda(\eta) \equiv i[\lambda, \eta], \quad \eta, \lambda \in \mathfrak{g} \tag{40}$$

where the above result is obtained by writing $g = e^{-it\eta}$ in Eq. (39) and taking the derivative at $t = 0$ afterwards. This is justified because $\mathfrak{g}$ consists of tangent vectors of G at the identity element. In the same way, we introduce the *coadjoint representation*, whose space of representation is $\mathfrak{g}^*$ with $\mathrm{Ad}^*_g = [\mathrm{Ad}_{g^{-1}}]^*$. It is defined such that the structure of the dot product is preserved

$$\langle \mathrm{Ad}^*_g u, \mathrm{Ad}_g v\rangle = \langle u, \mathrm{Ad}_{g^{-1}}\mathrm{Ad}_g v\rangle = \langle u, v\rangle. \tag{41}$$

By using Kirillov's orbit method [cite], the *coadjoint orbit* Γ is generated by the action of Ad^*_g to a reference element $u_0 \in \mathfrak{g}^*$:

$$\Gamma = \{\mathrm{Ad}^*_g u_0 \mid g \in G/H\}, \tag{42}$$

where H is the isotropic subgroup such that $\forall\ h \in H$, $\mathrm{Ad}^*_h u_0 = u_0$. Note that Γ is indeed the manifold of coherent states, where a coherent state is now associated with a point on Γ.

Based on Eq. (39), the tangent space of Γ at a point u is a subspace of $\mathfrak{g}^*$:

$$\begin{aligned} T(\Gamma_u) = \{\tilde{u} \in \mathfrak{g}^* \mid \langle \tilde{u}, w\rangle &= \langle \mathrm{ad}^*_v u, w\rangle \\ &= -\langle u, \mathrm{ad}_v w\rangle = -i\langle u, [v, w]\rangle,\ \text{for some } v \in \mathfrak{g}/\mathfrak{h}_u, w \in \mathfrak{g}\}, \end{aligned} \tag{43}$$

where $\tilde{u}$ represents the tangent vectors and

$$\mathfrak{h}_u = \{v \in \mathfrak{g} | \langle u, [v, w]\rangle = 0,\ u \in \mathfrak{g}^*, \text{and } \forall\ w \in \mathfrak{g}\} \tag{44}$$

is the Lie algebra of the isotropic group H at u. This tells us that the dot product between the tangent vector $\tilde{u} \in \mathfrak{g}^*$ and the 1-form $w \in \mathfrak{g}$ is equal to some commutator of w with another element v of $\mathfrak{g}/\mathfrak{h}_u$. The one-to-one map between $\tilde{u}$ and a commutator naturally leads to a differential 2-form acting on $T(\Gamma_u) \otimes T(\Gamma_u)$:

$$\omega(\mathrm{ad}^*_v u, \mathrm{ad}^*_w u) = \langle u, [v, w]\rangle \quad u \in \mathfrak{g}^*,\ v, w \in \mathfrak{g}/\mathfrak{h}_u, \tag{45}$$

or in component form $\omega(\mathrm{ad}^*_v u, \mathrm{ad}^*_w u) = i u^i v_j w_k c_i^{jk}$, where c_i^{jk} is the structure constant of the Lie algebra $\mathfrak{g}$. ω is an obvious 2-form because $\omega(\mathrm{ad}^*_v u, \mathrm{ad}^*_w u) = -\omega(\mathrm{ad}^*_w u, \mathrm{ad}^*_v u)$. Furthermore, ω is a *symplectic* 2-form because: 1. It is closed as ω only depends on the structure constant of the Lie algebra with $dc_i^{jk} = 0$. 2. It is non-degenerate as $v, w \in \mathfrak{g}/\mathfrak{h}_u$ and Eq. (44) implies that if $\omega(\mathrm{ad}^*_v u, \mathrm{ad}^*_w u) = 0,\ \forall\ \mathrm{ad}^*_w u \in \mathfrak{g}/\mathfrak{h}_u$, then $\mathrm{ad}^*_v u = 0$. In summary, the symplectic structure on the coadjoint orbit (manifold of coherent states) is inherited from the Lie algebra.

Given the symplectic structure on Γ, we are ready to define the Poisson bracket. Consider two functions $f(\eta)$ and $g(\eta)$ defined on Γ. At a particular point η_0 of Γ, the tangent vectors are $[\partial f(\eta)/\partial \eta^i]|_{\eta=\eta_0}$ and $[\partial g(\eta)/\partial \eta^i]|_{\eta=\eta_0}$, and the Poisson bracket is simply the action of the symplectic form introduced above on the tangent vectors

$$\{f(\eta), g(\eta)\}_{PB} \equiv \frac{\partial f(\eta)}{\partial \eta^j} \frac{\partial g(\eta)}{\partial \eta^k} c_i^{jk} \eta^i. \tag{46}$$

In chapter 2, we saw that the manifold of coherent states of point particles is the coadjoint orbit of the Heisenberg-Weyl group H_3. The corresponding Lie algebra h_3 is spanned by the generators $\eta^1 = q$, $\eta^2 = p$, and $\eta^3 = 1$, with the commutation relations $[\eta^1, \eta^2] = i\hbar\delta^{jk}\eta^3$, $[\eta^1, \eta^3] = [\eta^2, \eta^3] = 0$, where we have dropped the "particle" label and assuming they are identical. Based on Eq. (46), the Poisson bracket is then given By

$$\{f(\eta), g(\eta)\}_{PB} = \left[\frac{\partial f}{\partial \eta^1}\frac{\partial g}{\partial \eta^2} - \frac{\partial f}{\partial \eta^2}\frac{\partial g}{\partial \eta^1}\right]\eta^3, \tag{47}$$

where the factor $\hbar$ is dropped as an overall factor to follow the traditional definition for a Poisson bracket. We have again recovered Eq. (36) by using the natural symplectic structure on the coadjoint orbit of H_3 inherited from h_3.

In general, one can define the classical mechanics on the coadjoint orbit of an arbitrary Lie group. In this dissertation, we focus on the coadjoint orbit of the group H_3 and the SU(N) group. These two examples of coadjoint orbits fall into the category of the *Kähler manifold*, which has a complex structure and Riemannian structure in addition to the symplectic structure. The symplectic 2-form on a Kähler manifold takes the form

$$\omega = g_{jk} d\alpha^j \wedge d\bar{\alpha}^k, \tag{48}$$

where $\alpha^j, \bar{\alpha}^k$ are some complex coordinates and g_{jk} is the metric tensor of the coadjoint orbit. To see that g_{jk} is indeed a metric tensor, we consider $\Gamma(H_3)$, which is isomorphic to $\mathbb{C}$ with $\alpha = q + ip$ and $\bar{\alpha} = q - ip$. The "distance" between two coherent states on $\Gamma(H_3)$ is defined as

$$s(\alpha, \alpha') = -\ln |\langle\alpha|\alpha'\rangle|^2, \tag{49}$$

where the expression of $|\langle\alpha|\alpha'\rangle|^2$ is given in Eq. (2.15). Note that $0 < |\langle\alpha|\alpha'\rangle|^2 < 1$ implies that $s(\alpha, \alpha')$ is positive definite for $\alpha \neq \alpha'$. Finally, as expected, the "distance" is zero for $\alpha = \alpha'$: $s(\alpha, \alpha) = -\ln\langle\alpha|\alpha\rangle = -\ln 1 = 0$. Then by definition and using Eq. (2.15), the metric tensor is given by

$$g_{\alpha\alpha'} = \frac{\partial s(\alpha, \alpha')}{\partial\bar{\alpha}\partial\alpha'} = -\frac{1}{2\hbar}. \tag{50}$$

Consequently,

$$\omega = -\frac{1}{2\hbar} d\alpha \wedge d\bar{\alpha} = -\frac{1}{2\hbar} d(q+ip) \wedge d(q-ip) = \frac{i}{\hbar} dq \wedge dp, \tag{51}$$

where we recover the symplectic form for a point particle if we drop the overall factor $i/\hbar$. Similarly, for $\Gamma(\mathrm{SU}(N)) \cong \mathrm{CP}^{N-1}$, the "distance" function is given by

$$s(\{\alpha^j, \bar{\alpha}^j\}) = \ln(1 + \alpha^1\bar{\alpha}^1 + \ldots \alpha^{N-1}\bar{\alpha}^{N-1}), \tag{52}$$

and

$$g_{jk} = \frac{\partial \ln s}{\partial \bar{\alpha}^j \partial \alpha^k} \tag{53}$$

is the so-called *Fubini-Study* metric of CP^{N-1}. The corresponding Poisson bracket takes the form

$$\{f, g\} = g_{jk} \left(\frac{\partial f}{\partial \bar{\alpha}^j} \frac{\partial g}{\partial \alpha^k} - \frac{\partial f}{\partial \alpha^k} \frac{\partial g}{\partial \bar{\alpha}^j} \right). \tag{54}$$

C Classical to quantum correspondence

In this appendix, we use a square lattice antiferromagnet (SL-AFM) to illustrate the idea of classical to quantum correspondence for the dynamical spin structure factor $S(\boldsymbol{q}, \omega)$. Let us assume that the SL-AFM is described by the isotropic Heisenberg Hamiltonian

$$\hat{\mathcal{H}} = J \sum_{\langle i,j \rangle} \hat{\boldsymbol{S}}_i \cdot \hat{\boldsymbol{S}}_j, \tag{55}$$

where $J > 0$ is the exchange constant for the nearest neighbor pairs $\langle i, j \rangle$ of the square lattice. The system develops a long-range AFM order at $T = 0$ [see Fig. 1].

To simplify the calculation, with loss of generality, we choose the local quantization axis to be along the z-axis. This is justified because of the SU(2) invariance of the Heisenberg model Eq. (55)—the ordered moments pointing to different directions have the degenerate energy. To further simplify the calculation, we introduce a twisted reference frame, where the AFM ordering becomes a FM one. This can be done by rotating the spin reference frame of one of the two sublattices of the square lattice by an angle π along the z direction: $\hat{S}^x_{\boldsymbol{r}} \to \hat{S}^x_{\boldsymbol{r}}$ and $\hat{S}^{y,z}_{\boldsymbol{r}} \to -\hat{S}^{y,z}_{\boldsymbol{r}}$. Correspondingly, the Hamiltonian Eq. (55) takes the following form in the twisted frame

$$\tilde{\hat{\mathcal{H}}} = \sum_{\langle i,j \rangle} \left(\hat{S}^x_i \hat{S}^x_y - \hat{S}^x_i \hat{S}^x_y - \hat{S}^z_i \hat{S}^z_y \right). \tag{56}$$

We will first solve the problem quantum mechanically. By using Eq. (4.1) [1], and expand up to quadratic order in boson operators, we have

$$\mathcal{H}^{(2)} = S \sum_{\langle i,j \rangle} \left[b_i b_j + b^\dagger_i b^\dagger_j + b^\dagger_i b_i + b^\dagger_j b_j \right]. \tag{57}$$

We introduce the Fourier transform on the boson operator

$$b_i = \frac{1}{\sqrt{N}} \sum_{\boldsymbol{k}} e^{i\boldsymbol{k}\cdot\boldsymbol{r}} b_{\boldsymbol{k}}, \tag{58}$$

[1] Note that $\tilde{\hat{S}}^\mu = \hat{S}^\mu$ because we have chosen the quantization axis to be along the z axis

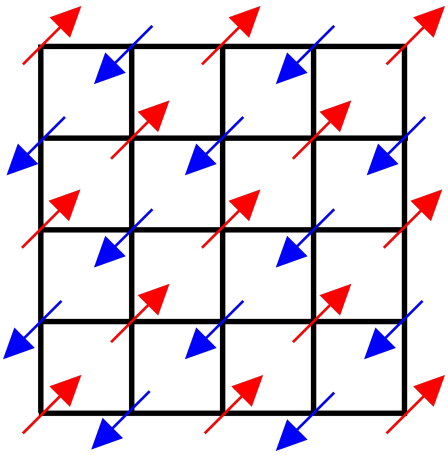


Figure 1: The AFM order on a square lattice at $T = 0$

where N is the number of sites. The quadratic Hamiltonian is then written as

$$\mathcal{H}^{(2)} = \sum_{\boldsymbol{k}} \left[A_{\boldsymbol{k}} b^\dagger_{\boldsymbol{k}} b_{\boldsymbol{k}} - \frac{1}{2} B_{\boldsymbol{k}} (b^\dagger_{\boldsymbol{k}} b^\dagger_{-\boldsymbol{k}} + b_{-\boldsymbol{k}} b_{\boldsymbol{k}}) \right], \tag{59}$$

where

$$A_{\boldsymbol{k}} = 4JS, \quad B_{\boldsymbol{k}} = -4JS\gamma_{\boldsymbol{k}}, \quad \gamma_{\boldsymbol{k}} = \frac{1}{4} \sum_{\boldsymbol{\delta}} e^{i\boldsymbol{k}\cdot\boldsymbol{\delta}} = \frac{1}{2} (\cos k_x + \cos k_y). \tag{60}$$

$\mathcal{H}^{(2)}$ is diagonalized by the standard Bogoliubov transform

$$b_{\boldsymbol{k}} = u_{\boldsymbol{k}} \beta_{\boldsymbol{k}} + v_{\boldsymbol{k}} \beta^\dagger_{-\boldsymbol{k}} \tag{61}$$

under conditions $u^2_{\boldsymbol{k}} - v^2_{\boldsymbol{k}} = 1$ and

$$u^2_{\boldsymbol{k}} + v^2_{\boldsymbol{k}} = \frac{A_{\boldsymbol{k}}}{\sqrt{A^2_{\boldsymbol{k}} - B^2_{\boldsymbol{k}}}}, \quad 2u_{\boldsymbol{k}} v_{\boldsymbol{k}} = \frac{B_{\boldsymbol{k}}}{\sqrt{A^2_{\boldsymbol{k}} - B^2_{\boldsymbol{k}}}}. \tag{62}$$

As a result, the linear spin-wave Hamiltonian takes the following form:

$$\mathcal{H}^{(0)} + \mathcal{H}^{(2)} = -2JS(S+1)N + \sum_{\boldsymbol{k}} \omega_{\boldsymbol{k}} \left(\beta^\dagger_{\boldsymbol{k}} \beta_{\boldsymbol{k}} + \frac{1}{2} \right), \tag{63}$$

where the spin-wave dispersion relation is given by

$$\omega_{\boldsymbol{k}} = \sqrt{A^2_{\boldsymbol{k}} - B^2_{\boldsymbol{k}}} = 4JS\sqrt{1 - \gamma^2_{\boldsymbol{k}}}. \tag{64}$$

Now we compute the dynamical spin structure factor $\mathcal{S}^{\mu\mu}(\boldsymbol{q}, \omega)$ [see Eq. (4.22) for definition] in the harmonic approximation. The spin operators in the lab reference frame are related to those in the twisted frame through

$$\hat{S}^x_{\boldsymbol{r}} \to \hat{S}^x_{\boldsymbol{r}} \quad \hat{S}^y_{\boldsymbol{r}} \to e^{i\boldsymbol{Q}\cdot\boldsymbol{r}} \hat{S}^y_{\boldsymbol{r}} \quad \hat{S}^z_{\boldsymbol{r}} \to e^{i\boldsymbol{Q}\cdot\boldsymbol{r}} \hat{S}^z_{\boldsymbol{r}}, \tag{65}$$

where $\boldsymbol{Q} = (\pi, \pi)$. By following the procedures discussed in Sec. 4.3.4, we have

$$\mathcal{S}^{xx}(\boldsymbol{q}, \omega) = \mathcal{S}^{yy}(\boldsymbol{q}, \omega) = \frac{S}{2}(u_{\boldsymbol{q}} + v_{\boldsymbol{q}})^2 \delta(\omega - \omega_{\boldsymbol{q}}) \tag{66}$$

$$\mathcal{S}^{zz}(\boldsymbol{q}, \omega) = \delta_{\boldsymbol{q},\boldsymbol{Q}} \delta_{\omega,0} \left[S^2 - 2S \frac{1}{N} \sum_{\boldsymbol{k}} v_{\boldsymbol{k}}^2 \right]. \tag{67}$$

Let us now consider the linearized L-L dynamics for the same problem. After taking classical limit of Eq. (56) based on SU(2) coherent states and using Eq. (2.50), we have

$$\begin{aligned}
\frac{d\tilde{S}_i^x}{dt} &= J \sum_{\langle,j\rangle} \left(\tilde{S}_i^y \tilde{S}_j^z - \tilde{S}_i^z \tilde{S}_j^y \right) \\
\frac{d\tilde{S}_i^y}{dt} &= J \sum_{\langle,j\rangle} \left(-\tilde{S}_i^z \tilde{S}_j^x - \tilde{S}_i^x \tilde{S}_j^z \right) \\
\frac{d\tilde{S}_i^z}{dt} &= J \sum_{\langle,j\rangle} \left(\tilde{S}_i^x \tilde{S}_j^y + \tilde{S}_i^y \tilde{S}_j^x \right).
\end{aligned} \tag{68}$$

We now propose the following mean-field ansatz

$$\tilde{S}_i^\mu(t) = \langle \tilde{S}_i^\mu \rangle + \delta \tilde{S}_i^\mu(t). \tag{69}$$

In the twisted frame, by choosing the quantization axis along the z direction, we have

$$\langle \tilde{S}_i^{x,y} \rangle = 0, \quad \langle \tilde{S}_i^z \rangle = S. \tag{70}$$

After plugging Eq. (69) into Eq. (68) and keeping terms to the linear order in $\delta \tilde{S}_i^\mu$, we obtain the linearized L-L equations

$$\begin{aligned}
\frac{d\delta\tilde{S}_i^x}{dt} &= J \sum_{\langle,j\rangle} \left(\delta\tilde{S}_i^y \langle \tilde{S}_j^z \rangle - \langle \tilde{S}_i^z \rangle \delta\tilde{S}_j^y \right) \\
\frac{d\delta\tilde{S}_i^y}{dt} &= J \sum_{\langle,j\rangle} \left(-\langle \tilde{S}_i^z \rangle \delta\tilde{S}_j^x - \delta\tilde{S}_i^x \langle \tilde{S}_j^z \rangle \right) \\
\frac{d\delta\tilde{S}_i^z}{dt} &= 0.
\end{aligned} \tag{71}$$

To make connections with the SWT calculation, we note that the fluctuations $\delta\tilde{S}^{\mu}$ are parameterized by two real independent numbers:

$$\delta\tilde{S}_i^x = \sqrt{S}x_i \quad \delta\tilde{S}_i^y = \sqrt{S}y_i \quad \delta\tilde{S}_i^z = \sqrt{S^2 - S(x_i^2 + y_i^2)} \simeq S - \frac{1}{2}(x_i^2 + y_i^2), \tag{72}$$

where we assume that the fluctuations away from the ordered moment are small. By taking the classical limit and using the mean-field ansatz (69), the Hamiltonian Eq. (56) is written as

$$\tilde{\mathcal{H}} = \tilde{\mathcal{H}}^{\mathrm{LLLD}} - NS^2 = S\sum_{\langle i,j\rangle}(z_i z_j + z_i^* z_j^* + z_i^* z_i + z_j^* z_j) - NS^2, \tag{73}$$

where $z_i = 1/\sqrt{2}(x_i + iy_i)$ and $\tilde{H}$ is the corresponding Hamiltonian of the linearized equations of motion (71). Notice that $\mathcal{H}^{\mathrm{LLLD}}$ can be obtained from $\hat{\mathcal{H}}^{(2)}$ (57) by replacing $\tilde{b}_i$ ($\tilde{b}_i^{\dagger}$) with z_i (z_i^*). As a result, after the Fourier transform and Bogoliubov transform on the variable $z_i(z_i^*)$, we have

$$\mathcal{H}^{\mathrm{LLLD}} = \sum_{\boldsymbol{k}} \omega_{\boldsymbol{k}} \tilde{z}_{\boldsymbol{k}}^* \tilde{z}_{\boldsymbol{k}}, \tag{74}$$

where $\omega_{\boldsymbol{k}}$ is identical to Eq. (64) and

$$z_{\boldsymbol{k}} = u_{\boldsymbol{k}} \tilde{z}_{\boldsymbol{k}} + v_{\boldsymbol{k}} \tilde{z}_{-\boldsymbol{k}}^*, \tag{75}$$

where $\tilde{z}_{\boldsymbol{k}}$ corresponds to the amplitude of the "normal mode" $\omega_{\boldsymbol{k}}$.

Now we compute the dynamical spin structure factor in the classical limit with the linearized dynamics. We note that

$$\begin{aligned}
\mathcal{S}^{xx}(\boldsymbol{q},\omega) &= \langle \delta S^x_{\boldsymbol{q},\omega} \delta S^x_{-\boldsymbol{q},-\omega}\rangle \\
&= \frac{S}{2}\delta(\omega - \omega_{\boldsymbol{q}})(u_{\boldsymbol{q}} + v_{\boldsymbol{q}})^2 \frac{\int d\tilde{z}_{\boldsymbol{q}} d\tilde{z}_{\boldsymbol{q}}^* (\tilde{z}_{\boldsymbol{q}}^* \tilde{z}_{\boldsymbol{q}}) e^{-\beta\tilde{\mathcal{H}}^{\mathrm{LLLD}}}}{\int d\tilde{z}_{\boldsymbol{q}} d\tilde{z}_{\boldsymbol{q}}^* e^{-\beta\tilde{\mathcal{H}}^{\mathrm{LLLD}}}} \\
&= \frac{S}{2}\delta(\omega - \omega_{\boldsymbol{q}}) \frac{1}{\beta\omega_{\boldsymbol{q}}}(u_{\boldsymbol{q}} + v_{\boldsymbol{q}})^2 = \mathcal{S}^{yy}(\boldsymbol{q},\omega),
\end{aligned} \tag{76}$$

and

$$\begin{aligned}\mathcal{S}^{zz}(\boldsymbol{q},\omega) &= \langle \delta S^x_{\boldsymbol{q},\omega} \delta S^x_{-\boldsymbol{q},-\omega} \rangle \\ &= \delta_{\boldsymbol{q},\boldsymbol{0}} \delta_{\omega,0} \left(S^2 - 2S \frac{1}{N} \sum_{\boldsymbol{k}} v^2_{\boldsymbol{k}} \langle \tilde{z}^*_{\boldsymbol{k}} \tilde{z}_{\boldsymbol{k}} \rangle \right) \\ &= \delta_{\boldsymbol{q},\boldsymbol{0}} \delta_{\omega,0} \left(S^2 - 2S \frac{1}{N} \sum_{\boldsymbol{k}} \frac{v^2_{\boldsymbol{k}}}{\beta \omega_{\boldsymbol{k}}} \right). \end{aligned} \tag{77}$$

Here we have explicitly demonstrated that the quantum mechanical result for the transverse spin structure factor (66) at $T = 0$ can be obtained after multiplying the classical result (76) by $\beta\omega$. This is the classical to quantum correspondence relation we mentioned in many places of this dissertation.

D Miscellaneous calculations for the SU(N) spin wave theory

D.1 Bogoliubov transformation for boson operators

The quadratic (generalized linear spin wave) Hamiltonian obtained from the $1/M$-expansion [see Eq. (4.9)] takes a general form in terms of the $N-1$ uncondensed SBs in momentum space:

$$\hat{\mathcal{H}}^{(2)} = \sum_{\boldsymbol{q}} \vec{b}^{\dagger}_{\boldsymbol{q}} \mathcal{H}^{(2)}(\boldsymbol{q}) \vec{b}_{\boldsymbol{q}}, \tag{78}$$

where $\vec{b}_{\boldsymbol{q}} = (\tilde{b}_{\boldsymbol{q},(m,\alpha)}, \tilde{b}^{\dagger}_{-\boldsymbol{q},(m,\alpha)})^T$ is a $2N_s/N_u(N-1)$-component vector, and $\mathcal{H}^{(2)}$ is a $2N_s/N_u(N-1) \times 2N_s/N_u(N-1)$ matrix. The label m goes over the N_s/N_u sublattice indices whereas α goes over the $N-1$ uncondensed SBs flavor indices. The above-mentioned quadratic Hamiltonian is diagonalized by introducing a Bogoliubov transformation on the bosonic operators $\vec{b}_{\boldsymbol{q}} = \mathcal{U}(\boldsymbol{q})\vec{\beta}_{\boldsymbol{q}}$, where $\mathcal{U}(\boldsymbol{q})$, instead of being unitary for fermionic systems, is *para-unitary* to preserve the canonical commutation relations between the bosonic operators before and after the transformation [43]. The n-th column of the matrix $\mathcal{U}(\boldsymbol{q})$ can be obtained by solving the following eigenvalue problem

$$A\mathcal{H}^{(2)}(\boldsymbol{q})\mathcal{U}_n(\boldsymbol{q}) = \epsilon_n(\boldsymbol{q})\mathcal{U}_n(\boldsymbol{q}), \tag{79}$$

where

$$A = \begin{pmatrix} \mathbb{I}_{[N_s/N_u(N-1)]\times[N_s/N_u(N-1)]} & 0 \\ 0 & -\mathbb{I}_{[N_s/N_u(N-1)]\times[N_s/N_u(N-1)]} \end{pmatrix}. \tag{80}$$

The matrix $A\mathcal{H}^{(2)}(\boldsymbol{q})$ has $N_s/N_u(N-1)$ pairs of positive and negative eigenvalues, and the spin wave energies are given by two times the positive energies $\omega_{\boldsymbol{q},n} = 2\epsilon_{\boldsymbol{q},n} > 0$:

$$\hat{\mathcal{H}}^{(2)} = \sum_{\boldsymbol{k},n} \omega_{\boldsymbol{k},n} \left(\beta^{\dagger}_{\boldsymbol{k},n}\beta_{\boldsymbol{k},n} + \frac{1}{2} \right). \tag{81}$$

D.2 Single-particle Green's function G

By using the Bogoliubov transformation (79), the explicit expression of the single-particle Green's function $G^{(0)}$ defined in Eq. (4.33) given as

$$G(\boldsymbol{q}; i\omega) = \sum_n \left\{ \frac{g_{n,-}(\boldsymbol{q})}{\omega_{\boldsymbol{q},n} - i\omega} + \frac{g_{n,+}(\boldsymbol{q})}{\omega_{-\boldsymbol{q},n} + i\omega} \right\}, \tag{82}$$

where

$$g_{n,-}(\boldsymbol{q}) = \begin{pmatrix} [\mathcal{U}_{11}(\boldsymbol{q})]_n \otimes [\mathcal{U}_{11}^\dagger(\boldsymbol{q})]_n & [\mathcal{U}_{11}(\boldsymbol{q})]_n \otimes [\mathcal{U}_{21}^\dagger(\boldsymbol{q})]_n \\ [\mathcal{U}_{21}(\boldsymbol{q})]_n \otimes [\mathcal{U}_{11}^\dagger(\boldsymbol{q})]_n & [\mathcal{U}_{21}(\boldsymbol{q})]_n \otimes [\mathcal{U}_{21}^\dagger(\boldsymbol{q})]_n \end{pmatrix}, \tag{83}$$

and

$$g_{n,+}(\boldsymbol{q}) = \begin{pmatrix} [\mathcal{U}_{21}^*(\bar{\boldsymbol{q}})]_n \otimes [\mathcal{U}_{21}^*(\bar{\boldsymbol{q}})]_n^\dagger & [\mathcal{U}_{21}^*(\bar{\boldsymbol{q}})]_n \otimes [\mathcal{U}_{11}^*(\bar{\boldsymbol{q}})]_n^\dagger \\ [\mathcal{U}_{11}^*(\bar{\boldsymbol{q}})]_n \otimes [\mathcal{U}_{21}^*(\bar{\boldsymbol{q}})]_n^\dagger & [\mathcal{U}_{11}^*(\bar{\boldsymbol{q}})]_n \otimes [\mathcal{U}_{11}^*(\bar{\boldsymbol{q}})]_n^\dagger \end{pmatrix}. \tag{84}$$

In the above expressions, we have used the 2×2 block matrix notations for $\mathcal{U}(\boldsymbol{q})$ and $\otimes$ denotes the tensor product between two column vectors.

D.3 Matsubara sum in the continuum channel

The following Matsubara summation results are useful (assuming $\xi_1, \xi_2 > 0$)

$$\begin{aligned}
\frac{1}{\beta}\sum_\omega \frac{1}{\xi_1 - i\omega}\frac{1}{\xi_2 - i\omega} &= -\frac{1}{\xi_2 - \xi_1}\left(\frac{1}{e^{-\beta\xi_1} - 1} - \frac{1}{e^{-\beta\xi_2} - 1}\right) \\
\frac{1}{\beta}\sum_\omega \frac{1}{\xi_1 + i\omega}\frac{1}{\xi_2 + i\omega} &= -\frac{1}{\xi_2 - \xi_1}\left(\frac{1}{e^{\beta\xi_1} - 1} - \frac{1}{e^{\beta\xi_2} - 1}\right) \\
\frac{1}{\beta}\sum_\omega \frac{1}{\xi_1 + i\omega}\frac{1}{\xi_2 - i\omega} &= -\frac{1}{\xi_2 + \xi_1}\left(\frac{1}{e^{\beta\xi_1} - 1} + \frac{1}{e^{-\beta\xi_2} - 1}\right).
\end{aligned} \tag{85}$$

In the limit $T \to 0$ or $\beta \to \infty$, only the third term is non-vanishing, we have

$$\frac{1}{\beta}\sum_\omega \frac{1}{\xi_1 + i\omega}\frac{1}{\xi_2 - i\omega} = \frac{1}{\xi_2 + \xi_1}. \tag{86}$$

By using the above results, Eq. (4.37) after the summation over ω' is written as

$$\chi^{\mu\nu}_{ct}(\boldsymbol{q};i\omega) = \frac{1}{N_u}\sum_{\boldsymbol{k}}\sum_{n,n'}\sum_{\{\alpha_i\}}\Xi^{\mu}_{\alpha_1\alpha_2}\Xi^{\nu}_{\alpha_3\alpha_4} \times\Bigg\{\frac{\left[g^{21}_{n,-}(\boldsymbol{k})\right]_{\alpha_1\alpha_3}\left[g^{12}_{n',+}(\boldsymbol{k}+\boldsymbol{q})\right]_{\alpha_2\alpha_4}}{\omega_{\boldsymbol{k},n}+\omega_{\boldsymbol{k}+\boldsymbol{q},n'}+i\omega} + \frac{\left[g^{21}_{n,+}(\boldsymbol{k})\right]_{\alpha_1\alpha_3}\left[g^{12}_{n',-}(\boldsymbol{k}+\boldsymbol{q})\right]_{\alpha_2\alpha_4}}{\omega_{\boldsymbol{k},n}+\omega_{\boldsymbol{k}+\boldsymbol{q},n'}-i\omega} + \frac{\left[g^{22}_{n,-}(\boldsymbol{k})\right]_{\alpha_1\alpha_4}\left[g^{11}_{n',+}(\boldsymbol{k}+\boldsymbol{q})\right]_{\alpha_2\alpha_3}}{\omega_{\boldsymbol{k},n}+\omega_{\boldsymbol{k}+\boldsymbol{q},n'}+i\omega} + \frac{\left[g^{22}_{n,+}(\boldsymbol{k})\right]_{\alpha_1\alpha_4}\left[g^{11}_{n',-}(\boldsymbol{k}+\boldsymbol{q})\right]_{\alpha_2\alpha_3}}{\omega_{\boldsymbol{k},n}+\omega_{\boldsymbol{k}+\boldsymbol{q},n'}-i\omega}\Bigg\}, \tag{87}$$

where we have again introduced the 2×2 block matrix notations for $g_{n,\pm}(\boldsymbol{q})$. Taking analytic continuation $i\omega = \omega \pm i0^+$ such that the causality is preserved [108], we have

$$\chi^{\mu\nu}_{ct}(\boldsymbol{q};\omega) = \frac{1}{N_u}\sum_{\boldsymbol{k}}\sum_{n,n'}\sum_{\{\alpha_i\}}\Xi^{\mu}_{\alpha_1\alpha_2}\Xi^{\nu}_{\alpha_3\alpha_4} \times\Bigg\{\frac{\left[g^{21}_{n,-}(\boldsymbol{k})\right]_{\alpha_1\alpha_3}\left[g^{12}_{n',+}(\boldsymbol{k}+\boldsymbol{q})\right]_{\alpha_2\alpha_4}}{\omega_{\boldsymbol{k},n}+\omega_{\boldsymbol{k}+\boldsymbol{q},n'}+\omega-i0^+} + \frac{\left[g^{21}_{n,+}(\boldsymbol{k})\right]_{\alpha_1\alpha_3}\left[g^{12}_{n',-}(\boldsymbol{k}+\boldsymbol{q})\right]_{\alpha_2\alpha_4}}{\omega_{\boldsymbol{k},n}+\omega_{\boldsymbol{k}+\boldsymbol{q},n'}-\omega-i0^+} + \frac{\left[g^{22}_{n,-}(\boldsymbol{k})\right]_{\alpha_1\alpha_4}\left[g^{11}_{n',+}(\boldsymbol{k}+\boldsymbol{q})\right]_{\alpha_2\alpha_3}}{\omega_{\boldsymbol{k},n}+\omega_{\boldsymbol{k}+\boldsymbol{q},n'}+\omega-i0^+} + \frac{\left[g^{22}_{n,+}(\boldsymbol{k})\right]_{\alpha_1\alpha_4}\left[g^{11}_{n',-}(\boldsymbol{k}+\boldsymbol{q})\right]_{\alpha_2\alpha_3}}{\omega_{\boldsymbol{k},n}+\omega_{\boldsymbol{k}+\boldsymbol{q},n'}-\omega-i0^+}\Bigg\}, \tag{88}$$

After using the fluctuation-dissipation theorem at $T=0$ (4.24), we have

$$\mathcal{O}^{\mu\nu}_{\rm tc}(\boldsymbol{q},\omega) = \frac{1}{N_u}\Bigg[\sum_{\boldsymbol{k}}\sum_{n,n'=1}^{2}\sum_{\{\alpha_i\}}\Xi^{\mu}_{\alpha_1\alpha_2}\Xi^{\nu}_{\alpha_3\alpha_4}\delta(\omega-\omega_{\boldsymbol{k},n}-\omega_{\boldsymbol{k}+\boldsymbol{q},n'}) \left(\left[g^{21}_{n,+}(\boldsymbol{k})\right]_{\alpha_1\alpha_3}\left[g^{12}_{n',-}(\boldsymbol{k}+\boldsymbol{q})\right]_{\beta\beta'} + \left[g^{22}_{n,+}(\boldsymbol{k})\right]_{\alpha_1\alpha_4}\left[g^{11}_{n',-}(\boldsymbol{k}+\boldsymbol{q})\right]_{\alpha_2\alpha_3}\right)\Bigg]. \tag{89}$$

We note that the first and third term in the curly bracket of Eq. (88) does not have imaginary part for $\omega > 0$. In summary, as evident from its name, $\mathcal{O}^{\mu\nu}_{ct}(\boldsymbol{q},\omega)$ probes the two-particle continuum

$$\mathcal{O}^{\mu\nu}_{\rm tc}(\boldsymbol{q},\omega) \sim \sum_{\boldsymbol{k}}\sum_{n,n'}\delta(\omega-\omega_{\boldsymbol{k},n}-\omega_{\boldsymbol{k}+\boldsymbol{q},n'}). \tag{90}$$

E Supplemental Info for Sec. 5.1

E.1 Expressions for the generalized linear spin-wave calculation

The expressions for the coefficients $A_{\boldsymbol{k},\alpha}$ and $B_{\boldsymbol{k},\alpha}$ of the quadratic Hamiltonian $\mathcal{H}^{(2)}$ (5.5) are:

$$\begin{aligned}
A_{\boldsymbol{k},+1} &= -8(x-1)x(2\tilde{J}+\tilde{J}') - (x-1)\tilde{D} + 2\big(x(1+\tilde{\Delta})-1\big)\tilde{J}\gamma^{xy}_{\boldsymbol{k}} + 2\big(x(1+\tilde{\Delta}')-1\big)\tilde{J}'\gamma^{z}_{\boldsymbol{k}},\\
B_{\boldsymbol{k},+1} &= -2\big(x(\tilde{\Delta}-1)+1\big)\tilde{J}\gamma^{xy}_{\boldsymbol{k}} - 2\big(x(\tilde{\Delta}'-1)+1\big)\tilde{J}'\gamma^{z}_{\boldsymbol{k}},\\
A_{\boldsymbol{k},-1} &= -16(x-1)x(2\tilde{J}+\tilde{J}') - (2x-1)D - 2(1-2x)^2(\tilde{J}\gamma^{xy}_{\boldsymbol{k}} + \tilde{J}'\gamma^{z}_{\boldsymbol{k}}),\\
B_{\boldsymbol{k},-1} &= 2(1-2x)^2(\tilde{J}\gamma^{xy}_{\boldsymbol{k}} + \tilde{J}'\gamma^{z}_{\boldsymbol{k}})
\end{aligned} \tag{91}$$

E.2 Cubic vertex functions

In this section, we derive the cubic and cubic-linear vertices given in Eq. (5.11) and Eq. (5.12). The cubic Hamiltonian has three contributions

$$\mathcal{H}^{(3)} = \mathcal{H}^{(3)}_{\text{intra}} + \mathcal{H}^{(3)}_{\text{inter}} + \mathcal{H}^{(3)}_{D}, \tag{92}$$

with

$$\begin{aligned}
\mathcal{H}^{(3)}_{\text{intra}} = \tilde{J} \sum_{\langle \boldsymbol{r},\boldsymbol{r}'\rangle,\nu} \sum_{\alpha,\beta=\pm1} \Bigg\{ \sum_{\alpha'=\pm1} a_\nu \big[2\tilde{\mathcal{S}}^{\nu}_{\alpha\beta}\tilde{\mathcal{S}}^{\nu}_{0\alpha'}\tilde{b}^{\dagger}_{\boldsymbol{r}\alpha}\tilde{b}_{\boldsymbol{r}\beta}\tilde{b}_{\boldsymbol{r}'\alpha'}\big] \\
- a_\nu\big[\tilde{\mathcal{S}}^{\nu}_{0\alpha}\tilde{\mathcal{S}}^{\nu}_{00}\big(\tilde{b}^{\dagger}_{\boldsymbol{r}\beta}\tilde{b}_{\boldsymbol{r}\beta}\tilde{b}_{\boldsymbol{r}\alpha} + 2\tilde{b}^{\dagger}_{\boldsymbol{r}'\beta}\tilde{b}_{\boldsymbol{r}'\beta}\tilde{b}_{\boldsymbol{r}\alpha}\big)\big] + h.c.\Bigg\},
\end{aligned}$$

$$\begin{aligned}
\mathcal{H}^{(3)}_{\text{inter}} = \tilde{J}' \sum_{\langle \boldsymbol{r},\boldsymbol{r}'\rangle,\nu} \sum_{\alpha,\beta=\pm1} \Bigg\{ \sum_{\alpha'=\pm1} b_\nu \big[2\tilde{\mathcal{S}}^{\nu}_{\alpha\beta}\tilde{\mathcal{S}}^{\nu}_{0\alpha'}\tilde{b}^{\dagger}_{\boldsymbol{r}\alpha}\tilde{b}_{\boldsymbol{r}\beta}\tilde{b}_{\boldsymbol{r}'\alpha'}\big] \\
- b_\nu\big[\tilde{\mathcal{S}}^{\nu}_{0\alpha}\tilde{\mathcal{S}}^{\nu}_{00}\big(\tilde{b}^{\dagger}_{\boldsymbol{r}\beta}\tilde{b}_{\boldsymbol{r}\beta}\tilde{b}_{\boldsymbol{r}\alpha} + 2\tilde{b}^{\dagger}_{\boldsymbol{r}'\beta}\tilde{b}_{\boldsymbol{r}'\beta}\tilde{b}_{\boldsymbol{r}\alpha}\big)\big] + h.c.\Bigg\},
\end{aligned}$$

$$\mathcal{H}^{(3)}_{D} = \frac{\tilde{D}}{2}\sum_{\boldsymbol{r}}\sum_{\alpha,\beta=\pm1}\big[\tilde{\mathcal{A}}_{0\alpha}\tilde{b}^{\dagger}_{\boldsymbol{r}\beta}\tilde{b}_{\boldsymbol{r}\beta}\tilde{b}_{\boldsymbol{r}\alpha} + h.c.\big],$$

To simplify the notation, we will write a particular term of (92) (in momentum space) as (I) $= \tilde{b}^{\dagger}_{\bar{\boldsymbol{q}}_1,\alpha}\tilde{b}_{\boldsymbol{q}_2,\beta}\tilde{b}_{\boldsymbol{q}_3,\gamma}f(\boldsymbol{q}_i,t)$, with

$$f(\boldsymbol{q}_{1,2,3},t)=\begin{cases}1 & t=0\\ \gamma^{xy}_{\boldsymbol{q}_3} & t=1\\ \gamma^{z}_{\boldsymbol{q}_3} & t=2\end{cases}. \tag{93}$$

The Nambu spinor of the bosonic operators can be Bogoliubov transformed into the quasi-particle representation $\vec{b}_{\boldsymbol{k}}=\mathcal{U}(\boldsymbol{k})\vec{\beta}_{\boldsymbol{k}}$, where the matrix elements of $\mathcal{U}(\boldsymbol{k})$ are obtained from the Bogoliubov coefficients given in Eq. (5.8)

$$\begin{aligned}\mathcal{U}(\boldsymbol{k}) &= \begin{pmatrix}\mathcal{U}^{11}_{2\times2}(\boldsymbol{k}) & \mathcal{U}^{12}_{2\times2}(\boldsymbol{k})\\ \mathcal{U}^{21}_{2\times2}(\boldsymbol{k}) & \mathcal{U}^{22}_{2\times2}(\boldsymbol{k})\end{pmatrix}\\ &= \begin{pmatrix}u_{\boldsymbol{k},+1} & 0 & v_{\boldsymbol{k},+1} & 0\\ 0 & u_{\boldsymbol{k},-1} & 0 & v_{\boldsymbol{k},-1}\\ v_{\boldsymbol{k},+1} & 0 & u_{\boldsymbol{k},+1} & 0\\ 0 & v_{\boldsymbol{k},-1} & 0 & u_{\boldsymbol{k},-1}\end{pmatrix}.\end{aligned}$$

After applying the above-mentioned Bogoliubov transformation, we obtain

$$\begin{aligned}(\mathrm{I}) = \sum_{n_{1,2,3}}\Big\{ & F^{(a)}(\alpha\beta\gamma,n_{1,2,3};\boldsymbol{q}_{1,2,3},t)\beta_{\boldsymbol{q}_1,n_1}\beta_{\boldsymbol{q}_2,n_2}\beta_{\boldsymbol{q}_3,n_3}\\ &+F^{(b)}(\alpha\beta\gamma,n_{1,2,3};\boldsymbol{q}_{1,2,3},t)\beta^{\dagger}_{\bar{\boldsymbol{q}}_1,n_1}\beta^{\dagger}_{\bar{\boldsymbol{q}}_2,n_2}\beta^{\dagger}_{\bar{\boldsymbol{q}}_3,n_3}\\ &+F^{(c)}(\alpha\beta\gamma,n_{1,2,3};\boldsymbol{q}_{1,2,3},t)\beta^{\dagger}_{\bar{\boldsymbol{q}}_1,n_1}\beta^{\dagger}_{\bar{\boldsymbol{q}}_2,n_2}\beta_{\boldsymbol{q}_3,n_3}\\ &+F^{(d)}(\alpha\beta\gamma,n_{1,2,3};\boldsymbol{q}_{1,2,3},t)\beta^{\dagger}_{\bar{\boldsymbol{q}}_1,n_1}\beta_{\boldsymbol{q}_2,n_2}\beta_{\boldsymbol{q}_3,n_3}\\ &+L^{(c)}(\alpha\beta\gamma,n_{1,2,3};\boldsymbol{q}_{1,2,3},t)\delta_{\boldsymbol{q}_3,\bar{\boldsymbol{q}}_2}\delta_{n_3,n_2}\beta^{\dagger}_{\bar{\boldsymbol{q}}_1,n_1}\\ &+L^{(d)}(\alpha\beta\gamma,n_{1,2,3};\boldsymbol{q}_{1,2,3},t)\delta_{\boldsymbol{q}_2,\bar{\boldsymbol{q}}_1}\delta_{n_2,n_1}\beta_{\boldsymbol{q}_3,n_3}\Big\}.\end{aligned} \tag{94}$$

The explicit forms of $F^{(a,b,c,d)}$ and $L^{(c,d)}$ can be obtained by simple algebras, which are not shown here for neatness.

The "sink" ("source") function $F^{(a)}$ ($F^{(b)}$) is symmetric under permutations of all three legs (momenta and flavors). Consequently, we introduce the symmetrized functions

$$\tilde{F}^{(a)} \equiv \sum_{P(\boldsymbol{q}_{1,2,3};n_{1,2,3})} F^{(a)}, \qquad \tilde{F}^{(b)} \equiv \sum_{P(\boldsymbol{q}_{1,2,3};n_{1,2,3})} F^{(b)}.$$

Similarly, the "decay" function $F^{(c)}$ and the "fusion" function $F^{(d)}$ are symmetrized for the two outgoing and the two incoming legs, respectively,

$$\tilde{F}^{(c)} = \sum_{P(\boldsymbol{q}_{1,2};n_{1,2})} F^{(c)}, \; \tilde{F}^{(d)} = \sum_{P(\boldsymbol{q}_{2,3};n_{2,3})} F^{(c)}.$$

After inserting the above results into Eq. (92), we obtain the explicit forms of the cubic vertices in $V^{(3)}_{s/d}$ Eq. (5.11) and V^{L}_{α} in Eq. (5.12).

E.3 Quartic vertex

The quartic Hamiltonian is written as

$$\mathcal{H}^{(4)} = \mathcal{H}^{(4)}_{\text{intra}} + \mathcal{H}^{(4)}_{\text{inter}}, \tag{95}$$

with

$$\begin{aligned}\mathcal{H}^{(4)}_{\text{intra}} = \tilde{J} \sum_{\langle \boldsymbol{r},\boldsymbol{r}'\rangle,\nu} \sum_{\alpha,\beta=\pm 1} \Big\{ &\left[a_\nu \tilde{\mathcal{S}}^{\nu}_{00}\tilde{\mathcal{S}}^{\nu}_{00}\tilde{b}^{\dagger}_{\boldsymbol{r}\alpha}\tilde{b}^{\dagger}_{\boldsymbol{r}'\beta}\tilde{b}_{\boldsymbol{r}\alpha}\tilde{b}_{\boldsymbol{r}'\beta}\right] + \sum_{\alpha'\beta'=\pm 1}\left[a_\nu \tilde{\mathcal{S}}^{\nu}_{\alpha\beta}\tilde{\mathcal{S}}^{\nu}_{\alpha'\beta'}\tilde{b}^{\dagger}_{\boldsymbol{r}\alpha}\tilde{b}^{\dagger}_{\boldsymbol{r}'\alpha'}\tilde{b}_{\boldsymbol{r}\beta}\tilde{b}_{\boldsymbol{r}'\beta'}\right] \\ &- 2\sum_{\alpha'=\pm 1}\left[a_\nu \tilde{\mathcal{S}}^{\nu}_{\alpha\beta}\tilde{\mathcal{S}}^{\nu}_{00}\tilde{b}^{\dagger}_{\boldsymbol{r}\alpha}\tilde{b}^{\dagger}_{\boldsymbol{r}'\alpha'}\tilde{b}_{\boldsymbol{r}\beta}\tilde{b}_{\boldsymbol{r}'\alpha'}\right] - \sum_{\alpha'=\pm 1}\left[a_\nu \tilde{\mathcal{S}}^{\nu}_{\alpha 0}\tilde{\mathcal{S}}^{\nu}_{\beta 0}\tilde{b}^{\dagger}_{\boldsymbol{r}\alpha}\tilde{b}^{\dagger}_{\boldsymbol{r}'\beta}\tilde{b}^{\dagger}_{\boldsymbol{r}'\alpha'}\tilde{b}_{\boldsymbol{r}'\alpha'} + h.c.\right] \\ &- \sum_{\alpha'=\pm 1}\left[a_\nu \tilde{\mathcal{S}}^{\nu}_{\alpha 0}\tilde{\mathcal{S}}^{\nu}_{0\beta}\tilde{b}^{\dagger}_{\boldsymbol{r}\alpha}\tilde{b}^{\dagger}_{\boldsymbol{r}'\alpha'}\tilde{b}_{\boldsymbol{r}'\alpha'}\tilde{b}_{\boldsymbol{r}'\beta} + h.c.\right]\Big\}.\end{aligned}$$

Similarly to the cubic contribution, $\mathcal{H}^{(4)}_{\text{inter}}$ can be obtained from $\mathcal{H}^{(4)}_{\text{intra}}$ by substituting $\tilde{J} \to \tilde{J}'$, $a_\nu \to b_\nu$. The matrix elements appear in the normal ordering of the quartic vertex are defined

as:

$$\bar{N}^{\alpha\beta}_{\boldsymbol{r}\boldsymbol{r}'} \equiv \frac{1}{N}\sum_{\langle \boldsymbol{r},\boldsymbol{r}'\rangle}\langle b^\dagger_{\boldsymbol{r}\alpha} b_{\boldsymbol{r}'\beta}\rangle = \frac{1}{N}\sum_{\boldsymbol{k}}\sum_{n}\mathcal{U}^{21}_{\alpha,n}(\boldsymbol{k})\left[\mathcal{U}^{21}_{\beta,n}(\boldsymbol{k})\right]^* \cos\left[\boldsymbol{k}\cdot(\boldsymbol{r}'-\boldsymbol{r})\right],$$
$$\Delta^{\alpha\beta}_{\boldsymbol{r}\boldsymbol{r}'} \equiv \frac{1}{N}\sum_{\langle \boldsymbol{r},\boldsymbol{r}'\rangle}\langle b_{\boldsymbol{r}\alpha} b_{\boldsymbol{r}'\beta}\rangle = \frac{1}{N}\sum_{\boldsymbol{k}}\sum_{n}\mathcal{U}^{11}_{\alpha,n}(\boldsymbol{k})\left[\mathcal{U}^{21}_{\beta,n}(\boldsymbol{k})\right]^* \cos\left[\boldsymbol{k}\cdot(\boldsymbol{r}'-\boldsymbol{r})\right],$$
$$\bar{\Delta}^{\alpha\beta}_{\boldsymbol{r}\boldsymbol{r}'} \equiv \frac{1}{N}\sum_{\langle \boldsymbol{r},\boldsymbol{r}'\rangle}\langle b^\dagger_{\boldsymbol{r}\alpha} b^\dagger_{\boldsymbol{r}'\beta}\rangle = \frac{1}{N}\sum_{\boldsymbol{k}}\sum_{n}\mathcal{U}^{21}_{\alpha,n}(\boldsymbol{k})\left[\mathcal{U}^{11}_{\beta,n}(\boldsymbol{k})\right]^* \cos\left[\boldsymbol{k}\cdot(\boldsymbol{r}'-\boldsymbol{r})\right],$$

We note that some of these matrix elements are equal to zero because of the residual U(1) symmetry of the antiferromagnetic order. To obtain the normal-ordered Hamiltonian Eq. (5.15), we apply a mean-field (Hartree-Fock) decoupling to the quartic Hamiltonian Eq. (95), for example,

$$\begin{aligned}\tilde{b}^\dagger_{\boldsymbol{r}\alpha}\tilde{b}^\dagger_{\boldsymbol{r}'\beta}\tilde{b}_{\boldsymbol{r}\alpha}\tilde{b}_{\boldsymbol{r}'\beta} \simeq{}& \Delta^{\alpha\beta}_{\boldsymbol{r}\boldsymbol{r}'}\tilde{b}^\dagger_{\boldsymbol{r}\alpha}\tilde{b}^\dagger_{\boldsymbol{r}'\beta} + \bar{N}^{\beta\beta}_{\boldsymbol{r}'\boldsymbol{r}'}\tilde{b}^\dagger_{\boldsymbol{r}\alpha}\tilde{b}_{\boldsymbol{r}\alpha} + \bar{N}^{\beta\alpha}_{\boldsymbol{r}'\boldsymbol{r}}\tilde{b}^\dagger_{\boldsymbol{r}\alpha}\tilde{b}_{\boldsymbol{r}'\beta} + \bar{\Delta}^{\alpha\beta}_{\boldsymbol{r}\boldsymbol{r}'}\tilde{b}_{\boldsymbol{r}\alpha}\tilde{b}_{\boldsymbol{r}'\beta} \\ &+ \bar{N}^{\alpha\alpha}_{\boldsymbol{r}\boldsymbol{r}}\tilde{b}^\dagger_{\boldsymbol{r}'\beta}b_{\boldsymbol{r}'\beta} + \bar{N}^{\alpha\beta}_{\boldsymbol{r}\boldsymbol{r}'}\tilde{b}^\dagger_{\boldsymbol{r}'\beta}\tilde{b}_{\boldsymbol{r}\alpha}.\end{aligned} \tag{96}$$

The coefficients $V^{(4,N)}_{\alpha\alpha}$ that appear in the normal term of Eq. (5.15) can be derived after consecutive Fourier and Bogoliubov transformations.

E.4 One-loop diagrams in the long-wavelength limit

Without loss of generality, we consider an isotropic Heisenberg model, i.e. $\tilde{J} = \tilde{J}'$, $\tilde{\Delta} = \tilde{\Delta}'$ to show the $1/\boldsymbol{q}$ divergence of the one-loop diagrams involving the Goldstone mode. According to Eq. (5.8),

$$\lim_{\boldsymbol{q}\to 0} u_{\boldsymbol{q},+}, v_{\boldsymbol{q},+} = \sqrt{\frac{\tilde{J}d}{v_{\boldsymbol{0},+}}}\frac{1}{\sqrt{\boldsymbol{q}}}, -\sqrt{\frac{\tilde{J}d}{v_{\boldsymbol{0},+}}}\frac{1}{\sqrt{\boldsymbol{q}}} \tag{97}$$

where $v_{\boldsymbol{0},+} = 2\tilde{J}d\sqrt{\tilde{D}/(4\tilde{J}d^2)+1/d}$ is the spin wave velocity of the Goldstone mode and $d = 3$ is the spatial dimension of the lattice equal to half of the coordination number. Note that the cubic vertices are proportional to a product of the Bogoliubov coefficients of three legs

$$V^{(3)}_{d,s} \propto u(v)_{\boldsymbol{q}_1,\alpha}u(v)_{\boldsymbol{q}_2,\beta}u(v)_{\boldsymbol{q}_3,\gamma}. \tag{98}$$

For the decay and sink diagrams shown on the second line of Fig. 5.4 (a), we can choose, for instance, $\boldsymbol{q}_3 = \boldsymbol{q} \sim \boldsymbol{0}$, $\gamma = +1$ to contract with the leg of the long-wavelength bosons. Consequently,

$$\Sigma^{(d,s)}(+) \sim |V^{(3)}_{d,s}(\boldsymbol{q}_{1,2}, \boldsymbol{q}; \alpha\beta+)|^2 \sim (1/\sqrt{\boldsymbol{q}})^2 \sim 1/q. \tag{99}$$

As for the cubic-linear diagrams, we need to choose two legs to contract with the long-wavelength boson, implying that

$$\Sigma^{(cl)}(+) \sim V^{(3)}_{d}(\boldsymbol{0}, -\boldsymbol{q}\boldsymbol{q}; - + +) \sim 1/q. \tag{100}$$

Finally, notice that $V^{(4,N)}_{++} \sim 1/q$ in the long-wavelength limit, because the quadratic forms of the transverse boson in Eq. (96) after the Bogoliubov transformation are proportional to $u(v)_{\boldsymbol{q},+1}u(v)_{\boldsymbol{q},+1}$. By adding up all diagrams in $\mathcal{O}(M^0)$, we have verified that the coefficient of the $1/q$-factor vanishes, implying that the Goldstone mode is preserved after the one-loop correction.

E.5 Estimation of the quantum critical point (QCP)

Let us recall that the linear order term $\hat{\mathcal{H}}^{(1)}$ $\mathcal{O}[M^{3/2}]$ vanishes in the expansion of the Hamiltonian [see Eq. (4.9)] because the mean-field value of (the order parameter) θ or x given in Eq. (5.4) corresponds to the state with minimal classical energy. As we mentioned in Sec. 5.1.3, $\hat{\mathcal{H}}^{(3)}_l$ is a linear term $\mathcal{O}[M^{1/2}]$ that originates from the normal-ordering of the cubic term [see Eq. (5.12)]. Consequently, the presence of $\hat{\mathcal{H}}^{(3)}_l$ leads to a renormalization in the order parameter $x = \sin^2\theta$. In the GLSWT+one-loop approximation, such renormalization is taken into account by including the so-called cubic-linear diagrams [see Fig. 5.4]. We may also wonder the corresponding renormalization effects by enforcing $\hat{\mathcal{H}}^{(1)} + \hat{\mathcal{H}}^{(3)}_l = 0$. For $Ba_2FeSi_2O_7$, the linear order term is written as

$$\hat{\mathcal{H}}^{(1)} = 4\sqrt{N_s}\sqrt{x(1-x)}(2x-1)(2\tilde{J}+\tilde{J}')(u_{\boldsymbol{0},-1} + v_{\boldsymbol{0},-1})(\beta^\dagger_{\boldsymbol{0},-1} + h.c.) \tag{101}$$

and the cubic-linear term is given as

$$\hat{\mathcal{H}}_l^{(3)} = \sum_{T=1}^{5} V_{c-l}^{(3;T)} (\beta_{\mathbf{0},-1}^\dagger + h.c.), \tag{102}$$

where $V_{c-l}^{(3;T)}$ are results of integration over the first Brillouin zone, i.e., $(1/N_s \sum_{\boldsymbol{q}})$

$$\begin{aligned}
V_{c-l}^{(1)} &= \frac{8Jd\sqrt{(1-x)x}}{\sqrt{N_s}} \sum_{\boldsymbol{q}} \left(v_{\boldsymbol{q},+1} v_{\mathbf{0},-1} v_{\boldsymbol{q},+1} \gamma_{\boldsymbol{q}} + v_{\boldsymbol{q},+1} u_{\mathbf{0},-1} v_{\boldsymbol{q},+1} \gamma_{\boldsymbol{q}} \right), \\
V_{c-l}^{(2)} &= \frac{2\sqrt{(1-x)x}\left(2Jd(1-2x) - \frac{1}{2}D\right)}{\sqrt{N_s}} \sum_{\boldsymbol{q}} \left(v_{\boldsymbol{q},+1} v_{\boldsymbol{q},+1} v_{\mathbf{0},-1} + v_{\boldsymbol{q},+1} v_{\boldsymbol{q},+1} u_{\mathbf{0},-1} \right), \\
V_{c-l}^{(3)} &= \frac{8Jd\sqrt{(1-x)x}(1-2x)}{\sqrt{N_s}} \sum_{\boldsymbol{q}} \left(v_{\boldsymbol{q},+1} v_{\boldsymbol{q},+1} v_{\mathbf{0},-1} \gamma_{\mathbf{0}} + v_{\boldsymbol{q},+1} v_{\boldsymbol{q},+1} u_{\mathbf{0},-1} \gamma_{\mathbf{0}} \right), \\
V_{c-l}^{(4)} &= \frac{2\sqrt{(1-x)x}\left(2Jd(1-2x) - \frac{1}{2}D\right)}{\sqrt{N_s}} \sum_{\boldsymbol{q}} \left(v_{\boldsymbol{q},-1} v_{\boldsymbol{q},-1} v_{\mathbf{0},-1} + v_{\boldsymbol{q},-1} v_{\mathbf{0},-1} v_{\boldsymbol{q},-1} \right. \\
&\quad + u_{\mathbf{0},-1} u_{\boldsymbol{q},-1} v_{\boldsymbol{q},-1} + v_{\mathbf{0},-1} u_{\boldsymbol{q},-1} v_{\boldsymbol{q},-1} \\
&\quad \left. + v_{\boldsymbol{q},-1} u_{\mathbf{0},-1} v_{\boldsymbol{q},-1} + v_{\boldsymbol{q},-1} v_{\boldsymbol{q},-1} u_{\mathbf{0},-1} \right), \\
V_{c-l}^{(5)} &= \frac{16Jd\sqrt{(1-x)x}(1-2x)}{\sqrt{N_s}} \sum_{\boldsymbol{q}} \left(v_{\boldsymbol{q},-1} v_{\boldsymbol{q},-1} v_{\mathbf{0},-1} \gamma_{\mathbf{0}} + v_{\boldsymbol{q},-1} v_{\mathbf{0},-1} v_{\boldsymbol{q},-1} \gamma_{\boldsymbol{q}} \right. \\
&\quad + u_{\mathbf{0},-1} u_{\boldsymbol{q},-1} v_{\boldsymbol{q},-1} \gamma_{\boldsymbol{q}} + v_{\mathbf{0},-1} u_{\boldsymbol{q},-1} v_{\boldsymbol{q},-1} \gamma_{\boldsymbol{q}} \\
&\quad \left. + v_{\boldsymbol{q},-1} u_{\mathbf{0},-1} v_{\boldsymbol{q},-1} \gamma_{\boldsymbol{q}} + v_{\boldsymbol{q},-1} v_{\boldsymbol{q},-1} u_{\mathbf{0},-1} \gamma_{\mathbf{0}} \right).
\end{aligned} \tag{103}$$

After adding up $\hat{\mathcal{H}}^{(1)} + \hat{\mathcal{H}}_l^{(3)}$, we find the renormalized $\tilde{x}$ by requiring a vanishing coefficient of $\beta_{\mathbf{0},-1}^\dagger$. Then we plug $\tilde{x}$ into Eq. (91) and ask the corresponding changes in the quasiparticle dispersion relations Eq. (5.5). We note that this calculation does not lead to results of a particular order in M, i.e., it is a *non-perturbative* calculation (not controlled by M). Consequently, it gives an incorrect dispersion relation for the transverse mode T_1 (complex frequencies): the Goldstone mode is no longer preserved. Nevertheless, we can still look for the corresponding non-perturbative effects in the longitudinal mode L as it is gapped in the AFM phase.

Figure 2 shows the comparison of the dispersion relations obtained from the GLSWT, GLSWT+one-loop, and the non-perturbative calculations. We see that near the ordering wave vector $\boldsymbol{Q}_m$ (indicated by the orange vertical line), the non-perturbative calculation gives the smallest gap for the L-mode. Recall that the L-mode becomes gapless at the QCP, that signals a quantum phase transition from the AFM phase to the quantum paramagnetic phase (QPM). As a result, the critical $\alpha_c = \tilde{J}/\tilde{D}$ is obtained by requiring $\omega_L(\boldsymbol{Q}_m) = 0$. Then the results given in Fig. 2 imply that the non-perturbative calculation would predict the largest α_c compared to the GLSWT calculation and the perturbative calculation. Interestingly, it turns out that non-perturbative effects captured by the above-mentioned non-perturbative calculation become dominant upon approaching the QCP from the AFM side. To verify this argument, we compared the value of α_c obtained from the non-perturbative calculation for the isotropic model ($\tilde{J} = \tilde{J}'$, and $\tilde{\Delta} = \tilde{\Delta}' = 1$) against a quantum Monte-Carlo (QMC) simulation on the same model [173]: In 3D, QMC predicts $\alpha_c = 0.1$, and the non-perturbative calculation gives practically the same value ($\alpha_c = 0.1000(5)$ for the latter); In 2D, QMC predicts $\alpha_c = 0.178$, whereas the non-perturbative calculation gives $\alpha_c = 0.17(6)$. The amazing agreement of α_c between the non-perturbative calculation and the QMC simulation suggests that we can use the above-mentioned non-perturbative calculation to estimate the QCP for $Ba_2FeSi_2O_7$, given it is a quasi-2D system ($\tilde{J}'/\tilde{J} = 0.1$). We have, for $Ba_2FeSi_2O_7$ ($\tilde{J}' = 0.1\tilde{J}$, and $\tilde{\Delta} = \tilde{\Delta}' = 1/3$), $\alpha_c \simeq 0.158$. We note that the parameters set $\mathcal{A}$ $\alpha_{\text{GLSW}} = 0.152$ extracted from fitting the experiment with the GLSWT place $Ba_2FeSi_2O_7$ on the QPM side of the phase diagram, whereas the parameters set $\mathcal{B}$ obtained from the GLSWT+one-loop correction ($\alpha_{\text{GLSW+one loop}} = 0.187$) place the material at the magnetically ordered phase of the exact phase diagram.

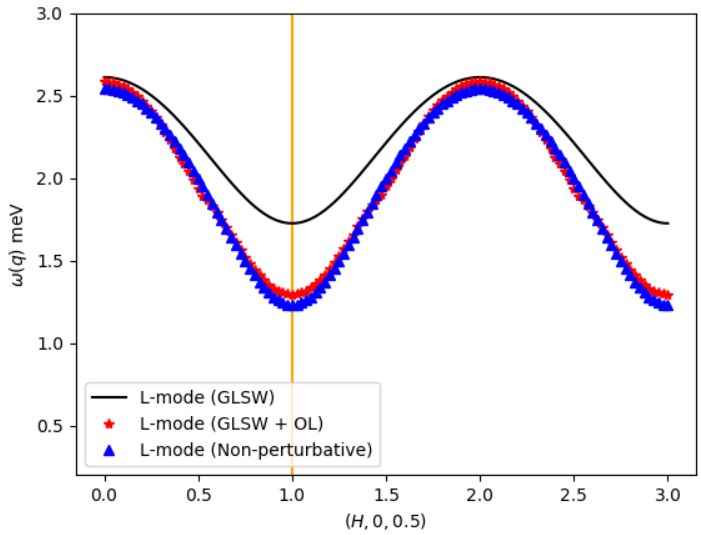


Figure 2: Dispersion relations for the longitudinal mode L obtained from the SU(3) generalized linear spin wave theory (GLSWT) calculation (black line), GLSWT+one-loop correction calculation (red stars), and the non-perturbative calculation (blue triangles) described in this section. The orange vertical line denotes the position corresponding to the AFM ordering wave vector $\boldsymbol{q} = (\pi, \pi, \pi)$ in the magnetic lattice or $(1, 0, 0.5)$ in the chemical lattice. All results in this figure are obtained by using parameter set $\mathcal{B}$ listed in Table 5.1.

F Berry phase and solid angle in CP^2

F.1 Continuum limit

Topological soliton solutions of the classical color field become well-defined in the continuum limit that holds for $\lambda \gg a$, where λ is the characteristic wave-length of the spin configuration and a is the lattice parameter. In this limit, we use a Taylor expansion to express the value of the field n_j^m on the site j (with coordinates $\boldsymbol{r}_j$) in terms of the field n_i^m on the neighboring site located at $\boldsymbol{r}_i$:

$$n_j^m = n_i^m + r_{ij}\partial_k n_i^m + O\left(r_{ij}^2\right) \tag{104}$$

where $\boldsymbol{r}_j = \boldsymbol{r}_i + r_{ij}\boldsymbol{e}_k, r_{ij} = |\boldsymbol{r}_i - \boldsymbol{r}_j|$ (r_{ij} coincides with the lattice parameter a when i and j are nearest-neighbor sites) and $\boldsymbol{e}_k$ is a unit vector that points in the k-direction of the plane. Since the lattice spin Hamiltonians that we will consider include only interactions between spins on neighboring sites, we can use Eq. (104) to define a continuum limit of the spin Hamiltonian by replacing the sum over lattice sites with the integral $a^{-2}\int \mathrm{d}^2x$.

Since the color field takes a constant value n_∞ at spatial infinity for skyrmion configurations, the base plane $\mathbb{R}^2$ can be compactified to S^2. Thus, these spin textures are characterized by the topological degree (or skyrmion charge) of the mapping $\mathbf{n} : S^2 \mapsto CP^2$:

$$C = -\frac{i}{32\pi}\int \mathrm{d}x\mathrm{d}y\varepsilon_{jk}\,\mathrm{Tr}\left(\mathbf{n}\left[\partial_j\mathbf{n}, \partial_k\mathbf{n}\right]\right) \tag{105}$$

It is important to note that there is a one-to-one correspondence between the color field $\mathbf{n}_j$ and $\boldsymbol{Z}_j$ that defines a coherent state. In other words, we can also express the Hamiltonian and the skyrmion density in terms of the $\boldsymbol{Z}_j$ field that in the continuum limit becomes a $\boldsymbol{Z}(\boldsymbol{r})$ field. We can think of both alternative descriptions as the classical limit of the Schrödinger and the Heisenberg representations. In the former case, the dynamical variables are wave functions that become coherent states with coordinates $\boldsymbol{Z}_j$. In the latter case, the dynamical variables are operators $\hat{T}_j^\mu$ (observables), which in the classical limit are replaced by their expectation value $\left\langle T_j^\mu \right\rangle$ that coincides with the color field n_j^μ.

Depending on the application, it may be more convenient to work with one representation of the classical SU(3) spin field or with the other one. For this reason, it is useful to derive an expression of the skyrmion density in terms of the $\boldsymbol{Z}_j$-field. As expected, the skyrmion density defined in Eq. (105) turns out to be proportional to the Berry curvature of the $\boldsymbol{Z}(\boldsymbol{r})$ field. To demonstrate this statement we just need to introduce the SU(3) Berry connection,

$$\mathcal{A}(\boldsymbol{r}) = i \left\langle \boldsymbol{Z} \left| \nabla_{\boldsymbol{r}} \right| \boldsymbol{Z} \right\rangle \tag{106}$$

and the corresponding SU(3) Berry curvature:

$$\mathcal{B}(\boldsymbol{r}) = \nabla \times \mathcal{A}(\boldsymbol{r}). \tag{107}$$

According to Stokes theorem, the integral of the Berry connection over a closed loop $\mathcal{C}$ is equal to the integral of the Berry curvature over the oriented surface enclosed by $\mathcal{C}$:

$$\oint_C \mathcal{A}_j dx^j = \int_{S_C} \left[\partial_x \mathcal{A}_y - \partial_y \mathcal{A}_x\right] \mathrm{d}x\mathrm{d}y. \tag{108}$$

Our next goal is to demonstrate that the skyrmion density is proportional to the Berry curvature:

$$\partial_x \mathcal{A}_y - \partial_y \mathcal{A}_x = -\frac{i}{16} 2 \,\mathrm{Tr}\left(\mathfrak{n}\left[\partial_x \mathfrak{n}, \partial_y \mathfrak{n}\right]\right) = -\frac{i}{16} \varepsilon_{jk} \,\mathrm{Tr}\left(\mathfrak{n}\left[\partial_j \mathfrak{n}, \partial_k \mathfrak{n}\right]\right). \tag{109}$$

To demonstrate this equivalence, we first need to demonstrate that the infinitesimal "geodesic" SU(3) spin rotation that transforms the coherent state $|\boldsymbol{Z}(\boldsymbol{r})\rangle$ into $|\boldsymbol{Z}(\boldsymbol{r}+\delta\boldsymbol{r})\rangle$ up to a phase factor $e^{i\delta\varphi}$ is:

$$e^{i\delta\varphi}|\boldsymbol{Z}(\boldsymbol{r}+\delta\boldsymbol{r})\rangle = \hat{U}_{\boldsymbol{r}+\delta\boldsymbol{r},\boldsymbol{r}}|\boldsymbol{Z}(\boldsymbol{r})\rangle = \left(\mathbb{I} - \frac{i}{4} f_{\mu\upsilon\eta} n^\mu \partial_{\boldsymbol{r}} n^\nu \cdot \delta\boldsymbol{r} T^\eta\right)|\boldsymbol{Z}(\boldsymbol{r})\rangle. \tag{110}$$

In other words,

$$\hat{U}_{\boldsymbol{r}+\delta\boldsymbol{r},\boldsymbol{r}} = \mathbb{I} + i\hat{\boldsymbol{w}} \cdot \delta\boldsymbol{r} = \mathbb{I} - \frac{i}{4} f_{\mu\upsilon\eta} n^\mu \hat{T}^\eta \partial_{\boldsymbol{r}} n^\upsilon \cdot \delta\boldsymbol{r}. \tag{111}$$

To demonstrate this statement, we need to show that the operator field $\mathfrak{n}(\boldsymbol{r})$ is transformed into $\mathfrak{n}(\boldsymbol{r}+\delta\boldsymbol{r})$

$$\begin{aligned}\hat{U}_{\boldsymbol{r}+\delta\boldsymbol{r},\boldsymbol{r}}\mathfrak{n}(\boldsymbol{r})\hat{U}^{\dagger}_{\boldsymbol{r},\delta\boldsymbol{r}} =&\mathfrak{n}(\boldsymbol{r})+\frac{i}{4}f_{\mu\nu\eta}n^{\mu}\partial_{\boldsymbol{r}}n^{\nu}\cdot\delta\boldsymbol{r}\left[\mathfrak{n}(\boldsymbol{r}),\hat{T}^{\eta}\right]=\mathfrak{n}(\boldsymbol{r})+\frac{1}{4}n^{\alpha}n^{\mu}f_{\mu\nu\eta}f_{\alpha\epsilon\eta}\hat{T}^{\epsilon}\partial_{\boldsymbol{r}}n^{\nu}\cdot\delta\boldsymbol{r}\\ =&\mathfrak{n}(\boldsymbol{r})+\frac{1}{4}n^{\alpha}n^{\mu}\partial_{\boldsymbol{r}}n^{v}\cdot\delta\boldsymbol{r}\hat{T}^{\epsilon}\left[\frac{8}{3}\left(\delta_{\mu\alpha}\delta_{v\epsilon}-\delta_{\mu\epsilon}\delta_{\alpha v}\right)+4\left(d_{\mu\alpha\eta}d_{v\epsilon\eta}-d_{v\alpha\eta}d_{\mu\epsilon\eta}\right)\right].\end{aligned} \tag{112}$$

By using the following relationships that can be obtained from the constraint given in Eq. (11) of the main text:

$$\partial_{\boldsymbol{r}}n^{m}n^{m} = 0, \tag{113}$$

$$\partial_{\boldsymbol{r}}n^{m} = 3d_{mqp}n^{p}\partial_{\boldsymbol{r}}n^{q}, \tag{114}$$

$$d_{\mu\alpha\eta}n^{\mu}n^{\alpha} = \frac{2}{3}n^{\eta}, \tag{115}$$

$$\frac{2}{3}n^{\eta}d_{v\epsilon\eta}\partial_{r}n^{\nu} = \frac{2}{9}\partial_{r}n^{\epsilon}, \tag{116}$$

$$d_{v\alpha\eta}\partial_{r}n^{v}n^{\alpha} = \frac{1}{3}\partial_{r}n^{\eta}, \tag{117}$$

$$\frac{1}{3}d_{\epsilon\alpha\eta}n^{\mu}\partial_{r}n^{\eta} = \frac{1}{9}\partial_{r}n^{\epsilon}, \tag{118}$$

we obtain the desired result:

$$\hat{U}_{\boldsymbol{r}+\delta\boldsymbol{r},\boldsymbol{r}}\mathfrak{n}(\boldsymbol{r})\hat{U}^{\dagger}_{\boldsymbol{r}+\delta\boldsymbol{r},\boldsymbol{r}}=\mathfrak{n}(\boldsymbol{r})+\partial_{\boldsymbol{r}}\mathfrak{n}(\boldsymbol{r})\cdot\delta\boldsymbol{r}=\mathfrak{n}(\boldsymbol{r}+\delta\boldsymbol{r}). \tag{119}$$

Since $\partial_{\boldsymbol{r}}|\boldsymbol{Z}\rangle = i\hat{w}_{\delta\boldsymbol{r}}|\boldsymbol{Z}\rangle$, we have:

$$\begin{aligned}\partial_x\mathcal{A}_y-\partial_y\mathcal{A}_x &= i\left(\partial_x\langle\boldsymbol{Z}|\right)\left(\partial_y|\boldsymbol{Z}\rangle-\partial_y\langle\boldsymbol{Z}|\right)\left(\partial_x|\boldsymbol{Z}\rangle\right)=\\ &= i\left\langle\boldsymbol{Z}\left|[\hat{w}_x,\hat{w}_y]\right|\boldsymbol{Z}\right\rangle-\frac{1}{16}f_{\mu\nu\eta}f_{\eta\gamma\epsilon}f_{\alpha\beta\gamma}n^{\mu}n^{\eta}n^{\epsilon}\partial_x n^{\nu}\partial_y n^{\beta}\\ &= \frac{1}{4}f_{\alpha\beta\gamma}\partial_x n^{\gamma}\partial_y n^{\beta}n^{\alpha}\\ &= -\frac{i}{8}\operatorname{Tr}\left(\mathfrak{n}\left[\partial_x\mathfrak{n},\partial_y\mathfrak{n}\right]\right)=-\frac{i}{16}\varepsilon_{jk}\operatorname{Tr}\left(\mathfrak{n}\left[\partial_j\mathfrak{n},\partial_k\mathfrak{n}\right]\right),\end{aligned} \tag{120}$$

where we have used the following relationships:

$$n^\mu n^\epsilon f_{\mu\nu\eta} f_{\gamma\epsilon\eta} = \frac{8}{3}(n^\gamma n^\nu - \frac{4}{3}\delta_{\nu\gamma}) + 4(n^\mu n^\epsilon d_{\mu\gamma\eta} d_{\nu\epsilon\eta} - \frac{2}{3} d_{\nu\gamma\eta} n^\eta), \tag{121}$$

$$\begin{aligned} \partial_x n^\nu n^\mu n^\epsilon f_{\mu\nu\eta} f_{\gamma\epsilon\eta} &= -\frac{32}{9}\partial_x n^\gamma + \frac{4}{3} n^\mu d_{\mu\gamma\eta} \partial_x n^\eta - \frac{8}{9}\partial_x n^\gamma \\ &= -\frac{32}{9}\partial_x n^\gamma + \frac{4}{9}\partial_x n^\gamma - \frac{8}{9}\partial_x n^\gamma = -4\partial_x n^\gamma. \end{aligned} \tag{122}$$

This concludes the demonstration of Eq. (109). From this result and Eq. (105), we obtain:

$$C = -\frac{i}{32\pi}\int \mathrm{d}^2 x \varepsilon_{jk} \,\mathrm{Tr}\left(\mathfrak{n}\left[\partial_j \mathfrak{n}, \partial_k \mathfrak{n}\right]\right) = \frac{1}{2\pi}\int \mathrm{d}x\ \mathrm{d}y \left(\partial_x \mathcal{A}_y - \partial_y \mathcal{A}_x\right). \tag{123}$$

F.2 On the lattice

For lattice systems, the color field is only defined on discrete lattice points. Thus, to compute the skyrmion number of a given spin configuration we must introduce an interpolation procedure that allows us to to define the spin configuration on any point of the plane $\mathbb{R}^2$. This can be done by connecting color fields $\mathfrak{n}_j$ and $\mathfrak{n}_k$ on nearest-neighbor sites j and k along the geodesic in CP^2. According to this prescription, the contribution to the skyrmion number of a given triangular plaquette jkl of the triangular lattice is:

$$\rho_{jkl} = -\frac{i}{32\pi}\int_{\Delta_{jkl}} \mathrm{d}x\mathrm{d}y \varepsilon_{jk} \,\mathrm{Tr}\left(\mathfrak{n}\left[\partial_j \mathfrak{n}, \partial_k \mathfrak{n}\right]\right), \tag{124}$$

where $\triangle_{jlk}$ is the triangle formed by the lattice sites jkl. Consequently, the total skyrmion number is equal to the sum of this contribution over all the triangles jkl of the triangular lattice:

$$C = \sum_{\Delta_{jkl}} \rho_{jkl}. \tag{125}$$

Our next step is to demonstrate that:

$$\rho_{jkl} = \frac{1}{2\pi}\left(\gamma_{jl} + \gamma_{lk} + \gamma_{kj}\right), \tag{126}$$

where

$$\gamma_{kj} = \arg\left[\langle \boldsymbol{Z}_k \mid \boldsymbol{Z}_j \rangle\right] \tag{127}$$

is the Berry connection on the bond $j \to k$ and

$$\gamma_{jl} + \gamma_{lk} + \gamma_{kj} = \oint_{\Delta_{jkl}} \mathcal{A}_j dx^j \tag{128}$$

is the Berry phase associated with the triangle jkl. From Eqs. (108) and (105), we have

$$\rho_{jkl} = -\frac{i}{32\pi} \int_{\Delta_{jkl}} \mathrm{d}x\mathrm{d}y \varepsilon_{jk} \,\mathrm{Tr}\left(\mathfrak{n}\left[\partial_j \mathfrak{n}, \partial_k \mathfrak{n}\right]\right) = \frac{1}{2\pi} \oint_{\Delta_{jkl}} \mathcal{A}_j dx^j. \tag{129}$$

Consequently, we just need to demonstrate Eq. (126).

We first note that, *up to a phase factor* $e^{i\delta\varphi}$, the "geodesic" SU(3) spin rotation that connects the coherent states $|\boldsymbol{Z}(\boldsymbol{r})\rangle$ and $|\boldsymbol{Z}(\boldsymbol{r}+\delta\boldsymbol{r})\rangle$ is the one given in Eq. (22) and it can be rewritten as

$$e^{i\delta\varphi}|\boldsymbol{Z}(\boldsymbol{r}+\delta\boldsymbol{r})\rangle = \hat{U}_{\boldsymbol{r},\delta\boldsymbol{r}}|\boldsymbol{Z}(\boldsymbol{r})\rangle = \left(\mathbb{I} + \frac{i}{4}\left[\mathfrak{n}(\boldsymbol{r}), \partial_{\boldsymbol{r}}\mathfrak{n}(\boldsymbol{r})\right]\delta\boldsymbol{r}\right)|\boldsymbol{Z}(\boldsymbol{r})\rangle. \tag{130}$$

The next observation is that:

$$\mathfrak{n}(\boldsymbol{r})|\boldsymbol{Z}(\boldsymbol{r})\rangle = \frac{2}{\sqrt{3}}|\boldsymbol{Z}(\boldsymbol{r})\rangle \tag{131}$$

by definition of the coherent state $|\boldsymbol{Z}(\boldsymbol{r})\rangle$. Consequently, we have

$$e^{i\delta\varphi} = \left\langle \boldsymbol{Z}(\boldsymbol{r}+\delta\boldsymbol{r}) \left| \left(\mathbb{I} + \frac{i}{4}\left[\mathfrak{n}(\boldsymbol{r}), \partial_{\boldsymbol{r}}\mathfrak{n}(\boldsymbol{r})\right]\delta\boldsymbol{r}\right) \right| \boldsymbol{Z}(\boldsymbol{r}) \right\rangle \tag{132}$$

or

$$e^{i\delta\varphi} = \langle \boldsymbol{Z}(\boldsymbol{r}+\delta\boldsymbol{r}) \mid \boldsymbol{Z}(\boldsymbol{r})\rangle + \left\langle \boldsymbol{Z}(\boldsymbol{r}) \left| \left(\frac{i}{4}\left[\mathfrak{n}(\boldsymbol{r}), \partial_{\boldsymbol{r}}\mathfrak{n}(\boldsymbol{r})\right]\delta\boldsymbol{r}\right) \right| \boldsymbol{Z}(\boldsymbol{r}) \right\rangle = \langle \boldsymbol{Z}(\boldsymbol{r}+\delta\boldsymbol{r}) \mid \boldsymbol{Z}(\boldsymbol{r})\rangle, \tag{133}$$

where we have used that $\langle \boldsymbol{Z}(\boldsymbol{r}) \left|\left[\mathfrak{n}(\boldsymbol{r}), \partial_r \mathfrak{n}(\boldsymbol{r})\right]\right| \boldsymbol{Z}(\boldsymbol{r})\rangle = 0$ because of Eq. (131). This important result shows that, to linear order in $\delta\boldsymbol{r}$, the Berry phase accumulated by the

rotation of the coherent state state $|\boldsymbol{Z}(\boldsymbol{r})\rangle$ along a geodesic of CP^2 is equal the the overlap $\langle \boldsymbol{Z}(\boldsymbol{r}+\delta\boldsymbol{r}) \mid \boldsymbol{Z}(\boldsymbol{r})\rangle$.

Let us consider now the Berry phase that is obtained when the coherent state $|\boldsymbol{Z}_j\rangle$ is rotated into the coherent state $|\boldsymbol{Z}_k\rangle$ along the SU(3) geodesic that connects these two points. After dividing the rotation $\hat{U}_{\boldsymbol{r}_k,\boldsymbol{r}_j}$ into a product of $N\to\infty$ small rotations:

$$\hat{U}_{\boldsymbol{r}_{kj}/N} = \exp\left\{\frac{i}{4N}\left[\mathfrak{n}\left(\boldsymbol{r}_j\right),\mathfrak{n}\left(\boldsymbol{r}_k\right)\right]\right\}, \tag{134}$$

$$\begin{aligned}\gamma_{kj} &= \arg\left[\left\langle \boldsymbol{Z}_k\left|\hat{U}_{\boldsymbol{r}_k,\boldsymbol{r}_j}\right|\boldsymbol{Z}_j\right\rangle\right] = \arg\left[\left\langle \boldsymbol{Z}_k\left|\left(\hat{U}_{\boldsymbol{r}_{kj}/N}\right)^N\right|\boldsymbol{Z}_j\right\rangle\right]\\ &= \arg\left[\left\langle \boldsymbol{Z}_k\left|\hat{U}_{\boldsymbol{r}_{kj}}/N\right|\boldsymbol{Z}\left(\boldsymbol{r}_k-\boldsymbol{r}_{kj}/N\right)\right\rangle\left\langle \boldsymbol{Z}\left(\boldsymbol{r}_k-\boldsymbol{r}_{kj}/N\right)\left|\hat{U}_{\boldsymbol{r}_{kj}/N}\ldots\right|\boldsymbol{Z}\left(\boldsymbol{r}_j+\boldsymbol{r}_{kj}/N\right)\right\rangle\right.\\ &\left.\times\left\langle \boldsymbol{Z}\left(\boldsymbol{r}_j+\boldsymbol{r}_{kj}/N\right)\left|\hat{U}_{\boldsymbol{r}_{kj}}/N\right|\boldsymbol{Z}_j\right\rangle\right],\end{aligned} \tag{135}$$

where $\boldsymbol{r}_{kj}\equiv\boldsymbol{r}_k-\boldsymbol{r}_j$ and the last identity is obtained by inserting expansions of the identity between the unitary operations in an orthonormal basis that includes the coherent state $|\boldsymbol{Z}\left(\boldsymbol{r}_j+n\boldsymbol{r}_{kj}/N\right)\rangle$ for the identity operator that is inserted on the left of $\left(\hat{U}_{\boldsymbol{r}_{kj}/N}\right)^n$ with $1\le n\le N$. After taking the $N\to\infty$ limit and using Eq. (133),

$$\begin{aligned}&\lim_{N\to\infty}\arg\left[\left\langle \boldsymbol{Z}\left(\boldsymbol{r}_j+(n+1)\boldsymbol{r}_{kj}/N\right)\left|\hat{U}_{\boldsymbol{r}_{kj}/N}\right|\boldsymbol{Z}\left(\boldsymbol{r}_j+n\boldsymbol{r}_{kj}/N\right)\right\rangle\right]\\ &=\lim_{N\to\infty}\arg\left[\left\langle \boldsymbol{Z}\left(\boldsymbol{r}_j+(n+1)\boldsymbol{r}_{kj}/N\right)\mid\boldsymbol{Z}\left(\boldsymbol{r}_j+n\boldsymbol{r}_{kj}/N\right)\right\rangle\right]\end{aligned} \tag{136}$$

we obtain the desired result:

$$\gamma_{kj} = \arg\left[\left\langle \boldsymbol{Z}_k\left|\hat{U}_{\boldsymbol{r}_k,\boldsymbol{r}_j}\right|\boldsymbol{Z}_j\right\rangle\right] = \int_0^{|\boldsymbol{r}_k-\boldsymbol{r}_j|}\left\langle \boldsymbol{Z}(a)\left|\partial_a\right|\boldsymbol{Z}(a)\right\rangle \mathrm{d}a \tag{137}$$

with $|\boldsymbol{Z}(a)\rangle = \hat{U}_{\boldsymbol{r}_j+a\hat{\boldsymbol{r}}_{kj},\boldsymbol{r}_j}\left|\boldsymbol{Z}\left(\boldsymbol{r}_j\right)\right\rangle$ and $\hat{\boldsymbol{r}}_{kj}\equiv\boldsymbol{r}_k-\boldsymbol{r}_j/\left|\boldsymbol{r}_k-\boldsymbol{r}_j\right|$, which implies Eq. (128).

G Mapping between color field and SU(3) coherent states

Eq. (126) is clearly very useful when we are working with coherent states (the $\boldsymbol{Z}$-field) instead of working with the color field $\mathbf{n}(\boldsymbol{r})$. In the latter case, it may be useful to find a coherent state $|\boldsymbol{Z}(\boldsymbol{r})\rangle$ associated with the field $\mathbf{n}(\boldsymbol{r})$ to keep using the simple formula provided by Eq. (126) . Note that the coherent state $|\boldsymbol{Z}(\boldsymbol{r})\rangle$ is defined up to a phase factor (gauge freedom), which does not affect the value of the Berry phase on a closed loop. Correspondingly, we just need a procedure that allows us to find some state $|\boldsymbol{Z}(\boldsymbol{r})\rangle$ (a particular gauge choice) for a given $\mathbf{n}(\boldsymbol{r})$.

Eq. (10) of the main text establishes a mapping $|\boldsymbol{Z}_j\rangle \to \mathbf{n}(\boldsymbol{r})$ between an SU(3) coherent state $|\boldsymbol{Z}(\boldsymbol{r})\rangle$ and the color field $\mathbf{n}(\boldsymbol{r})$. Let us find the inverse mapping $\mathbf{n}(\boldsymbol{r}) \to |\boldsymbol{Z}_j\rangle$ keeping in mind that a coherent states are defined up to a phase factor (gauge freedom). Given the highest weight state, $|+1\rangle$ that satisfies:

$$\hat{T}_j^3 |+1\rangle = \frac{2}{\sqrt{3}} |+1\rangle , \tag{138}$$

we can obtain the coherent state $|\boldsymbol{Z}(\boldsymbol{r})\rangle$ by applying an SU(3) transformation $\hat{U}$ that satisfies

$$\begin{aligned} |\boldsymbol{Z}_j\rangle &= \hat{U}_j |+1\rangle \\ \mathbf{n}_j &= \frac{2}{\sqrt{3}} \hat{U}_j \hat{\tilde{T}}_j^3 \hat{U}_j^\dagger . \end{aligned} \tag{139}$$

This immediately implies that $|\boldsymbol{Z}(\boldsymbol{r})\rangle$ is the highest-weight eigenstate of the color field $\mathbf{n}(\boldsymbol{r})$

$$\mathbf{n}_j |\boldsymbol{Z}_j\rangle = \frac{2}{\sqrt{3}} |\boldsymbol{Z}_j\rangle , \tag{140}$$

and allows us to obtain the coherent state $|\boldsymbol{Z}(\boldsymbol{r})\rangle$ for given color field $\mathbf{n}(\boldsymbol{r})$. As expected, the normalized eigenstate $|\boldsymbol{Z}(\boldsymbol{r})\rangle$ is defined up to a multiplicative phase factor.

Vita

Hao Zhang was born in 1994 and grew up in Chongqing, China. In 2012, he attended the physics department at Sichuan University (Chengdu, China) as an undergraduate student. Subsequently, he received a B.S. in physics in 2016. In the same year, he came to the University of Tennessee to pursue a Ph.D. degree in physics. He joined the group of Prof. Cristian Batista to study theoretical condensed matter physics in May of 2017 and worked for five years as a research assistant before receiving his Ph.D. in 2022. He will continue working in the area of quantum magnetism as a postdoc.